Deciphering the Origins of FRBs Using Local Universe CHIME/FRB Discoveries

Mohit Bhardwaj

Doctor of Philosophy

Department of Physics
McGill University
Montreal, Quebec, Canada

November 2022

A thesis submitted to McGill University in partial fulfillment of the requirements of the degree of Doctor of Philosophy

Abstract

Fast radio bursts (FRBs) are one of astronomy's greatest mysteries. These millisecond-duration radio pulses are powerful enough to be observed from distant galaxies. Although over a thousand FRBs have been discovered to date, their origin remains a hotly debated topic primarily due to the dearth of FRBs with known hosts. A promising method to narrow down FRB origins is by identifying their hosts and/or multi-wavelength counterparts. More importantly, with milliarcsecond localization precision, it is possible to study the FRBs' local environment in the host, which is crucial to test if the FRB progenitors constitute an old or young stellar population. However, due to the limited sensitivity of telescopes operating in the optical and X-ray wavebands, multi-wavelength follow-up is most promising for local Universe sources ($z < 0.1$).

The Canadian Hydrogen Intensity Mapping Experiment (CHIME) is a transit radio telescope operating in the frequency range of 400-800 MHz. Due to its enormous field-of-view ($\sim$220 sq.deg.), large collecting area (8000 sq.m.), broad frequency coverage (400-800 MHz), and highly sophisticated software back-end, CHIME has revolutionized the FRB field by discovering the majority of all known FRB sources to date. For some of the CHIME FRBs, we acquire raw voltage data that can facilitate localization to sub-arcminute or a few arcminutes precision. This angular resolution can be sufficient to identify host galaxies of local Universe FRBs due to the low chance association probability.

In this thesis, we discuss the pipeline that facilitates the identification of plausible host galaxies of the local Universe CHIME FRBs. Using this pipeline, we identified host galaxies of the two closest extragalactic FRBs discovered to date, FRB 20200120E and FRB 20181030A. FRB 20200120E has the dispersion measure of 87.82 pc cm^{-3}, which is the lowest recorded from an FRB to date. The FRB appears on the outskirts of M81 (projected offset $\sim$ 20 kpc), a spiral galaxy at a distance of 3.6 Mpc, but well inside its extended HI and thick disks. We search for prompt X-ray counterparts in *Swift*/BAT and *Fermi*/GBM data, and for two of the FRB 20200120E bursts, we rule out coincident SGR 1806$-$20-like X-ray bursts. For FRB 20181030A, we identify NGC 3252, a star-forming spiral galaxy located at the distance of $\approx$ 20 Mpc, as its most likely host. With the discovery of this second-closest extragalactic FRB, we argue that a population of young millisecond magnetars alone cannot explain the observed volumetric rate of repeating FRBs.

In addition to these two closest extragalactic FRBs, we perform follow-up studies of two nearby repeating CHIME FRBs, FRB 20180814A and 20190303A. For FRB 20180814A, the second repeating FRB discovered in 2018, we find an early-type lenticular galaxy at the spectroscopic redshift of 0.068 as its plausible host. If this galaxy is not the FRB host, we argue that the host of FRB 20180814A will be the faintest host known to date. For FRB 20190303A, we identify a merging pair of star-forming spiral galaxies at the spectroscopic redshift of 0.064 as its most likely host. These two vastly different host associations clearly highlight the complex nature of FRB host and progenitor populations.

Abrégé

Les sursauts radio rapides (FRB) constituent lún des plus grands mystéres de lástronomie. Ces impulsions radio dúne durée de quelques millisecondes sont suffisamment puissantes pour être observées depuis des galaxies lointaines. Bien que plus dún millier de FRBs aient été découverts á ce jour, leur origine reste un sujet trés débattu, principalement en raison de la rareté des FRBs dont les hôtes sont connus. Une méthode prometteuse pour déterminer lórigine des FRB consiste á identifier leurs hôtes etou leurs homologues á plusieurs longueurs d'onde. Plus important encore, avec une précision de localisation de l'ordre de la milliarcseconde, il est possible d'étudier l'environnement local des FRBs dans l'hôte, ce qui est crucial pour vérifier si les progéniteurs des FRBs constituent une population stellaire jeune ou vieille. Cependant, en raison de la sensibilité limitée des télescopes fonctionnant dans les bandes d'ondes optiques et X, le suivi multi-longueur d'onde est plus prometteur pour les sources de l'Univers local ($z < 0.1$).

The Canadian Hydrogen Intensity Mapping Experiment (CHIME) est un radiotélescope de transit fonctionnant dans la gamme de fréquences de $400-800$ MHz. Grâce á son énorme champ de vision (220 degrés carrés), á sa grande surface de collecte (8000 métres carrés), á sa large couverture en fréquence (400-800 MHz) et á son logiciel trés sophistiqué, CHIME a révolutionné le domaine des FRB en découvrant la majorité des objets suivants de toutes les sources de FRB connues á ce jour. Pour certains des FRBs de CHIME, nous acquérons des données de tension brutes qui peuvent faciliter la localisation avec une précision inférieure á la minute d'arc ou á quelques minutes d'arc. Cette résolution angulaire peut être suffisante pour identifier les galaxies hêtes des FRBs de l'Univers local en raison de la faible probabilité d'association fortuite.

Dans cette thése, nous discutons du pipeline qui facilite l'identification des galaxies hôtes plausibles des FRBs de l'Univers local CHIME. En utilisant ce pipeline, nous avons identifié les galaxies hôtes des deux FRBs extragalactiques les plus proches découverts á ce jour, FRB 20200120E et FRB 20181030A. FRB 20200120E a une mesure de dispersion de 87.82 pc cm^{-3}, ce qui est la plus faible enregistrée á ce jour pour un FRB. Les FRB apparaissent á la périphérie de M81 (décalage projeté $\sim$ 20 kpc), une galaxie spirale á une distance de 3.6 Mpc, mais bien á l'intérieur de ses disques HI étendus et épais. Nous recherchons des contreparties rapides en rayons X dans les données de *Swift*/BAT et *Fermi*/GBM, et pour deux des sursauts FRB 20200120E, nous excluons les sursauts X coïncidents de type SGR 1806−20. Pour le FRB 20181030A, nous identifions NGC 3252, une galaxie spirale de formation d'étoiles située á une distance d'environ 20 Mpc, comme son hôte le plus probable. Avec la découverte de ce deuxiéme FRB extragalactique le plus proche, nous soutenons qu'une population de jeunes magnétars millisecondes ne peut pas expliquer á elle seule le taux volumétrique observé de FRBs répétés.

En plus de ces deux FRBs extragalactiques les plus proches, nous effectuons des études de suivi de deux FRBs CHIME répétitifs proches, les FRB 20180814A et 20190303A. Pour FRB 20180814A, le deuxiéme FRB répétitif découvert en 2018, nous trouvons une galaxie lenticulaire de type précoce au redshift spectroscopique de 0.068 comme son hôte plausible. Si cette galaxie n'est pas l'hôte du FRB, nous soutenons que l'hôte du FRB 20180814A sera l'hôte le plus faible connu á ce jour. Pour le FRB 20190303A, nous identifions une paire fusionnée de galaxies spirales á formation d'étoiles au redshift spectroscopique de 0.064 comme son hôte le plus probable. Ces deux associations d'hôtes trés différentes soulignent clairement la nature complexe des populations hôtes et progénitrices des FRB.

Acknowledgements

It has been a roller coaster ride to reach this stage in my career, and I owe much of my success to individuals who provided assistance, support, and unending encouragement along the way. Working on the CHIME project has so far been the most thrilling experience of my scientific career. Numerous discussions and feedback from the members of the CHIME/FRB collaboration have assisted me to strengthen my weaknesses and develop my strengths. To everyone who helped make this thesis a reality, I extend my most genuine and heartfelt appreciation.

First and foremost I wish to thank my advisor, Dr. Victoria Kaspi. Despite her hectic schedule, she is always there for her students. Her passion for FRBs, eagerness for new ideas, and ability to lead a large team are contagious! She gave me the freedom to explore my ideas while at the same time acting as a rudder to ensure that I did not deviate from my primary objective of submitting this Ph.D. thesis on time. She never hesitated to give her honest feedback, which pushed me to become a better researcher. I can always look to her as a source of inspiration and encouragement. Saint Kabir Das, a 15th-century Indian mystic poet, penned one of my favourite couplets, which I think captures the profound impact of having her as my supervisor more effectively than I could ever do in my own words:

गुर कुम्हार सिख कुंभ है गढ़ गढ़ काढ़ै खोट
अंतर हात सहार दै बाहर बाहै चोट

In English, it translates as follows: a true teacher (“guru") is akin to the potter, and the student to the pot. The guru strokes the outside of the pot to shape it while supporting it from within with their other hand so that it does not break. Such is the intensity of their care and concern to make the disciple (student) righteous. Vicky, you have my deepest gratitude and admiration for being a guru to me.

I would also like to express my gratitude to Dr. Bryan Gaensler, whom I am honoured to call my mentor. He is one of the most conscientious individuals I have ever met. He was there whenever I needed guidance. Despite of his hectic schedule, I cannot recall a time when he did not respond to my slack message within a day! I had so many fascinating academic conversations with him, and he never once made me realized that he was a renowned professor of astronomy and I was merely a PhD student; this is something I wish to emulate in my own life. Thanks so much, Bryan! I am looking forward to continuing to learn from you.

Additionally, I would want to thank Dr. Matt Dobbs, who taught me the importance of knowing your instruments and developing a sharp eye for detail in research. I thank Dr. Shriharsh Tendulkar, a friend and mentor, who was one of the reasons I decided to undertake multi-wavelength follow-ups of FRBs. I would also like to convey my gratitude to the members for the CHIME/FRB project office: Dr. Patrick (Jojo) Boyle, Chitrang Patil, Shiny Brar, and Dr. Emily Petroff, for being resourceful and supportive. I thank Adam Gilbert, Dr. Dallas Wulf, Dr. Daniele Michilli, Dr. Emmanuel Fonseca, Dr. Seth Seigel, Dr. Saurabh Singh, and for their guidance and help in the projects presented in this thesis.

I would also want to thank the following friends I made in Montreal with whom I have so many cherished memories: Prashansa, Rahul, Gaurav, Raghav, Andrew, Shivendra, Deniz, Lisa, Samskruthi, Sujatha, Riya, Satinder, Ranjani, Paul, Arnab, Sabrina, Matheus, and Aaron. A special thanks to Sujatha, who was always there for me through my troubles and joys. This list of acknowledgements would be incomplete without mentioning my best friends – Harish, Arpit, and Ravina – who motivated and pushed me to pursue a scientific career. I would also like to thank the members of Vicky's group at McGill for their unwavering support and for making working on FRBs at McGill a very rewarding experience.

Lastly, I cannot thank my family enough for their constant love, care, encouragement, and pride in my achievements. I greatly appreciate their unwavering support. Without their

grace and love, I would not be here today. Ma, Papa, Bhaiya, and Di — I will always love you!

Preface

Contribution to Original Knowledge and Contribution of Authors

Chapter 1 provides a literature review on fast radio bursts (FRBs), with a focus on topics pertinent to this thesis.

Chapter 2: Analog Bad-channel Classifier for CHIME

Chapter 2 provides a brief summary of the front-end and analog chain of the CHIME telescope. It also presents an automatic pipeline developed to identify bad hardware channels of the CHIME telescope, which is currently being used as one of the tools to monitor experimental health and data-integrity of CHIME (CHIME Collaboration et al., 2022). I developed the pipeline under the guidance of Dr. Matt Dobbs and Dr. Seth Siegel. I was a member of the CHIME/Cosmology back-end commissioning team from 2017 to 2019, where I contributed to the understanding of various artifacts in CHIME data.

Chapter 3: The CHIME/FRB Project Overview

Chapter 3 summarizes the CHIME correlators, the CHIME/FRB real-time pipeline and the baseband pipeline. Being a member of the CHIME/FRB collaboration, I helped with the commissioning of the CHIME/FRB back-end, particularly the assembly and the installation of the computing nodes. I was also a member of the data quality team for the CHIME/FRB system, and along with Dr. Paul Scholz, I was responsible for updating the CHIME/FRB repeater webpage[1].

Chapter 4: FRB-λ: Pipeline to Identify Hosts of Nearby CHIME FRBs

Chapter 4 describes the pipeline that identifies plausible host galaxy candidates of nearby CHIME/FRBs with baseband localizations. I developed and implemented the pipeline, based on discussions with members of the CHIME/FRB collaboration, especially the following members of the CHIME/FRB project office: Shiny Brar and Dr. Tarik Zegmott.

I have utilized the pipeline and its numerous routines in the analyses described in the following publications: CHIME/FRB Collaboration et al. (2019a), CHIME/FRB Collaboration et al. (2019c), Fonseca et al. (2020), Marcote et al. (2020), Leung et al. (2021), Bhardwaj et al. (2021a), Kirsten et al. (2021), Bhardwaj et al. (2021b), Rafiei-Ravandi et al. (2021), CHIME/FRB Collaboration et al. (2022), Curtin et al. (2022), and The LIGO Scientific Collaboration et al. (2022).

Chapter 5: A Nearby Repeating Fast Radio Burst in the Direction of M81

This chapter reports on discovery of the lowest-DM FRB to date, FRB 20200120E with CHIME. Using the CHIME/FRB baseband localization region of the FRB, we identified M81 as its most likely host. The FRB is now conclusively found to be associated with an M81 globular cluster (Kirsten et al., 2021) that we identified. The contents of this chapter originally appeared in the following paper published in the Astrophysical Journal Letters:

M. Bhardwaj, B. M. Gaensler, V. M. Kaspi, T. L. Landecker, R. Mckinven, D. Michilli, Z. Pleunis, S. P. Tendulkar, B. C. Andersen, P. J. Boyle, T. Cassanelli, P. Chawla, A. Cook, M. Dobbs, E. Fonseca, J. Kaczmarek, C. Leung, K. Masui, M. Mnchmeyer, C. Ng, M. Rafiei-Ravandi, P. Scholz, K. Shin, K. M. Smith, I. H. Stairs, and A. V. Zwaniga. A Nearby Repeating Fast Radio Burst in the Direction of M81. ApJ, 910, 2.

The author contributions are as follows: Dr. Daniele Michilli estimated baseband localizations of the two FRB 20200120E bursts and contributed to the Section 2.1. Dr. Ziggy

[1] see: https://www.chime-frb.ca/repeaters.

Pleunis made Figure 5.1, estimated best-fit DMs of the FRB bursts, and contributed to the Section 2.2. Dr. Ryan Mckinven determined the polarization properties of the bursts and authored the text in Section 2.3. Dr. Emmanuel Fonseca determined the burst widths and scattering timescales which are reported in Table 5.1. Flux and fluence results for bursts reported in Table 5.1 were obtained using web-based tools internal to CHIME/FRB. The flux/fluence pipeline code was originally developed and written by Bridget Andersen.

I performed all the other analysis and wrote remainder of the manuscript. Dr. Victoria Kaspi provided guidance throughout the research and writing process. All other co-authors are members of the CHIME/FRB collaboration who provided feedback on the analysis and the paper draft.

Chapter 6: A Local Universe Host for the Repeating Fast Radio Burst FRB 20181030A

This chapter reports on the association of the repeating FRB 20181030A discovered by CHIME/FRB Collaboration et al. (2019c) with a nearby star-forming spiral galaxy, NGC 3252, at a distance of 20 Mpc, making it the second closest extragalactic FRB discovered to date. The contents of this chapter originally appeared in the following paper published in the Astrophysical Journal Letters:

M. Bhardwaj, A. Y. Kirichenko, D. Michilli, Y. D. Mayya, V. M. Kaspi, B. M. Gaensler, M. Rahman, S. P. Tendulkar, E. Fonseca, A. Josephy, C. Leung, M. Merryfield, E. Petroff, Z. Pleunis, P. Sanghavi, P. Scholz, K. Shin, K. M. Smith, and I. H. Stairs. A Local Universe Host for the Repeating Fast Radio Burst FRB 20181030A. ApJ, 919, 2.

The author contributions are as follows. Dr. Daniele Michilli estimated baseband localizations of the four FRB bursts and made Figure 6.1. Dr. Aida Kirichenko led GTC MOS and long-slit observations and contributed to the text in Section 2.3. Dr. Divakara Mayya calibrated the long-slit spectrum of NGC 3252, and wrote Section 6.1. S/N-optimized burst DMs reported in Table 6.1 were obtained using web-based tools internal to CHIME/FRB. The S/N-optimized DM pipeline code was originally developed and written by Dr. Ziggy Pleunis. Dr. Emmanuel Fonseca determined the burst widths and scattering timescales which are reported in Table 5.1. Flux and fluence results for bursts reported in Table 5.1

were obtained using web-based tools internal to CHIME/FRB. The flux/fluence pipeline code was originally developed and written by Bridget Andersen. I performed all the other analysis and wrote remainder of the manuscript. Dr. Victoria Kaspi provided guidance throughout the research and writing process. All other co-authors are members of the CHIME/FRB collaboration who provided feedback on the analysis and the paper draft.

Chapter 7: A Search for the Host Galaxy of FRB 20180814A

This chapter reports on the search for the host of the repeating FRB 20180814A discovered by CHIME/FRB Collaboration et al. (2019c). From our search, we found PanSTARRS-DR1 J042256.01+733940.7, a nearby (z= 0.06835) passive red spiral galaxy, as the only plausible host within the 2σ baseband localization region. The contents of this chapter are part of a manuscript which will soon be submitted to the Astrophysical Journal:

D. Michilli, **M. Bhardwaj**, et al., Interferometric localization of repeating Fast Radio Bursts detected by CHIME/FRB, to be submitted to The Astrophysical Journal[2].

The combined baseband localization of FRB 20180814A is estimated by Dr. Daniele Michilli. GTC observations are reduced by Dr. Aida Kirichenko, which are discussed in Section 3.4. I completed all other analyses and wrote the chapter.

Chapter 8: A Search for the Host Galaxy of FRB 20190303A

This chapter reports on the likely association of the repeating FRB 20190303A discovered by Fonseca et al. (2020) with a local Universe merging pair of two star-forming galaxies at a redshift of 0.064, SDSS J135159.17+480729.0 and SDSS J135159.87+480714.2. The contents of this chapter are part of a manuscript which will soon be submitted to the Astrophysical Journal:

D. Michilli, **M. Bhardwaj**, et al., Interferometric localization of repeating Fast Radio

[2]Both first and second authors contributed equally to the publication.

Bursts detected by CHIME/FRB, to be submitted to The Astrophysical Journal[2].

The combined baseband localization of FRB 20180814A is estimated by Dr. Daniele Michilli. I performed all of the FRB 20190303A host association analyses presented in this work and authored the chapter.

Contents

List of Figures

List of Tables

Chapter 1

Introduction

Fast radio bursts (FRBs) are an exciting new frontier for astrophysics. These extremely powerful radio blasts can travel cosmological distances and emit more energy than the Sun does in a thousand years, despite lasting only a few thousandths of a second (Petroff et al., 2021). The first FRB, FRB 20010724A, was serendipitously discovered in 2007 by Lorimer et al. (2007); hence, it is also known as 'the Lorimer burst' (see Figure 1.1). However, FRBs were not universally accepted as an astrophysical phenomenon then. The initial skepticism was mainly due to the possibility of the Lorimer burst to be an electromagnetic interference. Indeed, the discovery of a microwave oven at the Parkes Observatory in Australia as the source of 'perytons' (Petroff et al., 2015), millisecond-duration radio signals of terrestrial origin that mimic several characteristics of FRBs (Burke-Spolaor et al., 2011), bolstered suspicions about FRBs' astrophysical origin. It was not until the discovery of five more FRBs (Keane et al., 2012, Thornton et al., 2013) that their astrophysical origin became widely accepted. Furthermore, the hypothesis that FRBs are likely cosmological transients gained momentum only in 2017 when FRB 20121102A, the first repeated FRB ever discovered, was localized to an irregular star-forming dwarf galaxy at z = 0.1927 (Chatterjee et al., 2017, Tendulkar et al., 2017).

Since the discovery of the Lorimer burst, over 800 FRBs have been reported to date[1]. Recently, The CHIME/FRB Collaboration et al. (2021) estimated the all-sky rate of bright

[1] For a complete list of known FRBs, see `https://www.herta-experiment.org/frbstats/` or the TNS (Yaron et al., 2020).

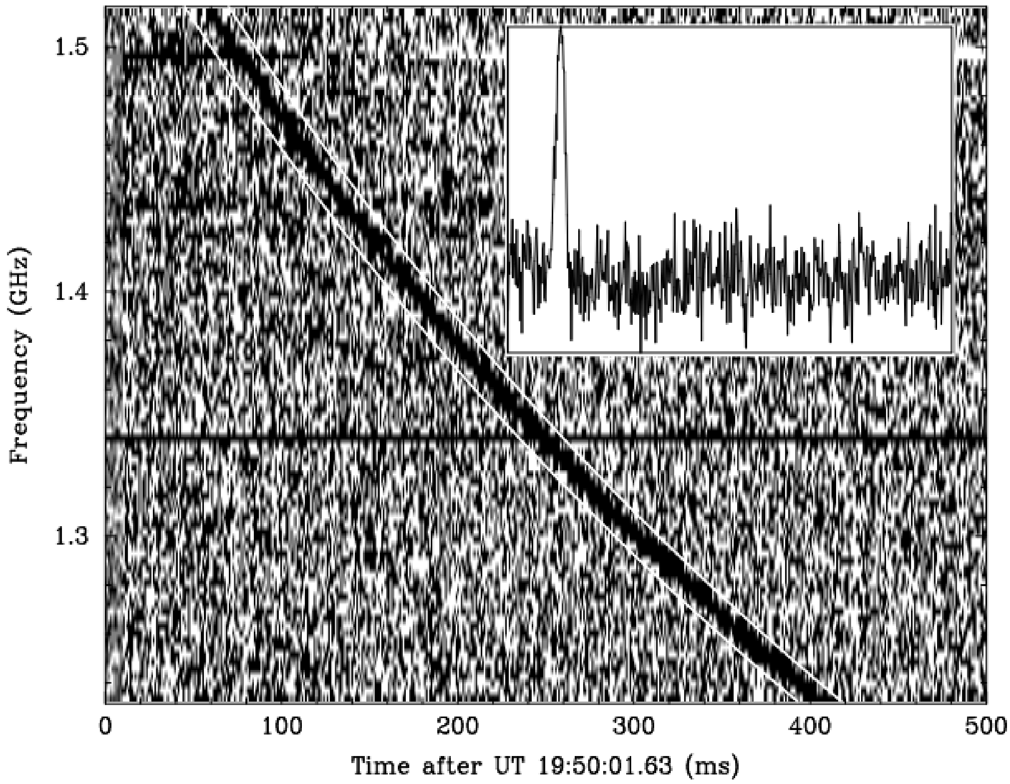

Figure 1.1: Frequency versus time (“waterfall") plot of FRB 20010724A aka Lorimer burst. The white arcs around the pulse (black curve) represent the predicted delay for a DM of 375 pc cm^{-3}. The time series obtained after correcting for dispersive delay and summing the signal in all frequency channels is shown in the inset. Figure from Lorimer et al. (2007).

FRBs ($\geq$ 5 Jy ms) to around 800 events per day, and established the isotropy of the sky distribution of FRBs (Josephy et al., 2021) making them a fairly common astrophysical radio transient. However, the origin of FRBs continues to be a subject of intense debate, owing in part to a limited sample of localized FRBs. Furthermore, the FRBs exhibit a diverse range of phenomenology: most of the discovered bursts are apparently non-repeating (simply non-repeating FRBs from hereon), but a small fraction are observed to repeat. Among the repeating FRBs, two thus far have shown evidence of periodic repetitions (CHIME/FRB Collaboration et al., 2020b, Cruces et al., 2020, Rajwade et al., 2020). As a result, a plethora of theories has been proposed to explain the FRB sources' disparate behaviour (see Platts et al., 2018, for a catalogue of proposed models). In fact for much of FRB history, there have been more theories about what the origins of FRBs are than there were detected FRBs. Regardless of that, these radio bursts hold great promise for cosmological studies (Macquart et al., 2020). As these bursts of radiation travel through space and pass through ionized gases, their lower-frequency emissions are delayed relative to their higher-frequency ones, causing otherwise sharp pulses to broaden. This broadening is quantified by a parameter called dispersion measure (DM). We can estimate the amount of ionized baryons the radio waves travelled through on their way to Earth by measuring their DMs. FRBs are thus an excellent astrophysical probe for studying ionized baryonic matter throughout the Universe.

This chapter is organized as follows: In Section 1, we describe major observational characteristics of FRBs and in Section 2, we summarize the constraints derived about the nature of FRB progenitors using the properties of FRB host galaxies and their local environment. In Section 3, we discuss the FRB origin problem including major proposed FRB progenitor models and emission mechanisms. Finally, we present the outline of this thesis in Section 4.

1 Major FRB observable

In this section, we review major characteristics of FRBs that can help us understand their sources and the properties of propagating media. A typical FRB pulse traverses through multiple uniquely characterized media on its way to Earth, including the circumburst medium, the ionized gas in the interstellar medium (ISM) of the host galaxy, the intergalactic medium (IGM), and the ionized gas in the halo and disk of the Milky Way, all of which leave their imprints on the FRB pulse. These imprints, in turn, allow FRBs to be used as probes of intervening plasma. It is also important to study these propagation effects in order to infer the intrinsic properties of FRBs. We briefly summarize significant FRB observables below, but readers are urged to refer to Lorimer and Kramer (2004) for a more detailed description.

1.1 Dispersion measure

Dispersion measure (DM) is unarguably the most important observable of FRBs that is used to differentiate them from anthropogenic signals as well as radio emission from Galactic neutron stars. In scientific terms, DM is defined as the integral column density of free electrons n_e along the propagation path (l) of FRBs from source S to observer O:

$$\mathrm{DM} = \int_{\mathrm{S}}^{\mathrm{O}} \mathrm{n_e dl}. \tag{1.1}$$

The FRB DMs consist of the DM contribution from the Milky Way ISM, Milky Way halo, IGM (including the contribution from the halos of intervening galaxies), and the host (which consists of the contribution from the host ISM, halo, and circumburst medium) such that,

$$\mathrm{DM_{FRB}} = \mathrm{DM_{host}}/(1+\mathrm{z}) + \mathrm{DM_{MW}} + \mathrm{DM_{MW,halo}} + \mathrm{DM_{IGM}}. \tag{1.2}$$

Currently, we know FRBs of DM as large as 3037 pc cm^{-3} (The CHIME/FRB Collaboration et al., 2021) and as small as 88 pc cm^{-3} (see Chapter 5). As almost all FRBs (with the sole exception of the SGR 1935+2154 radio bursts detected by CHIME/FRB and STARE2; Bochenek et al., 2020, CHIME/FRB Collaboration et al., 2020a) known to be extragalactic, their dispersion measure is significantly larger in general than the expected DM contribution from the Milky Way's interstellar medium, which can be calculated using electron density models in the Galaxy (Cordes and Lazio, 2002, Yao et al., 2017). More importantly, the excess-DM of FRBs (after subtracting the Galactic contribution) is found to correlate well with the redshifts of the FRB sources with a considerable scatter (Macquart et al., 2020). Hence, the excess-DM is often used as a proxy for FRB source's redshift. In fact, by assuming that the contribution of the host galaxy and the circumburst medium is negligible, one can estimate the maximum possible redshift for an FRB source using several analytically derived $\mathrm{DM_{IGM}}$−redshift relationships (for example, $\mathrm{DM_{IGM}} \approx 930\mathrm{z}$ pc cm^{-3} at low redshifts; Macquart et al., 2020).

1.2 Scattering

FRBs are excellent probes of the inhomogeneous and turbulent intervening medium (Cordes et al., 2016). The inhomogeneities in the electron density along the FRB sight-line can produce phase modulation of the FRB emission resulting in the fluctuation of intensity over different frequency bandwidths and timescales. This phenomenon is called scintillation.

The inhomogeneities in the propagating media also scatter FRB pulses resulting in the broadening of otherwise sharp pulses producing a characteristic asymmetric "exponential tail" feature that is seen in the time series of many FRBs. In fact, about 30% of FRBs exhibit this scattering feature, that can be clearly differentiated from the intrinsic FRB pulse profile (Chawla et al., 2022). Many authors argue that these propagation effects are likely dominated by either the local environment, or the interstellar medium of the host galaxy (Chawla et al., 2022, CHIME/FRB Collaboration et al., 2019b, Cordes et al., 2016, Masui et al., 2015, Ocker et al., 2022). Hence, scintillation and/or scattering measurements of FRBs can be useful in constraining the local environment of FRBs (Masui et al., 2015) and can help in improving Galactic electron density models (Main et al., 2022).

1.3 Polarization properties

FRBs are highly polarized sources of radio emission (Petroff et al., 2021). Their polarization properties can reveal the nature of FRB local environment, as well as the FRB emission mechanism, hence, can play a crucial role in uncovering FRB progenitor models. There are three relevant polarization observables for FRBs: (1) rotation measure (RM), (2) polarization position angle (PA), and (3) polarization fraction (more importantly, fraction of linearly polarized emission). Note that these parameters are only available for handful of them (~ 30; Caleb and Keane, 2021) where full Stokes polarization data products were saved. Therefore, due to small sample size, caution should be used when interpreting the inferences about the FRB population using the polarization observables. Now, we summarize major observations made using the three polarization properties.

When a linearly polarized FRB pulse propagates through diffuse magnetized plasma in the Universe from its source (S) to the observer (O), its plane of polarization rotates with frequency; this phenomena is called Faraday rotation. The degree of rotation induced by the magneto-ionized medium is quantified by the RM, which is defined as follows,

$$\mathrm{RM} = 0.81 \int_{\mathrm{S}}^{\mathrm{O}} \mathrm{B}_{||} \mathrm{n_e} \mathrm{dl}, \tag{1.3}$$

where $\mathrm{B}_{||}$ is the magnetic field aligned parallel to the direction of the propagation of the FRB pulse. RMs can offer important clues to the origins of FRBs. For example, the extremely large and variable RM of the repeating FRBs 20121102A and 20190520B (Anna-Thomas et al., 2022, Michilli et al., 2018) suggests a young compact object embedded in dense and highly-magnetized local environment as their source (Margalit and Metzger, 2018, Zhang, 2018). Non-repeating FRBs, on the other hand, have RMs that are several orders of magnitude smaller and are comparable to those of Galactic pulsars (Wang et al., 2020b). However, it is unclear whether there is a substantial difference between repeating and non-repeating FRBs premised on the fairly small sample size of available RMs.

Apart from RMs, the fraction of polarized flux density of FRB emission, quantified by polarization fraction, and how it changes with frequency can also help in constraining the emission mechanism. Almost all existing FRB emission models predict FRBs to be 100% linearly polarized sources (Lyubarsky, 2021, and references therein). However, a subset of FRBs were discovered to exhibit significant circular polarization (for example, FRB 20140514A), and a very small fraction showed no polarization at all (for example, FRB 20150418A) (Caleb and Keane, 2021). It is yet unclear if the low linear polarization fraction (zero in the case of FRB 20150418A) is intrinsic to the emission mechanism or caused by propagation effects, such as Faraday conversion (Beniamini et al., 2022), or due to instrumental biases (Hilmarsson et al., 2021). Interestingly, Feng et al. (2022) reported that wide-band polarization measurements of some repeating FRBs showed a trend of lower polarization fraction at lower frequencies, which could be explained using multi-path scattering of FRBs due to their highly dynamic circumburst environment. However, it is uncertain if the low polarization fraction observed in several non-repeating FRBs may be attributed to this effect.

Finally, the polarization position angle across the burst phase provides additional constraints on FRB emission models. The polarization position angle is the angle between the plane of linear polarization and the plane of reference (linked to the radio telescope's polarized feeds). For instance, a good fraction of FRBs show constant polarization angle. This could be attributed to short emission timescale and depends on the location of emitting particles (Lyubarsky, 2021). However, some non-repeating FRBs exhibit variable polarization position angles, for example FRB 20180301A (Luo et al., 2020), contrary to what have seen in the case of many repeating FRBs (CHIME/FRB Collaboration et al., 2019c, Fonseca et al., 2020, Michilli et al., 2018). It is very hard to explain diversity of PAs in relativistic shock models, whereas, magnetospheric emission models can easily accommodate such variations (Luo et al., 2020) (see Section 3.2). But in literature, there exists examples, for instance Crab pulsar's giant pulses (GPs), where constant PAs are observed in one specific mode (high frequency interpulse mode), and variable PA behaviour is noted in another mode (main pulse mode) (Jessner et al., 2010). It is yet to be seen if there exists such bi-modality in the PA behaviour of FRBs.

1.4 Duration

FRBs show intrinsic widths or durations of around $\sim \mu$s - ms timescales (Caleb and Keane, 2021, Petroff et al., 2021). Many FRBs are temporally unresolved by their discovery telescopes, and in some cases, targeted follow-up observations of repeating FRBs using sensitive radio telescopes found temporal structures $\lesssim 1\ \mu$s (Majid et al., 2021, Nimmo et al., 2022b). Using the causality argument, in the absence of any bulk relativistic motion, the very short FRB duration implies a small emitting region of characteristic size $\lesssim c\Delta t$ = 300 km $\frac{\Delta \mathrm{t}}{1\mathrm{ms}}$. This favours a neutron star and an accreting stellar mass black hole as promising sources (Zhang et al.).

1.5 Repetition and periodicity

Fast radio bursts (FRBs) are observed to be either repeating or apparently non-repeating (one-off). The vast majority of FRBs falls in the apparently non-repeating category and only a small fraction of FRBs (around 2 dozen) are known to repeat (CHIME/FRB Collaboration et al., 2019a,c, Fonseca et al., 2020, Kumar et al., 2019, Lanman et al., 2022, Luo et al., 2020, Niu et al., 2022, Spitler et al., 2016, Chapter 5) in spite of the fact that some of them have been intensively monitored to search for possible repeating bursts (James et al., 2020, Petroff et al., 2015, Shannon et al., 2018). However, it is possible that non-repeating FRBs are produced by sources that have long periods of quiescence, or that the sources emit repeat bursts that are too faint to be detected by present radio telescopes. Therefore, whether all FRBs repeat remains an unsolved mystery (Ai et al., 2021, Caleb et al., 2019, James, 2019, Palaniswamy et al., 2018, Ravi, 2019). On a positive note, the repetition enabled milliarcsecond localization of repeating FRBs (Kirsten et al., 2021, Marcote et al., 2017, Marcote et al., 2020, Nimmo et al., 2022b) as well as the first unambiguous identification of the host galaxy (Chatterjee et al., 2017, Marcote et al., 2017, Tendulkar et al., 2017).

More interesting, among repeating FRBs, two thus far have shown evidence of periodic repetitions: FRB 20180916B with a period of $\approx$ 16.3 days (CHIME/FRB Collaboration et al., 2020b), and FRB 20121102A with a period of $\approx$ 160 days (Cruces et al., 2020, Rajwade et al., 2020). It is still unclear if all repeating FRBs would show periodic repetition if observe long enough.

Recently, CHIME/FRB Collaboration et al. (2022) reported the detection of the multi-component FRB 20191221A which showed periodicity of 216.8 ms with a significance of 6.5σ. Similarly, Pastor-Marazuela et al. (2022) discovered FRB 20201020A with Apertif (van Leeuwen et al., 2022), which showed regularly spaced five sub-bursts with periodicity of 0.415 ms (significance $\approx\ 2.5\sigma$). This short-timescale periodicity is different from the long-term periodicity that the two repeating FRBs discussed above showed. It supports a neutron-star origin of these short-timescale periodic FRBs (Zhang, 2020). Long-timescale periodicity, on the other hand, can be addressed within the context of binary (Dai and Zhong, 2020, Ioka and Zhang, 2020, Lyutikov et al., 2020) or precession models (Levin et al., 2020, Yang and Zou, 2020, Zanazzi and Lai, 2020).

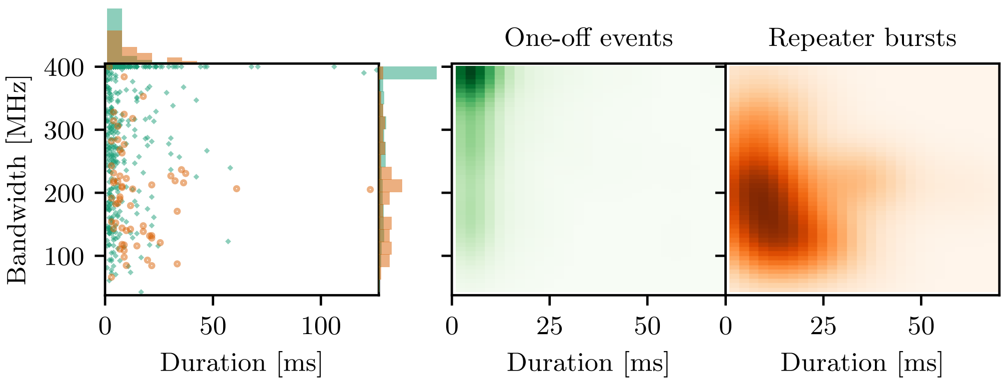

Figure 1.2: A comparison of the durations and bandwidths of CHIME/FRB Catalogue-1 FRBs. Blue diamonds represent non-repeating FRBs, while red open circles show repeating FRBs. The normalized histograms on the right indicate that non-repeating FRBs are narrower in width and have a greater bandwidth than repeating FRBs, which are wider in width and occupy a smaller bandwidth. Figure from Pleunis et al. (2021).

1.6 Pulse morphology

The FRB light-curve data exhibit a plethora of spectral and temporal structures. Even after excluding spectral features caused by the propagation effects, such as scattering and scintillation, there are variety of seemingly intrinsic burst morphologies that can be a powerful proxy for understanding burst emission and propagation. For example, repeating FRBs show complex spectral and temporal downward-drifting sub-structures, which have previously been established as a characteristic spectro-temporal feature of repeating FRBs (CHIME/FRB Collaboration et al., 2019c, Day et al., 2020, Fonseca et al., 2020, Hessels et al., 2019). This includes micro-structures on timescales of $\sim$ 60 ns - 100 μs (Cho et al., 2020, Farah et al., 2018, Majid et al., 2021, Nimmo et al., 2021, 2022a). This constrains the size of the emission region to be as small as around 20 m (ignoring any bulk relativistic motion). Recently, Pleunis et al. (2021) considered the burst morphologies of all FRBs in the first CHIME/FRB catalogue (The CHIME/FRB Collaboration et al., 2021, see Chapter 3) and identified different archetypes of burst morphology. They compared the temporal widths and frequency bandwidths of non-repeating FRBs with those of repeating bursts and found a statistically significant observed difference between the two, with repeater bursts on average having a longer duration and being narrower in bandwidth (see Figure 1.2). This difference could be due to beaming or propagation effects, or it could be intrinsic to the populations.

1.7 Energetics

Once their hosts have been identified, FRB fluxes and fluences can be converted into isotropic-equivalent luminosities and energies. Note that there is no evidence yet that FRBs radiate isotropically. Nevertheless, the isotropic-equivalent peak luminosity (energy) of localized cosmological FRBs vary from $\sim 10^{38}$ erg s^{-1} (10^{35} erg) to $\sim 10^{46}$ erg s^{-1} (10^{43} erg) (Zhang, 2020). However, in case of local Universe FRBs, FRBs 20200120E (see Chapter 5) and 20181030A (see Chapter 6), the estimated isotropic luminosities can be as low as few 10^{36} erg s^{-1} (10^{33} erg). Nevertheless, the energy and luminosity of FRBs is orders of magnitude larger than those of Galactic pulsars (see Figure 1.3). Note that true energetics could be considerably smaller if FRBs are beamed emission by a factor given by f_b =

$\max(\Delta\Omega/4\pi, 1/4\gamma^2)$, where $\Delta\Omega$ and γ are the solid angle of the FRB emission beam and the bulk Lorentz factor of the FRB emitting particles, respectively.

Knowing the luminosities (energies) of several FRBs, it is possible to constrain the FRB luminosity/energy function, which is the FRB event rate per unit cosmic co-moving volume per unit luminosity(energy) and characterizes the fundamental properties of the FRB population. The luminosity or energy function can then be used to investigate FRB origins and possible progenitors (Arcus et al., 2021, Hashimoto et al., 2020a,b, 2022, James et al., 2022, Locatelli et al., 2019, Lu and Piro, 2019, Lu et al., 2020b, Luo et al., 2018, 2020, Macquart and Ekers, 2018, Shin et al., 2022). We note that the true shape and form of the FRB luminosity or energy function is still unclear. Nevertheless, several authors used either a power-law or a Schechter function to model them. Nothing concrete has been derived from those analyses, primarily due to the paucity of localized FRBs. Additionally, follow-up analyses using the Five-hundred-meter Aperture Spherical Telescope (FAST) for two repeating FRBs, FRBS 20121102A and 20201124A, reveal substantially different energy distributions. The cumulative energy energy distribution of FRB 20201124A is best fitted by a broken power law (Xu et al., 2021), whereas the energy distribution of FRB 20121102A is found to be bimodal and best characterized by a combination of a log-normal function and a generalized Cauchy function (Li et al., 2021). Therefore, it is unclear whether all FRBs have a universal energy function.

1.8 Multi-wavelength counterparts

To unveil the nature of FRB sources and test different progenitor models, detailed follow-up of the possible multi-wavelength counterparts of FRBs is one important way forward. Such studies in the past have helped in proving the existence of two separate classes of gamma ray bursts (Kulkarni, 2018). FRBs so far have been solely a radio phenomenon, with the exception of FRB-like radio bursts from a Galactic magnetar SGR 1935+2154, where contemporaneous X-ray emission was detected by a number of X-ray telescopes (Bochenek et al., 2020, CHIME/FRB Collaboration et al., 2020a, Li et al., 2020, Mereghetti et al., 2020, Ridnaia et al., 2020).

Several FRB models (see Section 3) predict prompt multi-wavelength counterparts. For

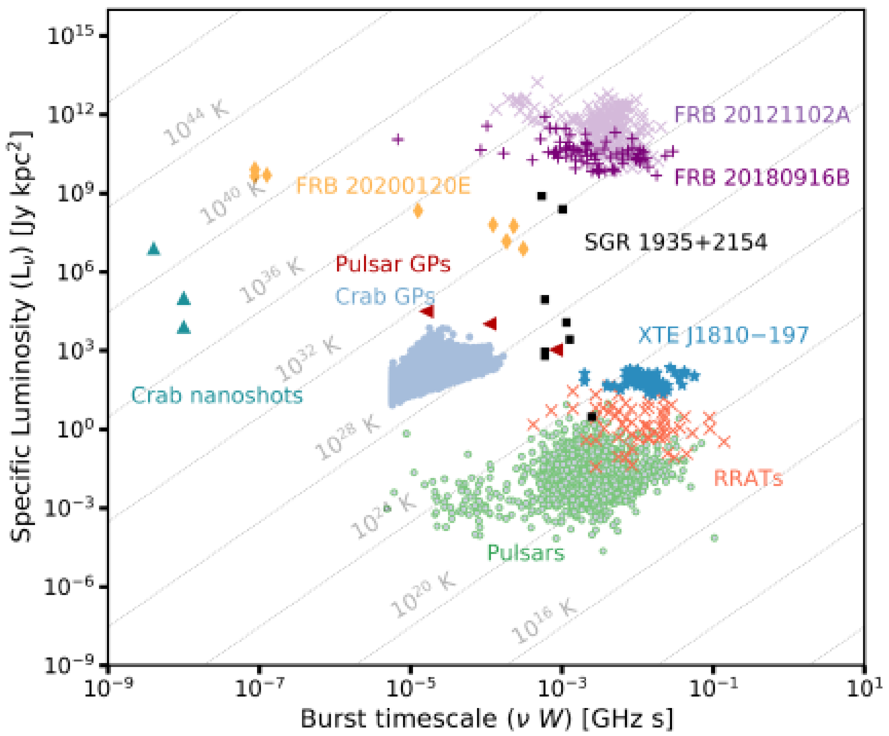

Figure 1.3: Phase space of ∼GHz radio transients. The grey diagonal lines denote constant brightness temperature contours. Figure from Caleb and Keane (2021).

example, the synchrotron maser model predicts nearly contemporaneous emission in γ-ray, X-ray and optical/NIR bands on sub-second timescales (Metzger et al., 2019). However, these predicted counterparts can only be detected for local Universe FRBs. There have also been multi-wavelength follow-up campaigns and archive searches for FRBs that spatially and/or temporally coincide with cataclysmic events like soft gamma repeaters, supernovae and gamma ray bursts, but no confirmed association has been made to date (Anumarlapudi et al., 2020, Casentini et al., 2020, Cunningham et al., 2019, Curtin et al., 2022, DeLaunay et al., 2016, Madison et al., 2019, Marnoch et al., 2020, Martone et al., 2019, Men et al., 2019, Mereghetti et al., 2021, Núñez et al., 2021, Palaniswamy et al., 2014, Sakamoto et al., 2021, Scholz et al., 2017, 2020, Tendulkar et al., 2016, Verrecchia et al., 2021).

Interestingly, only two FRBs, FRBs 20121102A and 20190520B (Chatterjee et al., 2017, Niu et al., 2022), were found to be spatially associated with a persistent radio source

(PRS), despite radio follow-up observations of other localized FRBs reaching lower flux limits (Bannister et al., 2019, Bhandari et al., 2020, 2022, Heintz et al., 2020, Law et al., 2022). However, the nature of those PRSs and their connection with the FRB sources are still unclear. Constraints from radio light curves and X-ray limits can be explained by invoking either a low-luminosity active Galactic nucleus or a dense circumburst nebula (Bassa et al., 2017, Cao et al., 2017, Chen et al., 2022, Dai et al., 2017, Kashiyama and Murase, 2017, Law et al., 2022, Scholz et al., 2016).

2 Host galaxies & local environments

The vast majority of FRBs observed to date were discovered using radio telescopes with limited angular resolution. However, to fully realize their potential as cosmic probes, more precise localization of FRBs that enable host identification is required. Moreover, detailed studies of FRB hosts and their local environments are a promising way to unveil the nature of FRB sources (Li and Zhang, 2020, Nicholl et al., 2017). Currently, only ~ 20 published FRBs have been sufficiently well localized on the sky to allow their host galaxies to be identified.[2] These localized FRBs except FRBs 20200120E (3.6 Mpc; see Chapter 5) and 20181030A (20 Mpc; see Chapter 6) are located at redshifts ranging from 0.03 to 0.66 where the detailed study of the FRB local environment is limited by the sensitivity of current telescopes.

In 2017, the first host identification was made using direct interferometric localization of repeat bursts from FRB 121102 (Chatterjee et al., 2017), the first repeating FRB ever discovered (Spitler et al., 2016). From optical follow-up studies, the FRB source was found to be located in a star-forming region of a faint (absolute r-band magnitude ≈ -17 AB mag) low-metallicity dwarf irregular galaxy at z = 0.1927 (Bassa et al., 2017, Tendulkar et al., 2017). Because of the similarities to the hosts of long GRBs and superluminous supernovae (SLSNe), young and highly-active magnetar models were proposed as the origin of the FRB (Margalit and Metzger, 2018, Metzger et al., 2019). However, FRB 20121102A host later was found to be significantly different from the host of later localized FRBs (Heintz et al., 2020), making it an outlier. It wasn't until 2022 that the host of another repeating FRB

[2] See http://frbhosts.org/ (visited on 01/07/2022).

20190520B was discovered in a galaxy similar to that of FRB 20121102A, which also had a spatially coincident persistent radio source (Niu et al., 2022). This suggested that there might be a distinct class of FRBs like FRBs 20121102A and 20190520B.

Overall, according to the limited sample of localized hosts, FRBs inhabit a wide range of hosts and local environments (See Figure 1.4; Bhandari et al., 2022, Heintz et al., 2020). This is true even if we consider only the hosts of localized repeating FRBs. For example, FRB 20180916B located in a nearby spiral galaxy with a low star-formation rate (≈ 0.0166 $M_\odot$ yr^{-1}; Marcote et al., 2020) has projected offset of 250 pc from the nearest starforming region, not expected if the FRB source is a young neutron star (Tendulkar et al., 2020). More surprisingly, the source of the closest extragalactic FRB 20200120E (see Chapter 5) was found to be located in an M81 globular cluster (Kirsten et al., 2021), which harbours extremely old stellar population. The latter discovery provides the strongest evidence yet of the existence of multiple FRB populations.

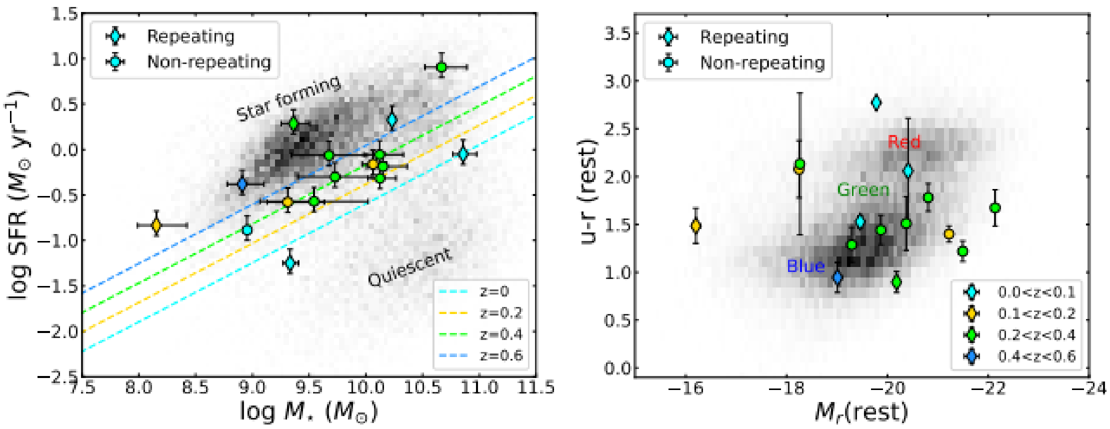

Figure 1.4: Star-formation rate and stellar mass distributions (left), and restframe colour-magnitude (right) of FRB host galaxies compared to galaxies at z< 0.6 taken from the PRIMUS survey. Figure from Bhandari et al. (2022).

From the demographic analysis of the limited sample of FRB hosts, it is observed that the host galaxies of known repeating FRBs tend to be less massive and less luminous on average, compared to that of non-repeating FRBs (Bhandari et al., 2022). Moreover, the FRB locations in the hosts in most cases show significant offsets from the galaxy centres. According to a high spatial resolution Hubble optical and near-infrared data analysis of a subset of FRB hosts, most FRBs are not located in regions of elevated local star formation and stellar mass surface densities compare to their hosts' mean global values (Mannings et al., 2020). Overall, FRBs, both repeating and non-repeating, are found in a variety of galaxy types and it is not yet clear if the two populations are intrinsically different. However, we caution that the sample sizes considered in these analyses were small. Hence, more localizations are required to make robust conclusions about the FRB host population. Fortunately, this will change in the next two-three years when telescopes, such as CHIME/FRB outriggers (Cassanelli et al., 2022), the Deep Synoptic Array (DSA)-110 (Hallinan et al., 2019) and the Commensal Real-time ASKAP Fast Transients Survey (CRAFT; Macquart et al., 2010), will add several hundreds of host associations every year.

3 What produces FRBs?

Despite the fact that over 800 FRBs have been published to date, the origins of FRBs remain an unsolved mystery. This is partly due to the fact that we have a small sample of localized FRBs and constraints are mainly derived using radio observations (except SGR 1935+2154 bursts). It should be highlighted that the FRB origin problem can be split into two parts: first, what sorts of FRB sources can produce FRBs? Second, how do the proposed FRB sources generate powerful bursts of highly coherent and short-duration radiation? The first question is more tractable than the second, and it is concerned with physically possible astrophysical systems capable of accounting for FRB observables such as all-sky rate, redshift distribution, host properties, and local environments. The second question involves identifying plausible emission mechanisms that can explain the observed temporal and spectro-polarimetric properties of FRBs which is far more challenging to address. The following two sections provide a quick overview of our current understanding of the FRB source and emission models.

3.1 Emission mechanism model

The short duration and high luminosity of FRBs suggest an extremely large brightness temperature, T_b, which is estimated according to the Rayleigh-Jeans law:

$$T_b \sim 10^{35}\,\mathrm{K}\frac{F_{\nu,\mathrm{Jy}} D^2_{\mathrm{Gpc}}}{\tau^2_{\mathrm{ms}} \nu^2_{\mathrm{GHz}}}, \tag{1.4}$$

where $F_{\nu,\mathrm{Jy}}$ is the flux density of the FRB in Jansky, τ_{ms} is the pulse width or duration in ms, D_{Gpc} is the distance of the FRB source in Gpc, and ν_{GHz} is the observation frequency in GHz. The temperature of 10^{35} K is neither physically possible for a radiating source, nor is there any known incoherent process that can achieve it (Rybicki and Lightman, 1986). Therefore, the extremely high brightness temperature implies that the FRB radiation mechanism is coherent, i.e., radiation is produced by the “clump" of charges that are emitting radiation in-phase (Melrose, 2017).

There are currently two leading categories of emission models to explain the high brightness temperature of FRBs (Lyubarsky, 2021, and references wherein). First, pulsar emission-like models, which use magnetopheric disturbances around compact objects to generate FRBs (e.g. Lu and Kumar, 2018), and the second are relativistic shock models (Babul and Sironi, 2020, Lyubarsky, 2014), which were earlier used to explain gamma ray burst prompt emission (Duncan and Thompson, 1992, Gruzinov and Waxman, 2019).

In the first category, the theoretically most plausible models are the ones that either invoke local disturbances, such as crustal movements or starquakes induced flares (Beloborodov, 2017, Parfrey et al., 2013, Wang et al., 2018, 2019), and sudden interactions with external plasma streams (Dai et al., 2016, Sridhar et al., 2021, Yang and Zhang, 2020, Yang et al., 2020, Zhang, 2017), which trigger magnetic reconnection events in the magnetosphere. The reconnection events in turn produce relativistic magnetosonic waves which eventually escapes as FRBs, or coherent curvature emission from charged bunches (Ghisellini and Locatelli, 2018, Katz, 2018, Kumar and Bošnjak, 2020, Kumar et al., 2017, Wang et al., 2020a), similar to pulsar radiation mechanisms (Cordes and Wasserman, 2016). In these models, one main requirement is that the compact object must have magnetic field significantly greater than 10^{12} G (Lu et al., 2020a), hence, require the compact object to be a magnetar. This scenario is shown in Figure 1.5(a).

In the second category, the idea is to produce coherent bunches of charged particles via maser synchrotron mechanisms in relativistic shocks outside the magnetosphere of the compact object (Beloborodov, 2020, Lyubarsky, 2020, Metzger et al., 2019). In this model, it is required that the pre-shock outflow is highly magnetized and the shock itself is mildly relativistic (Lorentz factor ~ 100; Margalit and Metzger, 2018). Additionally, the magnetized pre-outflow condition requires the compact object to have magnetic field $> 10^9$ G (Wang and Lai, 2020). This scenario is shown is shown in Figure 1.5(b).

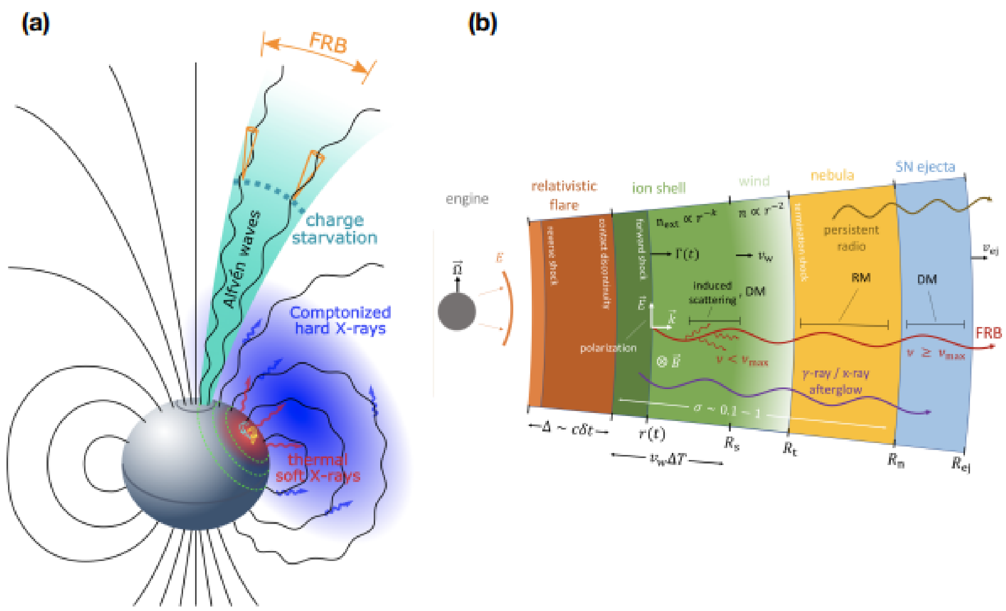

Figure 1.5: Animated representations of the two main types of FRB radiation models: a) pulsar-like models that invoke a compact object's magnetosphere; and b) GRB-like models that invoke relativistic shocks powered by a compact central engine. Figure from Zhang (2020).

3.2 FRB source model

Because both of the emission models outlined above require a strongly magnetized central engine, neutron stars and accreting black holes are the most likely FRB source candidates according to them. There are theories that invoke exotic sources, such as strange or quark stars (Geng et al., 2021, Zhang et al., 2018), axion stars (Iwazaki, 2017, Raby, 2016), white holes (Barrau et al., 2014), and cosmic strings (Brandenberger et al., 2017, Ye et al., 2017, Zadorozhna, 2015), as FRB progenitors. However, because the physical existence of these sources is unproven, we will not discuss them in this section. For more detailed discussion on them, see the FRB Theory Catalogue[3].

There are also models that invoke cataclysmic events like mergers of compact objects (neutron stars, black holes, and white dwarfs) and gamma ray bursts to explain intrinsically non-repeating FRBs (Deng et al., 2018, Falcke and Rezzolla, 2014, Kashiyama et al., 2013, Totani, 2013, Zhang, 2014) or repeating FRBs as predecessors to these events (Falcke and Rezzolla, 2014, Liu, 2018, Mingarelli et al., 2015). However, all-sky rates of the cataclysmic events are orders of magnitude lower than that of FRBs (Ravi, 2019). Deep multi-wavelength follow-ups and archive searches also yielded no promising results (see Section 1.8). But, it is still possible that a small fraction of FRBs can be associated with these transient events.

3.3 Magnetars as FRB sources

Magnetars or strongly magnetized neutron stars (with typical surface magnetic field of $\sim 10^{14}$ Gauss), identified observationally as short gamma repeaters (SGRs) or anomalous X-ray pulsars (Kaspi and Beloborodov, 2017), are one of the most popular FRB source candidates (Zhang, 2020). Their ultimate energy source is the neutron star's magnetostatic energy. It is proposed that both SGRs and FRBs are produced by the decay of this energy store via mechanisms such as massive flares (Lyubarsky, 2021) Note that typical SGR energy budget is orders of magnitude larger than the energy inferred for some of the brightest bursts of localized repeaters (Kaspi and Beloborodov, 2017). Therefore, unlike rotation-powered FRB models, where the energy is extracted from the rotation of the neutron star, there is no fundamental limitation on the radiated power.

Among all the proposed FRB source models, the prospects of magnetars to be the source of FRBs is the highest, especially after the detection of FRB-like radio bursts from

[3] https://frbtheorycat.org/index.php

a Galactic magnetar, SGR 1935+2154, which suggests that at least some FRBs can be produced by magnetars (Bochenek et al., 2020, CHIME/FRB Collaboration et al., 2020a). Additionally, they satisfy major requirements of both the emission models (see Section 3.2). More importantly, the magnetars via SGRs also satisfy the FRBs' all-sky rate constraint (Bochenek et al., 2020, Margalit et al., 2020).

Magnetars are thought to be formed by the core-collapse of the highly magnetized massive stars (Muno et al., 2006) or by binary neutron star mergers (Duncan and Thompson, 1992, Giacomazzo and Perna, 2013) or possibly by the accretion induced collapse (AIC) of white dwarf and binary white dwarf merger (Ruiter et al.). In that case, we do expect magnetars to be found in both young as well as old stellar systems. Therefore, the discovery of repeating FRBs in star-forming regions (such as FRBs 20121102A and 20190520B; Chatterjee et al., 2017, Niu et al., 2022) as well as in a globular cluster (FRB 20200120E; Kirsten et al., 2021) is not unusual. However, there is no observational evidence for any magnetar born from a neutron star merger or AIC; all confirmed Galactic magnetars are close to the Galactic Plane, and several of them possess supernova remnants, strongly suggesting that they are young neutron stars (e.g. Olausen and Kaspi, 2014). Therefore, more FRB localizations and firm associations of extragalactic FRBs with magnetars are needed before concluding that FRBs are indeed powered by magnetars.

4 Thesis outline

The objective of this thesis is to advance our current understanding of the origins of FRBs by using local Universe CHIME/FRB discoveries. This thesis is organized into nine chapters, some of which have been adapted from published papers. In Chapter 2, we introduce the Canadian Hydrogen Intensity Mapping Experiment (CHIME) and describe one of the pipelines which identifies malfunctioning analog components of the telescope. Chapter 3 describes the CHIME/FRB project and the CHIME/FRB real-time detection pipeline. Chapter 4 discusses the pipeline that facilitates the identification of plausible host galaxies of the local Universe CHIME FRBs. In Chapter 5, we report the discovery of the closest extragalactic FRB known to date, FRB 20200120E, which is located at the outskirts of M81 (projected offset ~ 20 kpc), a spiral galaxy at a distance of 3.6 Mpc. Chapter 6 reports on the discovery of the second closest extragalactic FRB, FRB 20181030A, to a local Universe star-forming spiral galaxy, NGC 3252, and discusses the implications of this association on proposed FRB source models. In Chapter 7, we describe our search for the host galaxy of FRB 20180814A, the first repeating FRB discovered by the CHIME/FRB Collaboration in August 2018 (CHIME/FRB Collaboration et al., 2019a) and the second one ever discovered. Chapter 8 reports on the identification of the most likely host for FRB 20181030A, a repeating FRB discovered by Fonseca et al. (2020), to be a merging pair of star-forming galaxies at $z = 0.064$, the first such host to date. Finally, Chapter 9 summarizes the conclusions of each chapter and details prospects for future research.

Chapter 2

Analog Bad-channel Classifier for CHIME

1 Introduction

The Canadian Hydrogen Intensity Mapping Experiment (CHIME) is a transit interferometer working in the frequency range of 400-800 MHz. It was originally conceived to map the neutral Hydrogen, the most abundant baryonic matter in the Universe, in the redshift range of 0.8-2.5. This redshift range maps to a specific phase of the history of the Universe where dark energy, arguably the most mysterious component of the Universe, became dominant and started accelerating the rate of the Universe's expansion. Fortuitously, CHIME is also well suited for different ancillary back-ends that cater to specific scientific goals: CHIME/-Cosmology, CHIME/FRB, and CHIME/Pulsar. CHIME/Cosmology works in the visibility space resulting from cross-correlation and time averaging the digitized voltage signal from different antenna pairs or baselines. CHIME/FRB and CHIME/Pulsar, on the other hand, form fast Fourier transform (FFT) beams (Amiri et al., 2018, Masui et al., 2019, Ng et al., 2017).

All three CHIME back-ends receive the digitized sky signal from the same CHIME front-end; therefore, their anticipated scientific objectives are contingent on the performance and health of the CHIME front-end. For instance, knowledge of the CHIME primary beam is of paramount importance for all the CHIME projects. Moreover, calibration and sensitivity of the instrument are influenced by the stability of the front-end electronics.

Hence, we need an automated pipeline that identifies issues in the CHIME telescope front-end to maintain data integrity. In this chapter, we describe the pipeline that is designed to identify bad analog channels or issues in the front-end of the CHIME telescope. Here, an analog channel consists of all the components of the CHIME telescope except the cylindrical reflectors that the cosmic signal interacts with until the end of the signal digitization stage. Henceforth, we use the word ‘channel’ to describe the latter component of CHIME front-end system.

The organization of this chapter is as follows: Section 2 provides a short overview of the CHIME telescope analog chain that the bad analog channel classifier is designed to work on. In Section 3, we underline the need of a bad-channel identification pipeline. Section 4 describes the core assumptions that went into the pipeline, and also explains the tests that the pipeline performs to evaluate the goodness of a channel. In Section 5.1, Section 5.2, and Section 5.4, we elucidate chronologically all the stages involved in the bad channel classification. Section 6 reports on the major results of the pipeline that demonstrate its utility in identifying bad channels. In Sections 7 and 8, we discuss several limitations of the pipeline. Section 9 highlights different strategies that can be employed to evaluate the effectiveness and completeness of the pipeline. Finally, Section 10 concludes the chapter speculating on the future applicability of this pipeline.

2 CHIME analog chain overview

In this section, we present an overview of the CHIME telescope analog chain that receives, filters, amplifies, and digitizes the sky signal that is used by the CHIME correlators for cross-correlation and/or beam-forming. A schematic diagram of the CHIME Analog chain is shown in Figure 2.1. The pipeline is designed to identify hardware issues in the analog portion of the system. Henceforth, we use the word ’channel’ to describe a typical analog chain.

2.1 CHIME analog chain

The CHIME analog chain (see Figure 2.1) consists of cylindrical reflectors and dual-polarization feeds (front-end), and a series of analog components that bring the sky signal

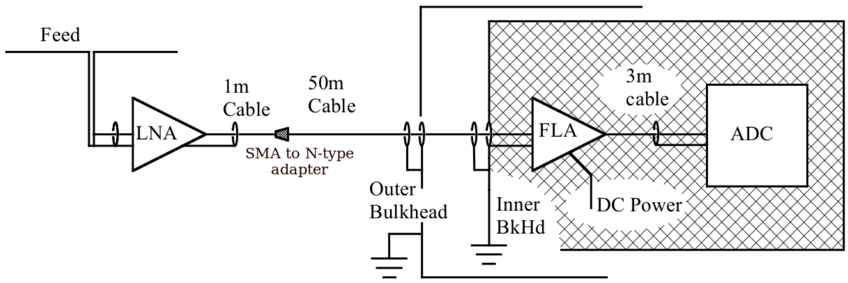

Figure 2.1: Block diagram of a typical channel. Signal collected by a dual polarized feed after reflection from the cylinder passes through a low noise amplifier (LNA) and then via $\approx$ 1-m cable to a 50-m N-type coaxial cable to the receiver hut, which is double shielded. Filter amplifiers (FLA) on the inside surface of the inner RF chamber wall define the instrument passband and transmit the signal to the analog-to-digital converters (ADC). Credit: Rick Smegal (Engineer, UBC)

from a feed to an analog-to-digital converter (ADC) located in an RF-sealed environment on the ground near to the telescope. The sky signal is first reflected by a CHIME cylinder to a four-clover dual-polarization feed that is coupled to a low noise amplifier (LNA) which boosts the signal by 37-45 dB depending on the frequency of the signal and adds minimal noise (T_e = 35 K). The signal from the amplifier is then linked to a segment of coaxial cable that converts the SubMiniature version A (SMA) connection to an N-size connection (AMC58 or equivalent). The amplified signal is then transmitted by LMR-400 50-m coax cable to the double-shielded receiver hut. The signal is then band-passed and amplified further to optimize it for ADC digitalization. The following paragraphs describe each of these components briefly. For more details, refer to Bandura et al. (2014).

- **CHIME Cylinders**

  The CHIME telescope consists of 4 cylinders ,each 100-m long and 20-m wide, making a total collecting area of $\sim$ 8000 m^2. They are parabolic along their short axes, with a focal length of 5 m, and flat along their long axes (Figure 2.2). Each cylinder has 256 dual-polarization feeds spaced 0.31 m apart, for a total of 2048 inputs to the CHIME back-end. The field of view is a long North-South stripe, covering approximately the entire sky visible at Penticton latitude of 49.3 degrees (Note that the telescope response goes to zero near horizon making N-S beam-width $\sim 120°$) and $1.3°$ to $2.5°$ wide, depending on the wavelength. CHIME has no moving parts and scans the sky as the Earth rotates making it a "drift-scan" telescope. The reflecting surface of the cylinder is a 19-mm-spacing mesh made of galvanized-steel and bolted to the steel cylindrical support structure.

Figure 2.2: Front-view of a CHIME cylinder. Credit: CHIME Collaboration

- **Feed**

  CHIME Feeds are cloverleaf antennas (Figure 2.3) which are compact and broad-band dual-polarization feeds. The meeting end of petals, that have differential signals for each polarization, are combined through tuned baluns to form one single-ended output. For details on the feed design and optimization, refer to Deng and Campbell-Wilson (2014).

- **Low Noise Amplifier**

  A Low Noise Amplifier (LNA) boosts a very low-power signal without significantly degrading its signal-to-noise (SNR) ratio. In CHIME, it is directly attached to the balun to form one single-ended output (Figure 2.4). The LNA achieves a noise temperature ≈ 25 K across the CHIME band, and its gain decreases smoothly from $\approx$

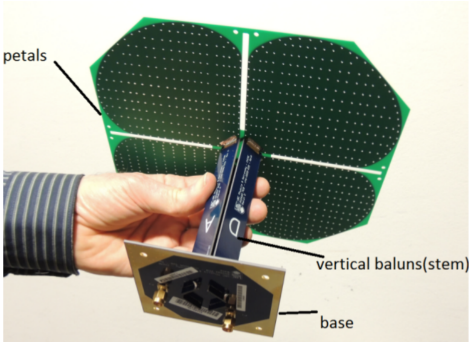

Figure 2.3: Cloverleaf dual-polarization CHIME feed. Credit: CHIME Collaboration

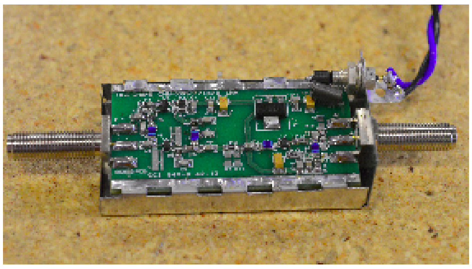

Figure 2.4: CHIME Low Noise Amplifier. Credit: CHIME Collaboration

45 dB at 400 MHz to $\approx$ 37 dB at 800 MHz.

- **Filter Amplifier and Analog-to-digital Converter (ADC)**

  The signals from CHIME antennas are sent to the receiver hut that primarily holds two important components: the filter linear amplifier (FLA), and digitizer (a part of the 'F'-engine; see Chapter 3). A filter amplifier is a second stage amplifier that defines the 400-800 MHz bandpass and amplifies the incoming signal. The second stage amplifier signal is then input into an ADC that converts the time domain analog signal into digitized signal. It consists of custom McGill boards designed for signal processing applications called 'ICE' boards (Bandura et al., 2016), shown in Figure 2.5. Each ICE board has a field programmable gate array (FPGA) for data processing, and an Arm processor for easier interfacing with the control computers. Each ICE board has 2 mezzanine cards, and a typical mezzanine card has 2 ADC chips on it. An ADC chip has 4 inputs, so each ICE board has 16 inputs in total. The boards are packed together into crates of 16, and 8 of these crates handle the 2048 inputs from the CHIME receivers. The CHIME F-engine transforms the data from the ADCs into the frequency domain and channelizes it into 1024 channels of resolution 0.39 MHz each, using a polyphase filter bank (PFB; Harris and Haines, 2011). The digitized and channelized digital data then go to the 'X'-engine of the CHIME correlator which is discussed in Chapter 3. The input data rate processed by the 'F'-Engine is 13 terabits/sec. This rate is enormous and unlike that of any other radio telescope in the world.

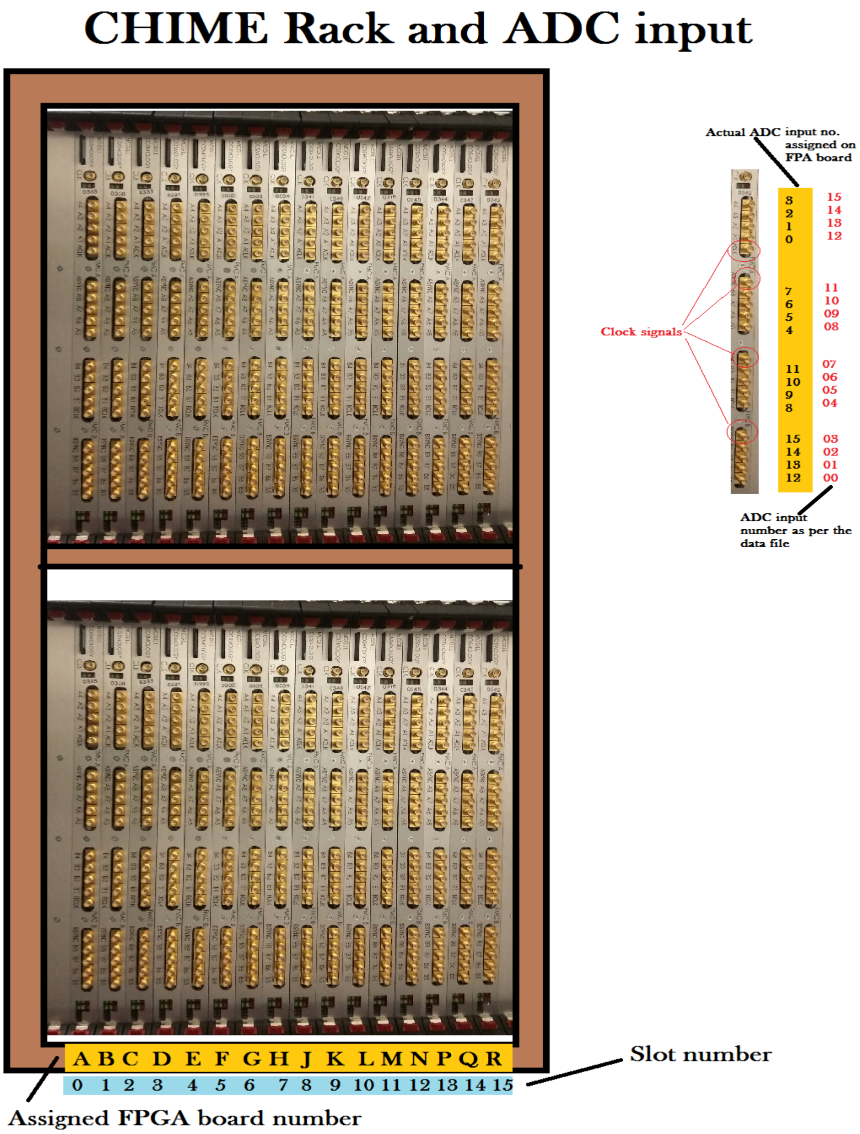

Figure 2.5: A CHIME Rack that holds signals from 512 feeds. CHIME has 4 such racks that digitize and channelize signals from 2048 feeds.

The input data that go into the pipeline is the digitized voltage for each channel that is identified with three key values- ‘crate’:0-7, ‘slot’:0-15,‘input’:0-15. As discussed in the previous paragraph, each rack consists of 16 FPGA boards, each of which is given a specific slot number or simply a ‘slot’. Each slot has 16 inputs where each ‘input’ handles one channel. Figure 2.5 shows a schematic diagram of a typical rack that holds signals from 512 feeds (CHIME has 4 such racks).

3 Need for a bad channel detection pipeline

The reasons that make CHIME a sensitive radio telescope are its large field-of-view (≥ 200 degrees square), large collecting area, wide frequency coverage, and powerful correlators. However, they also make CHIME a highly complex experiment in terms of electronics and output data products. Consequently, there are stringent calibration requirements to be met for achieving the cosmology science objectives (knowledge of the beam and gain calibration with great precision, see Newburgh et al. (2014), Shaw et al. (2015). Lastly, CHIME handles and processes an enormous amount of data per second. For instance, the total data rate digitized by the F-Engine is 13.1 Tb/s for the 2048 time-streams and it is not practical to save every bit of data on disk. All of these requirements necessitate the timely identification and correction of hardware issues. The primary aim of the pipeline is to identify bad channels (channels with instrumental issues) within time cadence (currently, 30 minutes). In the next section, we discuss in detail how this pipeline produces a list of bad channels.

4 Bad analog channel classifier: basic principles

In the above section, we discussed the importance of timely identification and mitigation of the issues pertaining to the analog chain system of CHIME. Here, we introduce the pipeline. We firstly introduce the underline assumptions about the system, the astronomical signal, and the environment around the telescope. Then we discuss two tests that the pipeline performs to identify the bad channels, and lastly, we elucidate the overall process flow of the pipeline.

4.1 Assumptions

The pipeline was initially based on two fundamental assumptions:

- **Sky signals are time-stationary Gaussian noise**. An astrophysical signal received by a radio telescope consists of emissions from many independent radiating sources. These sources radiate electromagnetic waves that have random phases. The same applies to the noise from a telescope's receiver system. Therefore, the signal received by the telescope can be described as time-stationary Gaussian noise (For detailed discussion on this, see Chapter 1 of Chengalur et al., 2007). This is the basis of one of the tests (Histogram test) performed by the pipeline to identify bad channels and construct good channel templates, both of which are discussed in the following sections.
- **All channels are subjected to nearly identical conditions**. The CHIME telescope has 2048 channels, and each channel has an identical electronic structure, with the exception that half of them are sensitive to a specific polarization and, thus, to different RFI environments and sky signals. Therefore, the pipeline treats both polarizations differently. With this, we can assume that all channels of a given polarization are nearly identical in terms of electronics and the sky each one sees. This assumption is the basis of using outlier statistics to identify bad channels.

In the next section, we discuss the steps the pipeline follows to identify good channels. However, first we discuss the two tests that are central to the bad channel classification scheme which the pipeline employs.

4.2 Tests

Histogram test

The histogram test identifies channels showing either a non-Gaussian voltage distribution or having rms voltage outside a certain threshold. The former condition is undesirable as per our first assumption, and is indicative of a possible instrumental issue in the analog chain of that feed. On the other hand, the latter condition prevents an ADC going into a non-linear regime, and also to reduce the quantization noise; we do not want the input voltage rms to be either too low or too high. As discussed by Mena-Parra et al. (2018), there is an optimal range for the input rms for which the effect of quantization noise is negligible. This range depends on the number of bits of the ADC. In the case of CHIME which employs 8-bit

ADC, that range is 3-5 bits rms, or 8-32 ADC units. It is preferable to be in the low range of that interval in order to leave some room for unanticipated strong RFI. Therefore, we set the optimal rms input level between 8-16 ADC units. In the histogram test, we compute the Spearmann correlation between the good channel template and the template of a given channel.

FFT test

The FFT test identifies anomalous spectrum characteristics associated with various instrumental artifacts. To accomplish this, we compute the power spectrum of all 2048 channels by squaring each channel's fast Fourier transform (FFT) spectrum. Note that our dataset for the FFT and Histogram tests consists of 2048 contiguous data voltage samples digitized at 2.56 μs. Similar to the histogram test, we compute the Spearmann correlation between the power spectrum of each channel and the good channel power spectrum template. Two spectral features of the power spectrum are particularly important for identifying bad channels: first, RFI bands, and second, the overall one-sided Gaussian continuum of the power spectrum. More detail about these features are discussed in Section 5.2.

5 Pipeline: block-wise description

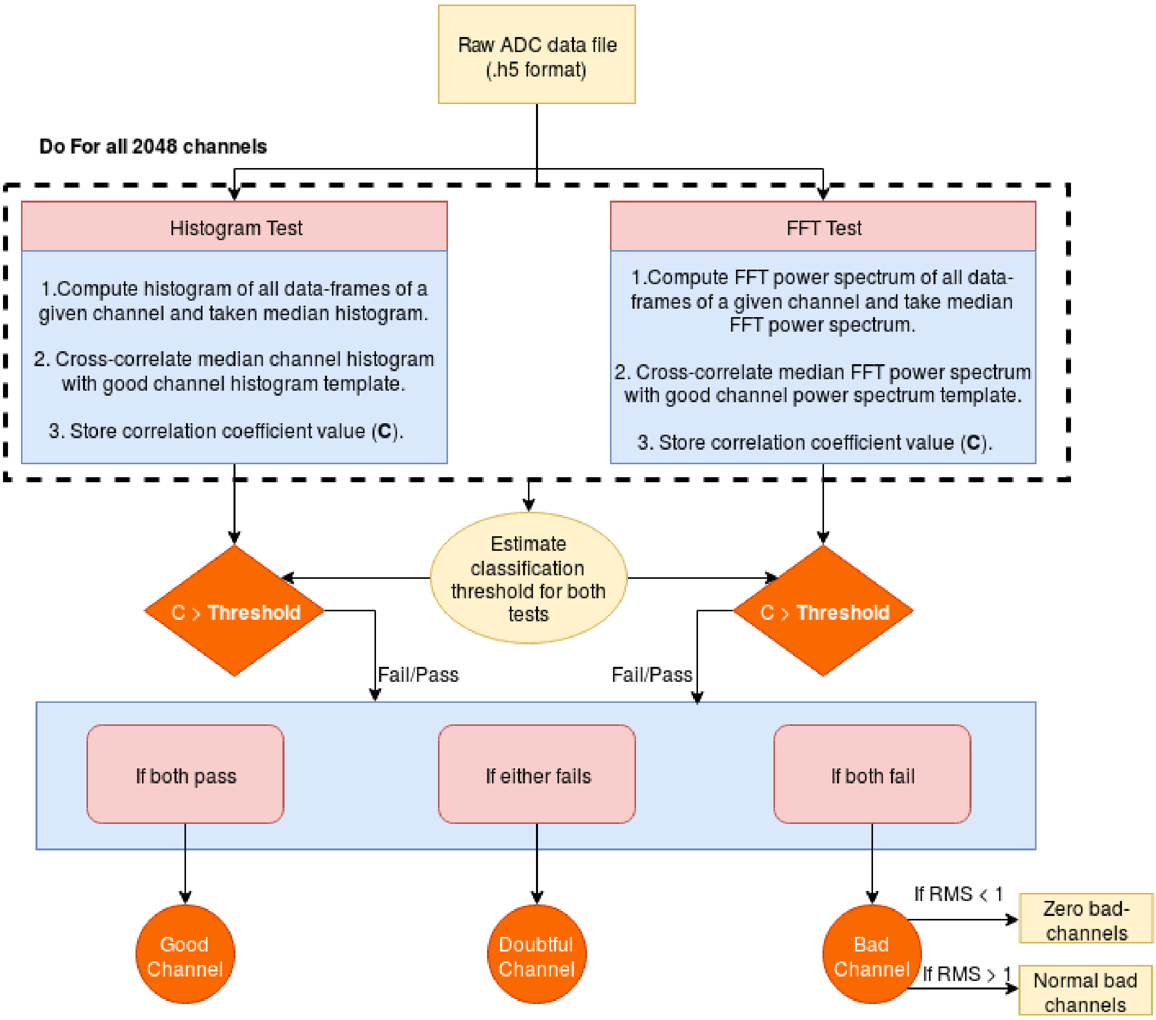

Figure 2.6: Pipeline flow-diagram

5.1 Stage 1: create good channel template

In both tests, we cross-correlate histogram and power spectrum templates of a channel with respective good channel templates. Here, we describe a good channel as a channel free from unwanted instrumental artifacts. The pipeline first screens channels that have rms voltage between 8 ADC units and 16 ADC units that is in accordance with the condition that minimizes the quantum noise in the CHIME ADC. A typical raw data file is made up of 64 time-streams of all 2048 channels which gives us 131,072 time-streams to create the good channel templates. Following the step of screening rms voltage values, the second step is to check the normal distribution of a given time-stream. There are many flavors of normality test but we used D'Agostino test (d'Agostino, 1971) and Pearson's normality test (D'Agostino and Pearson, 1973) that combine statistical parameters like skew and kurtosis to test for the normality. The pipeline rejects all the time-streams whose p-value (normality test) < 0.05 (Fisher, 1992). However, it is possible that p > 0.05 for data that do not follow normal distribution. However, our sample size is big enough (2048 raw voltages) to make the latter effect implausible (Ghasemi and Zahediasl, 2012). After that, the pipeline generates FFT power spectrum and raw-voltage histogram templates for the shortlisted time-streams. Finally, the median histogram and FFT power spectrum template are selected as a representative of good channels.

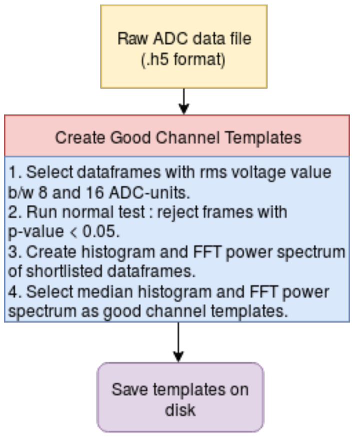

Figure 2.7: Adaptive Thresholding: Flow-chart

More importantly, as shown in Figure 2.8, beam shapes of two polarizations of the CHIME telescope are quite different in terms of gain and beam-width. Hence, the signal received by the two polarization can be systematically different. Therefore, we make two good channel templates for both tests, one for each polarization, and the two polarizations are treated separately in all the analysis steps of the pipeline that are discussed in the next few sections.

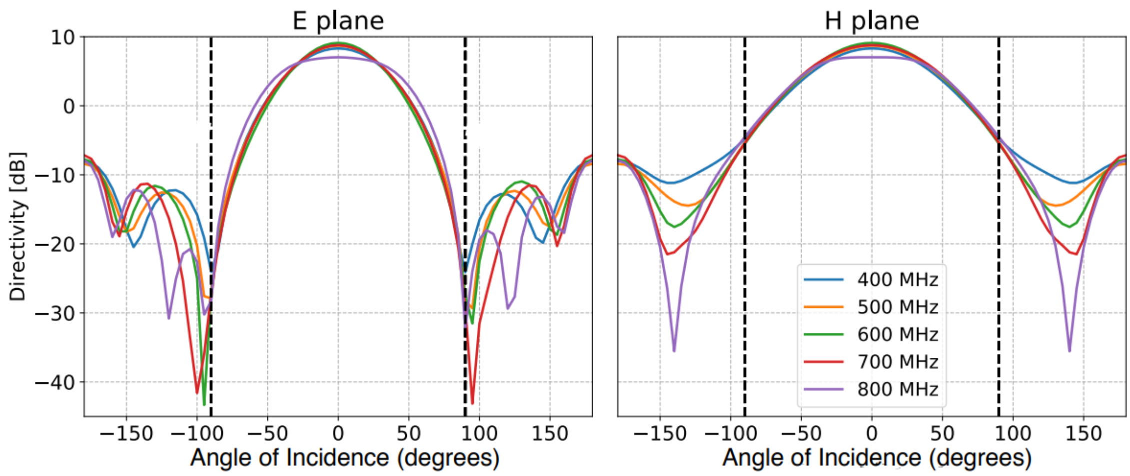

Figure 2.8: Modelled angular response of a CHIME feed in the E and H planes at multiple CHIME band frequencies. N-S beam is narrower in beam-width than the E-W beam. The vertical dashed lines in panels E and H planes correspond to the boundaries of the reflector for X (North-South) and Y (East-West) polarized radiation at ± 90 degrees, respectively. Note that the angular response in the E plane is smaller half-power beam-width than in the H plane. Figure from CHIME Collaboration et al. (2022).

5.2 Stage 2: identify bad analog feeds

Once we have good channel templates for both tests, the next step is to correlate them with the FFT power spectrum and histogram templates of every channel, and compute Spearmann correlation coefficients. We use Spearmann correlation because it determines the strength and direction of the monotonic relationship between the two variables rather than the linear relationship which Pearson correlation estimates. Also, the Spearmann test is observed to be much more stable to statistical fluctuations than Pearson's correlation test (Bonett and Wright, 2000). Once we get the correlation coefficients, the next step is to decide the classification thresholds for both tests that is discussed in the next section. With those thresholds, we divide channels dichotomously into good and bad channels. However, the pipeline classified channels into three categories to account for channels near the threshold boundary; this is discussed in the next section. After that, the final task is to combine the two results; that is discussed in Section 5.4. Note that the steps discussed below are performed separately for both polarization.

5.3 Adaptive thresholding

As discussed above, both tests compute Spearmann correlation coefficients between the good channel templates and the test templates for each channel. Once the coefficients are computed for all 2048 channels, we use the Otsu thresholding technique to identify appropriate classification threshold (Vala and Baxi, 2013). It is an effective binarization technique that is easy to automate (Trier and Jain, 1995). The Otsu's thresholding method involves iterating through all the possible threshold values and calculating the variance for the number of channels at each side of the threshold (i.e. two classes). The aim is to find the threshold value that minimizes the weighted within-class variance and maximizes between-class variance. We compute the Otsu-threshold for both tests. In order to calculate the threshold for classifying bad channels, we adopt a conservative scheme: the thresholds are estimated by considering only channels with Spearmann cross-correlation coefficients $>$ Threshold$_{Otsu}$ (Both tests). With those channels, we estimate the new threshold via an extreme outlier condition: First-quartile $-$ 3 $\times$ Inter-quartile range (IQR) (Tukey, 1970). This is to make sure that the chances of false negative classifications are low.

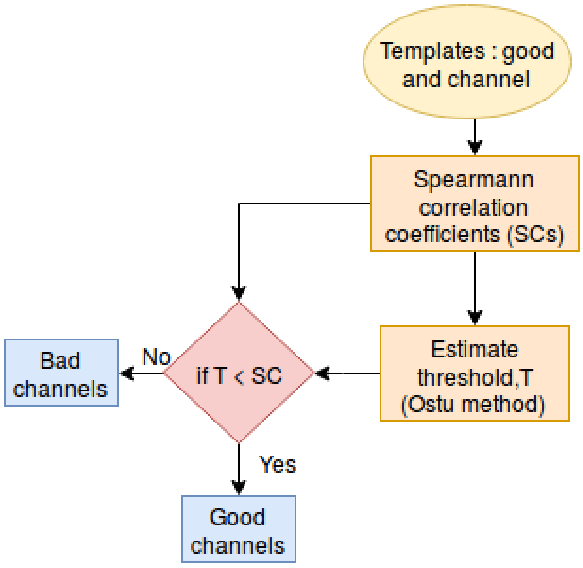

Figure 2.9: Adaptive Thresholding: Flowchart

Currently, the algorithm estimates thresholds for both tests adaptively using the data in-hand. This method is favoured because we assume that RFI (the most dominant signal in our data) is highly non-stationary. Moreover, this will also accommodate any change in the system parameters like system temperature. If the RFI on a long run shows any sort of periodicity or correlation, then one can use a constant threshold as well. To compare the efficiency of these two techniques, we first estimated a constant threshold by averaging over 30 sidereal days of night-time data. We then used this threshold to classify night-time data collected during September, 2018, and compared the classification with the one we get from adaptive thresholding. The classification plots for both techniques are showing in Figures 2.10 and 2.11; for better visualization, we assigned values to each classification: good channels = 1, doubtful channels = 0.5, and bad channels = 1. As we expect that the channels that show hardware problems would not change classification in a short period of time, the higher observed variability in case of constant thresholding makes it less robust than adaptive thresholding where bad channel flags are significantly more stable.

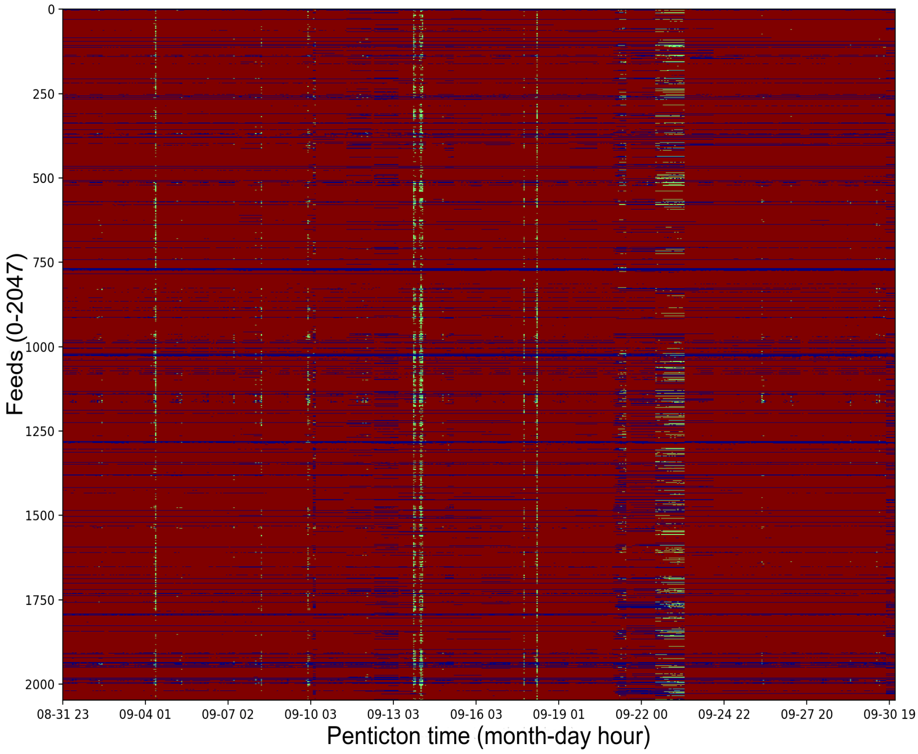

Figure 2.10: Classification of 2048 channels using constant thresholding technique: good, doubtful, and bad channels are assigned 1 (red), 0.5 (green), and 0 (black) values, respectively.

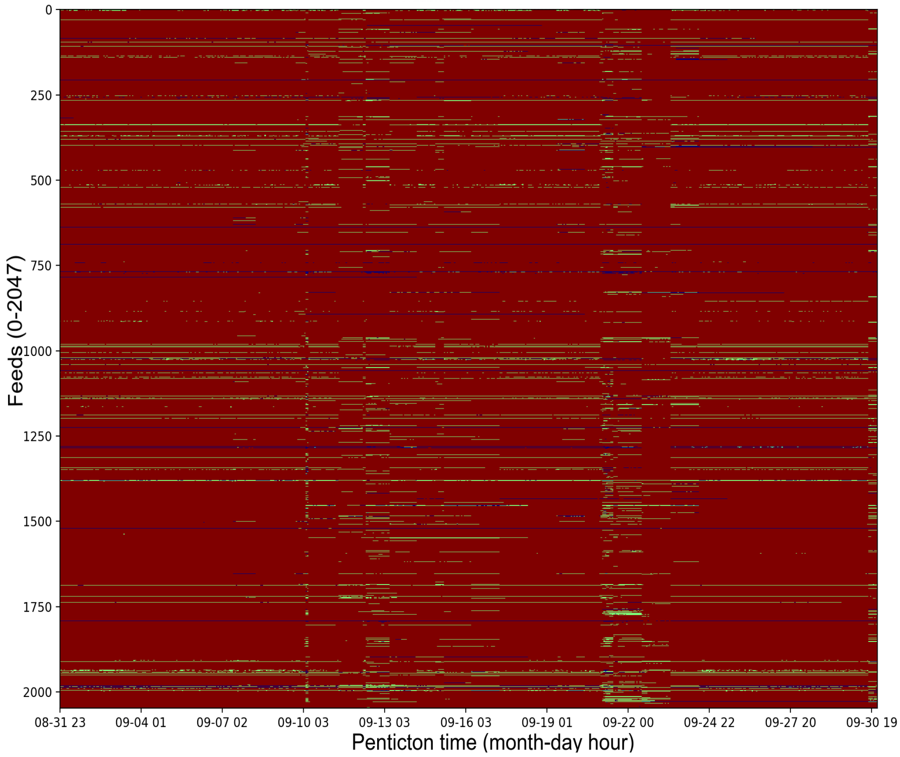

Figure 2.11: Classification of 2048 channels using adaptive thresholding technique: good, doubtful, and bad channels are assigned 1 (red), 0.5 (green), and 0 (black) values, respectively.

5.4 Stage 3: merging results from the two tests

After stage 2, we have a list of classified channels from the histogram test (T-1 test) and the FFT test (T-2 test). In order to merge their results, we have devised a two-stage classification scheme that is shown in Figure 2.12. The first step weighs the results of the previous classification and independently assigns weights to each channel based on the criteria discussed below. We give more weight to the FFT test results because many of the instrumental artifacts are more pronounced in the FFT power spectrum (refer to Section 6). As shown in Figure 2.12, for each test separately, we first subtract the computed threshold (Stage-2) from the correlation coefficient of all the channels, and then compute the median, 25th-percentile (Q_{25}) and inter-quartile range (IQR) values. The minimum of the median and zero is assign to a variable 'A'. Similarly, variable 'B' = Q_{25} , and variable 'C'

= Q_{25} - 1.5$\times$IQR (criterion for 'moderate' outlier; Tukey, 1970). After that, each channel is weighted and a new classification is assigned to all 2048 channels depending on the criteria showed in the decision block of Figure 2.12. Though the initial weights are selected on an ad hoc basis, the rationale is as follows: a good channel is one that either both tests classify as 'Good', or when the histogram test classification is 'Good' but the channel is a borderline case for the FFT test (i.e. weak outlier as per the quartile statistics). In contrast, a channel is categorized as 'Bad' if both the tests classify it in that category. A channel is classified as 'Doubtful' in all other scenarios. This classification is finally used to group all 2048 channels. However, doubtful channels are considered as 'Good' in the current flagging framework. We further categorize 'Bad' channels for internal assessment based on their rms voltage values; if the rms voltage is larger than one, the channel is classified as 'Non-zero bad', otherwise, the channel is classified as 'Zero bad'.

The reason we reclassify channels is to abate the strictness of the stage-2 classification. We observed that the pipeline is quite conservative in flagging bad channels. Moreover, the Ostu's threshold method is more likely to classify good channels as bad especially those who are near to the lower edge of the good channel cluster. Therefore, using quartile statistics, the pipeline reduces the latter bias.

Finally, the doubtful channels represent channels that are in the grey area of our classification. These will exist in any reasonable classification scheme. Although they are regarded as good channels by the flagging broker, they are stored as doubtful in the database and are closely monitored for potential hardware issues.

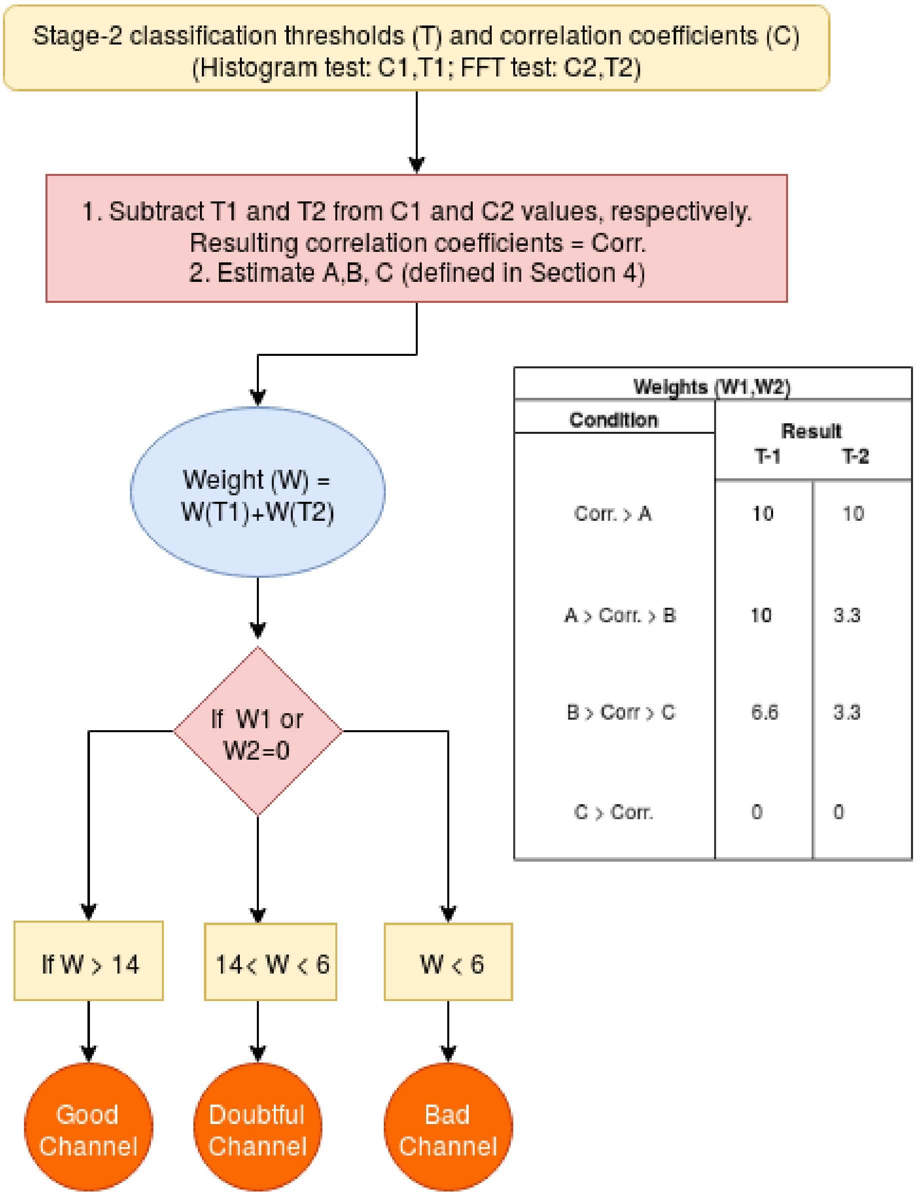

Figure 2.12: 2nd-stage channel classification: Flow-diagram

6 Results

In this section, we discuss several bad channel categories that the pipeline has identified. The channels that are consistently identified as bad in these categories are confirmed to be defective by on-site personnel, who then perform the appropriate repairs. This illustrates the pipeline's ability to identify the faulty channels for which it was designed.

6.1 Instrumental artifacts identified

We have identified seven categories of bad channels based on a common feature/morphology observed either in the FFT template or in the histogram template. Although it is a difficult and ongoing task to associate these observed artifacts with a specific hardware issue, we speculated potential sources that could trigger these notable characteristics in each class.

- **ADC digitization Malfunctioning**

  We saw a few bad channels with unusual histograms; one such channel is shown in Figure 2.13. More notably, the power spectra of these channels do not show any sign of an instrumental issue. The sharp cutoff in the histogram suggests that the problem might be related to ADC digitization. I simulated a random bit-flip scenario (flip one or more bits randomly) and bit-stuck scenario (one or more bits stuck to either 0 or 1 all the time), and was successfully able to simulate the observed histogram and power-spectrum. That clearly demonstrates that the algorithm is capable of detecting issues related to the ADC digitization.

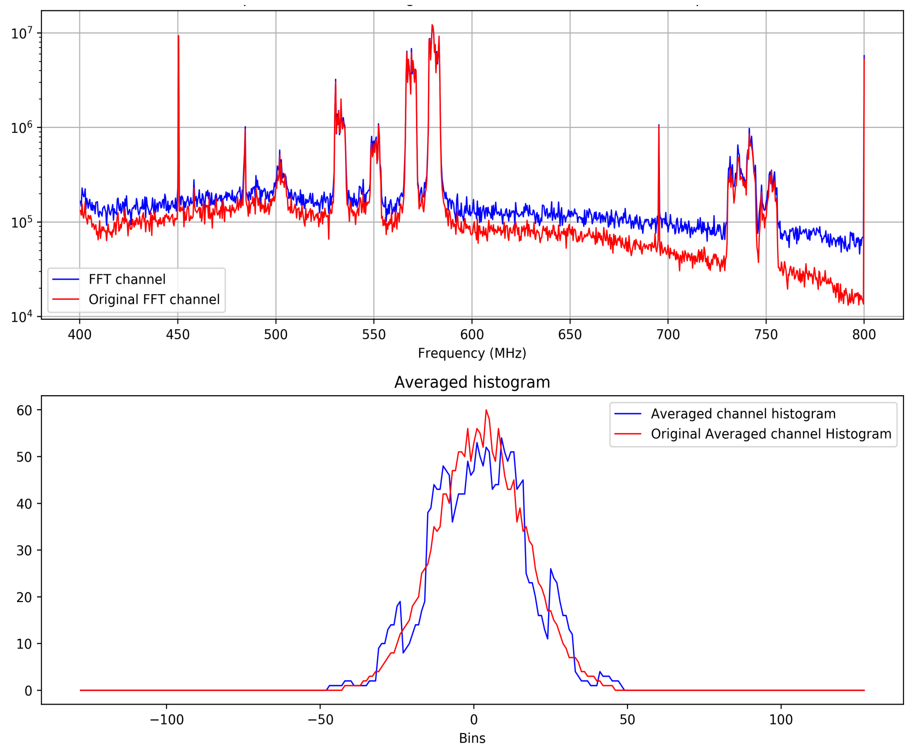

Figure 2.13: Instrumental artifact: Bit-flip - the top panel shows the power spectrum of the signal, and the bottom panel shows the ADC-voltage histogram of the signal. When the random bit-flip issue is not present, the original FFT (top panel; red) and the averaged channel histogram (bottom panel; red) templates represent the power spectrum of a channel. The second FFT power spectrum (blue, on top) and the histogram (blue, on bottom) are from when the channel was experiencing the random bit-flip issue. Two observations can be made from this: (1) the global shape of the power spectrum is unaffected by the random bit-flip issue, and (2) the ADC bit-flip issue is characterized by sharp wedge-like features in the histogram.

- **Cable Reflection** As discussed in the CHIME analog chain overview section, CHIME uses coaxial cables that take voltage data from the feed-line to the F-engine hut. These cables, if damaged or broken, would result in signal attenuation. Apart from that, these cables often show reflection phenomena due to imperfect interfaces. These reflected waves can be seen in the power spectrum of the digitized signal as sine wave(s) modulating the actual FFT of the sky signal. In Figure 2.14, we showed an example of an affected channel. From the FFT power spectrum plot, the sine modulation signature can be clearly seen.

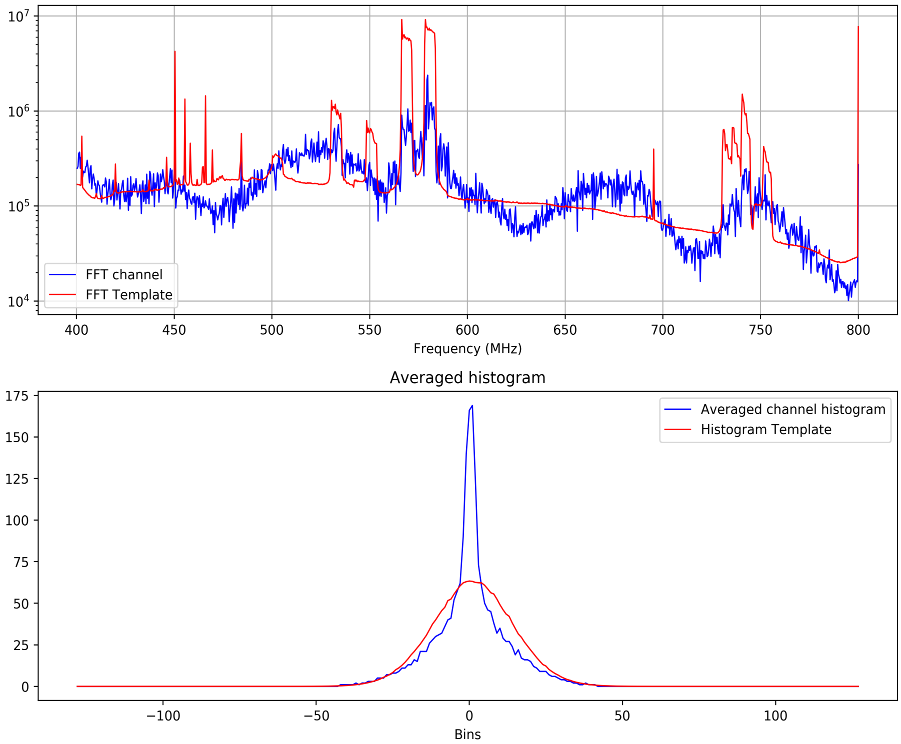

Figure 2.14: Instrumental artifact: cable reflection - top panel shows the power spectrum of the signal (blue), and bottom panel shows the ADC-voltage histogram of the signal (blue). The observed sine wave modulation in the power spectrum is a characteristic of the cable reflection. The good channel power spectrum (top panel; red) and histogram (bottom panel; red) templates are also shown for comparison.

- **Intermodulation Distortion (IMD)**

  Intermodulation distortion (IMD) results from two or more signals (tones, harmonics or their products) interacting in a non-linear network to produce additional undesirable signals. These additional signals (often called intermodulation products) occur mainly in active devices such as amplifiers and mixers. It often happens that the active devices are driven into the non-linear regime by a signal, and we see different harmonics or their products in the frequency band. The pipeline also detects the bad channels that show IMD, and one such channel is shown in Figure 2.15. Removing these channels is essential as they introduce unwanted systematics in the signal.

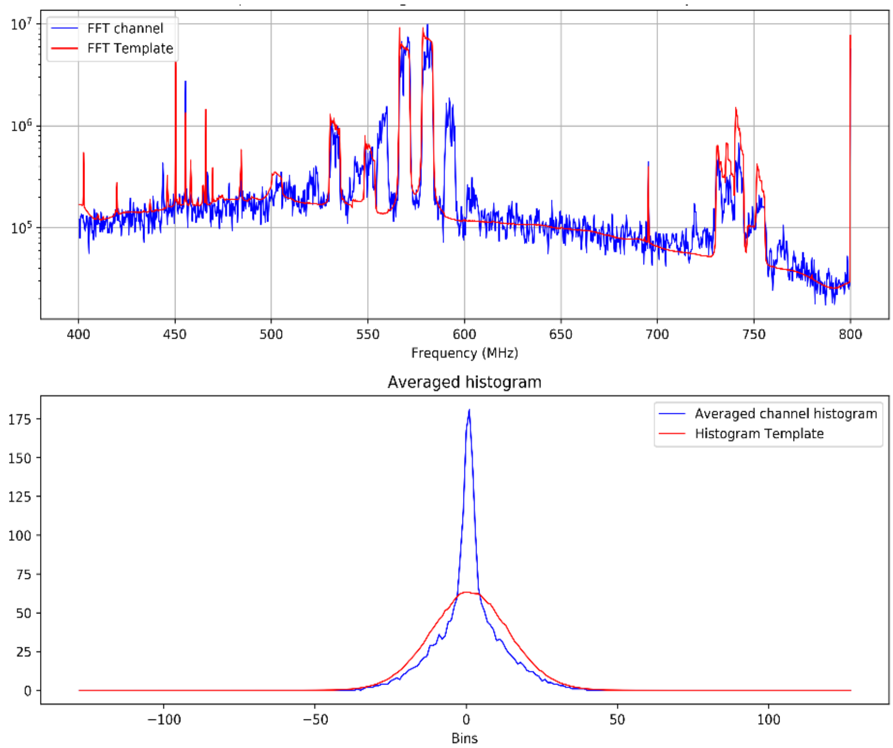

Figure 2.15: Instrumental artifact: Intermodulation distortion - top panel shows the power spectrum of the signal (blue), and bottom panel shows the ADC-voltage histogram of the signal (blue). The observed harmonic products near TV channels are due to the IMD. The good channel power spectrum (top panel; red) and histogram (bottom panel; red) templates are also shown for comparison.

- **Channels with No signal**

  Due to the absence of persistent RFI bands, these channels are classified solely by the FFT test. An example of a channel in this category is shown in Figure 2.16.

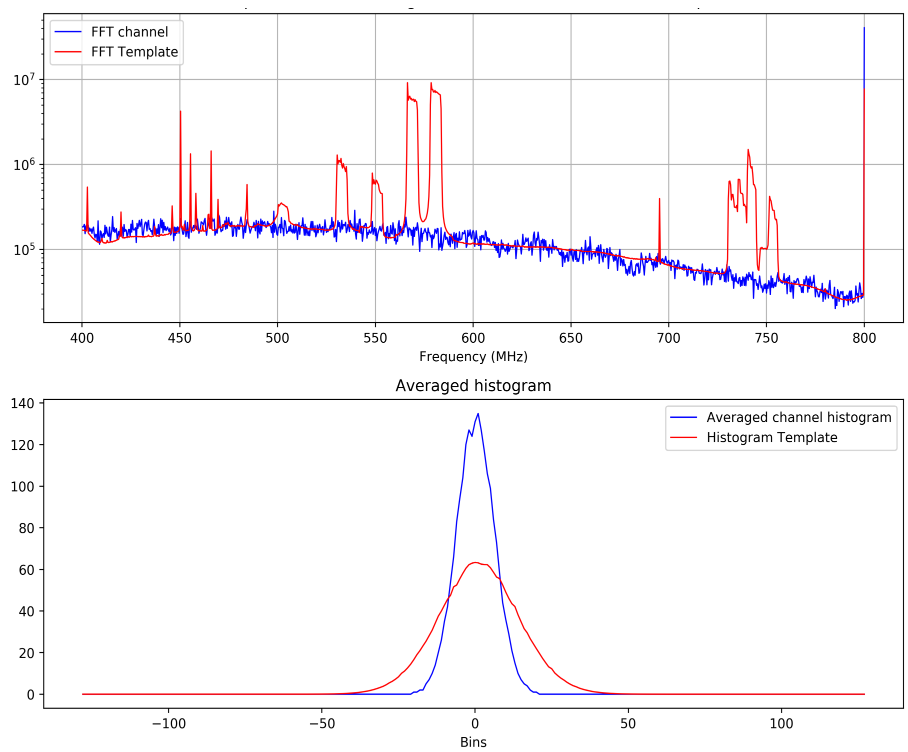

Figure 2.16: Blank/OFF channel - top panel shows the power spectrum of the signal blue, and bottom panel shows the ADC-voltage histogram of the signal blue. The absence of RFI bands in the signal power spectrum suggests that the channel is not sensing sky signal. The good channel power spectrum (top panel; red) and histogram (bottom panel; red) templates are also shown for comparison.

- **Noisy channels**

  These channels often show noisy histograms with spiky small scale structures, and the power spectrum with TV and mobile-communication bands having less power than a typical good template. An example is shown in Figure 2.17. Several factors, like high attenuation in the FLA, problems with the LNA, lossy connections, etc., may contribute to the high noise power.

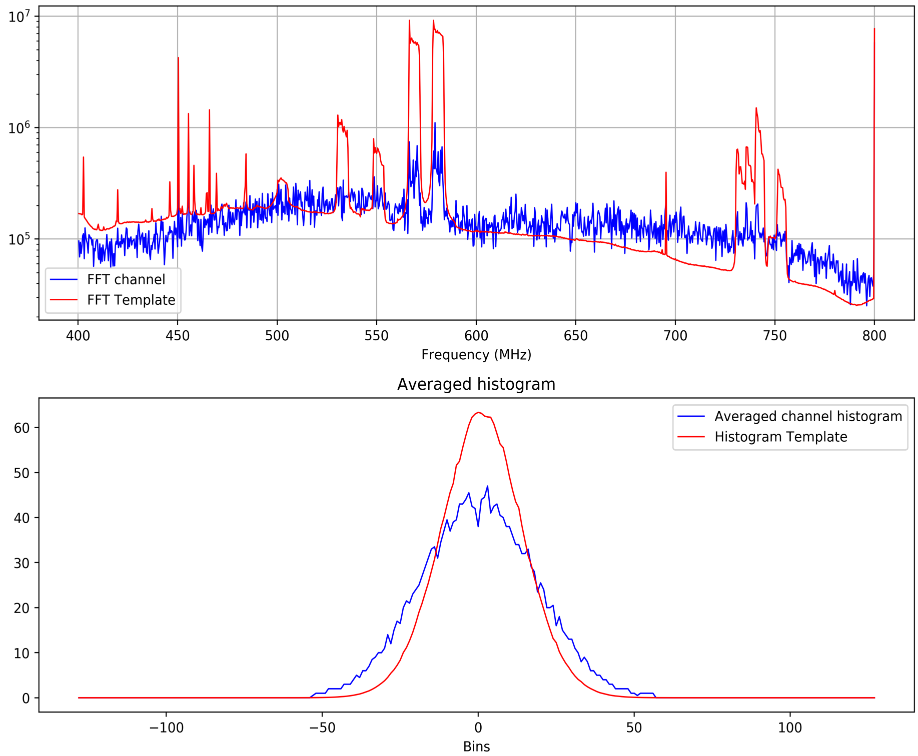

Figure 2.17: Instrumental artifact: noisy FFT power spectrum - top panel shows the power spectrum of the signal blue, and bottom panel shows the ADC-voltage histogram of the signal blue. The observed low power in the RFI bands and overall noisy power spectrum are indicatives of an instrumental issue. The good channel power spectrum (top panel; red) and histogram (bottom panel; red) templates are also shown for comparison.

- **High RMS Noise**

  As shown in Figure 2.18, it may happen that the signal has high power resulting in the saturation of the ADC data. These cases are identified by both the histogram test (histogram with very large standard deviation) and FFT test (lower signal level at 400 MHz). One example of such a channel is shown in Figure 2.18.

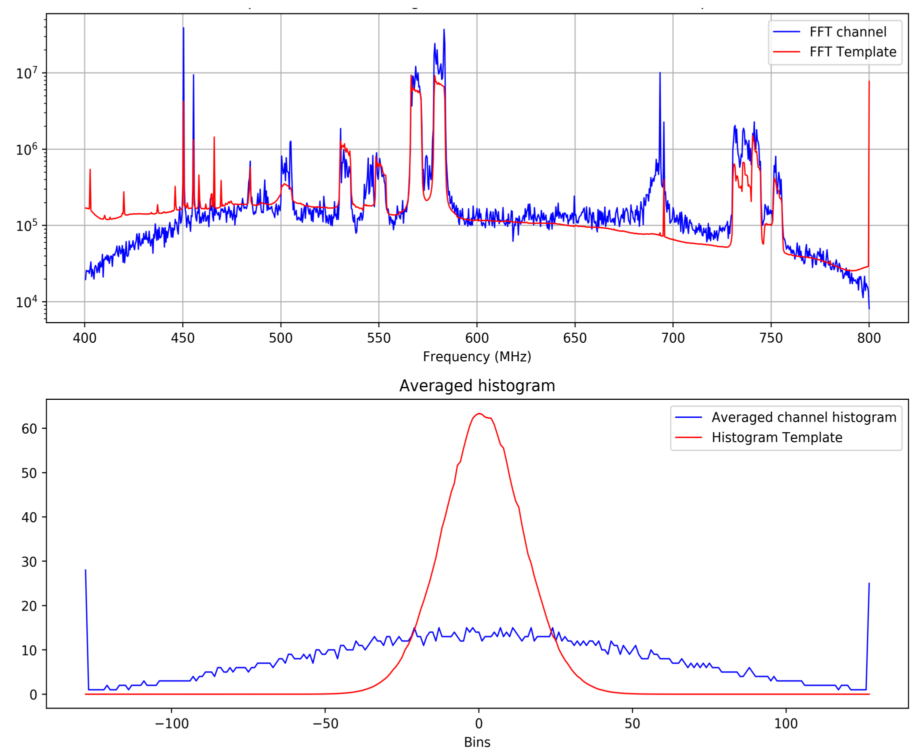

Figure 2.18: Instrumental artifact: high digitized rms voltage - top panel shows the power spectrum of the signal blue, and bottom panel shows the ADC-voltage histogram of the signal blue. From the histogram, it is clear that the signal has extremely high rms noise that is caused either by the wrong analog gain value of the active components, or by the noisy medium. The good channel power spectrum (top panel; red) and histogram (bottom panel; red) templates are also shown for comparison.

- **Other bad channel examples**

  We also showed a few examples of bad channel that are identified by the pipeline but we still are uncertain about their physical origins. Figure 2.20, for instance, depicts an FFT power spectrum with a wide hump-like pattern for which no plausible explanation exists. In Figure 2.19 and 2.20, the channels show an atypical trough near 700-750 MHz frequency band. These characteristics have been observed in a few channels, but their possible physical origins are debatable. Lastly, the pipeline also classifies channels that have either very low rms voltage or very high rms voltage. They are usually due to bad analog gains, or from severe RFI coupling and therefore their timely identification can result in the analog signal chain gain being corrected.

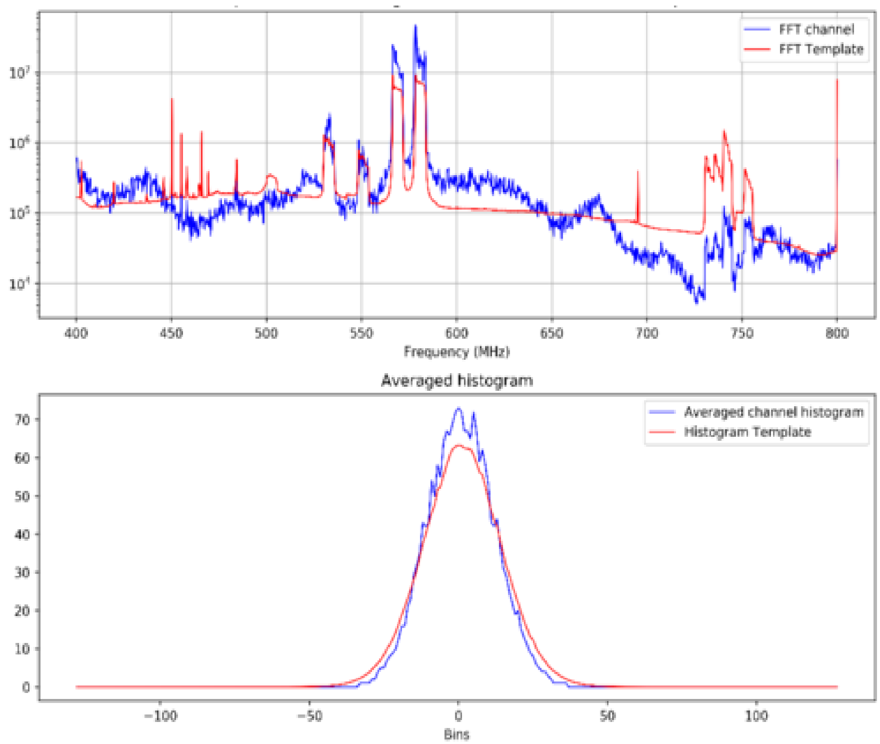

Figure 2.19: Unclassified instrumental artifact: trough near 700-750 MHz in the power spectrum - top panel shows the power spectrum of the signal blue, and bottom panel shows the ADC-voltage histogram of the signal blue. The observed trough near 700-750 MHz in the power spectrum (top panel) is indicative of a hardware issue whose origin is unknown. The good channel power spectrum (top panel; red) and histogram (bottom panel; red) templates are also shown for comparison.

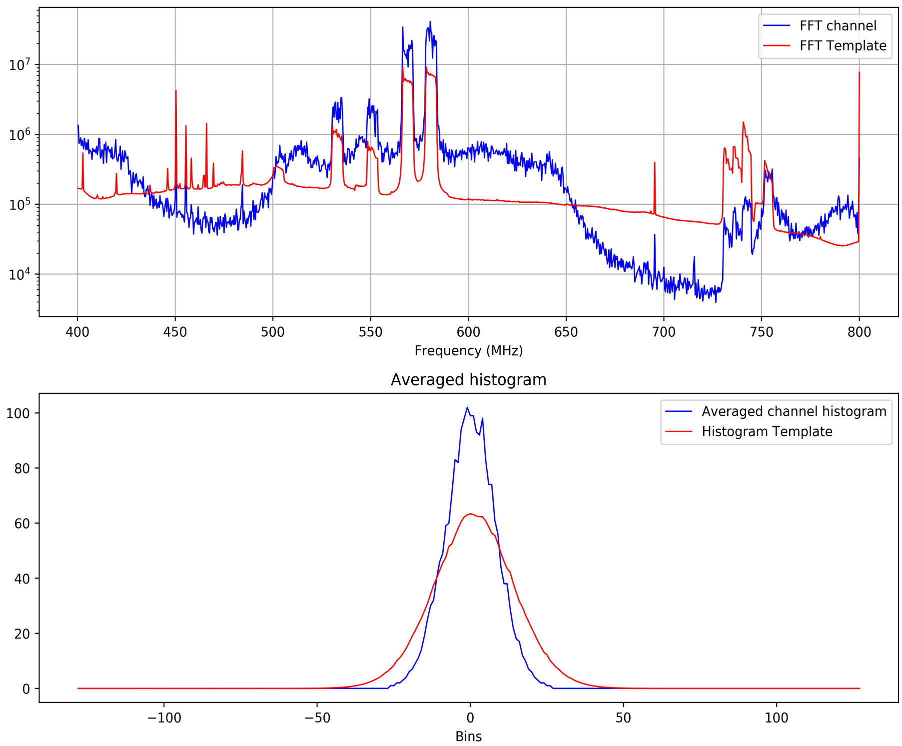

Figure 2.20: Unclassified instrumental artifact: flat, broad hump in the power spectrum - the top panel displays the signal's power spectrum blue, while the bottom panel displays the signal's ADC-voltage histogram blue. The observed flat hump in the power spectrum (top panel) is indicative of an unidentified hardware fault. For comparison, the good channel power spectrum (upper panel; red) and histogram (lower panel; red) templates are also displayed.

7 Limitations

As discussed in Section 2, the pipeline relies on two main assumptions: first, RFI environment is nearly identical for all the CHIME feeds; second, the sky signal is stationary random Gaussian noise. Apart from these, we have also assumed that all channels are identical in terms of the instrumental architecture. However, there are corner cases where these assumptions do not hold. Those cases are discussed in this section.

- **Stability of the classification**

In general, human intervention is needed to resolve instrumental problems. Therefore, if a channel is faulty, it should stay bad until it is manually corrected. However, we have observed that the classification of few channels change in 30 minutes. This implies that the cause is likely intermittent in nature or there are other less obvious hardware problems that we are not aware of. We, for now, focus on the first possible cause. We currently use 64 samples for each channel. This can influence the channel classification very close to the classification thresholds. This problem is mitigated by increasing the dynamic range of the coefficients of cross-correlation by scaling the templates so that the differentiating characteristics become easy to detect. This has reduced the number of feeds in the grey area of our classification scheme, where statistical fluctuation can change their classification (typically 3-5 out of 2048 channels). Increasing the number of data-frames can also reduce the effect of statistical variations on the bad channel classification. In practice as well, it improves the stability of bad channel classification. Therefore, once we are assured of the system stability, it would be beneficial to increase the sample size to at least 128.

- **Spatially variable environment**

  The persistent RFI bands observed in the CHIME frequency range are shown in Figure 2.21. While there is some degree of power variance in the RFI environment in the vicinity of CHIME, the change is not significant enough to challenge our second assumption. However, there are feeds that are more susceptible to the RFI than others. For example, feeds at the ends of the cylinders have a higher proportion of RFI. The pipeline does not currently offer an optimal solution for this issue, and it is an ongoing task to identify the best solution for these feeds as they also have different beam pattern. One possible solution is that these feeds should be monitored separately so that the relatively high RFI would not cause the feed to be flagged as bad by the algorithm; or the second solution could be to flag these feeds only when in both the tests they are extreme outliers. This is particularly important because they provide the longest baselines that are important for certain CHIME cosmology science objectives like map making and point source subtraction.

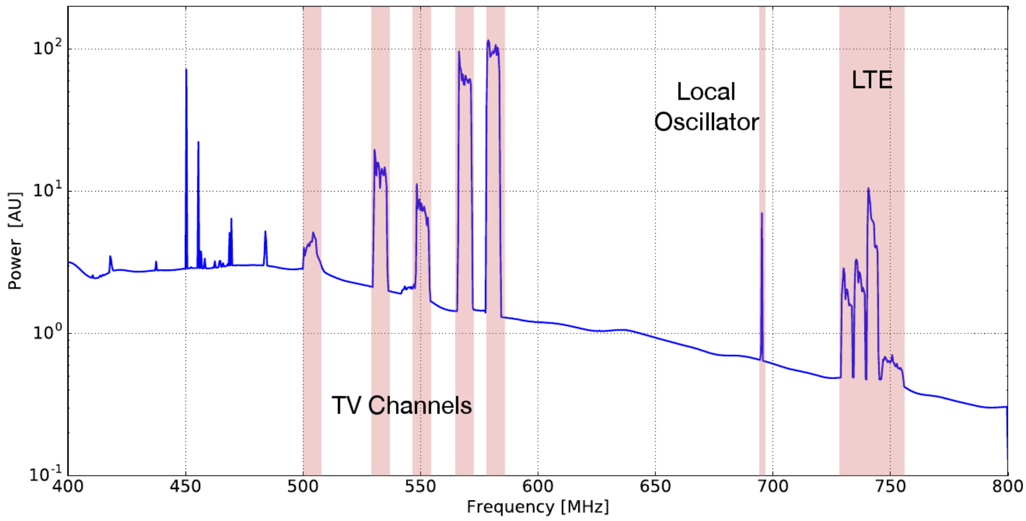

Figure 2.21: Persistent RFI bands in the CHIME frequency range 400-800 MHz.

8 The strange case of rain

At the end of October 2017, the pipeline suddenly flagged more than 100 channels as bad. This was unusual because we did not expect a significant number of channels abruptly develop instrumental faults. More interestingly, we found a strong correlation between bad channels and rain that is shown in Figure 2.22.

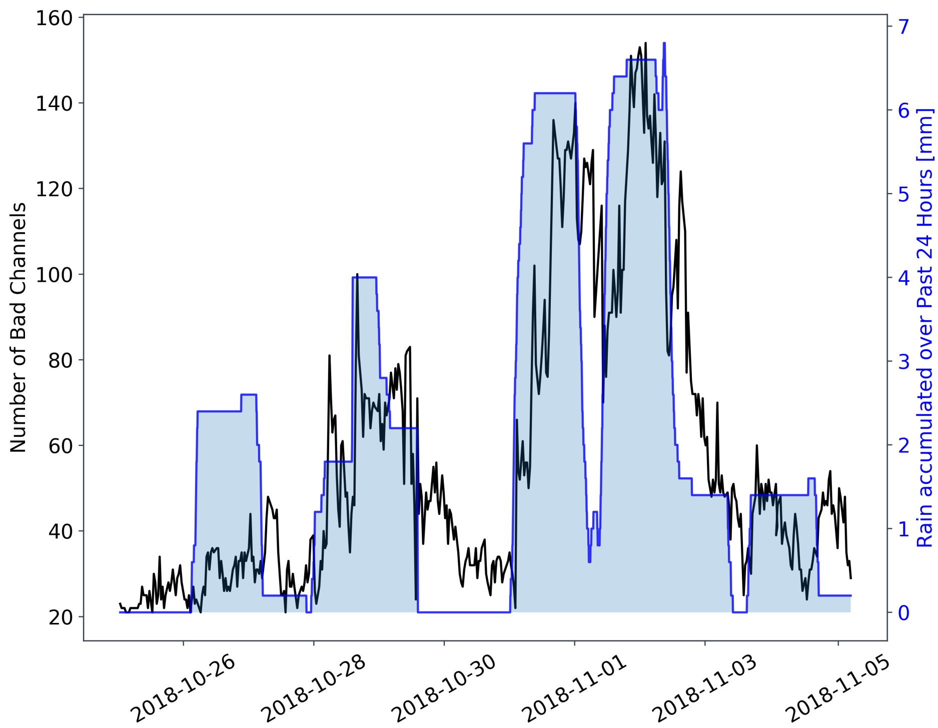

Figure 2.22: The plot shows that the amount of accumulated rain is highly correlated with the number of bad channels, i.e. during the period of rain we see a rapid increase in bad channels. The number of bad channels decreases to the level normally found once the rain water drains out of the system.

We also observed systematic effects of the rain on the good channel templates that are shown in Figure 2.23. There are three intelligible observations we can make: first, observations made during rainy days have a higher continuum level in the FFT power spectrum; second, RFI band, particularly broadband RFI bands shown in Figure 2.21, have lower power compared to what we experience during a typical day; lastly, we noticed that the width of the good channel histogram template is narrower during the time of rain. These observations suggest that during rain, some feeds are less sensitive to the signals from the sky (reduction in the RFI bands' power), and the water somehow results in increasing the system noise of those feeds (rise in continuum level). These observations strongly suggest that the rain has a considerable effect on the system stability, and proper waterproofing of the feed-lines is a desirable measure to be considered in CHIME. More in-depth analysis will be discussed in future work.

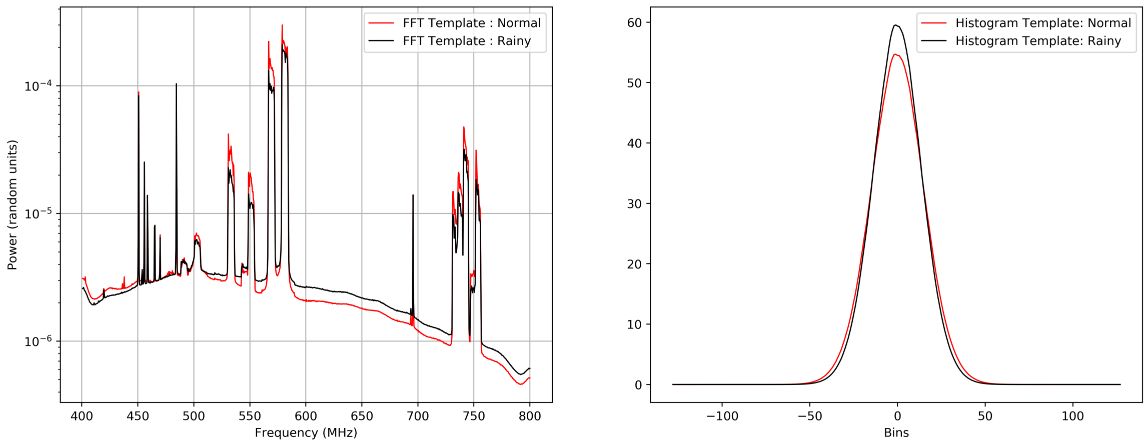

Figure 2.23: Comparison between good channel templates computed during a normal (dry) day and a rainy day.

We also found that the accumulation of water in the feed-line of CHIME is different for different feeds. This contradicts our assumption that the local environment is almost identically for all the feeds. Hence, it is not surprising that the pipeline does not identify all the affected channels but does detect a significant proportion of them, and has helped in identifying this previously unknown issue.

9 Pipeline evaluation

In Section 6, we show that the pipeline is effective in detecting different kinds of bad channels. In addition, we noted that the underlying assumptions entering the pipeline framework seem justified on a daily basis. In Section 7, however, we discuss how there are situations where either such assumptions break down or is not sufficient to handle corner cases. Therefore, we do not assert the pipeline's reliability in detecting all the bad channel cases, for example, rain affected channels. In any case, it is necessary to quantify the efficiency of the pipeline to detect all the bad channels. We have so far relied on the outlier statistics to identify the affected channels but we do not claim that this technique has an absolute validity. We must first know all the issues / artifacts that may impact our science goals in order to identify all the bad channels. Ng et al. (2017), Shaw et al. (2015), and Newburgh et al. (2014) discuss some criteria but those are not exhaustive. So far there has not been any simulation performed to quantify the effect of bad channels on the final data-product. This hinders us to either quantify or discuss different methods to evaluate the scientific impact of this pipeline. One possible method is to use point sources; we can study the effect of bad channels on the fringe patterns of the point sources in the visibility data. Another possible method is to estimate the noise level at which the voltage data for each channel are dominated by the systematics, and compare the estimated noise level to the desired sensitivity we want to achieve as per the scientific goals of CHIME. This is the strategy we intend to employ in the near future.

10 Conclusion

In this chapter, we present the pipeline designed to discover bad channels that must be identified promptly in order to maintain data integrity. One of the advantages of this pipeline is its ability to automatically identify bad channels every 30 minutes. The cadence of 30 minutes is set by the rate at which digitized voltage data from each of the 2048 channels are saved for monitoring the telescope's data quality. The pipeline saves time that our on-site staff would have spent manually identifying problematic channels. We describe the underlying framework of the pipeline, adaptive thresholding and cross-correlation techniques, to identify bad channels. We then demonstrate the pipeline's utility for finding channels with various hardware-related defects. We also evaluate the pipeline's fundamental assumptions and conclude that they are applicable to CHIME and other similar radio interferometric arrays. For completeness, we investigate various scenarios where the pipeline is not designed to work optimally due to the limitations of the underlying assumptions. Finally, we discuss possible approaches to increase the pipeline's efficiency while dealing with those scenarios.

This is a new pipeline of its kind that uses correlation statistics and adaptive thresholding to classify bad channels. Due to the advantages discussed in this chapter, there is good scope for such a pipeline in other multi-array radio telescopes, such as Murchison Widefield Array (MWA; Lonsdale et al., 2009), LOw Frequency ARray (LOFAR; Butcher, 2004), Hydrogen Epoch of Reionization Array (HERA; DeBoer et al., 2017), Hydrogen Intensity and Real-time Analysis eXperiment (HIREX; Newburgh et al., 2016), DSA-2000 (Hallinan et al., 2019), and Square Kilometer Array (SKA; Ellingson, 2005).

Chapter 3

The CHIME/FRB Project Overview

1 Introduction

In Chapter 2, we provide a brief summary of the front-end and analog chain of the CHIME telescope. In this chapter, we describe the CHIME correlator in Section 2 and the CHIME/FRB detection pipeline in Section 3. The CHIME/FRB project is a software-driven experiment, and using the powerful CHIME correlator and a specialized FRB search backend, we are able to make several landmark discoveries some of which are discussed in Section 4. Finally, as baseband localization regions are used in the work presented in Chapters 5, 6, 7, and 8, we describe the CHIME/FRB baseband pipeline in Section 5.

2 CHIME correlator

The primary function of the CHIME correlator is to convert analog time-domain raw voltage signals into digitized and channelized data that can be used by its three main projects: the CHIME/Cosmology project (CHIME Collaboration et al., 2022), the CHIME/FRB project (CHIME/FRB Collaboration et al., 2018), and the CHIME/Pulsar project (CHIME/Pulsar Collaboration et al., 2021). A schematic diagram of the CHIME telescope signal path is shown in Figure 3.1. The CHIME correlator has a hybrid FX design, where the 'F'-engine of the correlator digitizes and channelizes raw voltage data from 2048 signal paths using 128 custom FPGA boards. The 'X'-engine of the correlator then receives data from the

'F'-engine and computes data products that the three projects require for their science. The detailed discussion of the FX correlator is presented in CHIME Collaboration et al. (2022). We present a high-level overview of the F-engine and X-engine in Sections 2.1 and 2.2, respectively.

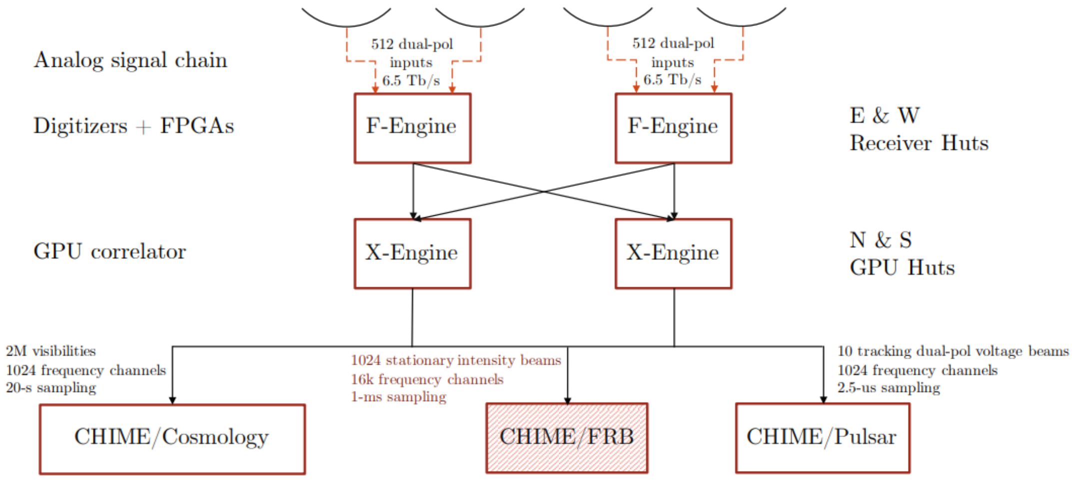

Figure 3.1: Schematic of the signal pathway for the CHIME telescope, as described in Section 2. The illustration depicts four cylindrical paraboloid CHIME dishes (black arcs), the correlator (F- and X-Engines), and the three projects that use CHIME data. The orange segments with dashes represent coaxial cables transmitting analog signals from the 256 dual-polarized feeds on each cylinder to the F-Engine. The black segments illustrate digital data sent across optical fibre. Note that the total input data rate of the F-Engine is 6.6 Tb/s and the data transmission rate to the CHIME/FRB backend is 142 Gb/s. Figure from CHIME/FRB Collaboration et al. (2018).

2.1 F-engine

The F-engine consists of 128 "ICE" motherboards (Bandura et al., 2016) placed in eight rack-mounted crates and linked with each other with custom high-speed, full-mesh back-planes. They are housed in two 20-ft steel shipping containers, called East and West receiver huts, retrofitted with radio-frequency shielding enclosures. The East receiver hut is located midway between the 1st and 2nd cylinders and the west receiver hut is located midway between the 3rd and 4th cylinders, halfway along their lengths. Each hut contains the electronics that handle data from their neighbouring cylinders. Each of the 128 "ICE" motherboards digitizes analog sky-signal from 16 inputs at the sampling rate of 800 MHz with 8-bit accuracy. The digitized data are then sent in frames of 2048 samples to a polyphase filter bank unit, which channelizes the signal into 1024 frequency bins with a bandwidth of 0.39 MHz. The channelized data are then rounded to 1024 [4+4] bit complex values per frame after applying a programmable gain and phase offset to the data. Finally, the channelized data are reorganized among the motherboards, which is required to facilitate desired computation processes by the X-engine nodes, such as spatial cross-correlation, RFI flagging, and multiple real-time beamforming. The stages of data shuffling are described in Bandura et al. (2016).

2.2 X-engine

The X-engine performs spatial correlations for the CHIME/Cosmology backend and additional computationally intensive operations required by other CHIME projects, such as FFT beamforming which is described in Section 3.1 as a part of the CHIME/FRB pipeline. The X-Engine is placed in two 40-ft shipping containers adjacent to the west most cylinder and mid-way along its length. These operations are carried out by 256 liquid-cooled nodes, each of which contains four GPU chips (Denman et al., 2020) and each GPU chip independently processes one frequency channel data. Note that the X-engine also has a memory buffer which stores 35.5 s of digitized and channelized voltage (baseband) data from all 2048 inputs, which can be saved to disk upon detection of a candidate FRB event (see Section 3.4).

3 CHIME/FRB pipeline

The CHIME/FRB system consists of a real-time software pipeline which searches for dispersed pulsed radio bursts of an astrophysical origin. Apart from FRBs, the CHIME/FRB pipeline also detects other short-duration radio signals, such as single pulses from Galactic pulsars and RFI.

The pipeline has five different stages, named L0 through L4. L0 performs FFT beamforming and up-channelization operations described in Section 3.1. L1, discussed in Section 3.2, performs RFI excision, dedispersion and identifies candidate events in each syn-

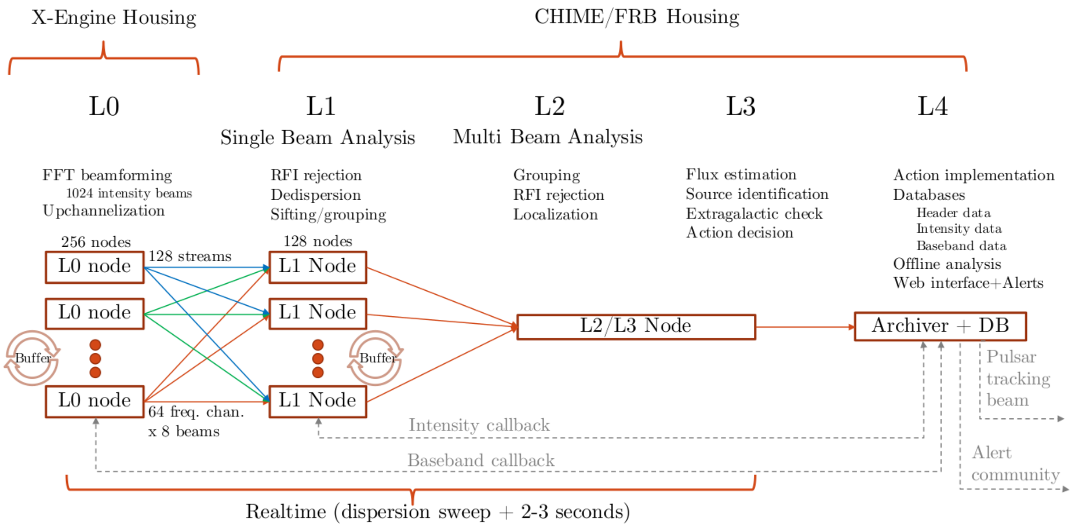

Figure 3.2: Schematic of the CHIME/FRB pipeline. L0 performs the beamforming and up-channelization. L1 performs RFI excision and incoherent dedispersion. The L2 and L3 stages group events detected in multiple beams and perform their classification into various categories. L4 stores detected events in a database and implements actions flagged in the L3 stage. L4 also initiates data callbacks. Data are continuously buffered by the L0 and L1 stages for baseband and intensity data callback, respectively. More details are provided in Section 3. Figure from CHIME/FRB Collaboration et al. (2018).

thesized beam. The L2 and L3 stages described in Section 3.3 and Section 3.4, respectively, combine the detection information for events in multiple beams and classifies the events. Finally, L4 stores the detection information for all events in a database and implements different actions based on the event classification which are discussed in Section 3.5.

To guide the reader through the flow of the pipeline, a schematic of the detection pipeline is shown in Figure 4.2. We present a high-level overview of the operations performed at each stage in the following subsections. Further details are presented in CHIME/FRB Collaboration et al. (2018).

3.1 L0: beamforming and up-channelization

CHIME/FRB employs a phased array mode in order to localize FRBs to a localization region of $\sim$ few 10s of arcminutes in real-time, where signal from all input feeds are coherently summed to form more directional beams using the technique called beamforming. Moreover, due to the regularly spaced dual-polarized CHIME feed configuration, it is possible to use fast Fourier transform (FFT) to form 1024 intensity beams (summing both polarization signals of each input feed), which significantly reduces the computation cost to $\mathcal{O}(\mathrm{N}\log\mathrm{N})$ compared to a traditional discrete Fourier transform (DFT) $\mathcal{O}(\mathrm{N}^2)$; here N is the number of input feeds (= 1024). Detailed description of this stage is presented in Ng et al. (2017) CHIME has an octave bandwidth (400-800 MHz), and the formed beams are highly chromatic, especially in the East-West direction due to sub-Nyquist spatial sampling (feed-separation/observed-wavelength $\approx$ 27 - 54 > 0.5 = Nyquist–Shannon sampling limit; Shannon, 1949). Therefore, in order to make spatially static formed beams, the data are zero-padded by a factor of two before the FFT to form 512 redundant beams, from which a subset of beams at each frequency is selected which are closest to the 256 desired pointings. Note that the formed beams are evenly spaced in sinθ, where θ is the zenith angle, such that in the N-S direction, the beams are formed between $\theta = -60°$ and $\theta = 60°$. Consequently, the formed beams are more elongated closer to the horizon then at zenith. In the E-W direction, the beam spacing was tuned to 0.4° to reduce beam overlap while simultaneously expanding the overall sky coverage. Note that beam spacing in both directions is a tunable parameter. Lastly, as the angular resolution decreases with increasing wavelength of the measured light, the generated beams are broader, resulting in significant overlap at lower frequencies.

Next, to mitigate the effect of dispersive smearing induced by intervening cold plasma along the FRB sightline, an FFT up-channelization is performed by the GPU nodes after beamforming. This is necessary because the CHIME/FRB pipeline searches FRBs with DMs as large as 13000 pc cm^{-3} using a incoherent dedispersion framework (see Section 3.2). Under this framework, frequency channels of width $\Delta\nu_{\mathrm{channel}}$ (in MHz) would retain a residual delay $\Delta \mathrm{t}_{\mathrm{channel}}$ given by (from Lorimer and Kramer, 2004),

$$\Delta \mathrm{t}_{\mathrm{channel}} \approx 8.3 \times 10^6\ \mathrm{DM}\Delta\nu_{\mathrm{channel}}\nu^{-3}\mathrm{ms}. \tag{3.1}$$

For a fiducial FRB of DM = 1000 pc cm^{-3}, the $\Delta\nu_{\mathrm{channel}}$ = 0.39 MHz at a frequency (ν) = 600 MHz would result in a $\Delta \mathrm{t}_{\mathrm{channel}} \approx$ 15 ms. As the residual delay in this case is significantly larger than the typically observed intrinsic width of FRBs $\sim$ 1 ms (see Chapter 1), this would significantly reduce the signal-to-noise (S/N) of the FRB signal (Cordes and McLaughlin, 2003).

In order to decrease $\Delta\nu_{\text{channel}}$, 128 successive time bins of raw voltage data are added and Fourier transformed. Now, the resulted power spectrum is downsampled by a factor of 8. Finally, successive three transformed values are averaged and the two orthogonal polarizations are summed to produced intensity data for each formed beam with the frequency and time resolution of 24.4 kHz and 0.983 ms, respectively.

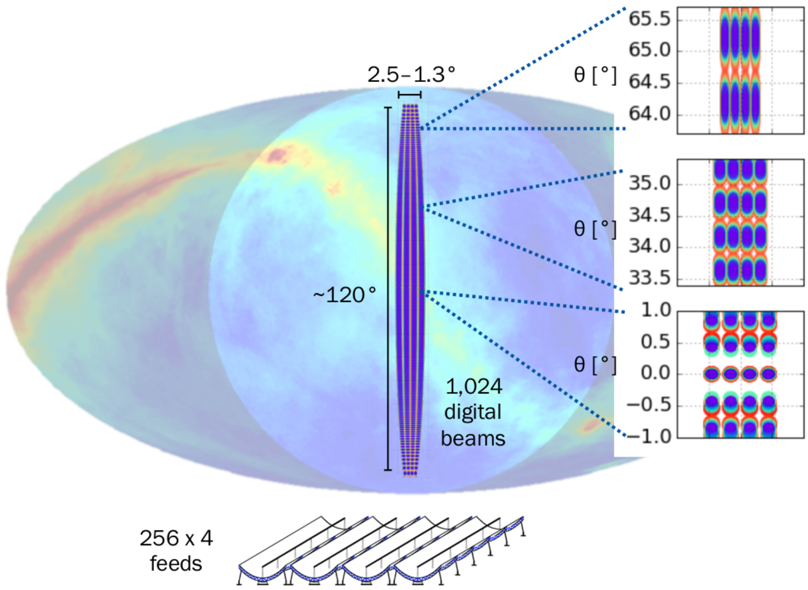

Figure 3.3: A schematic of the beamforming process used by CHIME/FRB. Each of the four cylinders has 256 dual-polarized feeds, and provides an instantaneous field of view of $\sim$ 250 square degrees. Its beamwidth in the East-West is 1.3°-2.5° (frequency dependent) and $\sim$ 120° in the North-South direction. Using FFT beamforming, described in Section 3.1, the L0 stage forms 1024 intensity beams. As seen in the three insets on the right (blue, green, and red colour represent formed beams at 800 MHz, 600 MHz, and 400 MHz, respectively), the formed beams are highly chromatic and their on-sky shape depends on their pointing angle from the zenith. Figure from Pleunis (2021), but first created by Liam Connor; beam calculations performed by Cherry Ng.

3.2 L1: dedispersion and FRB search per beam

This part of the pipeline performs RFI excision, dedispersion and identifies candidate events in each of the 1024 synthesized beams. It runs on a dedicated cluster with 128 CPU nodes where each node processes 8 formed beams.

The first part of the pipeline performs RFI mitigation using a custom RFI cleaning package `rf_pipeline` (Rafiei-Ravandi and Smith, 2022) that performs a series of detrending and clipping operations on the intensity data in both frequency and time domain. The clipping operation eliminates statistical outliers and replaces them with the mean intensity or a user-defined constant value. Similarly, the detrending operation removes polynomial trends from the data. The pipeline was trained with data from the CHIME Pathfinder telescope, which is a 1/10th size prototype version of CHIME situated at DRAO and hence observes a similar RFI environment. The RFI-cleaned data are then dedispersed.

Conventionally, two methods are employed to dedisperse pulsed radio signals: coherent and incoherent dedispersions. The coherent dedispersion technique deconvolves the interstellar dispersion transfer function from the complex voltage signal and restores the original Nyquist time resolution of the sampled voltage signal (Hankins and Rickett, 1975). In the incoherent dedispersion technique, data are shifted in time to compensate for the dispersion delay between channels, but dispersive smearing between channels is not addressed (Lorimer and Kramer, 2004) Coherent dedispersion offers major advantages over incoherent dedispersion, but at the risk of a greater computing burden. Therefore, the incoherent dedispersion approach is used in the CHIME/FRB real-time pipeline.

L1 performs incoherent dedispersion using a computationally efficient dedispersion package, `bonsai` (CHIME/FRB Collaboration et al., 2018). It implements the tree dedispersion algorithm (Taylor, 1974, Zackay and Ofek, 2017) which performs a dedispersion transform converting intensity data I(t, ν) to I(t, DM) by summing over all possible dispersion sweeps along the frequency axis. However, prior to this transformation, `bonsai` regrids the intensity data in time-ν^{-2} space, where the dispersed pulses would appear straight line. Due to momeory restrictions, the dedispersion is performed over the same intensity data, but with five different time resolutions ($\Delta t_{\rm tree}$) = 0.983 ms, 1.966 ms, 3.932 ms, 7.864 ms, and 15.729 ms. Also, besides DMs, `bonsai` searches signals over three more parameters: spectral index (β) , pulse arrival time (t), and pulse width (W). For W, the search is performed in each tree for four integral multiple of $\Delta t_{\rm tree}$, i.e. W = [1, 2, 3, 4] $\times \Delta t_{\rm tree}$. we selected two β for the search, β = $\pm$3, which increases our sensitivity to narrow-band bursts with emission at either edge of the band. Therefore, it produces a 4D array of signal-to-noise (S/N) values. This 4D array is then "coarse-grained" in arrival time and DM, and the candidate with the highest S/N candidate in the downsampled bins is selected. The algorithm finds local maxima in a region spanning 10 pc cm^{-3} in DM and 0.25 s in time. If any of these maxima have S/Ns greater than a tunable threshold (8.5σ), then it is classified as an L1 event and processed further. Information about an L1 event is stored in a metadata file called the "L1 header". The header includes the DM of the event, S/N, pulse arrival time at 400 MHz and coordinates of the beam where the event was detected.

Additionally, a ring buffer has been implemented for each node, which stores $\sim$ 240s worth of data at any time. To insure that the full dispersive sweep for high-DM events can be captured, the data are incrementally downsampled over time.

3.3 L2: multi-beam grouping and RFI mitigation

L1 header data from all 1024 formed beams are provided to a single CPU node to perform the L2 and L3 operations. Once all L1 headers for a single time block have been received, the DBSCAN clustering technique is used to group them (Ester et al., 1996). L1 event grouping is essential for event classification and refining the L1 header parameters. L1 events are only grouped together if their DMs, arrival times, and sky positions all match within user-defined criteria. The position criterion, for example, permits events detected in surrounding beams to be clustered. Because bright events can be detected in several beams, those detections are pooled together, and the localization region is adjusted such that the event's location is assigned to the position of the beam with the highest observed SNR . Following the grouping stage, the grouped data packet are provided to a machine learning algorithm developed using scikit-learn (Pedregosa et al., 2011), which assigns it a classification between 0 (RFI) and 10 (astrophysical).

3.4 L3: galactic inferences and action specification

The L3 stage of the pipeline makes logical inferences using the header data of L2 events. The first main inference is made about the nature of the source; whether it is Galactic or extragalactic. For this, based on the event's DM and localization region, the two Galactic free electron density models, YMW16 (Yao et al., 2017) and NE2001 (Cordes and Lazio, 2002), are queried, and the event's DM is compared to the maximum Galactic DM prediction of the two models towards the event's sky position using the criteria shown in Table 3.1. Moreover, the DM and sky-position of the L2 event are simultaneously compared to a database of known sources (Galactic pulsars and known FRBs), which is part of the real-time pipeline and is manually updated to incorporate particularly freshly human-verified FRB sources. This is the system that allows for the detection of repeating FRB sources in real time that is reported to public via the CHIME/FRB VOEvent Service[1].

Table 3.1: CHIME/FRB pipeline classification criteria for L3 event.

Classification	Criterion
Extragalactic	$\mathrm{DM}_{\mathrm{L2\ event}} - \mathrm{DM}^{b}_{\max} > 5\sigma^{a}$
Ambiguous	$2\sigma \leq \mathrm{DM}_{\mathrm{L2\ event}} - \mathrm{DM}_{\max} \leq 5\sigma$
Galactic	$\mathrm{DM}_{\mathrm{L2\ event}} - \mathrm{DM}_{\max} \leq 2\sigma$

[a] The combined statistical and systematic error in the DM measurements of the L2 event ($\mathrm{DM}_{\mathrm{L2\ event}}$) is represented by σ.
[b] $\mathrm{DM}_{\max} = \max(\mathrm{DM}_{\mathrm{YMW16}},\mathrm{DM}_{\mathrm{NE2001}})$

The L3 stage is also in charge of deciding if any predetermined actions should be triggered by L4. A collection of action rules is stored in the form of customisable file that may be examined in real time. L3 raises flags when specified action rules are found to be applicable. These flags trigger the L4 stage to carry out particular actions. These actions include saving the event's intensity and baseband data to disk, or sending alerts via the Virtual Observatory Events (VOEvent) framework (Petroff et al., 2017), which has been used by astronomers all over the world for multi-wavelength follow-up observations of CHIME

[1]Here is the official web-page of the CHIME/FRB VOEvent Service: https://www.chime-frb.ca/voevents.

FRBs.

3.5 L4: event database and action executioner

L4, the final stage of the CHIME/FRB pipeline, is executed on a dedicated CPU node on-site which is also real-time backed up to a computer at McGill University. L4 serves three primary purposes. First, it performs the operations specified by L3. For example, it calls a callback from the ring-buffer of intensity data from L1 or complex baseband data from L0 based on the flag raised by L3 for specific events. It should be noted that the L4 pipeline executes all actions for an event in parallel. Second, it hosts an event database, which stores information for all events as well as data products from L3 actions that have been implemented by L4. It also assigns a unique ID to each event, RFI or astrophysical – that the CHIME/FRB pipeline detects. Third, it functions as an online interface, allowing CHIME/FRB collaboration members to access the L4 database and classify candidate FRBs as RFI or astrophysical based on their dedispersed dynamic spectra.

4 Major CHIME/FRB accomplishments

The scientific impact of the CHIME/FRB project can be easily assessed by looking at the numerous discoveries that have transformed the field of FRBs. Note that at the time of the commissioning of the CHIME/FRB pipeline, it was uncertain whether FRBs could be detected below 700 MHz, as numerous low-frequency searches yielded negative results (CHIME/FRB Collaboration et al., 2019b, and references therein). Currently, more than three thousand FRBs have been discovered using the CHIME/FRB real-time pipeline, and a number of them have proven to be seminal results. The following sections highlight two major milestones of the CHIME/FRB project.[2]

4.1 The First CHIME/FRB catalogue

The first CHIME/FRB catalogue reported 536 FRBs including 62 bursts from 18 previously reported repeating sources in its first year of operations, i.e. 2018 July 25 to 2019 July 1

[2]Visit the following web-page for a comprehensive list of CHIME/FRB publications: https://chime-experiment.ca/en.

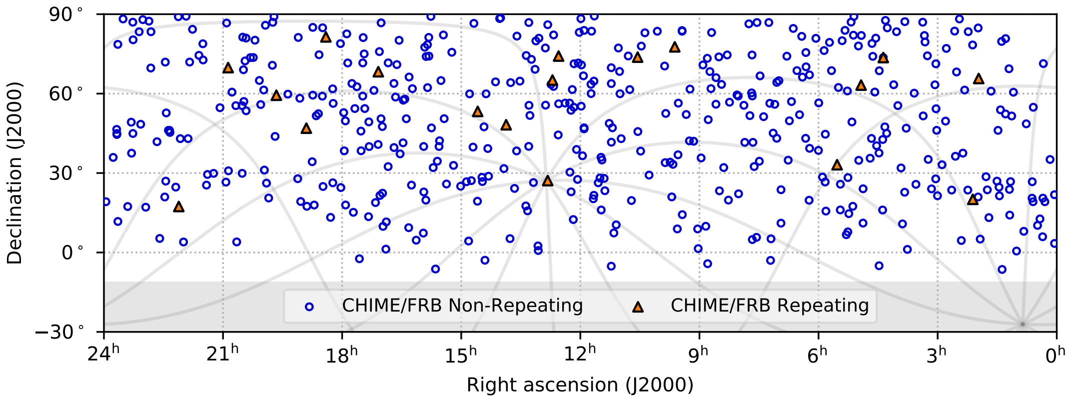

Figure 3.4: The distribution of FRBs from Catalogue-1 in Equatorial coordinates. Repeating FRB sources are depicted as orange triangles, whereas non-repetitive FRB sources are represented as hollow circles. Figure from The CHIME/FRB Collaboration et al. (2021).

(shown in Figure 3.4). As the FRBs reported in the catalogue are observed with uniform selection effects using a single instrument, it is well suited for several FRB population studies. Here are some of the main results published so far using the first CHIME/FRB catalogue (thereafter labelled as Catalogue-1) sample:

1. The power-law index for the cumulative fluence distribution of the Catalogue-1 FRBs is estimated to be $-1.40 \pm 0.11(\text{stat.})^{+0.06}_{-0.09}(\text{sys.})$, which is compatible with a non-evolving population in Euclidean space (The CHIME/FRB Collaboration et al., 2021).
2. The all-sky rate of bright FRBs (≥ 5 Jy ms) of DMs > 100 pc cm^{-3} that have scattering time at 600 MHz < 10 ms is calculated as $[820 \pm 60(\text{stat.})^{+220}_{-200}(\text{sys.})]$/sky/day[3] (The CHIME/FRB Collaboration et al., 2021).
3. The sky distribution of the Catalogue-1 FRBs is compatible with their origin from an isotropic extragalactic population (Josephy et al., 2021).
4. Bursts from repeating FRB sources are typically narrower in bandwidth and longer in duration than those from non-repeating FRBs (Pleunis et al., 2021).
5. We find a statistically significant cross-correlation between the Catalogue-1 FRBs and low-redshift galaxies suggesting that FRBs are located within the dark matter halos of the galaxies (Rafiei-Ravandi et al., 2021).

[3]Note that the revised all-sky rate is $[525\pm30(\text{stat.})^{+142}_{-131}(\text{sys.})]$ bursts sky^{-1} day^{-1} (Shin et al., 2022).

6. There is evidence of a substantial population of FRBs with a scattering duration at 600 MHz longer than 10 milliseconds. Chawla et al. (2022) employed a Monte Carlo–based population synthesis study using the properties of the Catalogue-1 FRBs and inferred that the circumburst media of FRBs should, on average, have more severe properties than usual Galactic plane media.

4.2 Bright millisecond radio bursts from a Galactic magnetar

CHIME/FRB on 28 April 2020 detected two extremely bright millisecond radio bursts separated by 28.91 ± 0.02 ms from a known Galactic magnetar SGR 1935+2154 (CHIME/FRB Collaboration et al., 2020a). The bursts were so luminous that they were detected far from the CHIME meridian as noted from the 'comb-like' spectral structure seen in the dedispersed waterfall plots shown in Figure 3.5. The high peak flux density of the two bursts ($\sim 7 \times 10^{36}$ erg s^{-1}), which is comparable to the faintest bursts from extragalactic FRBs, clearly suggests that magnetars can produce at least a fraction of FRB population. Additionally, this discovery has significantly reduced the large luminosity gap between what was previously observed from Galactic sources and what is detected from extragalactic FRBs. Finally, the detection of X-ray emission contemporaneous with the SGR 1935+2154 radio bursts suggests that at least some FRBs could have prompt X-ray counterparts (Bochenek et al., 2020, CHIME/FRB Collaboration et al., 2020a, Li et al., 2020, Mereghetti et al., 2020, Ridnaia et al., 2020). However, such X-ray emission currently can only be detected for nearby FRBs (for more discussion on this, see Chapter 1).

5 Baseband pipeline

The CHIME/FRB real-time pipeline processes the intensity data that has a temporal and spectral resolution of ≈ 1 ms and ≈ 24 kHz, respectively. Moreover, the formed intensity beams can localize FRBs to a sky region of around a few tens of arcminutes. For example, the CHIME/FRB formed beams at zenith provide the angular resolution of $\sim 15' - 30'$ across the CHIME band. This localization precision is not sufficient to robustly identify FRB host galaxies (Eftekhari and Berger, 2017). However, as CHIME is a radio interferometric array, it is possible to get more precise localization via coherent beamforming

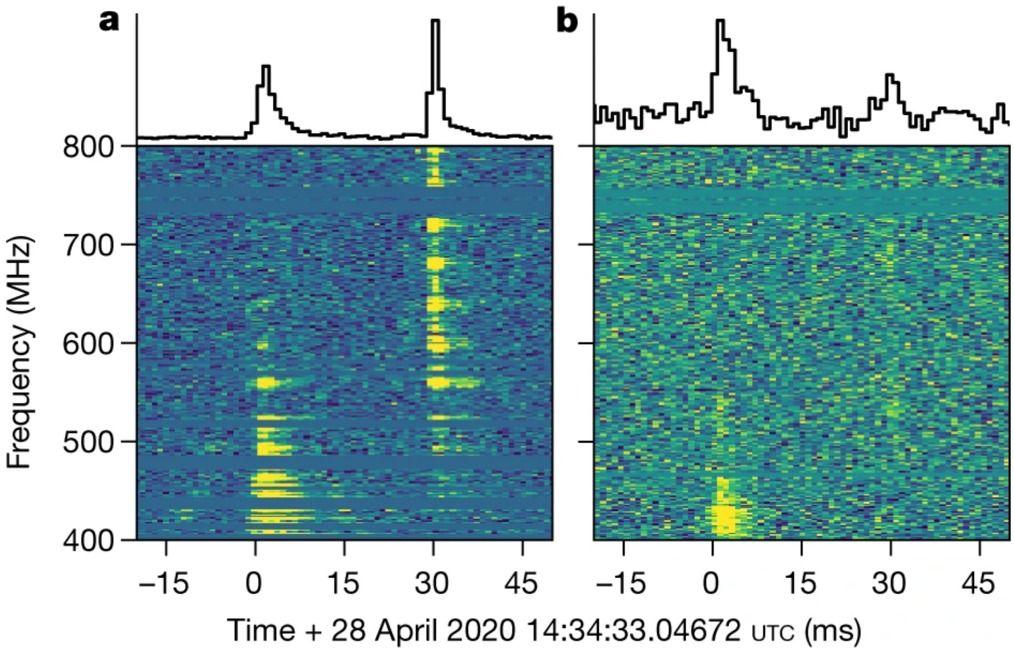

Figure 3.5: Total intensity normalized dedispersed “waterfall" plots of the detections by CHIME/FRB (a) and by the Algonquin Park 10-m radio telescope in Ontario, Canada (b), relative to the geocentric best-fit arrival time of the first CHIME/FRB burst from SGR 1935+2154. The CHIME/FRB bursts have a ’comb-like’ spectral morphology as a result of their detection in a beam sidelobe. Figure from CHIME/FRB Collaboration et al. (2020a).

using raw CHIME voltage (“baseband") data (Masui et al., 2017). For that, CHIME/FRB has commissioned a baseband recording system which processes the baseband data of FRBs that are triggered by L4 (see Section 3.5). Once triggered via L4, the baseband pipeline automatically processes stored baseband data and localizes a burst on the sky with a precision of $\sim \frac{8}{\mathrm{S/N}}$ arcmin (Michilli et al., 2020). For FRB bursts with high S/N and low extragalactic DM contribution, it is possible to identify the host galaxies using their baseband localization regions (see Chapter 4). In addition to host identification of nearby FRBs, baseband data also facilitate analyses, such as FRB polarimetry (Mckinven et al., 2021), studying FRB morphologies and sub-structures at a temporal resolution of $\sim \mu$seconds (CHIME/FRB Collaboration et al., 2022) using coherent dedispersion (see Section 3.2), and studying strong gravitational lensing of FRBs by primordial black holes (Kader et al., 2022, Leung et al., 2022). In the subsequent sections, we provide an overview of the CHIME/FRB baseband pipeline and its application in achieving more precise localization.

5.1 Overview of the CHIME/FRB baseband pipeline

As outlined by Michilli et al. (2020), the CHIME/FRB system possesses a baseband backend capable of recording the channelized voltages from each of the 1024 dual linear feeds. Channelization occurs through a Field Programmable Gate Array (FPGA) in the F-engine (see Section 2.1) to produce a spectrum with 1024 channels (each 0.39 MHz wide) every 2.56 μs. A programmable gain and phase offset are applied to each frequency channel, and the data are rounded to 4 + 4 bit complex numbers.

The system is configured to automatically record baseband data for events detected by the real-time system through implementation of a memory buffer that allows storage of 35.5 seconds of baseband data at a given time. Note that there is a latency of ~ 14 seconds between the time an FRB signal arrives the telescope and the realtime pipeline triggering the baseband dump. At CHIME frequencies and bandwidth, the usable data buffer of ~ 20 seconds roughly corresponds to a maximum DM of $\sim 1000\,\mathrm{pc\,cm^{-3}}$. Triggered events with larger DMs result in incomplete recordings with missing data at the top of the band. Typically, 100 ms of baseband data for each frequency channel are stored around the FRB's time of arrival (TOA). After adding buffer time to account for the FRB DM and TOA uncertainty, an average of $\sim$ 100 GB of baseband data are stored for a triggered event. There is a tunable S/N threshold to trigger baseband dump. For example, the SNR threshold of 8 $\sim$ can results in 10 baseband triggers per day.

Shortly after baseband data are recorded, a processing pipeline is launched and are composed of *refinement*, *localization* and *analysis* stages (Michilli et al., 2020). Figure 3.6 provides a summary of major steps involved in each of the three stages. Please refer to Michilli et al. (2020) for a detailed explanation of the CHIME/FRB baseband pipeline. Briefly, at the *refinement* stage, baseband data are used to improve the initial parameters of the FRB signal measured by the real-time pipeline. First, a set of beams are formed around the initial FRB sky position and the FRB signal detected by each of the formed beams is then coherently dedispersed at the real-time CHIME/FRB pipeline estimated DM value.

Currently, the grid of beams utilized to refine the initial localization produces three beams in the north-south direction and ten beams in the east-west direction making the total search area ~ 1.1 times 0.25 deg^2. Then, the total intensity of the FRB signal in all the formed beams is estimated as a function of time and frequency. The resulting 2D array is then downsampled in time such that the time resolution of the new array is three times the pulse width of the FRB signal estimated by the real-time pipeline. For each frequency channel and time bin, the S/N is calculated by normalizing the off-pulse rms to an average of zero and a standard deviation of one. This is done separately for each frequency channel and beam. In this process, RFI is iteratively removed to avoid any bias in the S/N measurements. Finally, the initial estimate position for the *localization* stage is the position of the beam with the highest S/N ratio. In the *localization* stage, which is described in Section 5.2, a single tied-array beam is formed in the direction of the refined localization position from the *refinement* stage and is employed as input in the analysis stage alongside other data from the pre-processing of the event (e.g., RFI channel mask, etc.). Finally, at the *analysis* stage, input data, which a matrix of complex voltages in frequency, polarization and time after refining the position and DM of the FRB signal at the *refinement* and *localization* stages, are supplied to a number of scientific pipelines designed for other scientific goals, such as polarimetry (Mckinven et al., 2021).

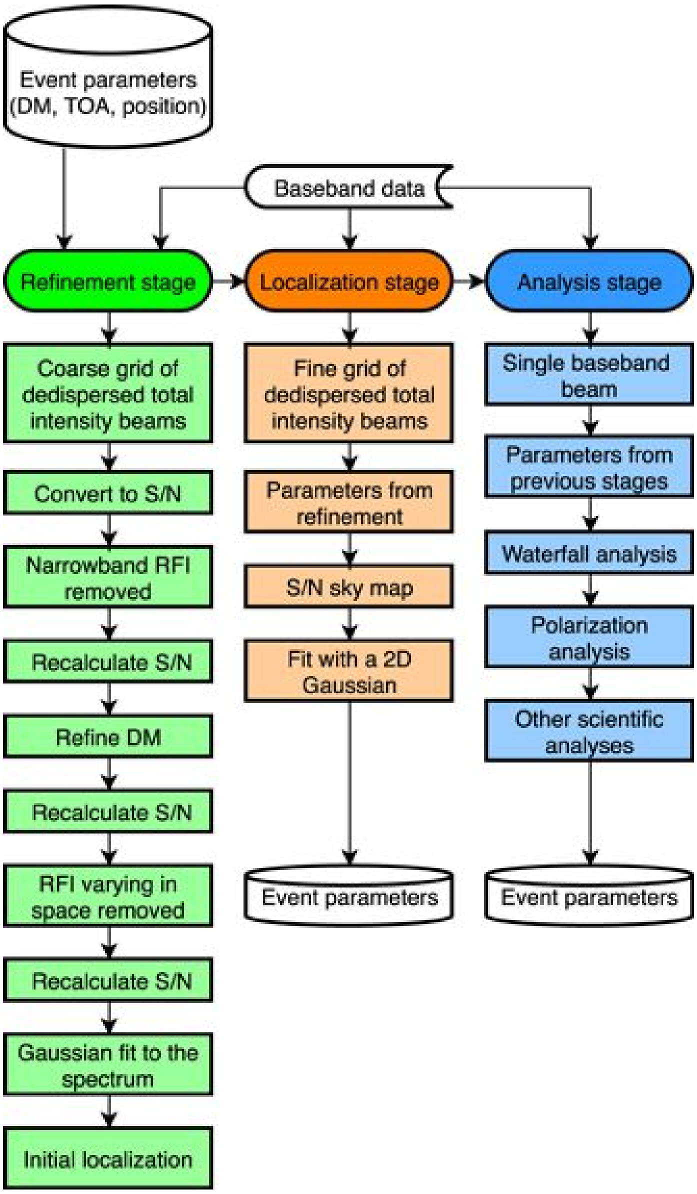

Figure 3.6: Illustration of the CHIME/FRB baseband pipeline processing of the triggered baseband data. Each of the three baseband pipeline stages is represented by a distinct colour. Individual tasks constituting the three stages are displayed in rectangular boxes beneath each branch and are highlighted with a lighter shade of the colour used to identify the three stages. Symbols for data and metadata are rendered in white colour. Figure from Michilli et al. (2020).

5.2 Baseband localization

Here we briefly describe how the output of the *refinement* stage is processed at the *localization* stage. The detailed discussion on this topic is presented in Michilli et al. (2020). First, the source localization is further refined using coherent beamforming techniques. Briefly, a grid of 5×5 beams is formed around the *refinement* stage's output localization region and a signal-to-noise ratio (S/N) value is calculated for each of them at the time of the burst candidate. Then, the resulting intensity map of the signal is fitted with a 2D Gaussian function approximating the sensitivity response of CHIME's formed beam.

A sample of pulsars and VLBI localized FRBs' positions are used to assess the localization capability of the baseband processing pipeline and estimate the impact of unaccounted systematic effects. A calibration for our localizations θ and their uncertainties σ is then estimated and is given by

$$\begin{aligned} \theta_x^i \pm \sigma_x^i &\rightarrow \left(\theta_x^i + 0.16'\right) \pm \left(\sqrt{\left(1.1\sigma_x^i\right)^2 + 0.19'^2}\right) \\ \theta_y^i \pm \sigma_y^i &\rightarrow \left(\theta_y^i + 0.17'\right) \pm \left(\sqrt{\left(1.1\sigma_y^i\right)^2 + 0.19'^2}\right), \end{aligned} \tag{3.2}$$

where x and y are celestial coordinates centred on CHIME and running in the East-West (x) and South-North (y) directions. For each source, we calculate a weighted average position based on the localization region of single bursts, accounting for the systematics defined in Eq. 3.2.

All the localization regions using in Chapters 5, 6, 7, and 8 have been corrected with this calibration. In the following five chapters, we describe the application of baseband localization regions to locate the hosts of nearby FRBs.

Chapter 4

FRB-λ: Pipeline to Identify Hosts of Nearby CHIME FRBs

1 Introduction

In Chapter 1, we discussed the importance of identifying FRB host galaxies in order to solve the FRB origin problem. FRBs, with the exception of FRB-like bursts from the Galactic magnetar SGR 1935+2154 (Bochenek et al., 2020, CHIME/FRB Collaboration et al., 2020a), have only been observed at radio wavelengths with no credible afterglow emission reported to date. Therefore, the only viable method currently available to identify their host galaxies is to localize FRBs to a sufficiently small region on the sky so that their association with galaxies or other astrophysical objects can be made on the basis of a low-chance association probability (P_{cc}), as has been done for all well-localized FRBs to date.

Since July 2017, CHIME/FRB has detected more than 3000 FRBs with DMs ranging between 88 and 3037 pc cm^{-3} (The CHIME/FRB Collaboration et al., 2021, & Chapter 3). The CHIME/FRB real-time pipeline estimates a localization from header data for all FRB events, but this localization precision is $\sim$ several tens of arcminutes (see Chapter 3). For bright FRBs (detection S/N ≥ 12), CHIME/FRB also saves raw voltage or "baseband data" that can facilitate their localization to sub-arcminute or a few arcminutes precision via the CHIME/FRB baseband localization pipeline (Michilli et al., 2020, see Chapter

3). To robustly associate a typical CHIME FRB of DM $\sim$ 400 pc cm^{-3} to its host, we need localization precision of $\lesssim 1''$ (Eftekhari and Berger, 2017). Therefore, most of the CHIME FRBs can't be robustly associated with galaxies even with baseband localizations. However, CHIME FRBs with low extragalactic DMs (or simply low excess-DMs)[1] can be associated with their hosts using baseband localizations.

As the maximum distance to the FRB hosts can be reasonably estimated from their excess-DMs, FRBs with low excess-DMs are expected to be nearby sources. For instance, using the Macquart relation (Macquart et al., 2020), an FRB with an excess-DM of 100 pc cm^{-3} would have a maximum redshift of 0.1. If this low excess-DM FRB is localized using the CHIME/FRB baseband pipeline to a localization region of radius $\sim$ $1'$, the number density of galaxies as faint as the faintest FRB host discovered to date (FRB 20121102A with absolute r-band magnitude $M_r = -17$ AB mag; Tendulkar et al., 2017) is expected to be small, hence, making any plausible association with such a host a rare coincidence ($P_{cc} \leq 10\%$). This can also be inferred from Figure 4.1. Therefore, CHIME/FRB baseband localizations can be useful in identifying host galaxies of nearby FRBs.

Low excess-DM FRBs (≤ 100 pc cm^{-3}) have an additional advantages. First, at the redshift of 0.1 (maximum redshift of an FRB with the excess-DM $\lesssim 100$ pc cm^{-3}), the faintest FRB host discovered to date ($M_r = -17$ AB mag; Tendulkar et al., 2017) would have an apparent r-band magnitude of $\lesssim 22$ AB mag. There are several archival wide-sky optical surveys, such as the Sloan Digital Sky Survey (SDSS Abdurro'uf et al., 2022), the Panoramic Survey Telescope and Rapid Response System (Pan-STARRS) survey (Chambers et al., 2016), and DESI (Dark Energy Spectroscopic Instrument) survey (DESI Collaboration et al., 2016), are sufficiently deep to detect galaxies of r-band magnitude ≤ 22 AB mag. Therefore, the hosts of nearby FRBs can be identified in the above archival optical survey data. Second, as discussed in Chapter 1, several FRB emission models predict their prompt multi-wavelength counterparts, which can be crucial in solving the FRB origin problem. However, these proposed counterparts can only be detected for nearby FRBs ($<$ 100 Mpc; Scholz et al., 2020), which explains why prior targeted searches for prompt FRB analogues yielded null results. So, nearby FRBs are the most promising sources for detecting pro-

[1]Excess-DM of an FRB is calculated by subtracting the predicted DM contribution of the Milky Way ISM (Cordes and Lazio, 2002, Yao et al., 2017) from its DM.

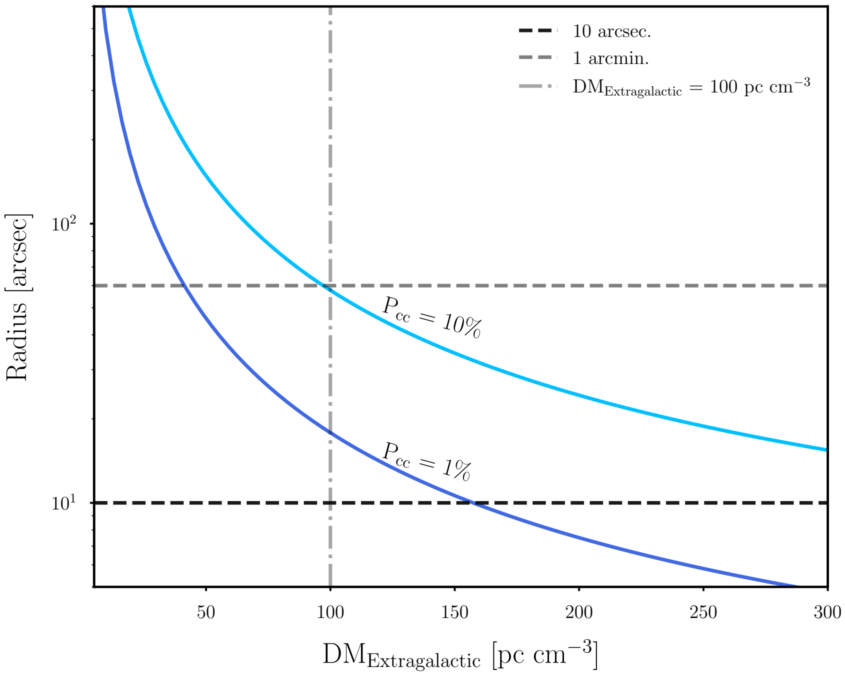

Figure 4.1: Probability curves for a Pcc = 0.01 and 0.1 as a function of extragalactic DM and localization radius of FRBs. Note that FRBs with extragalactic DMs $\approx$ 100 pc cm^{-3} can be associated with a dwarf, star-foming galaxy, like the FRB 20121102A host, with the P_{cc} of 0.01 and 0.1 using the localization precision of $\approx 20''$ and $60''$, respectively. The plot is produced using the first formalism discussed in Section 3.

posed FRB prompt and/or afterglow emissions via multi-wavelength follow-up campaigns, and to facilitate those, it is advantageous to identify their host swiftly. With this objective in mind, we commissioned a pipeline that we named 'FRB-λ' which searches archival optical data and identifies promising host candidates of low excess-DM CHIME/FRBs. This pipeline is fully automated and containerized for easy installation and operation. In Section 2, we outline the key modules of the pipeline, whereas in Section 7, we allude to some of its technical features and discussed a number of planned upgrades that we hope to implement in the near future. Finally, in Section 4, we conclude. Currently, the FRB-λ pipeline is employed to find host galaxies of over a dozen of low-DM FRB candidates (excess-DM $<$ 100 pc cm^{-3}; Bhardwaj et al., in prep), and we discuss four of those in Chapters 5, 6, 7, and 8.

2 FRB-λ pipeline

In this section, we describe the FRB-λ pipeline that we use to identify plausible host galaxy candidates of CHIME FRBs, especially the low excess-DM ones. The schematic representation of the FRB-λ pipeline is shown in Figure 4.2. The pipeline is written in the `Python` programming language and follows a modular structure, which makes it fairly simple to add new features to the current framework (see Section 7). In addition, the pipeline is containerized with the `Docker` software, enabling streamlined installation and configuration at the operating system level (Morris et al., 2017).

The pipeline takes the following six input parameters:

1. right ascension of the FRB (Ra),
2. 1σ uncertainty in Ra (Ra_err),
3. declination of the FRB (Dec),
4. 1σ uncertainty in Dec (Dec_err),
5. position angle of the localization ellipse (PA; default: zero), and
6. dispersion measure (DM) of the FRB.

The pipeline can also retrieve these parameters directly from the CHIME/FRB L4 database using the CHIME/FRB API service[2]. In this case, the user only needs to provide the FRB event number as input to the pipeline.

Using these six user-provided inputs, the pipeline first searches archival wide-sky optical survey databases and identifies all plausible galaxy candidates detected in the 2σ localization region of the FRB (see Section 2.1). Note that the size of the localization region is a tunable parameter. It then searches databases of the two infrared surveys, the Wide-field Infrared Survey Explorer (WISE Wright et al., 2010) and the Two Micron All Sky Survey (2MASS Skrutskie et al., 2006), to identify infrared counterparts of the identified galaxies, which is useful in characterizing the nature of identified host galaxies (see Section 2.4).

[2] `chime-frb-api` is a public python library that can access CHIME/FRB backend, such as CHIME/FRB databases, event headers, calibration products, and cluster jobs. This link provides further information: `https://chimefrb.github.io/frb-api/`.

The pipeline also estimates the FRB's maximum redshift (see Section 2.2) and the chance association probability of finding the identified galaxies in the FRB localization region (see Section 3). These estimates are required to determine whether a particular galaxy is associated with the FRB. Following the completion of the pipeline's execution, the following data products are saved to disk:

1. FRB localization region plots,
2. WISE colour-colour classification plot,
3. identified galaxy optical and infrared flux catalogue,
4. P_{cc} plots,
5. FRB Maximum redshift estimates (plot and a text file containing the content of the plot), and
6. Pan-STARRS g-, r-, and z-band fits images covering the full FRB localization region.

The pipeline saves all output files by default in the directory where it is installed on the system, but the user can also supply the path to the desired location on the system to the pipeline using an optional argument, `path`.

We now describe the main components of the pipeline in the following sections. To illustrate various data products generated by the pipeline, we present the pipeline's outputs for a low excess-DM FRB (DM = 111.6 pc cm^{-3}), FRB 20181223C. The FRB was reported in the first CHIME/FRB catalogue (The CHIME/FRB Collaboration et al., 2021), and is now found to be associated with a nearby star-forming galaxy at z = 0.03024 using a more precise baseband localization (Bhardwaj et al., in prep).

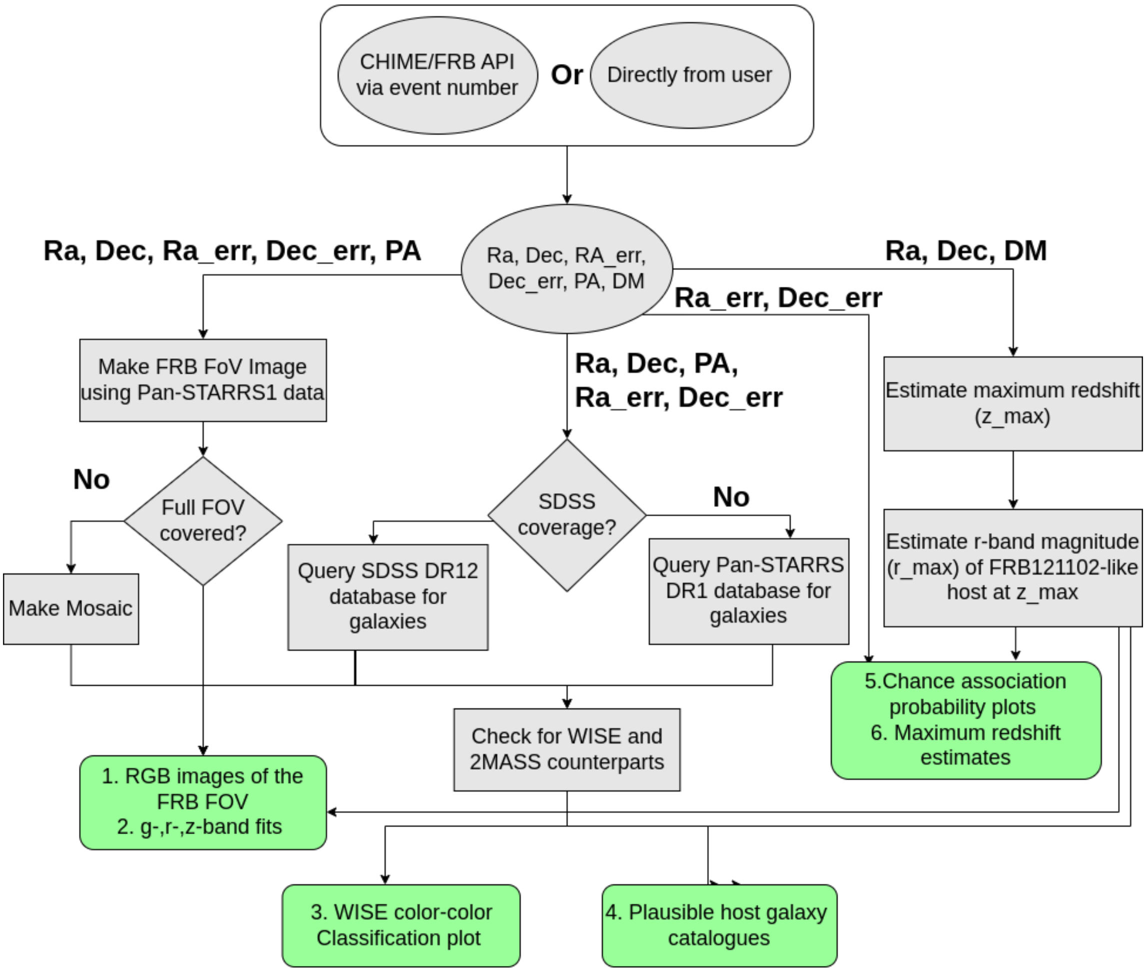

Figure 4.2: Schematic representation of the FRB-λ pipeline. The required input parameters for the three main process branches at the top are also shown in the flow diagram. In the current framework, the pipeline only looks for plausible host galaxy candidates in the SDSS and Pan-STARRS archive databases. However, more process/decision boxes will be added to the pipeline when more wide-sky deep optical survey data are made publicly available. Outputs of the pipeline are shown in green boxes.

2.1 Host candidate identification

In order to identify plausible host candidates within the FRB localization region, the pipeline queries the database of the following wide-sky optical surveys: the Sloan Digital Sky Survey (SDSS Abdurro'uf et al., 2022) and the Panoramic Survey Telescope and Rapid Response System (Pan-STARRS) survey (Chambers et al., 2016). Table 4.1 lists major attributes of the two optical surveys. As Pan-STARRS covers the full CHIME field-of-view (all sky above declination $> 11°$; CHIME/FRB Collaboration et al., 2018), it is the default choice of the pipeline. However, as the SDSS DR15 catalogue is more sensitive than that of the Pan-STARRS DR1 (see Table 4.1), when the FRB localization region is fully covered by the SDSS, the pipeline uses the SDSS DR15 catalogue to identify plausible host galaxy candidates. Another advantage of using the SDSS catalogue is that it provides star/galaxy classification along with photometric redshifts for all classified galaxies. These attributes are not yet available in the Pan-STARRS DR1 catalogue.

When the FRB localization region is covered by the SDSS DR15 catalogue, the pipeline queries the online SDSS DR15 database (Aguado et al., 2019). It returns the coordinates of all identified galaxies as well as their flux magnitudes (Petrosian magnitudes; see Section 2.5) in the five SDSS bands (u, g, r, i, and z; see Table 4.1) along with their photometric redshift estimates. If the spectroscopic redshifts of the identified galaxies are available, the pipeline saves those rather than their photometric redshifts.

Table 4.1: Major features of the optical and infrared wide-sky surveys queried by the FRB$-\lambda$ pipeline.

Survey	Sky coverage	Resolution arcseconds	Photometric bands	Limiting magnitude mag.
SDSS DR12	25% sky	1.3[a]	u, g, i, r, z	22.0, 22.2, 22.2, 21.3, 20.5
Pan-STARRS PS1	sky above Dec = $-30°$	1.31, 1.19, 1.11, 1.07, 1.02	g, i, r, z, y	22.0, 21.8, 21.5, 20.9, 19.7
2MASS	All sky	2	J, H, K_s	15.8, 15.1, 14.3
WISE	All sky	6.1, 6.4, 6.5, 12.0	W1, W2, W3, W4	16.6, 16.0, 10.8, 6.7

[a] Median point source function full-width half maxima of the r-band.

If the SDSS does not cover the FRB localization region, the pipeline queries the Pan-STARRS DR1 catalogue and retrieves the coordinates and flux magnitudes (Kron magnitudes; see Section 2.5) in the five Pan-STARRS bands (g, r, i, z, and y; see Table 4.1) for all extended sources in the FRB localization region. For that, it uses the 'Qual' flag which the Pan-STARRS DR1 catalogue saves for all of its sources. Apart from informing whether the source is extended in the stacked Pan-STARRS images, the value of Qual flag (Q hereafter) also indicates whether the detected object is real or likely an artifact.

As per the prescription provided by Magnier et al. (2020b), the pipeline selects those Pan-STARRS catalogue sources that are located within the FRB localization region and satisfy the following constraint: $52 \ < \mathrm{Q} < \ 64$[3]. This would ensure that the detected source is (1) extended in the Pan-STARRS DR1 data, (2) is present in multiple epoch datasets, and (3) is unlikely to be a measurement artifact. However, this criterion alone does not efficiently remove false positives – sources that are not galaxies. These cases include bright stars with saturated DR1 stacked measurements and very faint stars which, due to atmospheric effects, appear extended. To remove these false positives, we use the difference between r-band PSF and Kron magnitudes of the identified extended sources ($\Delta_{\mathrm{kron-psf}}$ hereafter). Note that both the PSF and Kron r-band magnitudes are available for all sources reported in the Pan-STARRS DR1 catalogue. As per the prescription proposed by Farrow et al. (2014) to remove 98% of false positives, the pipeline only selects those extended sources that satisfy the following relations:

$$\Delta_{\mathrm{kron-psf}} < 0.018 \times (r_{\mathrm{kron}} - 21)^2 + 0.120 \times (r_{\mathrm{kron}} - 21) - 0.192 \tag{4.1}$$

and

$$\Delta_{\mathrm{kron-psf}} > 0.417 \times (r_{\mathrm{kron}} - 21) - 1.759, \tag{4.2}$$

Equations 4.1 and 4.2 are meant to remove faint stars, image artifacts, and bright stars with saturated Pan-STARRS DR1 stacked measurements. Moreover, Farrow et al. (2014) noted that these cuts, by construction, had very little effect on the completeness of real galaxies.

Recently, Beck et al. published a neural network source classification and photometric redshift catalogue for Pan-STARRS DR1, which they called PS1-STRM. This catalogue includes photometric redshifts of all Pan-STARRS DR1 sources identified as galaxies[4] Moreover, their galaxy classifications are in excellent agreement with those determined using the scheme described above (Beck et al.). As the catalogue has only recently made

[3]For more information on this flag, see: https://outerspace.stsci.edu/display/PANSTARRS/PS1+Object+Flags.

[4]Except a few regions of the Northern hemisphere; see Beck et al..

public, it is yet to be incorporated in the current version of the pipeline[5].

Finally, irrespective of whether the SDSS covers the FRB localization region, the pipeline queries the Pan-STARRS DR1 database to retrieve g-, r-, and z-band images of the FRB localization region. This is mostly done to reduce the pipeline's complexity. The overall image quality of both surveys is comparable, with the exception of a minor difference in sensitivity. If the retrieved images do not fully cover the FRB localization region, the pipeline again queries the database to download images of the missing region till the full localization region is covered. The pipeline then coadds retrieved images of each of the three Pan-STARRS bands using the software, `Montage` (Berriman and Good, 2017), to create mosaic images. We use `Montage` because it maintains the spatial and calibration integrity of input images while being computationally efficient. These images are saved on disk as outputs of the pipeline. The pipeline then uses these images to make an RGB (using Pan-STARRS's g-band (B:blue), r-band (G:green), and z-band (R:red) data) plot of the FRB localization region that includes all identified host galaxy candidates. Additionally, at the end of its execution, the pipeline makes another RGB plot that includes only those galaxies whose extinction corrected r-band magnitudes are $\leq$ that of the faintest FRB host known to date (FRB 20121102A host) at the maximum estimated redshift (see Section 2.2). To illustrate this, we present the two localization region plots generated by the pipeline for FRB 20181223C in Figure 4.3. Note that the only difference between the top and bottom plots is that the top plot contains all six identified galaxies within the 2σ localization region, whereas the bottom plot shows only four galaxies with r-band magnitudes $\leq$ to the apparent r-band magnitude of the FRB 20121102A host at the estimated maximum redshift of 0.077 (see Section 2.2) = 20.64 AB mag. However, all the identified SDSS DR15 catalogue galaxies detected within the FRB localization region (top plot of Figure 4.3) are considered in our host association analysis.

[5]We use a separate script to query the PS1-STRM catalogue for photometric redshifts of the selected galaxies.

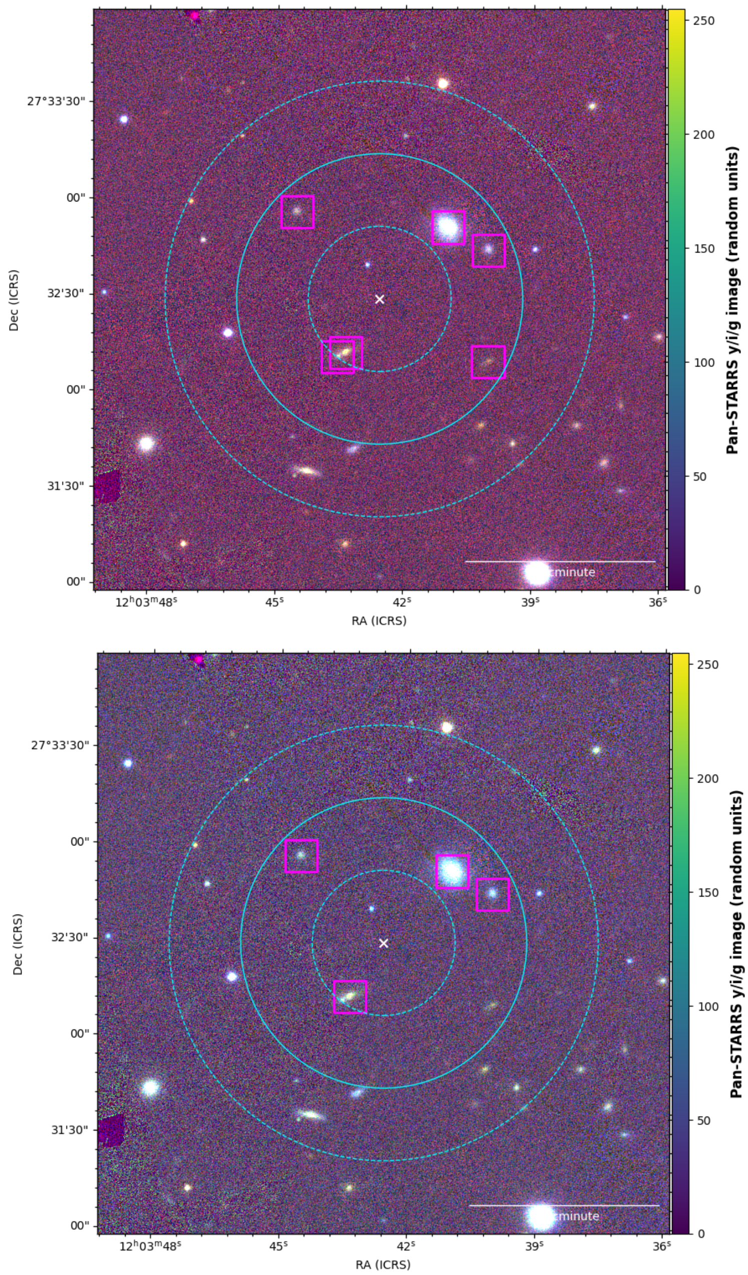

Figure 4.3: FRB localization region plots generated by the FRB-λ pipeline using the baseband localization region (1σ, 2σ, and 3σ contours are shown in the plots) of FRB 20181223C. The top plot shows all identified SDSS DR15 catalogue galaxies within the 2σ region, whereas the bottom plot only highlights those that satisfy our r-band magnitude constraint, i.e., m$_r \leq 20.64$ mag (see Section 2.1).

2.2 Maximum FRB redshift estimation

In order to make sure that archival optical images are sensitive to detect the FRB 20121102A host (faintest host discovered to date), the pipeline estimates the maximum redshift (z_{max}) of an FRB using a Monte-Carlo (MC) sampling technique. Additionally, the z_{max} value is useful in the chance association probability calculation discussed in Section 3. The pipeline samples the priors (that correspond to the components that contribute to the FRB DM) specified in Table 4.2 3000 times. Although the sample size = 3000 was chosen arbitrarily, we noted that increasing it would have no major effect on the predicted z_{max} values.

Table 4.2: Priors used in the MC sampling method described in Section 2.2.

DM component	Model name	Units	Prior	Reference[a]
Host galaxy DM (DM_{host})	'Early'-type host[b]	pc cm^{-3}	23	1
	'Late'-type host[b]	pc cm^{-3}	35	1
	'Zero' host contribution	pc cm^{-3}	0	-
Milky Way DM (DM_{MW})	'NE2001 model	pc cm^{-3}	N(VALUE[d], 20% times VALUE)[c]	2
	'YMW16 model	pc cm^{-3}	N(VALUE[d], 20% times VALUE)[c]	3
Milky Way halo DM ($DM_{MW,halo}$)	'PZ19' model	pc cm^{-3}	U(50,80)	4
	'Dolag' model	pc cm^{-3}	30	5

[a] Note – References: (1) Xu and Han (2015) and Walker et al. (2020); (2) Cordes and Lazio (2002); (3) Yao et al. (2017); (4) Prochaska and Zheng (2019); (5) Dolag et al. (2015).

[b] DM_{host} simulations by Xu and Han (2015) and Walker et al. (2020) found DM_{host} for typical sites in inclination-averaged early-type & dwarf galaxies and for face-on late-type galaxies to be 23 pc cm^{-3} and 35 pc cm^{-3}, respectively.

[c] Here 'U(lower limit, upper limit)' is a uniform distribution, and 'N(mean, standard deviation)' is a normal distribution.

[d] The pipeline uses the python package, `PyGEDM`, that provide an interface to the YMW16 (Yao et al., 2017) and NE2001 (Cordes and Lazio, 2002) electron density models (Price et al., 2021). It takes Ra and Dec of the FRB to gives the predicted DM contribution of the Milky Way ISM.

The pipeline estimates DM_{IGM} for each sample using the following relation, DM_{IGM} = $DM - DM_{MW} - DM_{MW,halo} - DM_{host}/(1+z)$. From DM_{IGM}, the pipeline estimates redshift for each sample using the following relation,

$$DM_{IGM} = 805 \text{ pc cm}^{-3} \frac{f_{IGM}}{0.83} \int_0^z \frac{(1+z')dz'}{\sqrt{\Omega_m(1+z')^3+\Omega_\lambda}}, \tag{4.3}$$

where f_{IGM} is the baryon fraction of the fully ionized IGM, which for local Universe is estimated to be 0.83 (Fukugita et al., 1998), and Ω_λ & Ω_m are present-day dark energy and matter densities, which we assumed to be 0.693 and 0.307, respectively (Planck Collaboration et al., 2016). Note that as the DM_{IGM} relation (Equation 4.3) is a bijective function of redshift (z), given the value of DM_{IGM} one can estimate the corresponding redshift by simply taking the inverse of Equation 4.3[6].

However, before estimating the redshift for each sample, we need to account for spatial variations in the DM contribution of the IGM. For that, the pipeline adds a random value sampled from a Gaussian prior of mean = 0 and $\sigma(DM_{IGM}) = 210\sqrt{z}$, as suggested by Kumar and Linder (2019). The $\sigma(DM_{IGM})$ is a reasonable approximation out to z = 3 of the observed spatial variations in the DM contribution of the IGM in cosmological simulations by McQuinn (2014). To estimate a conservative value of z for $\sigma(DM_{IGM})$, the pipeline estimates the mean FRB redshift by assuming that the excess-DM in each MC sample is solely contributed by the IGM (DM_{host} = 0 pc cm^{-3}) and use Equation 4.3.

Note that we use three priors for DM_{host} and two priors for both DM_{MW} and $DM_{MW,halo}$ giving in total 12 different z_{max} estimates, after taking all possible combinations of priors for each DM component.

Finally, the pipeline estimates a 90% upper limit on the redshift using the MC sample of redshifts for each of the 12 models. In Figure 4.4, we show the maximum redshift estimate output of the pipeline for FRB 20181223C. We also note that for all the FRBs with known hosts to date ($\sim$ 20), host galaxy redshifts are significantly smaller than the pipeline's largest z_{max} estimates for those FRBs. Therefore, in the second formalism of the P_{cc} analysis, which is discussed in Section 3, the pipeline uses the largest of the z_{max} estimates where the $DM_{host} = 0$ pc cm^{-3} prior is not used.

In all of our scientific publications, we estimate the maximum redshift of FRBs using an MCMC simulation framework, which applies a more realistic prescription for the DM_{IGM} prior. However, because of the above formalism is developed before and also its the computing cost of the described MC sampling method is negligible, the maximum red-

[6] A simple python code to estimate the redshift is available at https://github.com/Astronomer-Mohit/void-analysis/.

shift estimate provided by the FRB-λ pipeline is still instructive, particularly in the early stages of locating FRB hosts. In the subsequent upgrade of the pipeline, we will replace the aforementioned MC sampling approach with the MCMC simulation framework which is described in Chapter 7.

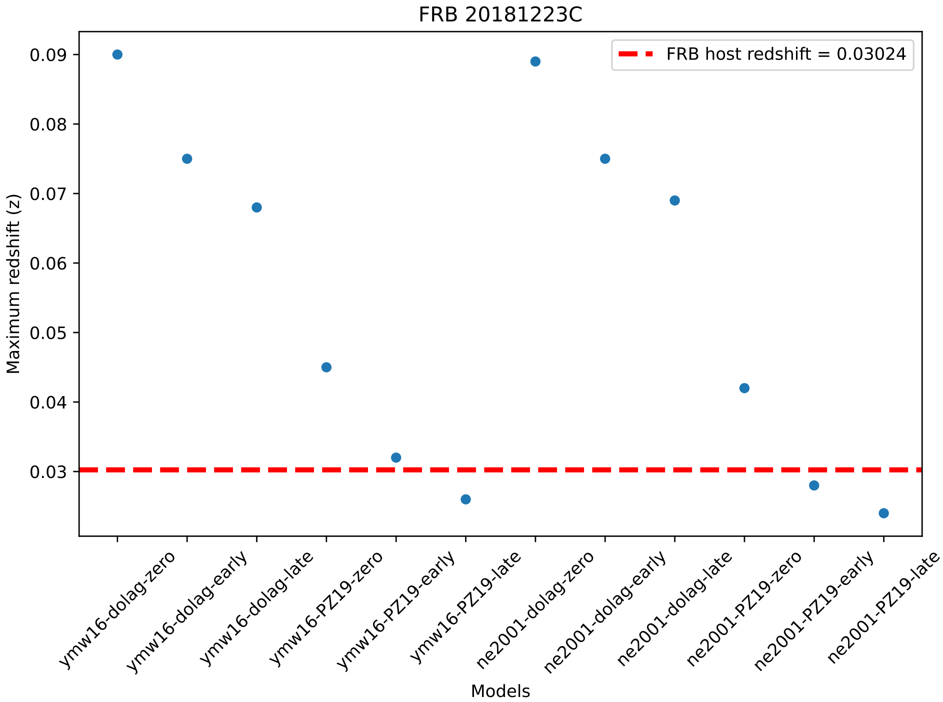

Figure 4.4: Maximum redshift estimate plot generated by the pipeline for FRB 20181223C. The red dotted line shows the redshift of the host (Bhardwaj et al., in prep). For more information, see Section 2.2.

2.3 Chance association probability estimation

As described in Section 1, the association of FRBs with their host galaxies is exclusively based on the framework of chance association probability (P_{cc}). In this section, we first describe the two formalisms that the pipeline follows to estimate P_{cc}. The detailed discussion on the two formalisms is presented in Bloom et al. (2002), Eftekhari and Berger (2017), Eftekhari et al. (2018), and Aggarwal et al. (2021).

In the first formalism, the pipeline estimates the probability of a chance occurrence for a galaxy of apparent r-band magnitude m_r in the FRB's 2σ localization region. Using the r-band galaxy number density function reported by Driver et al. (2016), the pipeline computes the projected areal number density of galaxies brighter than m_r, $\psi(\leq \mathrm{m_r})$. After that, assuming a Poisson sky-distribution of galaxies, the probability of a chance coincidence occurring within a radius R is calculated by the pipeline using the following relation:

$$\mathrm{P_{cc}} = 1 - \exp(-\pi \mathrm{R}^2 \psi(\leq \mathrm{m_r})), \tag{4.4}$$

where R is the effective radius that corresponds to the 2σ localization region of the FRB.

In the second formalism, we incorporate the maximum redshift ($\mathrm{z_{max}}$) estimate calculated by the pipeline (see Section 2.2). The pipeline first estimates the number of galaxies above the absolute r-band magnitude of the FRB 20121102A host (M_r = -17 AB mag; faintest host to date) to $\mathrm{z_{max}}$. For that, we consider two different number density estimates from Faber et al. (2007): (1) the 68% confidence limits on the number density of blue star-forming galaxies ($\mathrm{n_{blue}}$) $-$ like FRB 20121102A host $-$ with $M_r \leq -17$ AB mag to be [0.0085, 0.0165] $\mathrm{Mpc^{-3}}$, and (2) the 68% confidence limits on the number density of any galaxies ($\mathrm{n_{gal}}$) with $M_r \leq -17$ AB mag to be [0.017, 0.023] $\mathrm{Mpc^{-3}}$. These number density estimates are then multiplied with the comoving volume $\mathrm{V_{max}}$ out to $\mathrm{z_{max}}$ and the fractional area of the localization region on the sky $f_A = \pi$ R^2/4.123 $\times 10^4$, where R is again the effective radius that corresponds to 2σ localization region of the CHIME/FRB (in units of degrees) and 4.123 $\times 10^4$ is the total area of the celestial sphere in units of square degrees. The probability of chance coincidence is then estimated by the pipeline using the relation,

$$\mathrm{P_{cc}} = 1 - \exp(-\mathrm{V_{max}} \times \mathrm{f_A} \times \mathrm{n_{gal}} \text{ or } \mathrm{n_{blue}}). \tag{4.5}$$

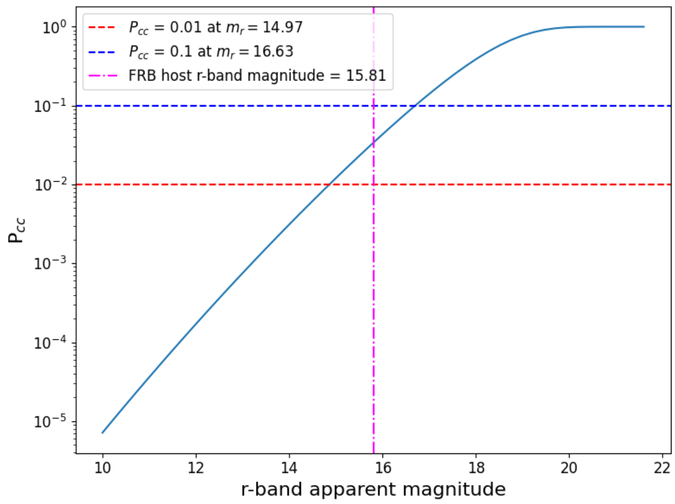

Figure 4.5: Pipeline generated P_{cc} plot for FRB 20181223C based on the first formalism discussed in Section 3 using the CHIME/FRB baseband localization region. The P_{cc} of the identified host galaxy (m_r = 15.8 AB mag, represented by the vertical magenta line) is $\approx$ 3%. The two horizontal lines denote P_{cc} = 10% (blue) and 1% (red), which intersect the P_{cc} curve at m_r = 16.63 AB mag and 14.97 AB mag, respectively.

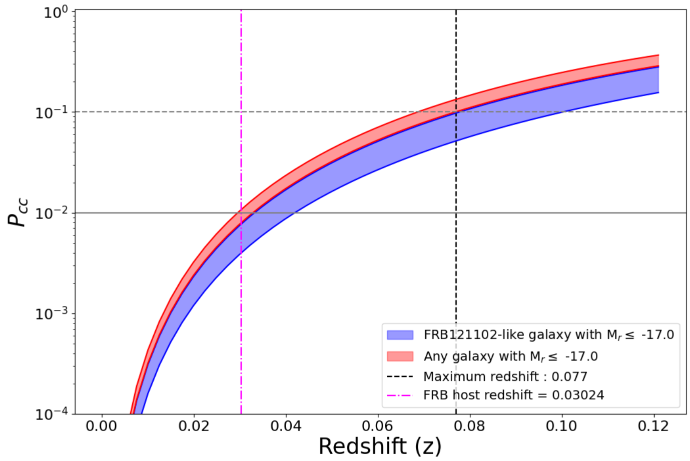

Figure 4.6: Pipeline generated P_{cc} plot for FRB 20181223C based on the second formalism discussed in Section 3 using the CHIME/FRB baseband localization region. The P_{cc} of finding an FRB 20121102A host-like or brighter galaxy within the FRB localization region to the z_{max} = 0.077 is $\leq$ 10%.

In Figure 4.5 and 4.6, we show the P_{cc} plots for FRB 20181223C produced by the pipeline using the two formalisms. The P_{cc} values are estimated using the baseband localization of the FRB. For the second formalism (shown in Figure 4.6), the pipeline first estimated the maximum redshift of FRB 20180916B = 0.077 (see Figure 4.4).

2.4 Classification of host candidates using infrared data

After selecting plausible FRB host candidates, the pipeline searches the following all-sky infrared surveys, 2MASS (Skrutskie et al., 2006) and WISE (Cutri et al., 2021, Wright et al., 2010), to identify potential infrared counterparts of the galaxies. Table 4.1 lists major attributes of the two infrared surveys. Note that multi-colour photometric data are useful since light from different parts of the electromagnetic spectrum reveals distinct physical processes occurring in galaxies. In addition, they aid in understanding the nature of the identified galaxies. Specifically, a significant number of broadband optical and infrared filters would allow us to generate detailed spectral energy distributions (SEDs) for the identified galaxies, which would facilitate the estimation of the galaxies' physical properties and photometric redshifts (Benítez, 2000, Wild et al., 2014).

The pipeline searches for infrared counterparts in the 2MASS and WISE source catalogues within the search radius of $2''$ and $6''$ around the coordinates of the identified galaxies, respectively, which were employed in several optical-infrared cross-matching analyses (Dong et al., 2011, Lang et al., 2016, Rutledge et al., 2000, Theissen et al., 2016). The search radii are based on the resolution of the surveys and are significantly larger than typically observed combined (in quadrature) astrometric uncertainties of the infrared and optical catalogues, i.e. $< 0.2''$ (Kurcz et al., 2016, Magnier et al., 2020a). Here we assume that when an infrared source is found for a given galaxy, then it is the counterpart. As the optical surveys have a better angular resolution, the number of sources within the search radius in other surveys always turns out to be either one or none.

As the optical surveys that the pipeline employs are more sensitive than the infrared ones, the pipeline does not find counterparts in 2MASS and/or WISE catalogue for most of the faint galaxies (m_r > 20 AB mag). In those cases, the pipeline automatically assigns a `NULL' value to the infrared band magnitudes. In case of detection, the pipeline retrieves catalogued flux values in the 2MASS (J, H, K_s) and WISE (W1, W2, W3, W4) broadband filters of the identified counterparts.

If the pipeline finds a WISE counterpart, it makes a WISE colour-colour classification plot using the W1-W3 and W2-W3 colours of identified galaxies, which provides important information about the nature of the FRB host candidate (for example, see Chapter 7). WISE mapped the sky at 3.4 (W1), 4.6 (W2), 12 (W3), and 22 (W4) μm with an angular resolution of 6.1″, 6.4″, 6.5″, and 12.0″, respectively (see Table 4.1). The main families of extragalactic sources that can be identified in the WISE data include star-forming galaxies (especially starburst galaxies), and galaxies with active nuclei (AGN) and quasars (QSO). Their positions in a representative WISE colour-colour (CC) diagram are shown schematically in the left panel of Figure 4.7. As can be seen in the CC diagram, Different classes of astrophysical sources occupy unique regions. Note that since WISE colours are normalized to Vega, colours of blackbody emission are close to 0 (Wright et al., 2010). On the other hand, sources that are either embedded in dust shells or whose radiation experience high dust extinction are redder in the CC diagram. This is because the absorbed radiation is reprocessed to longer wavelengths shifting the source's infrared colour to red. Therefore, WISE classification provides a novel perspective on the characteristics of galaxies, which is useful for understanding the nature of FRB hosts (Nikutta et al., 2014). Figure 4.7 was produced by the pipeline for FRB 20181223C, where we can see the locations of the identified galaxies (all except one) with a WISE counterpart.

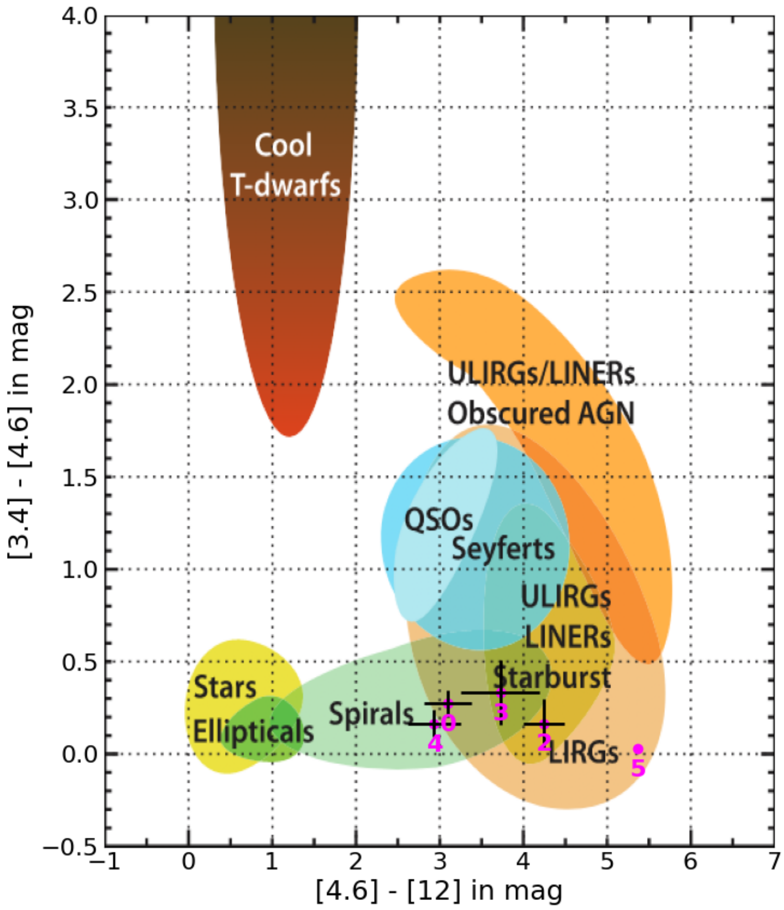

Figure 4.7: WISE colour-colour classification diagram showing the locations of various types of astrophysical objects. As described in Section 2.4, thermal sources with little extinction (stars and early-type galaxies) have colours close to zero, whereas spiral galaxies are red in W2-W3, and luminous infrared galaxies (LIRGs) and ultraluminous infrared galaxies (ULIRGs) tend to be red in both colours. This plot is produced by the FRB-λ pipeline for galaxies (numbered as per their indexes in the saved flux catalogue file; see Section 2.5) within the baseband localization region of FRB 20181223C where the pipeline found a WISE counterpart. The background WISE colour-colour classification plot is taken from Wright et al. (2010).

2.5 Making flux catalogue

After identifying host galaxy candidates and their infrared counterparts, the final step is to save the coordinates, flux magnitudes, and other relevant parameters (photometric/spectroscopic redshifts) to disk. The flux catalogue will be used in various useful analyses. For example, in the absence of archival spectroscopic and photometric redshift values, the multi-colour photometric fluxes in the catalogue can be used directly by a publicly available photometric redshift code, `EAZY` (Brammer et al., 2008), to estimate photometric redshifts of identified galaxies. Additionally, broadband photometry data in the flux catalogue are used in modelling the stellar population of the host galaxy in order to estimate its main physical properties, such as stellar age, dust content, star formation history, metallicity, stellar mass, and star formation rate. In chapters 6, 7, and 8, the pipeline-produced flux catalogues are employed in modelling host stellar population using a Bayesian inference spectral energy distribution (SED) fitting code, `Prospector` (Johnson et al., 2019, Leja et al., 2017).

Before saving optical and infrared flux magnitudes in the flux catalogue, the pipeline corrects for Galactic extinction using a python package, `dustmaps` (Green, 2018). In addition to the extinction corrected magnitudes in their original units, the pipeline adds new columns of fluxes (in 'erg/s/cm2/Hz'; converted from magnitudes) to the catalogue. This is done for two reasons: first, it facilitates direct comparison between optical and infrared catalogue magnitudes, and second, stellar population modelling and photometric redshift estimation packages, such as `EAZY`, Fitting and Assessment of Synthetic Templates (`FAST` Kriek et al., 2009), and `Prospector`, require all fluxes in the same units. The pipeline employs the following conversion formulae which are taken from their main survey publications:

For Pan-STARRS DR1 sources, the fluxes are reported in AB magnitude. To convert Kron magnitudes into flux densities in 'erg/s/cm^2/Hz', we use the following conversion formula,

$$\mathrm{F[erg/s/cm^2/Hz]} = 10^{-\mathrm{F_{kron}[AB\ mag]}/2.5} \times 3631 \times 10^{-23}. \tag{4.6}$$

For galaxies identified in the SDSS DR15 catalogue, the pipeline saves the Petrosian magnitudes[7] which are are expressed as inverse hyperbolic sine (or "asinh") magnitudes (for more information, see Lupton et al., 1999). To convert asinh magnitudes into flux densities in 'erg/s/cm^2/Hz', we use the following conversion formula,

$$\mathrm{F[erg/s/cm^2/Hz]} = [\sinh[(-1\times\ln(10)\times(\mathrm{F_{petro}[mag]}))/2.5]-\ln(\mathrm{b})]\times 2\mathrm{b}\times \mathrm{f_o(Jy)}\times 10^{-23}, \tag{4.7}$$

where b = [1.4,0.9,1.2,1.8,7.4]$\times 10^{-10}$ and $\mathrm{f}_o(\mathrm{Jy})$ = [3767, 3631, 3631, 3631, 3565] for u, g, r, i, and z bands, respectively.

Finally, to convert 2MASS and WISE aperture magnitudes (all magnitudes are in the Vega system), we follow the prescription provided in (Cutri et al., 2021) and estimate respective flux densities using the following formula,

$$\mathrm{F[erg/s/cm^2/Hz]} = 10^{-(\mathrm{F_{kron}[\ mag]+C})/2.5} \times 3631 \times 10^{-23}, \tag{4.8}$$

where C = [0.893, 1.373, 1.840, 2.683, 3.319, 5.242, 6.604] are the zero-point corrections for J, H, Ks, W1, W2, W3, and W4 filters, respectively.

In case of no infrared detection, the pipeline inputs 'NULL' values in the flux density columns. After finishing the conversion, the pipeline saves the catalogue in the local directory or at the path provided by the user along with other pipeline outputs.

3 Discussion and future developments

In this section, we discuss several technical details of the pipeline and highlight some forthcoming upgrades to the pipeline's current version. The pipeline follows a modular framework, which can be seen in Figure 4.8. The main components of the pipeline are arranged so that modules with similar functionality can be grouped together. For example, all catalogue-query programs are stored in a single directory ('Catalogues'; see Figure 4.8) so that modules for querying various databases can be accessed by all. This eases debugging and avoids code redundancy. Additionally, this will permit the addition of upcoming deep optical and infrared surveys, such as the Canada-France Imaging Survey (CFIS; Fantin et al., 2019),

[7] Recommended for extended sources; see https://www.sdss.org/dr12/algorithms/magnitudes/.

the Legacy Survey of Space and Time (LSST; Ivezić et al., 2019), Dark Energy Survey (DES Abbott et al., 2018), the Euclid Wide Survey (EWS; Euclid Collaboration et al., 2022), Nancy Grace Roman Space Telescope (formally called the Wide-Field InfraRed Survey Telescope (WFIRST); Eifler et al., 2021), and SPHEREx (Crill et al., 2020), to the pipeline when they become publically accessible. These surveys will be specifically useful when the CHIME/FRB very-long baseline interferometry (VLBI) project (Cary et al., 2021, Cassanelli et al., 2022, Leung et al., 2021, Mena-Parra et al., 2022), consisting of three dedicated miniature version of a single CHIME cylinder located at continental baselines, will detect and localize FRBs with a precision of $\sim$ 50 mas.

The current version of the pipeline takes $\sim$ 10-15 minutes to finish its execution, which so far works fine for our scientific requirements. In any case, there is a scope to reduce the execution time by implementing a parallel computing framework. For instance, `Python` has an in-built parallel computing module `multiprocessing` to allow us to write parallel codes by spawning processes on the user's system. This could be potentially useful when querying various multi-wavelength catalogues for counterparts. Therefore, the use of parallel-computing modules can be implemented in the upcoming version of the pipeline. This will be especially beneficial when we add more analysis modules to the pipeline, such as employing the Probabilistic Association of Transients to Hosts (PATH) software package to estimate true host association probabilities for the identified host galaxy candidates (Aggarwal et al., 2021).

As discussed in Section 2.4, multi-band photometry data are an important resource for understanding the stellar population of the FRB host. Currently, the pipeline only queries two infrared catalogues, but in the next version, we plan to include wide-sky survey catalogues, such as Galaxy Evolution Explorer (GALEX - UV; Gil de Paz et al., 2007), ROSAT (X-ray; Boller et al., 2016), and other infrared catalogues, like UKIRT Infrared Deep Sky Survey (UKIDSS; Lucas et al., 2008). Finally, to make counterpart searches more efficient, we are exploring ways to directly query public astronomical data archives, such as the Mikulski Archive for Space Telescopes (MAST; Brasseur and Donaldson, 2020) and CasJob (OMullane et al., 2005).

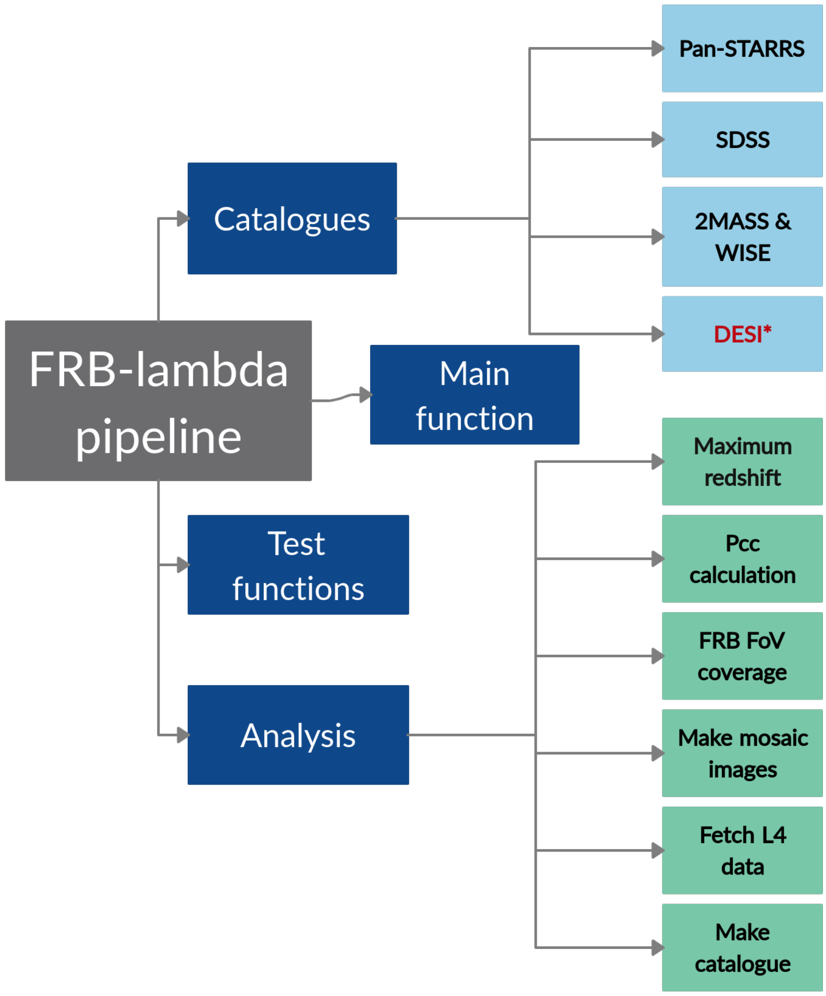

Figure 4.8: Schematic representation of the structure of the FRB-λ pipeline. The pipeline follows a modular design, with the top directory (right) comprising, in addition to the main script, three process-specific folders ('Catalogue, 'Analysis,' and 'Test function'). These three folders include routines that are categorized according to the specific function they perform. Note that the 'Test function' folder contains unit test scripts that allow users and developers to spot errors faster. Finally, although the 'DESI' catalogue query routine is not included in the current version of the pipeline, it can still be accessed by the user, if required. In a future version, it will be fully incorporated into the pipeline. Finally, 'Main function' is the script that the user would run to execute the pipeline.

4 Conclusion

In this chapter, we describe the FRB$-\lambda$ pipeline, a `Python`-based fully automated pipeline that identifies plausible host galaxy candidates of CHIME FRBs, particularly those with low excess-DM. The pipeline first searches archival optical survey data to identify all galaxies within the FRB localization region and then searches for possible infrared counterparts of the identified galaxies. It saves the identified galaxies' flux catalogue, which includes their coordinates, extinction-corrected flux magnitudes and flux densities, as well as their spectroscopic or photometric redshifts. In addition, it estimates the maximum redshift of the FRB and the chance association probability of discovering (1) a galaxy of a particular apparent r-band magnitude and (2) a galaxy similar to the faintest FRB host discovered to date in the comoving volume in the FRB localization region to the estimated maximum FRB redshift. Lastly, it generates FRB localization plots utilizing Pan-STARRS g-, r-, and z-band data, that also show the location of discovered galaxies. Since its inception, the pipeline has consistently been used to identify plausible host candidates for CHIME FRBs. We discuss four of them in Chapters 5, 6, 7, and 8.

Chapter 5

A Nearby Repeating Fast Radio Burst in the Direction of M81

1 Introduction

In this chapter we report the discovery of FRB 20200120E, a repeating FRB detected by the CHIME/FRB collaboration (CHIME/FRB Collaboration et al., 2018). The FRB dispersion measure (DM) of 87.82 pc cm^{-3} is the smallest reported for an FRB thus far, yet is significantly higher than the maximum expected from the Milky Way interstellar medium in this direction ($\sim$ 50 pc cm^{-3}). We have detected three bursts and one candidate burst from the source over the period 2020 January-November are described in Section 2. The baseband voltage data for the event on 2020 January 20 enabled a sky localization of the source to within $\simeq$ 14 sq. arcmin (90% confidence). In Section 3, we present evidence against the source being associated with the Milky Way or its halo, though the halo origin cannot yet be rejected conclusively[1]. We then describe our search for a host and propose that M81, a nearby early-type grand-design spiral galaxy at 3.63 ± 0.34 Mpc (Freedman et al., 1994, Karachentsev et al., 2002), is the most likely FRB host. We further show the FRB is unlikely to be beyond M81. In Section 4, we discuss the implications of this study and conclude in Section 5.

[1]The source is now conclusively found to be associated with an M81 globular cluster that we identified in Section 3.5 (Kirsten et al., 2021).

2 Observations & analysis

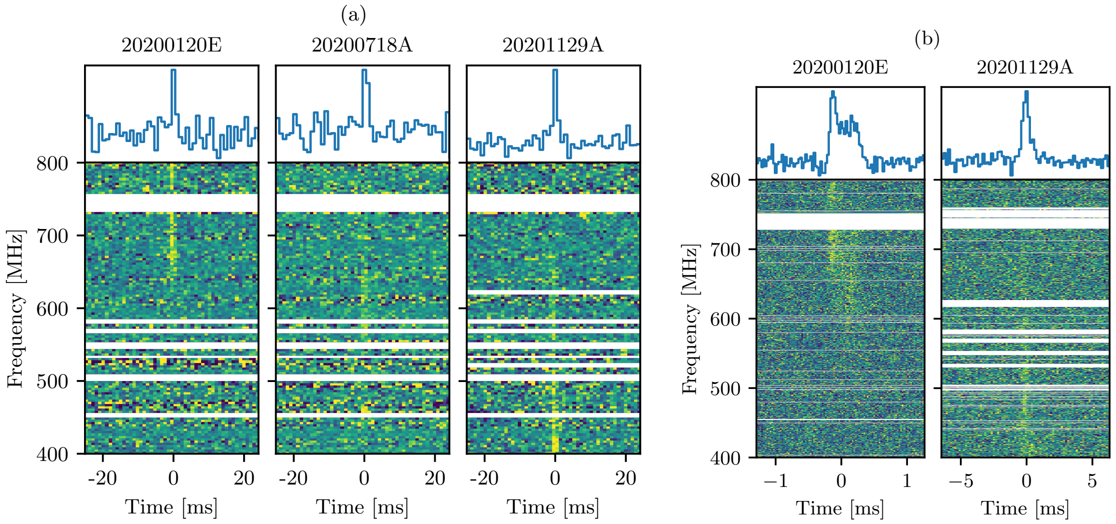

Figure 5.1: Frequency versus time ("waterfall") plots of three dedispersed bursts detected from FRB 20200120E. **(a)** The dedispersed waterfall plots of the three bursts made using total-intensity data, with temporal and spectral resolutions of 0.983 ms, and 3.125 MHz, respectively. See Table 5.1 for the burst properties. **(b)** The waterfall plots of two FRB 20200120E bursts, FRBs 20200120E and 20201129A, made using baseband data, which here are binned to have temporal resolution 0.0256 and 0.16384 ms, respectively, and spectral resolution 0.391 MHz. The horizontal white lines in the waterfall plots are flagged channels that are either bad (due to radio frequency interference) or are missing due to computer nodes in the CHIME system being offline. Lastly, the fourth possible burst did not have intensity or baseband data recorded (see Section 2.1), and therefore, is not shown here.

2.1 The repeating source FRB 20200120E

FRB 20200120E was discovered by CHIME/FRB on 2020 January 20 in the real-time pipeline. Offline analysis of the burst total-intensity data using `fitburst` (CHIME/FRB Collaboration et al., 2019a,b,c, Fonseca et al., 2020) measured a DM of 87.782 ± 0.003 pc cm^{-3} (see Tables 5.1 & 5.2). This event was also recorded by the CHIME/FRB baseband system. Using the recorded baseband data and our offline baseband localization pipeline (Michilli et al., 2020), we have localized the FRB to a sky area of ≈ 14 arcmin^2 (90% confidence region; see Table 5.2). The baseband localization is consistent with that inferred from the multi-beam intensity data detections, but is more precise as the full-array baseband data are used to estimate the localization region.

We detected three bursts and one candidate burst from the FRB source. For the second burst on 2020 July 18, the CHIME/FRB baseband system was undergoing maintenance, so we saved only total-intensity data at the nominal CHIME/FRB search resolution. On 2020 November 29, we detected a third burst for which baseband data were recorded. Following a procedure identical to that used for the January 20 burst, we estimate the 90% confidence localization region of the burst as: R.A. $= 09^{\rm h}57^{\rm m}42.^{\rm s}1 \pm 18.^{\rm s}9$ and Dec = $68^\circ48'57'' \pm 01'39''$. As the baseband localization region of the FRB from the 2020 January 20 burst is completely inside the latter localization region, we used the baseband localization region of the FRB in all our follow-up analyses. Later, while searching the CHIME/FRB event database, we found a fourth burst detected on 2020 February 6, having SNR 10.6, above the 10σ threshold that the CHIME/FRB pipeline uses to identify candidate FRB events (see Chapter 3). All the header data metrics, which are discussed in CHIME/FRB Collaboration et al. (2018), suggest that the source is astrophysical. However, due to an unidentified issue in the FRB data recording system, the intensity data of the 2020 February 6 burst were not saved. Therefore, we cannot confirm its astrophysical nature. Hence, we excluded it from the analyses in this work. In Table 5.1, we report basic properties of this burst from the header data.

Because the best-fit DMs and sky positions of the three bursts for which we have intensity and/or baseband data saved to disk are consistent, we conclude that the FRB is a repeater. Therefore, we adopt the Transient Name Server (TNS)[2] FRB naming convention, which gives the source the name of the first detected burst, FRB 20200120E. The TNS names of the bursts on 2020 July 18 and 2020 November 29 are FRBs 20200718A and 20201129A, respectively. As the intensity data of the FRB detected on 2020 February 6 were not saved, we did not request a TNS name for the burst.

[2]https://wis-tns.weizmann.ac.il/

Table 5.1: Properties of the bursts from FRB 20200120E.[a]

TNS Name	Day (yymmdd)	MJD	Arrival Time[b] (UTC @ 400 MHz)	SNR	DM (pc cm^{-3})	Width (ms)	Scattering Time (ms @ 600 MHz)	Fluence[c] (Jy ms)	Peak Flux Density[c] (Jy)	DM$^{d}_{\mathrm{bb}}$ (pc cm^{-3})	RM (rad m^{-2})
20200120E[f]	200120	58868	09:57:35.984(2)	22.9	87.782(3)	0.16(5)	<0.23	2.25(12)	1.8(9)	87.789(9)	-29.8(5)[g]
–	200206[e]	58885	08:50:45	10.6	88(1)	–	–	–	–	–	–
20200718A	200718	59048	22:12:31.882(1)	14.0	87.864(5)	0.24(6)	<0.17	2.0(7)	1.1(5)	–	–
20201129A[f]	201129	59182	13:31:29.8583(6)	19.3	87.812(4)	<0.1	0.22(3)	2.4(1.4)	1.7(1.2)	87.71(5)	-26.8(3)[g]

[a] Uncertainties are reported at the 1σ confidence level (cl). Reported upper limits are those of the 2σ cl.
[b] All burst times of arrival are topocentric.
[c] Fluence and peak flux density measurements represent lower bounds as we assumed that the bursts were detected at the centre of their detection beams.
[d] Optimized DM for the burst detected in the baseband data.
[e] Single beam event with sky position consistent with the FRB baseband localization stated in Table 5.2. However, the intensity data were not saved, so a TNS name has not been assigned. The reported DM and timestamp of the FRB were from the header data of the event.
[f] Burst parameters were estimated using the total-intensity data.
[g] Both RM measurements have an additional systematic uncertainty of 1.0 rad m^{-2}.

Table 5.2: Major Observables of FRB 20200120E.

Parameter	Value
R.A.(J2000)[a]	$09^{\mathrm{h}}57^{\mathrm{m}}56^{\mathrm{s}}.7 \pm 34^{\mathrm{s}}.6$
Dec. (J2000)[a]	$68°49'32'' \pm 01'24''$
l, b [b]	142.°19, +41.°22
DM[c]	87.818 ± 0.007 pc cm^{-3}
$\mathrm{DM}^{d}_{\mathrm{MW,NE2001}}$	40 pc cm^{-3}
$\mathrm{DM}^{d}_{\mathrm{MW,YMW16}}$	35 pc cm^{-3}
$\mathrm{DM}^{e}_{\mathrm{MW,WIM}}$	10−40 pc cm^{-3}
$\mathrm{DM}^{f}_{\mathrm{MW,N_H}}$	14−28 pc cm^{-3}
$\mathrm{DM}^{g}_{\mathrm{MW,halo}}$	30 pc cm^{-3}
Max. distance[h]	$\lesssim 135$ Mpc
RM[i]	$-28.3 \pm 0.6 \pm 1.0$ rad m^{-2}

[a] FRB position determined from baseband data saved for FRB 20200120E using the technique described by Michilli et al. (2020). The quoted uncertainty is the 90% cl.
[b] Galactic longitude and latitude for the baseband localization central coordinates.
[c] Weighted average DM of the three observed bursts (excluding the 2020 February 6 burst; see Table 5.1).
[d] Maximum DM model prediction along this line-of-sight for the NE2001 (Cordes and Lazio, 2002) and YMW16 (Yao et al., 2017) Galactic electron density distribution models.
[e] DM contribution of the Milky Way assuming that the ISM in the FRB sight-line is dominated by diffuse warm ionized medium (WIM); see Section 3.1.
[f] DM contribution of the Milky Way using the $\mathrm{N_H} - \mathrm{DM}$ relation from He et al. (2013); see Section 3.1.
[g] Milky Way halo prediction from the Dolag et al. (2015) hydrodynamic simulation. The Yamasaki and Totani (2020) model predicts a similar value $\sim$ 35 pc cm^{-3}. Note that both these values are smaller than the prediction from Prochaska et al. (2019), 50−80 pc cm^{-3}.
[h] Maximum luminosity distance (90% confidence upper limit) estimated using the Macquart relation (Macquart et al., 2020); see Section 3.2.
[i] Weighted average RM of the FRBs 20200120E and 20201129A.

2.2 Burst properties

Figure 5.1a shows dedispersed waterfall plots of the three named bursts, made using the estimate of each burst's DM, shown in Table 5.1, which is optimized to maximize the burst

SNR in the total-intensity data. We used the calibration methods described by CHIME/FRB Collaboration et al. (2019c) and Fonseca et al. (2020) to determine fluences of the three bursts (see Table 5.1), assuming the baseband localization position. Lastly, we employed the same modelling procedures that are discussed by CHIME/FRB Collaboration et al. (2019c) and Fonseca et al. (2020) for estimating widths, arrival times and scattering timescales from the calibrated total-intensity dynamic spectra of the three TNS named bursts. In the total-intensity data, the three named bursts show only one component, and therefore, we fitted a single-component profile.

We also show dedispersed waterfall plots for the two bursts for which we have baseband data saved to disk in Figure 5.1b. We separately optimized DMs of the bursts, FRBs 20200120E and 20201129A, by aligning sub-structure with the `DM_phase`[3] module (Seymour et al., 2019). We estimated best-fit DMs of 87.780 ± 0.009 and 87.71 ± 0.05 pc cm^{-3}, respectively. In the Figure we downsampled the data to have temporal and spectral resolution of 0.0256 and 0.16384 ms and 0.391 MHz, respectively. The dynamic spectrum of FRB 20200120E reveals downward drifting time-frequency sub-structures that are thus far exclusively observed in the dynamic spectra of repeating FRBs (CHIME/FRB Collaboration et al., 2019a,c, Day et al., 2020, Fonseca et al., 2020, Hessels et al., 2019). A detailed burst analysis of the two bursts using the baseband data is beyond the scope of this work and will be discussed in future work.

2.3 FRB rotation measure

Following a procedure similar to that outlined by Fonseca et al. (2020), a Faraday rotation measure (RM) for FRB 20200120E and FRB 20201129A were measured after applying RM-synthesis (Brentjens and de Bruyn, 2005, Burn, 1966) to the burst Stokes Q and U data and detecting a peak in the Faraday dispersion function (FDF). This initial measurement was refined by applying Stokes QU-fitting (O'Sullivan et al., 2012), modified to fit simultaneously for parameters characterizing the astrophysical signal as well as those corresponding to known systematics. In particular, a delay between the X and Y polarizations, arising from different path lengths through the electronics of the system (such as cable delay), produces mixing between Stokes U-V parameters (Mckinven et al., in prep.). A

[3] https://github.com/danielemichilli/DM_phase

best-fit model is determined by a nested sampling implementation of QU-fitting that includes an additional parameter, τ, characterizing the delay between the two polarizations. Leakage corrected spectra are shown in Figure 5.2 along with model fits. Re-performing RM-synthesis on the cable-delay-corrected spectrum results in the FDFs shown in the right panel of Figure 5.2. We estimate the RM of FRB 20200120E and FRB 20201129A to be $-29.8 \pm 0.5 \pm 1.0$ rad m^{-2} and $-26.8 \pm 0.3 \pm 1.0$ rad m^{-2}. Quoted uncertainties correspond to the formal measurement and estimated systematic uncertainties, respectively. Ionospheric RM contributions have not been determined here but preliminary analysis indicates contributions of $\approx +(0.2 - 0.4)\,\mathrm{rad\,m^{-2}}$ (Sotomayor-Beltran et al., 2013). The difference between these two measured RM values therefore is unlikely to be significant. Moreover, both the bursts have nearly 100% linear polarization fraction. The Galactic foreground RM prediction in the FRB sight-line from Oppermann et al. (2012) model is -11 ± 8 rad m^{-2}. The low extragalactic RM and DM suggest that the FRB is unlikely to be located in a dense ionized region like a compact H II region or star-forming complex (Costa and Spangler, 2018, Haverkorn, 2015, Michilli et al., 2018, Mitra et al., 2003), or in the Galactic centre region of a host galaxy (Krause, 2008, Moss and Shukurov, 1996).

3 Determining the distance and host of FRB 20200120E

3.1 Could FRB 20200120E be Galactic?

In this section, we discuss the possibility that FRB 20200120E is Galactic. The maximum MW disk contribution to the DM along the FRB sight-line is 40 pc cm^{-3} from the NE2001 model (Cordes and Lazio, 2002), or 35 pc cm^{-3} from the YMW16 model (Yao et al., 2017). The observed FRB DM is significantly larger than the DM predictions of either model even after taking into account an 20% systematic uncertainty (Cordes and Lazio, 2002, Yao et al., 2017). If the FRB is Galactic, an H II region could contribute to the DM-excess of the FRB as discussed by Patel et al. (2018). We checked the Anderson et al. (2014) HII region catalogue, which is claimed to be complete for Galactic H II regions other than large diffuse and young hypercompact H II regions, and found none, unsurprising given the high Galactic latitude of the source (b $= +41.^\circ22$; see Table 5.2). We also did not find any CO emission within the FRB localization region in the Planck all-sky CO map (Planck

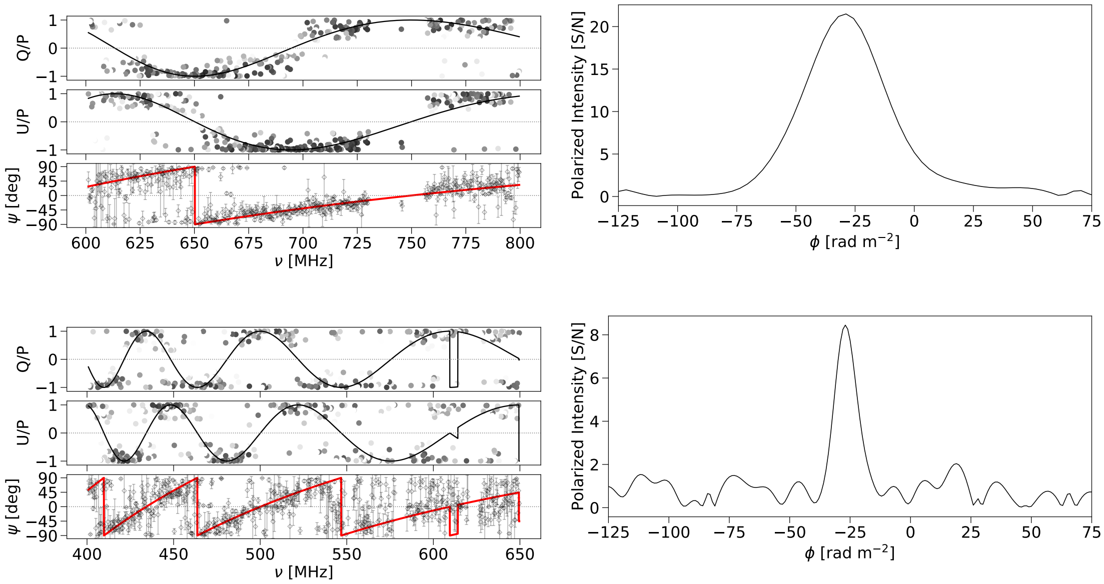

Figure 5.2: Summary plots of the RM detection methods of QU-fitting and RM-synthesis applied to the cable delay corrected spectra of FRB 20200120E (top row) and FRB 20201129A (bottom row). Left panel: Stokes Q, U normalized by the total linear polarization ($\mathrm{P} = \sqrt{\mathrm{Q}^2 + \mathrm{U}^2}$) and polarization angle, ψ, as a function of frequency with corresponding model fits. Frequency channels with significant polarized signal are highlighted through a greyscale that saturates at higher S/N. Right panel: The results of RM-synthesis showing each event's FDF constrained near the peak.

Collaboration et al., 2014) ruling out the presence of a young hypercompact H II region in a dense CO clumps of a molecular cloud complex (Dame et al., 2001). Finally, we searched the FRB uncertainy region in the Wisconsin Hα Mapper Northern Sky Survey (WHAM; Haffner et al., 2003) for the presence of any extended and diffuse Hα excess clump but did not find any. Therefore, it seems unlikely that an H II region is responsible for the observed DM-excess.

We consider two additional, independent maximum Galactic DM estimates. Using the observed Galactic hydrogen column density N_H in the FRB sight-line from the HI 4π survey (HI4PI) (HI4PI Collaboration et al., 2016), we find $N_H = 5.8 \times 10^{20}$ cm^{-2}. Using an empirically derived $\mathrm{N_H} - \mathrm{DM}$ relation from He et al. (2013), we calculated the Milky Way contribution to the DM in the direction of the FRB to be $\sim$14$-$28 pc cm^{-3}, significantly smaller than the DM of the FRB. Note, however, that this N_H–DM relation was estimated using radio pulsars, which are generally located near to the Galactic plane.

We also independently estimated the Milky Way disk DM that, at high Galactic latitudes, is dominated by the warm ionized medium (WIM) extending to a vertical distance $\sim$ 1$-$2 kpc above the Galactic plane (e.g., Hill et al., 2015). From the Planck all-sky free-free emission map (Adam et al., 2016), we find a total emission measure (EM) in the FRB sight-line of $\approx 7.8\ \mathrm{pc\ cm^{-6}}$. To estimate the WIM-dominated MW disk DM, we used a range of free electron density (N_e) values of the WIM from the literature (Gaensler et al., 2008, Ocker et al., 2020, Reynolds, 2004, Reynolds et al., 1995, Velusamy et al., 2012), $N_\mathrm{e} \approx 0.2 - 0.9$ cm^{-3}, and computed DM $= \mathrm{EM}/N_e \sim\ 10 - 40\ \mathrm{pc\ cm^{-3}}$. Moreover, Hill et al. (2007) estimated the mean dispersion measure, $\overline{\mathrm{DM}\sin|b|}$, for high-EM sight-lines (EM $\sin|b| > 2$ pc cm^{-6}) through the WIM to be 14.8 ± 0.9 pc cm^{-3}. At this FRB's Galactic latitude, this relation gives a mean Galactic DM of 22.5 ± 1.4 pc cm^{-3}. From all these estimates, it seems highly unlikely the source is within the Milky Way disk.

The DM contribution of the MW halo, $\mathrm{DM_{MW,halo}}$, which consists primarily of hot ionized circumgalactic gas extending out to a Galactocentric radius of $\sim$ 200 kpc, is poorly constrained (Keating and Pen, 2020). If we assume a halo DM contribution of 50$-$80 pc cm^{-3} as proposed by Prochaska et al. (2019), the FRB could be within the MW halo. However, two other MW halo DM models, those of Yamasaki and Totani (2020) and Dolag et al. (2015), predict $\mathrm{DM_{MW,halo}} \sim$ 30 pc cm^{-3}, which support an extragalactic origin for the FRB.

If the FRB is a MW halo object, the DM-excess of $\sim$ 50 pc cm^{-3} must be contributed by the hot coronal gas in the MW halo. Using different tracers of the hot gaseous medium ($10^5 - 10^7$ K; Tumlinson et al., 2017) that include emission and absorption lines of highly ionized species in the UV and X-ray (Miller and Bregman, 2015) and constraints from the diffuse soft X-ray background (Henley and Shelton, 2013), the electron density of the MW halo is estimated to be $\sim$ 10^{-3} cm^{-3} close to the Milky Way disk (Bregman and Lloyd-Davies, 2007) and $\sim$ 10^{-4} cm^{-3} at $\sim$ 50 kpc (Bregman et al., 2018), further reducing to $\sim$ 10^{-5} cm^{-3} near the virial radius of the Milky Way (Kaaret et al., 2020). Assuming a gas filling factor of unity and electron density of the coronal gas, $N_e \sim 10^{-3} - 10^{-4}$ cm^{-3}, we estimate the distance to the FRB source to be $\sim$ 50–500 kpc. As the Milky Way virial radius is $\sim$ 200 kpc (Dehnen et al., 2006), finding the FRB source at a distance $>$ 200 kpc implies that the source is extragalactic. Therefore, in further discussion, we use 50–200 kpc as a plausible distance range for a halo object.

In this scenario, it is possible that the FRB source could be associated with either a Milky Way satellite galaxy (Kaisina et al., 2019, Karachentsev and Kaisina, 2019) or globular cluster (Gaia Collaboration et al., 2018, Harris, 2010, Vasiliev, 2019), but no such catalogued source exists within or near (within $\sim 10^\circ$ radius circular sky area) to the FRB localization region (Contenta et al., 2017, Simon, 2019).

If the source is in the MW halo, the observed bursts could correspond to super-giant pulses (SGPs) from one of a young neutron star, millisecond pulsar, or rotating radio transient (RRAT). We now consider each of these possibilities in turn.

It is difficult to explain the existence of a young neutron star in the halo, given that these objects are expected to form only near the Galactic Plane. The fastest known runaway OB stars and young pulsars both have space velocities $\sim$ 1000 km s^{-1} (Brown, 2015, Chatterjee et al., 2005, Du et al., 2018), which would require $\sim$ 10^8 yr to traverse $50 - 200$ kpc. This is significantly longer than the typical lifetime of an OB star (tens of Myrs; Crowther, 2012) and inconsistent with the expectation of a young neutron star. On the other hand, it has been suggested (e.g. Giacomazzo and Perna, 2013) that young neutron stars can be formed by compact object mergers, which could occur in the halo. However, this formation mechanism has not been confirmed as actually occurring in nature.

Few millisecond pulsars (MSPs) are also known to emit SGPs (Johnston and Romani, 2004). In principle, an isolated MSP can exist at a distance of ~ 50 kpc. However, Galactic isolated MSPs that are known to produce SGPs are rare; only two (PSRs B1937+21 and B1821–24: Cognard et al., 1996, Romani and Johnston, 2001) such sources have been seen to do so out of a sample of $\sim\ 450$ known MSPs (Manchester et al., 2005). Moreover, assuming a SGP duration of $\sim\ \mu$s, the maximum isotropic energy observed from the brightest SGPs of PSR B1937+21 is $\sim\ 10^{20}$ erg (McKee et al., 2019). The isotropic burst energy of the FRB source, if located at a distance of ~ 50 kpc, would be $\sim\ 10^{22}$ erg, 100 times brighter than the brightest giant pulses observed from PSR B1937+21. Similar analysis using PSR B1821–24 SGPs would give an even larger energy difference (Johnson et al., 2013). Note that the energy difference would further increase if we assume the FRB source distance > 50 kpc.

Alternatively, the FRB source could potentially be explained as Crab-like SGPs from a $\sim\ 10^{8}$ year old rotating radio transient (RRAT) in the halo. However, it is unclear if an old RRAT can produce such pulses. For instance, the RRAT with the largest isotropic energy estimated using the distance and mean flux density values from the RRAT catalogue[4] is RRAT J1819$-$1458 with an energy of $\sim\ 10^{20}$ erg. This is again two orders of magnitude below the energy needed to power FRB 20200120E at a distance of 50 kpc.

Finally, FRB 20200120E shows complex spectral and temporal downward-drifting substructures (see Figure 5.1b), which have previously been established as a characteristic spectro-temporal feature of repeating FRBs (CHIME/FRB Collaboration et al., 2019c, Day et al., 2020, Fonseca et al., 2020, Hessels et al., 2019). Such structures are not known to be seen in pulsar or RRAT spectra, although some Crab SGPs have shown similar complex structure (Hankins and Eilek, 2007).

Overall, if FRB 20200120E is a MW halo object, we conclude that it would be the most distant Galactic neutron star yet discovered and would also need to be unusually energetic compared to known objects.

[4] `http://astro.phys.wvu.edu/rratalog/` (visited on 19/12/2020)

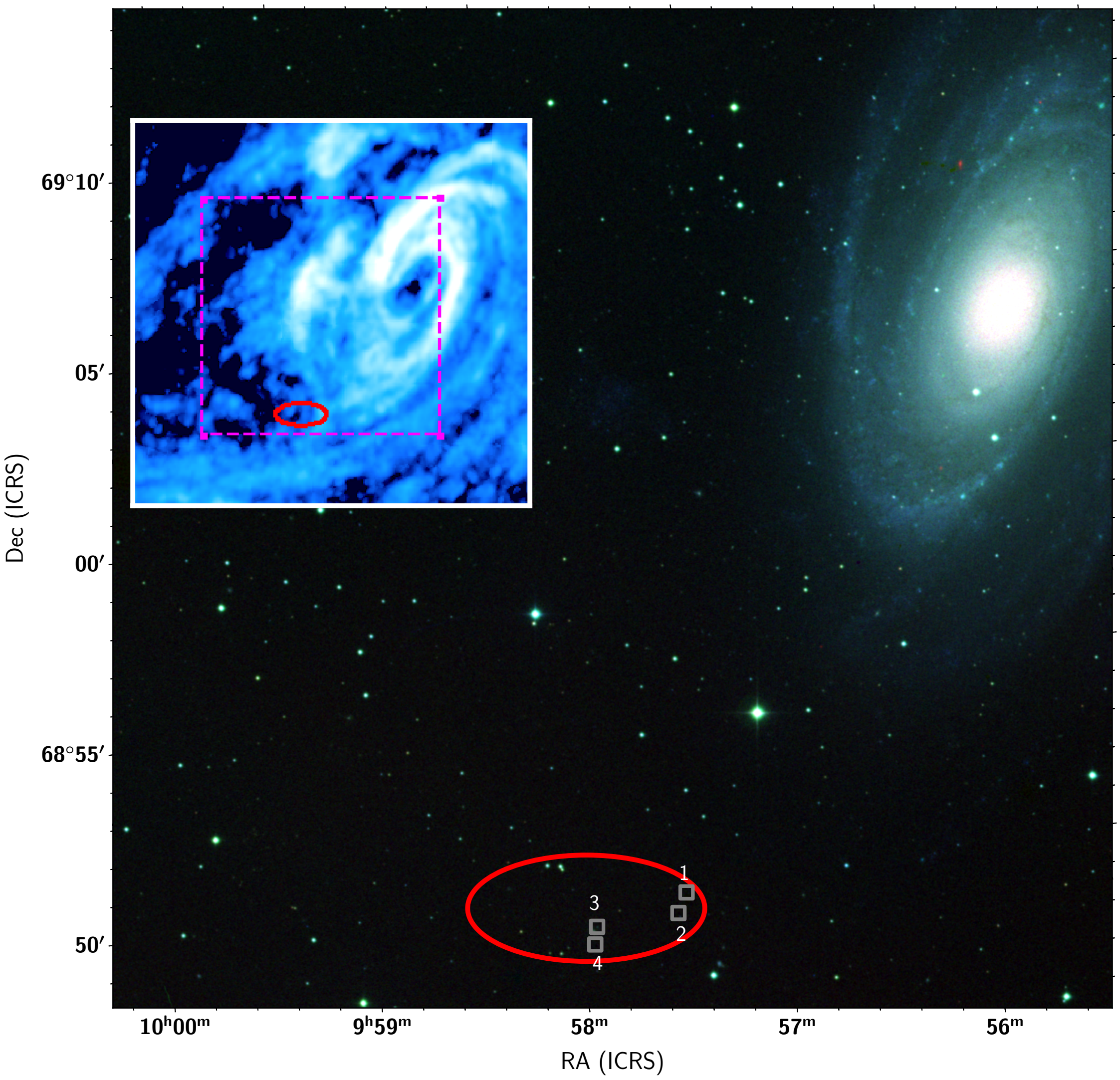

Figure 5.3: The Digital Sky Survey (DSS) RGB image of the region around M81. The red ellipse represents the 90% confidence localization region of FRB 20200120E. Source 1 is the catalogued M81 H II region, [PWK2012] 31 (Patterson et al., 2012), Source 2 is an X-ray source, [SPZ2011] 8 (Sell et al., 2011), Source 3 is an M81 globular cluster, [PR95] 30244, and Source 4 is the VLASS point radio source, VLASS1QLCIR J095756.10+684833.3 (Gordon et al., 2020). All the sources are found in the outer disk of M81. The inset image is the 21-cm line view of the M81 circumgalactic medium (Chynoweth et al., 2008); the dashed magenta box is the DSS image field-of-view.

3.2 Host galaxy search

In light of the challenges faced when associating FRB 20200120E with an object in the MW halo, we next consider whether it could be associated with an external galaxy. If we assume $\mathrm{DM_{halo}}$ = 30 pc $\mathrm{cm^{-3}}$ as predicted by the Dolag et al. (2015) and Yamasaki and Totani (2020) models, the extragalactic DM of the FRB, $\mathrm{DM_{EG}}$, is 18 and 23 $\mathrm{pc\ cm^{-3}}$ for the NE2001 and YMY16 Milky Way DM models, respectively (see Table 5.2). For a negligible host DM contribution, we estimate the maximum redshift of the FRB to be $\mathrm{z_{max}}$ $\approx$ 0.03 (90% confidence upper limit), or maximum luminosity distance of 135 Mpc, using the Macquart DM$-$z relation (Macquart et al., 2020). Therefore, if the FRB is extragalactic, we expect a nearby host galaxy within its location error region.

One possibility is that there is a faint dwarf galaxy, like that of FRB 121102, in the localization region of FRB 20200120E. An FRB 121102-like star-forming dwarf galaxy ($\mathrm{M_r} = -17$ AB mag; Tendulkar et al., 2017), if located at $\mathrm{z_{max}}$, would have r-band magnitude $\approx$ 19 AB mag. Within the FRB 90% confidence localization region, shown as a red ellipse in Figure 5.3, we identify one galaxy in the Dark Energy Spectroscopic Instrument (DESI) Legacy Imaging Survey photometric catalogue (Dey et al., 2019), 2MASX J09575586+6848551 with r-band magnitude = 15.35 AB mag. However, it is known to be at z = 0.19395(2) which is significantly further away than $\mathrm{z_{max}}$ (Huchra et al., 2012). Therefore, any dwarf host galaxy within the 90% confidence region must be fainter than the FRB 121102 host.

More interestingly, we find the FRB sight-line has a sky-offset from the M81 center, a nearby grand-design spiral galaxy, of $19.'6$. At the 3.6 Mpc distance of M81 (Karachentsev et al., 2002), this sky offset corresponds to a projected distance of 20^{+3}_{-2} kpc[5] from the centre of M81, well within the extended HI disk (see Figure 5.3) and thick disk of M81 ($\approx$ 25 kpc; Tikhonov et al., 2005). The FRB localization region is in the location where tidal interaction among M81 group members has resulted in the formation of star forming clumps. Observations in the visible band give only marginal sign of these sources, but they are extensively studied in the radio and X-ray bands. These sources are discussed in Section 3.5. Moreover, between the M81 group and Milky Way, we did not find any

[5] 90% c.l

catalogued field or Milky Way halo satellite galaxy. All these observations make M81 a plausible host galaxy for FRB 20200120E.

3.3 Can the proximity to M81 be by chance?

We now estimate the chance coincidence probability (P_{cc}) of finding an M81-like bright galaxy close to the FRB localization region. We define $P_{cc} = A_{Gal}/A_{CHIME}$, where A_{Gal} is the total angular sky area spanned by M81-like or brighter galaxies that are visible to CHIME, and A_{CHIME} is the total sky area visible to CHIME (sky area above Dec $\gtrsim -10°$; $\approx 61\%$ of the total sky area). To be conservative, we remove the Milky Way sightlines where the DM-excess of FRB 20200120E is less than the $\sim$ 10% systematic error on the maximum of the two different Milky Way DM model predictions (Cordes and Lazio, 2002, Yao et al., 2017), which we define as DM_{ex}. This DM-excess constraint (hereafter C1) removes 10% of the total sky visible to CHIME (mostly consisting of the Galactic plane), and we estimate A_{CHIME} = 20600 deg^2. Note that the CHIME sensitivity changes with declination, but this effect is likely insignificant in our case as all the nearby bright galaxies are within 30° of the zenith in the CHIME primary beam. Next, we use the catalogue of the local volume galaxies[6], which is complete for M81-like bright galaxies, and find three galaxies other than M81 that have extinction corrected B-band magnitudes, $m_B \leq 7.5$, m_B of M81[7]: M31 (Andromeda, m_B = 3.7 at 770 kpc), M33 (Triangulum, m_B = 6.1 at 930 kpc), and IC 342 (m_B = 7.2 at 3.28 Mpc). To estimate the total sky area of these galaxies, we use a circular region with an angular radius equivalent to a 20 kpc projected offset (of FRB 20200120E from M81) at their respective distances, which are $\approx 1.°49$, $1.°23$, $0.°35$, and $0.°31$ for M31, M33, IC 342, and M81, respectively. Using these values we estimate $A_{Gal} \approx 12.4$ deg^2, and hence, $P_{cc} = 6 \times 10^{-4}$.

[6] https://www.sao.ru/lv/lvgdb/introduction.php (visited on 19/12/2020)

[7] Though we have used B band magnitudes that are provided by the catalogue, the results would not change if we use other optical band magnitudes.

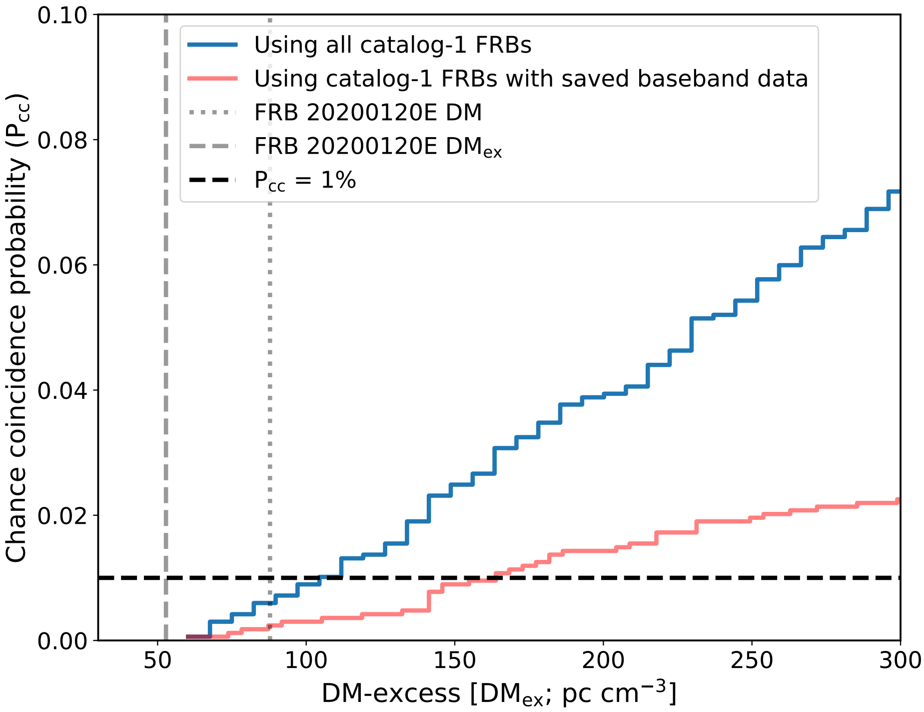

Figure 5.4: The chance coincidence probability of finding an M81-like galaxy as a function of the DM-excess (DM_{ex}) of FRBs in the first CHIME/FRB catalogue (The CHIME/FRB Collaboration et al., 2021) that satisfy the DM-excess constraint, C1, as discussed in Section 3.3. This takes into account the look-elsewhere effect by incorporating the number of FRBs in the CHIME/FRB catalogue with DM-excess $\leq$ DM_{ex} as a trial factor. FRB 20200120E has the lowest DM_{ex}, which gives $P_{cc} = 6 \times 10^{-4}$. At the DM of FRB 20200120E = 87.82 pc cm^{-3}, P_{cc} = 0.7%, which we consider as our conservative P_{cc} estimate. Moreover, the results would not change if we use minimum of the two different Milky Way DM model predictions (Cordes and Lazio, 2002, Yao et al., 2017) to estimate DM_{ex} (instead of the maximum predicted values used in the DM-excess constraint C1). Lastly, we also showed the chance coincidence probability when only Catalogue-1 FRBs with saved baseband data are used in correcting for the multiple testing problem.

As the presence of M81 is inferred post-hoc, it is essential to correct the chance coincidence probability for the problem of multiple testing (also known as the look-elsewhere effect), that tends to increase the false-positive rate of a discovery (Type I error; Maxwell et al., 2017). To account for this, we use the Bonferroni correction procedure (Armstrong, 2014, Bender and Lange, 2001). We consider all FRBs in the first CHIME/FRB catalogue (The CHIME/FRB Collaboration et al., 2021) that satisfy the excess-DM constraint C1. The Bonferroni correction inflates the P_{cc} to $1-(1-6\times10^{-4})^{N_{FRB,DM_{ex}}}$, where $N_{FRB,DM_{ex}}$ is the number of FRBs in the CHIME/FRB catalogue with the DM-excess $\leq \mathrm{DM_{ex}}$. Figure 5.4 shows the P_{cc} as a function of DM_{ex}. As FRB 20200120E has the lowest DM_{ex} in our sample, $N_{FRB,47.8}$ = 1, and therefore, P_{cc} = 6 $\times10^{-4}$. To be conservative, we also count the number of CHIME FRBs with DM-excess $\leq$ 87.82 pc cm^{-3}, the DM of FRB 20200120E, and estimate $N_{FRB,87.82} = 11$. This gives a value of $P_{cc} =$ 0.007.

There are several factors that make our P_{cc} estimate conservative. First, the Bonferroni correction becomes overly conservative as the number of events increase, and hence, undermines the significance of an unlikely observation (Nakagawa, 2004, Perneger, 1998). Second, we search prospective hosts for only those FRBs that have saved baseband data, which constitute a small fraction of the first CHIME/FRB catalogue FRBs. Therefore, it could be argued that we should have used only them when accounting for the multiple testing problem (Maxwell et al., 2017, Streiner and Norman, 2011). We also considered other nearby galaxies, except M81 satellite galaxies which are discussed in Section 3.5, that have projected angular offset less than or equal to that of M81 (19.’6) from the FRB, and for none is $P_{cc} < 10\%$, even before correcting for the multiple testing problem. However, note that the formalism of chance coincidence probability favours brighter galaxies over the fainter ones. If FRBs preferentially originate in a specific galaxy type, then the P_{cc} is not a good proxy of true a host association probability. We need more host associations to test the latter possibility.

Bayesian hypothesis testing is another method proposed to avoid the problem of multiple testing (Gelman et al., 2012, Scott and Berger, 2006). However, its success in avoiding the problem of multiple testing strongly depends on the choice of priors (de Heide and Grünwald, 2020, Rouder, 2014). With better knowledge of the nature of FRB hosts, it will eventually be possible to use a Bayesian framework to estimate true host association probabilities.

3.4 Could FRB 20200120E lie beyond M81?

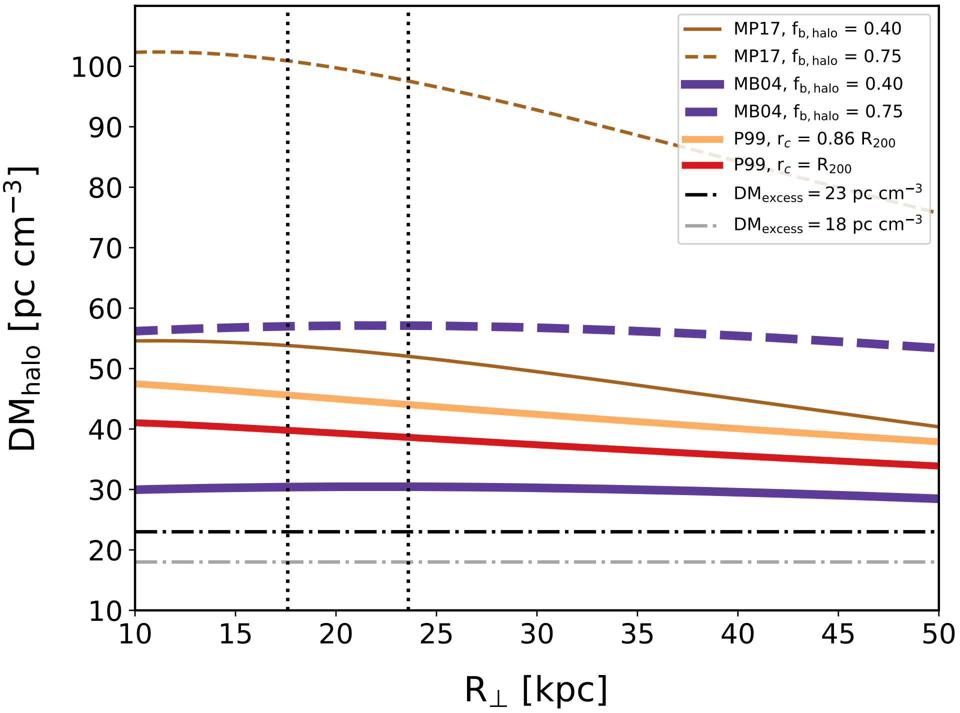

Figure 5.5: M81 DM_{halo} as a function of impact parameter of the FRB assuming M81 is a foreground galaxy. We used two modified versions of the Navarro–Frenk–White (NFW) halo profile discussed by Prochaska et al. (2019): MB04 (α = 2, $y_0 = 4$) and MP17 (α = 2, $y_0 = 2$); see Section 3.4 for detailed description. The DM profiles are plotted for two M81 halo baryon fractions: (1) $f_{b,halo} = 0.75$ (dash lines), a fiducial value that presumes that the halo has retained the mean cosmic baryons and that 25% of these baryons are in the galaxy as stars, collapsed objects, and interstellar medium (ISM; Fukugita et al., 1998);(2) $f_{b,halo} = 0.4$ (solid lines), the minimum value that Hafen et al. (2019) found in the FIRE simulation for a halo of mass $\sim 10^{12}$ $M_\odot$. The region between the vertical dotted lines represents the range of the FRB projected distance from the centre of M81 given the uncertainties in the FRB 90% confidence localization region.

Here we discuss the possibility of the FRB source being located beyond M81. In such a scenario, the CGM of M81 and its neighbouring galaxies will also contribute to the FRB DM.

M81 is a part of the nearby "M81 group," which contains prominent galaxies like M82, NGC 2403, NGC 4236, and several dwarfs (Karachentsev et al., 2002). Some of its members are in the process of merging, which makes the M81 group CGM rich in metals and gas (Al Najm et al., 2016). We estimate the DM contribution of the M81 halo assuming that the true host lies beyond M81.

The FRB 20200120E sight-line passes through the M81 halo with a very small impact parameter ($\sim$ 20 kpc), which is much less than the M81 virial radius of $\sim$ 210 kpc (Oehm et al., 2017). Therefore, we expect the M81 halo to contribute considerably to the FRB DM if the FRB is located beyond M81. To quantify this effect, we assume a density profile and several major M81 halo parameters, such as halo mass and virial radius. We first consider two halo gas profiles, proposed by Maller and Bullock (2004) (hereafter MB04) and Mathews and Prochaska (2017) (hereafter MP17)[8]. Both profiles are modified versions of the Navarro-Frenk-White (NFW) density profile (Merritt et al., 2005). For both profiles, we assume the following parametric form (Prochaska et al., 2019):

$$\rho = \frac{\rho_0}{(\frac{\mathrm{r}}{\mathrm{R_s}})^{1-\alpha}(\mathrm{y_0} + \frac{\mathrm{r}}{\mathrm{R_s}})^{2+\alpha}}. \tag{5.1}$$

Here for the MB04 profile, we adopt α = 2, y_0 $= 4$, and for the MP17 profile, α = 2, $y_0 = 2$. In Equation (5.1), ρ_0 is the central halo density, and $R_s = R_{200}/c$, where R_{200} is the scale radius that encloses a density of 200 times the critical density of the Universe, $\rho_{crit} = 3H^2/8\pi G$, and c is the concentration parameter defined as the ratio between the virial and scale radius of a halo. The values of these parameters for the M81 halo are $c = 10.29, R_{200}$ = 210 kpc, and $\rho_0 = 7.21 \times 10^{-3}$ $\mathrm{M_\odot}$ pc^{-3}, taken from Oehm et al. (2017). As suggested by Prochaska et al. (2019), we terminate the density profile at the M81 virial radius. Additionally, we need to assume a value for the fraction of baryons that is retained inside the virial radius of the M81 halo, $\mathrm{f_{b,halo}}$. For this, we consider two values: (1) $\mathrm{f_{b,halo}} = 0.75$ that assumes $\approx 25\%$ of the baryons exist in the galaxy as the interstellar medium (ISM), stars, and compact remnants (Fukugita et al., 1998), and (2) $\mathrm{f_{b,halo}}$ = 0.40 which is a lower limit that Hafen et al. (2019) found for $\sim$ $10^{12}\mathrm{M_\odot}$ mass halos in the Feedback in Realistic Environment (FIRE) simulation. The FIRE simulation is well suited

[8]The Dolag et al. (2015) and Yamasaki and Totani (2020) models are tailored to the Milky Way, and therefore, cannot be used here.

to study the CGM of simulated galaxies with high resolution and also takes into account the effect of gas inflow and outflow along with other factors that play important roles in the evolution of galaxies (Hopkins et al., 2014, 2018). To convert the dark matter density to that of baryons, $\rho_{\rm b}$, we use the cosmic baryon fraction = $\Omega_{\rm b}/\Omega_{\rm m}$ = 0.158 (Ade et al., 2016). Finally, we estimate the free-electron density using the relation: $\rm n_e = f_e(\rho_b/m_p)$[9], where $\rm f_e$ is the number ratio between free electrons and baryons in the halo (≈ 7/8; Tumlinson et al., 2017), and $\rm m_p$ is the proton mass. Using these parameters, we estimate the M81 $\rm DM_{halo}$ using the following equation:

$$\rm DM_{halo} = 2\int_0^{\sqrt{r_{max}^2 - R_\perp^2}} n_e dl. \tag{5.2}$$

In Equation (5.2), $\rm r_{max}$ is the maximum radius of integration through the M81 halo ($\rm R_{200}$ in our analysis) and $\rm R_\perp$ is the FRB impact parameter.

Apart from the modified NFW-halo density profiles, we also consider the entropy-floor singular isothermal sphere model of Pen (1999). The model invokes two phases of halo gas where in the inner region the gas is heated to constant entropy, and at radius (r) $\geq$ core radius ($\rm r_{\it c}$), the gas traces the halo mass isothermally. The gas density profile is defined as :

$$\rho(\rm r) = \left(\frac{f_g v_{circ}^2}{4\pi G}\right)\begin{cases} \frac{1}{r^2} & \text{if } r > r_c, \\ \frac{1}{r_c^2}(1+\frac{12}{25}\ln(\frac{r_c}{r}))^{1.5} & \text{if } r \leq r_c \end{cases} \tag{5.3}$$

Here $\rm f_g = 0.06h^{-1.5}$ and $\rm v_{circ} = (10GH_0M_h)^{1/3} \approx 154\ km\ s^{-1}$ are the gas fraction and circular velocity of the M81 halo of mass $\rm M_h = 1.3 \times 10^{12}\ M_\odot$ (Oehm et al., 2017) taken from Pen (1999) and Mo et al. (1998), respectively. We use two values of $\rm r_{\it c}$ in our analysis as suggested by Keating and Pen (2020): $\rm r_c = R_{200}$ and $\rm r_c = 0.86\ R_{200}$. To estimate the M81 halo DM, we use the procedure as discussed above.

Figure 5.5 shows our estimates of the M81 $\rm DM_{halo}$ as a function of $\rm R_\perp$. At the FRB $\rm R_\perp \sim$ 20 kpc, the minimum DM halo value (estimated using the MB04 profile and $\rm f_{b,halo}$

[9]We presume a flat ΛCDM (Planck Collaboration et al., 2016) model with the matter density, $\Omega_{\rm m} = 0.308$, baryonic matter density, $\Omega_{\rm b} = 0.0486$, dark energy density, $\Omega_\Lambda = 0.691$, and Hubble constant, $\rm H_0$ = 100 h $\rm km\ s^{-1} Mpc^{-1}$ with h = 0.6774.

= 0.4) is larger than the FRB DM-excess of 18−23 pc cm^{-3}, see Table 5.2). This argues against the FRB being beyond or even on the far side of the halo. To check if our most constraining M81 $\mathrm{DM_{halo}}$ estimate is conservative, we estimated the Milky Way $\mathrm{DM_{halo}}$ using the MB04 profile, $\mathrm{f_{b,halo}} = 0.4$, and other Milky Way halo parameters from Prochaska and Zheng (2019), and found $\mathrm{DM_{halo}} \approx 13$ pc cm^{-3}. This is smaller than the Dolag et al. (2015) and Yamasaki and Totani (2020) predictions in the FRB sight-line, $\sim$ 30 pc cm^{-3}. This demonstrates that our choice of halo density model does not bias the M81 $\mathrm{DM_{halo}}$ analysis.

Note that in our analysis, we consider only the M81 halo contribution. However, other members of the M81 group would also contribute to the FRB DM. For instance, we can calculate $\mathrm{DM_{halo}}$ of the M81 group by only considering the two nearest massive M81 group members other than M81, NGC 3077 ($\mathrm{R_{\perp}} \sim$ 36 kpc) and M82 ($\mathrm{R_{\perp}} \sim$ 59 kpc), with their respective halo parameters from Oehm et al. (2017). The total $\mathrm{DM_{halo}}$ of the M81 group we estimate using the MB04 density profile with $\mathrm{f_b} = 0.4$, the most conservative case in our analysis, is ≈ 75 pc cm^{-3} $> \mathrm{DM_{EG}}$ = 53−48 pc cm^{-3} (for a negligible Milky Way halo contribution). This further strengthens the conclusion that the FRB is unlikely to be beyond the M81 group. Should the FRB source turn out to be behind M81, it would suggest that the M81 group has lost most of its halo baryons.

As shown in Figure 5.3, the FRB localization region contains a significant amount of HI gas. Tikhonov et al. (2005) argued that the M81 thick disk extends to a galactocentric radius of 25 kpc, in which case the observed HI flux should be considered as a part of the M81 interstellar medium and hence, should make an additional DM contribution. In order to estimate the contribution of the HI disk ($\mathrm{DM_{HI}}$), we use the $\mathrm{N_H}$−DM relation from He et al. (2013). As discussed in Section 3.1, this relation is derived using nearby Milky Way radio pulsars, and so it is unclear whether it is valid for the M81 HI disk. Noting the similarity between the Milky Way and M81 projected HI distribution (Westpfahl et al., 1999), we use this relation for a rough estimate of $\mathrm{DM_{HI}}$. In the Very Large Array (VLA) image of the M81 group created by de Blok et al. (2018), the mean integrated HI flux intensity within the 90% localization region is 0.21 Jy beam^{-1} $\times$ km s^{-1}. The VLA D-configuration beam is modelled as an ellipse with major (θ_a) and minor (θ_b) axes 38.″01 and 30.″91, respectively, and position angle = 75°.5 that we get from the header data of the

21-cm map fits file made by de Blok et al. (2018)[10]. Assuming the HI gas to be optically thin, we estimate the integrated hydrogen column density, $N_H \approx 2 \times 10^{20}$ cm^2.

Using this N_H value in the N_H−DM relation, we estimate $DM_{HI} \sim 5 - 10$ pc cm^{-3}, over and above the contribution from the halo, further diminishing the probability that the FRB lies beyond the M81 group.

We conclude that FRB 20200120E is unlikely to lie beyond the M81 group. Therefore, if the FRB is an extragalactic source, its host is most likely located in the M81 group.

3.5 Interesting M81 group sources

In Section 3.4, we have shown that the FRB source is unlikely to be located beyond M81. Moreover, if we consider the MP17 halo density profile, the FRB is most likely to be located at the near side or in front of the M81 halo. However, with the MB04 and P99 halo density profiles, it is possible for the FRB to be present in the M81 extended HI disk. In any case, we searched for any catalogued M81 group satellite galaxy and did not find any within the FRB localization region. Within the M81 halo of sky-radius $\sim 3.^\circ 3$ (projected angular offset corresponding to the M81 virial radius, 210 kpc; Oehm et al., 2017), we found 42 dwarf satellite galaxies from the literature (Boerngen and Karachentseva, 1982, Boyce et al., 2001, Caldwell et al., 1998, Chiboucas et al., 2009, Froebrich and Meusinger, 2000, Karachentsev and Karachentseva, 2004, Karachentseva, 1968, Karachentseva et al., 1985, Okamoto et al., 2019, Smercina et al., 2017, Van den Bergh, 1966). We found a young dwarf irregular galaxy, Holmberg IX, and a dwarf spheroidal galaxy, KDG 64, at offsets of 13'.9 and 14'.3, respectively, from the centre of the FRB localization region. Note that the two galaxies have the offset greater than the 10 times their half light radius. However, using the M81 satellite number density, $\rho_g \approx 1.2$ deg^{-2}, and assuming a Poisson distribution within the M81 halo as found in the semi-analytic and N-body gas dynamics studies by Kravtsov et al. (2004), the chance coincidence probability (P_{cc}) of finding these two galaxies near the FRB localization region can be estimated using the relation from Bloom et al. (2002), $P_{cc} = 1 - e^{-\rho_g A}$, where A is the circular sky region of radius equals to the angular offset of the galaxies. We find $P_{cc} > 10\%$ for the galaxies.

[10]The image data can be directly downloaded from https://www.astron.nl/~blok/M81data/.

Within or close to the FRB localization region, we found an M81 globular cluster, [PR95] 30244 (Source 3 in Figure 5.3; Nantais and Huchra, 2010). Though unremarkable, its presence in the FRB localization region is still noteworthy as globular clusters in the Milky Way are known to host several exotic systems, like millisecond pulsars, blue stragglers and low-mass X-ray binaries (LMXBs) (Brodie and Strader, 2006). Moreover, as shown in Figure 5.3, we found an H II region, [PWK2012] 31 (Source 1), and an X-ray source, [SPZ2011] 8 (Source 2), within the FRB localization region. The presence of an HII region confirms that in situ star formation is actively taking place within the extended HI M81 disk. Additionally, Mouhcine and Ibata (2009) found a number of young stellar systems with ages of only a few tens of Myr in the M81 extended HI disk, which were formed during the tidal interaction of M81 with surrounding companion galaxies, most prominently NGC 3077 and M82. Therefore, it seems possible that a young neutron star – a possible FRB counterpart – associated with M81 is present within the FRB localization region. Lastly, Sell et al. (2011) estimated the counts in different X-ray sub-bands in the range 0.5−8 KeV. Using the X-ray colour-based source classification first proposed by Prestwich et al. (2003), if the X-ray source [SPZ2011] 8 is indeed an M81 source, we find that it can be either a high mass X-ray binary (HMXB), LMXB, or thermal supernova remnant. A future more precise FRB localization will tell us if the FRB is actually associated with any of these M81 sources.

3.6 Search for a persistent radio source

[11]

We also searched for a persistent radio source, like the one seen coincident with FRB 121102 by Chatterjee et al. (2017), within the 90% confidence localization region of the FRB. We searched archival data of the following surveys: the NRAO VLA Sky Survey (NVSS; Condon et al., 1998), the VLA Sky Survey (VLASS; Lacy et al., 2016), the Westerbork Northern Sky Survey (WENSS; Rengelink et al., 1997), and the Tata Institute of Fundamental Research Giant Metrewave Radio Telescope Sky Survey (TGSS; Intema et al., 2017). From the search, we identified only one point source in the VLASS image (2−4

[11] As the FRB source is now localized to the M81 globular cluster (Kirsten et al., 2021), [PR95] 30244 (see Section 3.5), we now know that the identified persistent radio source is not associated with the FRB.

GHz frequency band) above the 5σ noise threshold (≈ 0.6 mJy beam^{-1}). In the Canadian Initiative for Radio Astronomy Data Analysis VLASS Epoch 1 Quick Look (CIRADA VLASS QL) Catalog (Gordon et al., 2020), this source is catalogued as VLASS1QLCIR J095756.10+684833.3 with R.A = $09^{\rm h}57^{\rm m}56^{\rm s}$ and Dec.= $+68^{\rm d}48^{\rm m}33^{\rm s}$ (Source 4 in Figure 5.3). The estimated integrated and peak flux density of the source are 1.27 ± 0.19 mJy and 1.35 ± 0.11 mJy beam^{-1}, respectively. Using the 5-σ upper-limit from the NVSS image (1.4 GHz) of the FRB field-of-view of 2.15 mJy beam^{-1} and assuming a power-law dependence of the source flux density i.e., $S_\nu \propto S^\alpha$, we estimated a lower limit $\alpha > -0.61$. Note that the VLASS calibrated images are known to have a systematic that underestimates the flux density of identified sources by $\sim$ 10% (Gordon et al., 2020). Incorporating this in our spectral index estimate would increase the derived lower limit. Active galactic nuclei (AGN) are known to show variable light curves at all frequencies. Given a $\approx$ 20-yr gap between the NVSS and VLASS observations, the derived spectral index upper limit is not constraining if the radio source turns out to be a background AGN.

We then compared the VLASS source with the one that was found spatially associated with FRB 121102 (Chatterjee et al., 2017). At 3.6 Mpc, the isotropic luminosity of the radio source at 3 GHz, $\sim 10^{35}$ erg s^{-1}, would be $\sim 10^{4}$ times smaller than that of the FRB 121102 radio source. The isotropic luminosity would be $\sim 10^{8} - 10^{7}$ times smaller if the radio source is at distance $50-200$ kpc. We can rule out a canonical stellar-mass X-ray binary, as such a source always has radio luminosity smaller than 10^{33} erg s^{-1} at $\sim$ 1 GHz even when flaring (Gallo et al., 2018, Reines et al., 2020). A pulsar wind nebula (PWN) can give rise to a flat spectrum radio source ($\alpha > -0.4$; Reynolds et al., 2017, Slane, 2017). We searched for a possible optical counterpart of the radio source in the CFHT/MegaCAM image from Chiboucas et al. (2009) and found none. The 5-σ of r-band limit = 25.65 AB mag corresponds to an r-band flux of 1.5×10^{36} erg s^{-1} at 3.6 Mpc. If the radio source is a Crab-like PWN with radio-to-optical luminosity ratio $\leq 10^{-3}$ (Volpi et al., 2008), it should have been detected in the CFHT/MegaCAM r-band image. Moreover, Sell et al. (2011) observed M81, including the FRB field-of-view, using the *Chandra X-ray Observatory* and identified 276 X-ray point sources with sensitivity $\sim 10^{37}$ erg s^{-1}. However, there is no X-ray point source spatially coincident with the radio source. If the radio source is an M81 supernova remnant or PWN, its X-ray/radio flux ratio is likely $< 10^{-2}$; otherwise, it is most likely a background AGN. Note that these constraints are also valid if the FRB source is located at $50-200$ kpc. The persistent radio emission from X-ray binaries are orders of magnitude lower than their X-ray luminosities (Koljonen and Russell, 2019), therefore, a Galactic X-ray binary as the counterpart of the persistent radio source is also disfavoured from the constraints discussed above. Future follow-up observations of the persistent radio source and a milliarcsecond localization of the FRB may one day tell us if the radio source is associated with the FRB.

4 Discussion

We have shown that the sky location of the low-DM repeating FRB 20200120E appears superimposed on the extended HI and thick disks of the nearby spiral galaxy M81. Moreover, the low DM-excess of the FRB suggests that the FRB source is unlikely to be located beyond M81 group ($\sim$4 Mpc). We searched for galaxies closer than those associated with the M81 group within or near to the FRB localization region in the catalogue of the local volume galaxies (Karachentsev et al., 2013) and found none. Additionally, the coincidence probability of finding an M81-like galaxy close to the FRB localization region is small ($< 1\%$). Therefore, if extragalactic, the FRB is most likely associated with M81 which would make it by far the closest extragalactic FRB yet known. Lastly, given the observational constraints, we cannot reject the Galactic origin of the FRB.

4.1 Constraints on the Milky Way halo DM contribution

Under the assumption that FRB 20200120E is extragalactic, it can be used to set an upper limit on the MW halo DM contribution in this direction. If we consider the lowest of the two MW DM model estimates, $\mathrm{DM}_{\mathrm{MW,YMW16}}$ = 35 pc cm^{-3} and conservatively assume negligible IGM and host DM contribution, then $\mathrm{DM}_{\mathrm{MW,halo}} < 53$ pc cm^{-3}. This would be inconsistent with most of the $\mathrm{DM}_{\mathrm{MW,halo}}$ phase space proposed by Prochaska et al. (2019), i.e., $\mathrm{DM}_{\mathrm{halo}}$ = $50-80$ pc cm^{-3}. On the other hand, both the Dolag et al. (2015) and Yamasaki and Totani (2020) models predict $\mathrm{DM}_{\mathrm{halo}} \sim$ 30 pc cm^{-3}, lower than our upper limits. The halo may be clumpy (Kaaret et al., 2020, Keating and Pen, 2020), so it may still be possible to have significant variations in $\mathrm{DM}_{\mathrm{halo}}$ along different sight-lines. More such low-DM FRB localizations will help in constraining the structure and composition of the MW haGalo.

4.2 Comparison with SGR 1935+2154 radio bursts

Table 5.1 provides the peak flux density of FRB 20200120E bursts. At a distance of 3.6 Mpc, the isotropic radio luminosity of the bursts would be $\sim 10^{37}$ erg s^{-1} similar to those of the very bright SGR 1935+2154 radio bursts recently detected by CHIME/FRB and STARE2 (Bochenek et al., 2020, CHIME/FRB Collaboration et al., 2020a). In 2 yrs of CHIME/FRB observations, we have seen at least three bursts from the FRB 20200120E source. There are other low-DM FRBs within the CHIME/FRB sample that are presently under consideration. Careful study of the host galaxy candidates in their error regions (which are presently mostly larger than for FRB 20200120E) must be done to assert them as extragalactic, given the ever-present possibility of them being in the distant MW or MW halo. This work is underway and may be able to constrain the local volumetric FRB rate to compare with that inferred from SGR 1935+2154.

The proximity of FRB 20200120E makes it an attractive target for X-ray and gamma-ray telescopes. For a fiducial current high-energy telescope fluence detection sensitivity threshold of 10^{-10} erg cm^{-2}, high-energy bursts from nearby sources with energies $> 10^{41}$ erg s^{-1} should be detectable, and are sometimes seen from Galactic magnetars in outburst (see Kaspi and Beloborodov, 2017, for a review). Moreover, giant magnetar flares with total isotropic luminosity $\sim 10^{46}$ erg, like that from SGR 1806$-$20 (Palmer et al., 2005), should be easily detectable by the *Swift*/Burst Alert Telescope (BAT) and *Fermi*/GBM which have flux sensitivity of $\sim 10^{-7}$ erg cm^{-2} s^{-1} in the 15-150 keV band (A. Tohuvavohu, private communication) and $\sim 10^{-7}$ erg cm^{-2} s^{-1} in 50–300 keV band (von Kienlin et al., 2020), respectively. Unfortunately, *Fermi*/GBM was either not operational (transiting through the South Atlantic Anomaly region) or the FRB location was occulted by the Earth at all but one burst epoch. At the time of the 2020 February 6 burst, the FRB was visible to *Fermi*/GBM but no trigger was reported by the *Fermi* collaboration. Additionally, the *Swift*/BAT field-of-view (FOV) did not cover the FRB sky-position at the time of FRBs 20200120E and 20201129A. However, the FRB location was within the *Swift*/BAT FOV at the time of FRB 20200718A, and no coincident X-ray burst was reported by the *Swift* collaboration. Therefore, if the FRB source is at 3.6 Mpc, it seems unlikely that FRB 20200718A and the 2020 February 6 event were associated with SGR 1806−20-like giant flares.

4.3 Comparison with other repeating FRB hosts

Table 5.3: Notable properties of M81, the most promising host of FRB 20200120E.

Property	Value	Reference
SFR ($M_\odot$ yr^{-1})	0.4−0.8	Gordon et al. (2004)
Metallicity[a] [Z] (dex)	0.03	Kong et al. (2000)
Stellar mass ($M_\odot$)	(7.2 ±1.7) × 10^{10}	de Blok et al. (2008)
Effective radius (R_{eff}; kpc)	3.5	Sheth et al. (2010)
$(u\text{-}r)_0$ [b] (mag)	2.773(4)	Abazajian et al. (2009)
E(V-B)[c]	0.26	Kudritzki et al. (2012)
Absolute r-band mag. (AB)	−19.78	–
Inclination angle (°)	62	Karachentsev et al. (2013)
Luminosity distance (Mpc)	3.63 ± 0.34	Karachentsev et al. (2013)
Projected FRB offset from galaxy centre (kpc)[d]	20^{+3}_{-2}	This work

[a] Average metallicity relative to the Sun i.e., log($Z/Z_\odot$). However, at the FRB location, the metallicity is found to be sub-solar, i.e., [Z] < 0 (Williams et al., 2009).
[b] Milky Way extinction is corrected using the reddening map by Schlegel et al. (1998).
[c] Average value of the colour excess; at the FRB location, it is likely to be < 0.1 (Kudritzki et al., 2012).
[d] 90% confidence interval.

In contrast with the late-type galaxy hosts of the only three other localized repeating FRBs, FRBs 121102, 180916 and 190711 (Macquart et al., 2020, Marcote et al., 2020, Tendulkar et al., 2017), M81 is an early-type spiral galaxy of morphology SA(s)ab (Bosma, 1981). Table 5.3 lists its main physical properties. M81 also contains a low-luminosity AGN (Markoff et al., 2008), and is classified as a LINER Seyfert (Ho et al., 1996). Heintz et al. (2020) noted that the hosts of apparently non-repeating FRBs are typically more massive than those of repeating FRBs. However, M81 would be among the most massive FRB hosts known thus far[1] with stellar mass of 7.2 × 10^{10} $M_\odot$ (see Table 5.3). Lastly, if we ignore FRB 190523 for which the host association is not firm (Heintz et al., 2020, Macquart et al., 2020), FRB 20200120E would show the largest projected offset from the centre of its host ($\sim$ 20 kpc). This would be at odds with the offset distribution of the progenitors of long gamma-ray bursts and superluminous supernovae, which are found close to the centres of their respective hosts (Blanchard et al., 2016, Heintz et al., 2020, Lunnan et al., 2015, Mannings et al., 2020).

If FRB 20200120E is a classical magnetar, it would be surprising to find it at such a large offset from the centre of its host; known Galactic magnetars are all well within the optical disk of the Milky Way (Olausen and Kaspi, 2014). This same issue has been noted for other localized FRBs (Heintz et al., 2020). However, the M81 circumgalactic medium (CGM) is dynamic and rich in gas and metals (Chen, 2017). Sun et al. (2005) and Smercina et al. (2019) noted the existence of a diffuse stellar population embedded in the extended HI disk where in situ star formation is actively taking place. Lastly, Frederiks et al. (2007) and Hurley et al. (2010) have argued for the existence of a neutron star population, including a possible magnetar, in the CGM of M81.

5 Conclusions

We have reported on the detection of the repeating fast radio burst source FRB 20200120E discovered with CHIME/FRB. This source has very low DM, 87.82 pc cm^{-3}, though greater than what is expected from models of the Milky Way ISM along its line-of-sight. Due to large uncertainties in the Milky Way halo DM contribution, it is possible that the FRB source is within our halo. However, we find no catalogued Milky Way halo satellite galaxy or globular cluster within or near to the FRB localization region that can host the FRB source. Moreover, the presence of a solitary neutron star capable of producing FRB-like radio emission at a distance $\sim\ 50-200$ kpc seems unlikely. On the other hand, we identify M81, a nearby grand-design spiral galaxy at a distance of $\sim$ 3.6 Mpc, with an angular offset $\approx 19'$ and chance coincidence probability $< 10^{-2}$, making it a promising host candidate.

We have shown that the observed extragalactic DM component of the FRB is significantly lower than the model-predicted DM contribution from the M81 halo as a foreground galaxy. This suggests that the FRB host galaxy is unlikely to be located beyond M81, though the FRB may exist within the extended disk of M81. Therefore, if extragalactic, FRB 20200120E is most likely associated with M81. M81 is different from the hosts of other known repeating FRBs in spatial offset, stellar population age, and local environment. This supports an interesting diversity in repeater host properties that additional localizations will help understand. We also found that the FRB localization region contains the extended M81 HI-disk and a number of interesting M81 sources including an H II region ([PWK2012] 31), an X-ray binary ([SPZ2011] 8) and a VLASS source, VLASS1QLCIR J095756.10+684833.3. At a distance of 3.6 Mpc, it should be possible to detect prompt multi-wavelength counterparts of FRB 20200120E predicted by several FRB models, including the magnetar model. Some FRB models anticipate even greater luminosities in high energy bands than in the radio band (Burke-Spolaor, 2018, Chen et al., 2020, Yi et al., 2014). For example, in the synchrotron maser model of Metzger et al. (2019), shock-heated electrons gyrate to produce synchrotron radiation that sweeps through the γ-ray and X-ray bands, and in some cases, even extends to the optical band on sub-second timescales. Additionally, if radio bursts from FRB 20200120E are accompanied by X-ray bursts, as was seen in SGR 1935+2154 (Bochenek et al., 2020, CHIME/FRB Collaboration et al., 2020a, Li et al., 2020, Mereghetti et al., 2020, Ridnaia et al., 2020), detecting a coincident X-ray counterpart seems feasible, and would be a strong test of the magnetar origin of FRBs. Therefore, we encourage multi-wavelength follow-up of FRB 20200120E.

Chapter 6

A Local Universe Host for the Repeating Fast Radio Burst FRB 20181030A

1 Introduction

In this chapter, we report the identification of the most likely host for FRB 20181030A[1], a repeating FRB first reported by CHIME/FRB Collaboration et al. (2019c). Though its DM is only 103.5 pc cm^{-3}, this is significantly larger than the expected contribution in this direction from the Milky Way disk (33 and 41 pc cm^{-3}; Cordes and Lazio, 2002, Yao et al., 2017, respectively). CHIME/FRB Collaboration et al. (2019c) did not find any Galactic ionized and/or star-forming region in the direction of FRB 20181030A. Therefore, they concluded that the FRB should have a nearby extragalactic host. However, due to insufficiently precise localization of the FRB reported by CHIME/FRB Collaboration et al. (2019c), they could not make any firm association with a host. Since that report, CHIME/FRB has detected seven more bursts from the FRB (see Table 8.1).[2] For several of the FRB repeat bursts, raw voltage data were acquired, enabling localization of the FRB to a few arcminute precision, an improvement of over a factor of 200 in localization area. Within this localization region, we identify a local Universe spiral galaxy, NGC

[1]Formerly named as FRB181030.J1054+73.

[2]For a complete list, check `http://chime-frb.ca/repeaters/FRB20181030A` (visited on 1/07/2021).

3252 (Huchra et al., 1983), as its most likely host.

The chapter is organized as follows: In Section 2, we describe our search for the host of FRB20181030A. From the low chance coincidence probability (Section 2.1) and absence of any other viable host candidates in the FRB localization region (Section 2.2), we argue that NGC 3252 is a promising host for the FRB. We estimate notable physical properties of NGC 3252 in Section 4 and then discuss our archival multi-wavelength data search to identify any FRB plausible counterpart in Section 6. In Section 7, we discuss implications of this discovery, and conclude in Section 8.

2 Observations

The CHIME/FRB project first discovered two bursts from FRB 20181030A on 2018 October 30 (CHIME/FRB Collaboration et al., 2019c). The source's DM is larger than the predicted Galactic contribution in the FRB sight-line (See Table 8.2). After subtracting DM contributions from the Milky Way disk and halo, as shown in Table 8.2, the DM-excess of the FRB is $\sim 30 - 40$ pc cm^{-3}. Using the average Macquart relation (Equation 2 in Macquart et al., 2020), we estimate the redshift of the FRB to be $\sim 0.03 - 0.04$ assuming negligible host DM contribution. This suggests close proximity of the FRB host ($\lesssim 200$ Mpc). As of 2021 July 1, seven more bursts have been detected from the FRB[2]. Interestingly, all seven bursts were clustered in two different epochs on 2020 January 22, separated by ≈ 12 hours. This suggests a highly non-Poissonian waiting time distribution for the FRB bursts. Fortunately, four FRB 20181030A bursts have baseband data saved by the CHIME/FRB baseband system (bursts with reported $\mathrm{DM_{bb}}$ values in Table 8.1).

The baseband system of CHIME/FRB stores ~ 100 ms of channelized voltages around signals of interest (CHIME/FRB Collaboration et al., 2018). We have developed a pipeline to automatically process such baseband data and localize a burst on the sky with a precision of $\sim \frac{8}{\mathrm{S/N}}$ arcmin (Michilli et al., 2020). The detailed description of the pipeline is presented in Chapter 3. In the case of FRB 20181030A, we used the baseband data of its four detected bursts, FRBs 20200122A, 20200122B, 20200122D, and 20200122G, to estimate the localization region of the FRB. The dedispersed baseband data waterfall plots and major characteristics of the four FRB bursts are shown in Figure 6.1 and Table 8.1, respectively. Other burst properties, such as fluence and flux density, along with a detailed description of both the intensity and baseband data analysis of all newly discovered FRB 20181030A bursts will be presented elsewhere. Moreover, the available data are insufficient to estimate meaningful constraints on the FRB's periodicity. As the reported baseband localization uncertainties are statistical in nature (Michilli et al., 2020), we combined the localization regions of the four FRB bursts using a weighted average with inverse variance weights and localized the FRB to a sky area of ≈ 5.3 arcmin^2 (90% confidence region; see Table 8.2). Next, we use the baseband localization region of FRB 20181030A to search for a potential host galaxy.

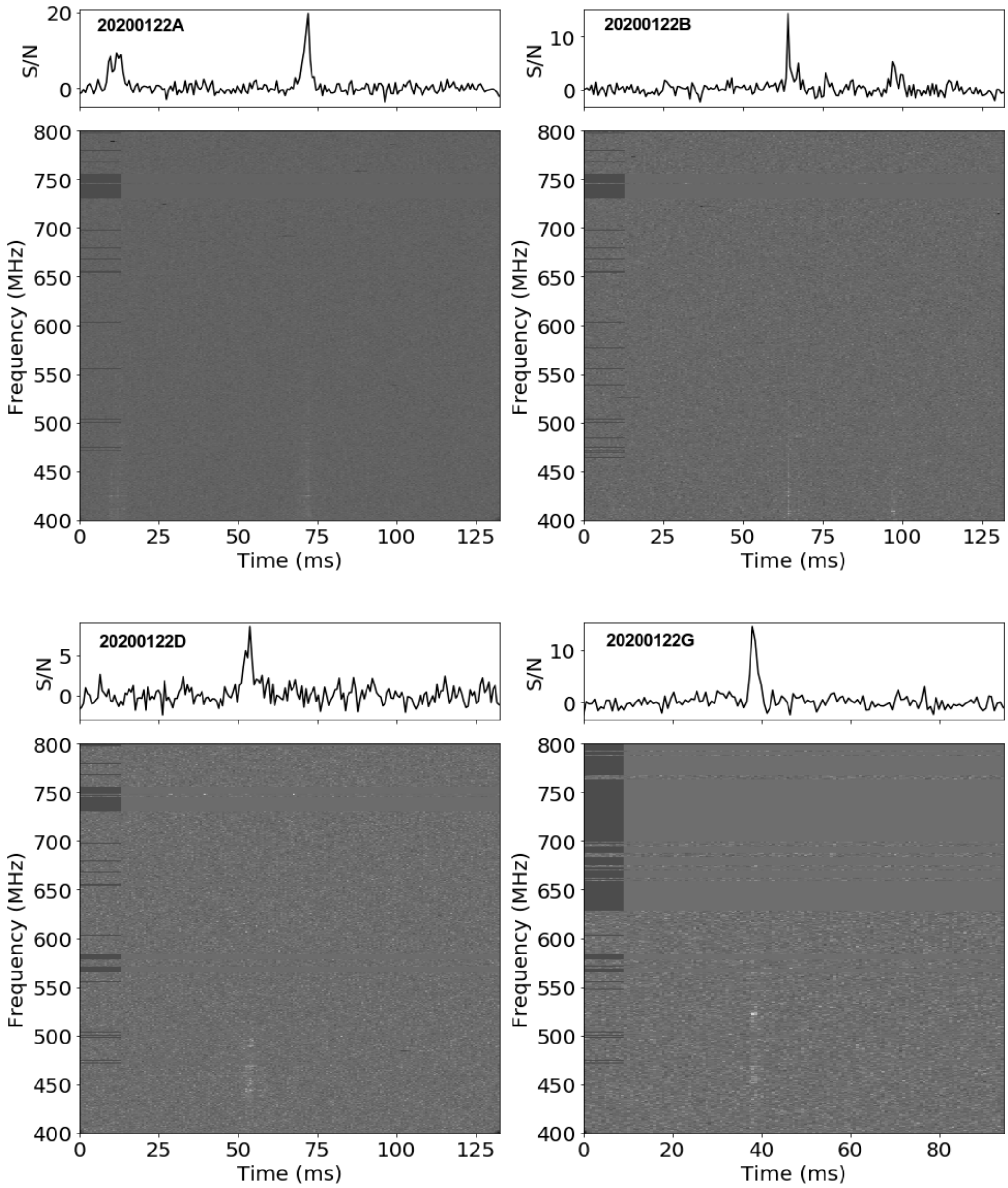

Figure 6.1: Frequency versus time (“waterfall") plots of the four dedispersed bursts detected from FRB 20181030A with saved baseband data. See Table 8.1 for their major burst properties. The waterfall plots are binned to have temporal resolution 0.655 ms and spectral resolution 0.391 MHz. Dark grey lines represent bad frequency channels that were flagged in this analysis. Note that FRBs 20200122A and 20200122B show sub-bursts separated by $\sim$ 60 ms and 30 ms, respectively. Detailed analysis of these sub-bursts will be reported elsewhere.

Table 6.1: Properties of the bursts from FRB 20181030A.

TNS Name	MJD	Arrival Time[a] (UTC @ 400 MHz)	S/N[b]	$\mathrm{DM}_{\mathrm{bb}}^{c}$ ($\mathrm{pc\ cm^{-3}}$)	DM^{d} ($\mathrm{pc\ cm^{-3}}$)
FRB 20181030A[e]	58421	04:13:13.1758(8)	32.5	–	103.5 ± 0.7
FRB 20181030B[e]	58421	04:16:21.6419(14)	17.1	–	103.5 ± 0.3
FRB 20200122A	58870	10:20:32.5805(3)	13.9	103.53 ± 0.02	103.40 ± 0.14
FRB 20200122B	58870	10:27:00.4412(3)	17.3	103.49 ± 0.02	103.47 ± 0.08
FRB 20200122C	58870	10:28:20(1)	8.3	–	103.1 ± 1.2
FRB 20200122D	58870	22:09:30.8575(3)	13.1	103.58 ± 0.19	103.7 ± 0.4
FRB 20200122E	58870	22:09:52(1)	10.4	–	103.27 ± 0.13
FRB 20200122F	58870	22:22:21(1)	8.9	–	103.7 ± 0.7
FRB 20200122G	58870	22:23:20.3080(3)	10.5	103.57 ± 0.10	103.7 ± 0.5

[a] All burst times of arrival are topocentric. For FRBs 20200122C, 20200122E, and 20200122F, the arrival times are reported by the CHIME/FRB real-time pipeline (CHIME/FRB Collaboration et al., 2018). For FRBs 20200122A, 20200122B, 20200122D, and 20200122G, the arrival times are estimated by the baseband pipeline (Michilli et al., 2020). Finally, the arrival times of FRBs 20181030A and 20181030B are taken from CHIME/FRB Collaboration et al. (2019c).
[b] For all except FRBs 20181030A and 20181030B, band-averaged signal-to-noise (S/N) ratios are estimated by the CHIME/FRB real-time pipeline.
[c] S/N-optimized DM for the bursts detected in the baseband data.
[d] S/N-optimized DM from intensity data (see CHIME/FRB Collaboration et al., 2019c, Fonseca et al., 2020).
[e] Data from CHIME/FRB Collaboration et al. (2019c).

Table 6.2: Major Observables of FRB 20181030A.

Parameter	Value
R.A.(J2000)[a]	$10^{\rm h}34^{\rm m}20^{\rm s}.1 \pm 30^{\rm s}.6$
Dec. (J2000)[a]	$73°45'05'' \pm 47''$
l, b	134.°81, +40.°06
DM[b]	103.5 ± 0.3 pc cm^{-3}
$\mathrm{DM}^{c}_{\mathrm{MW,NE2001}}$	41 pc cm^{-3}
$\mathrm{DM}^{c}_{\mathrm{MW,YMW16}}$	33 pc cm^{-3}
$\mathrm{DM}^{d}_{\mathrm{MW,halo}}$	30 pc cm^{-3}
Max. distance[e]	$\lesssim 225$ Mpc

[a] The 90% confidence localization region of the FRB.
[b] From CHIME/FRB Collaboration et al. (2019c).
[c] Maximum DM model prediction along this line-of-sight for the NE2001 (Cordes and Lazio, 2002) and YMW16 (Yao et al., 2017) Galactic electron density distribution models.
[d]Fiducial Milky Way halo prediction from the Dolag et al. (2015) hydrodynamic simulation and Yamasaki and Totani (2020) Milky Way Halo model.
[e] Corresponds to the maximum redshift of 0.05 (see Section 2.2).

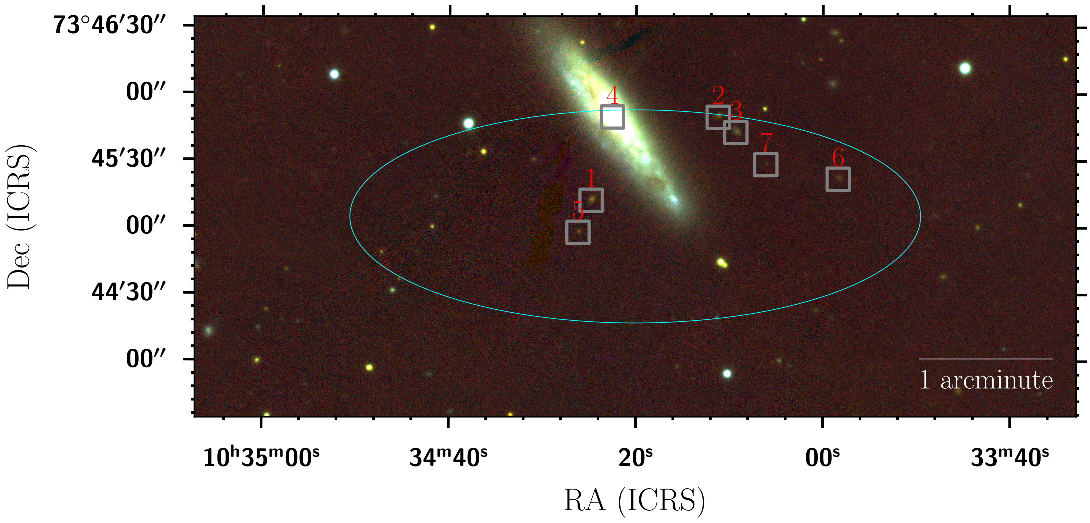

Figure 6.2: Pan-STARRS RGB-image of the FRB 20181030A 90% localization region (cyan ellipse). Grey boxes show the locations of 7 host galaxy candidates within the localization region (See Table 8.3); Source 4 is NGC 3252 at z = 0.0039, the most promising host galaxy of the FRB.

2.1 Host galaxy search

First, we argue below that the FRB is unlikely to be Galactic in origin. As noted by CHIME/FRB Collaboration et al. (2019c), there is no catalogued Galactic ionized region, satellite galaxy, or globular cluster in the direction of the FRB that could contribute to the FRB DM. Moreover, Ocker et al. (2020) estimated the mean DM through the Milky Way's warm ionized medium at large distances from the Galactic plane ($z > 2$ kpc), $\overline{\mathrm{DM}\sin|\mathrm{b}|}$ = 23.0 ± 2.5 pc cm^{-3}. At the FRB's Galactic latitude ($b = 40°$), it would give a mean Galactic DM of $\approx 36 \pm 5$ pc cm^{-3}. This agrees well with the prediction of the two Galactic DM models. The Milky Way halo DM contribution, $\mathrm{DM_{halo}}$, on the other hand, is poorly constrained. Recently, Kirsten et al. (2021) estimated the Milky Way halo contribution in the direction of FRB 20200120E to be $\lesssim$ 40 pc cm^{-3}. If this is also true for the FRB 20181030A sight-line, the FRB would be clearly extragalactic in origin. However, the halo may be clumpy (Kaaret et al., 2020), so it may still be possible to have significant variations in $\mathrm{DM_{halo}}$ along different sight-lines. Using the same argument as asserted in Chapter 5, an FRB with a DM-excess of $\sim$ 70 pc cm^{-3}, if Galactic, would require a very distant ($\gtrsim$ 100 kpc) and unusually energetic neutron star as its source. As discussed below, we have found an extragalactic host with a low chance coincidence probability. Therefore, Occam's razor argues for the extragalactic association.

Next, we searched the NASA Extragalactic Database (NED) for catalogued galaxies within the FRB 90% confidence localization region and found only one galaxy, NGC 3252, with a redshift (z) of 0.00385(2) (Masters et al., 2014). NGC 3252 is a bright (m_r = 12.58 AB mag) Scd Hubble-type edge-on spiral galaxy (de Vaucouleurs et al., 1991) at a luminosity distance of $\approx$ 20 Mpc. In Figure 8.2, we plotted the FRB localization region over a Pan-STARRS RGB image made using Pan-STARRS's g-band (B:blue), r-band (G:green), and z-band (R:red) data. In the Figure, NGC 3252 is the most prominent galaxy. Note that NED does not provide the depth of completeness of catalogued galaxies in their search results. Therefore, in Section 2.2, we describe our search of dwarf galaxies within the FRB localization region.

We now estimate the chance coincidence probability (P_{cc}) of finding an NGC 3252-like bright galaxy close to the FRB localization region. Briefly, we assume a Poisson distribution of galaxies across the sky and calculate the probability of finding one or more galaxies with m_r smaller than or equal to that of NGC 3252 (12.79 AB mag; without correcting for the Galactic extinction) by chance close to the FRB 90%-confidence localization region (5.3 acmin^2). Using the areal number density of NGC 3252-like or brighter galaxies, $n(\mathrm{m_r} \leq 12.79)$ = 0.2 deg^{-2} from Driver et al. (2016), we estimate $P_{cc} = 4.5 \times 10^{-4}$. However, as the presence of NGC 3252 is inferred post-hoc, we have corrected the P_{cc} to account for the problem of multiple testing (also known as the look-elsewhere effect) using the method described in Chapter 5. After considering all CHIME FRBs that were discovered before the first detected burst of FRB 20181030A and have the DM-excess $\leq$ 103.5 pc cm^{-3} (see Figure 6.3), we estimate the P_{cc} to be $<$ 0.0025.

We should point out, however, that our chance coincidence analysis favours brighter galaxies over fainter ones because the latter are more abundant and therefore more likely to be found in the FRB localization region by chance. Therefore, in the next section, we searched for faint galaxies within the FRB localization region.

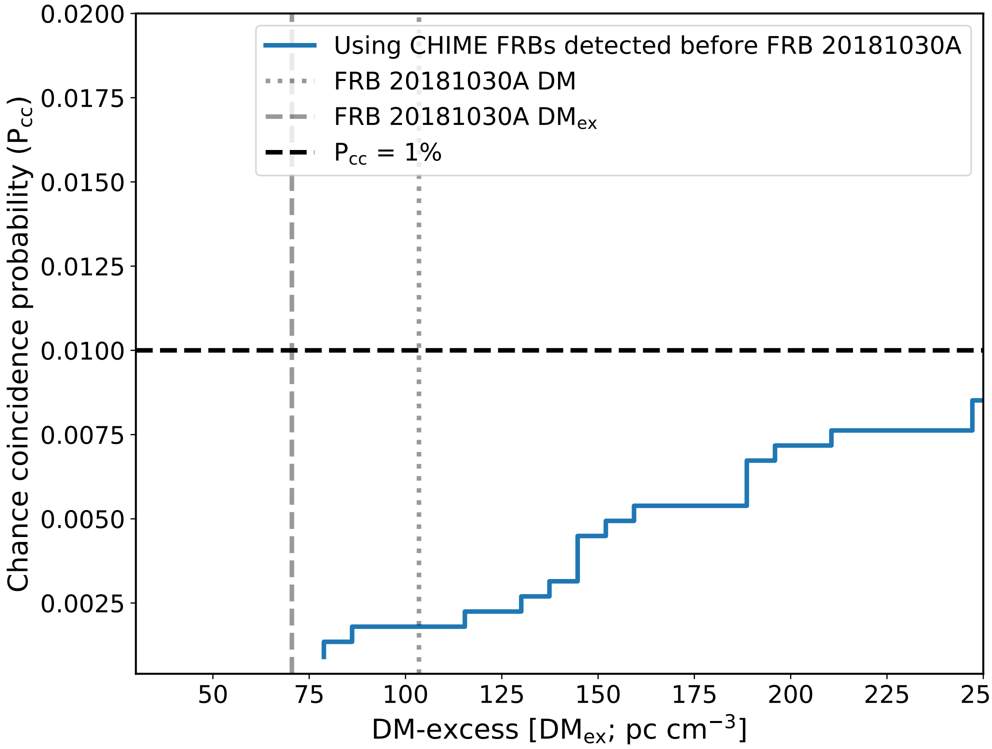

Figure 6.3: The chance coincidence probability of finding an NGC 3252-like galaxy as a function of the DM-excess (DM_{ex}) of CHIME FRBs detected before the first burst of FRB20181030A (see Section 2.1). As discussed in Chapter 5, the latter step takes into account the look-elsewhere effect. Given the DM of FRB 20181030A, 103.5 pc cm^{-3}, $P_{cc} < 0.0025$.

2.2 A dwarf host of FRB 20181030A?

In order to check if there exists any plausible dwarf galaxy within the FRB localization, we first estimated the maximum redshift of the FRB 20181030A host by performing a Markov Chain Monte Carlo (MCMC) simulation, which is discussed below.

We used a likelihood defined by the relation, $DM_{FRB} = DM_{host}/(1+z) + DM_{MW} + DM_{MW,halo} + DM_{IGM}$, where $DM_{FRB} = 103.5 \pm 0.3$ pc cm^{-3}. Table 7.3 summarizes the individual DM components and their respective priors. Similar to Keane et al. (2016) and Williams and Berger (2016), we modelled the Milky Way disk DM (DM_{MW}) as a Gaussian with a mean equal to the minimum of the two Galactic DM model predictions = 33 pc cm^{-3} (see Table 8.2; the maximum redshift estimate would be larger, and so more conservative), and a standard deviation (σ) = 20% of the mean DM_{MW} value, a commonly assumed uncertainty for both the models (Cordes and Lazio, 2002, Yao et al., 2017). Moreover, this is in agreement with the maximum DM estimate of the Milky Way disk along the FRB sight-line using the $\overline{\mathrm{DM}\sin|b|}$ estimate from Ocker et al. (2020) (see Section 2.1). For $DM_{MW,halo}$, we assumed a Gaussian distribution such that at 3σ, the $DM_{MW,halo}$ is either 0 or 80 pc cm^{-3}. This choice is motivated to account for the large uncertainty in the Milky Way halo DM contribution (Keating and Pen, 2020).

For DM_{host}, we assumed a log-normal probability distribution as suggested by Macquart et al. (2020),

$$\mathrm{p}(\mathrm{DM}_{\mathrm{host}}) = \frac{1}{\mathrm{DM}_{\mathrm{host}}\sigma_{\mathrm{host}}\sqrt{2\pi}}\exp\left[-\frac{(\log(\mathrm{DM}_{\mathrm{host}})-\mu_{\mathrm{host}})^2}{2\sigma_{\mathrm{host}}^2}\right], \tag{6.1}$$

with $e^{\mu_{host}}$ = 68.2 pc cm^{-3} and σ_{host} = 0.88. Similarly, for DM_{IGM}, we use a semi-analytical model that Macquart et al. (2020) computed to quantify the uncertainty in DM_{IGM} at a given redshift (z):

$$\mathrm{p}_{\mathrm{IGM}}(\Delta) = \mathrm{A}\Delta^{-\beta}\exp\left[\frac{-(\Delta^{-\alpha}-\mathrm{C}_0)^2}{2\alpha^2\sigma_1^2}\right], \tag{6.2}$$

where $\Delta = \mathrm{DM}_{\mathrm{IGM}}/\overline{\mathrm{DM}_{\mathrm{IGM}}(\mathrm{z})}$, C_0 is the normalization constant, σ_1 = 0.2 z$^{-0.5}$, $\alpha = 3$, $\beta = 3$, and $\overline{\mathrm{DM}_{\mathrm{IGM2}}(\mathrm{z})}$ is the average DM_{IGM} estimate which is a function of redshift and assumed cosmology[3], defined in Equation 2 of Macquart et al. (2020).

For the MCMC sampling, we used the `emcee` package (Foreman-Mackey et al., 2013), which implements an affine-invariant sampling algorithm proposed by Goodman and Weare (2010). We use 256 walkers of 20,000 samples after discarding 1000 burn-in samples from each walker, and thinned the samples by a factor of 100. To assess the convergence of the samplings, we estimated the mean proposal acceptance fraction = 42%, and the chain

[3]We adopt the Planck cosmological parameters (Planck Collaboration et al., 2016).

autocorrelation length ≈ 1.43. Both of the estimates are within the acceptable range as described in Gelman et al. (2013). Lastly, we also estimated convergence criterion for the redshift parameter, $\hat{R} \approx 1.09$ which implies good convergence of the MCMC (Gelman et al., 2013).

From the MCMC analysis, we marginalized the redshift posterior over all other priors and calculated a one-sided 95% Bayesian credible upper limit = 0.05. This is the maximum redshift of FRB 20181030A used in our analysis.

Table 6.3: Parameters used in the MCMC analysis described in Section 2.2.

Parameter	Symbol	Units	Prior
Host galaxy redshift	z	–	U(10^{-4},1)
Host galaxy DM	DM_{host}	pc cm^{-3}	LN($e^{68.2}$,0.88)
Milky way DM	DM_{MW}	pc cm^{-3}	N(33, 20%$\times$33)
Milky way halo DM	$DM_{MW,halo}$	pc cm^{-3}	N(40,33.33%$\times$40)
IGM DM	DM_{IGM}	pc cm^{-3}	Equation 4 from Macquart et al. (2020)

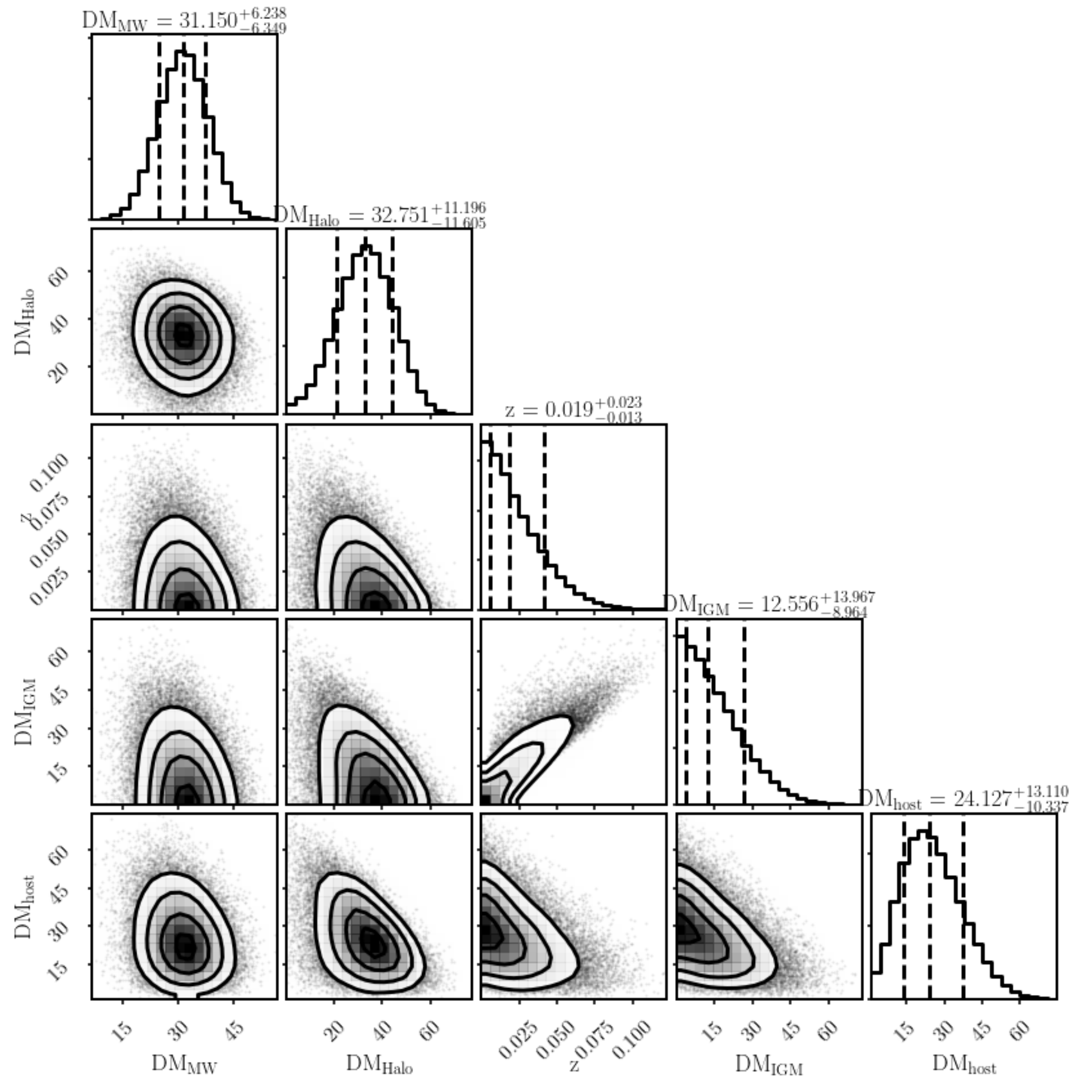

Figure 6.4: The results of a Markov-Chain Monte Carlo (MCMC) analysis discussed in Section 2.2. Constraints on different FRB 20181030A DM components are derived using a Bayesian framework. The marginalized distribution for each DM component is shown along the diagonal of the corner plot. All DM units are in pc cm^{-3}.

There are a few factors that make our maximum redshift estimate conservative. If the FRB host lies beyond NGC 3252, the FRB sight-line would traverse the NGC 3252 halo with a projected offset $\leq$ 14 kpc. Using the stellar mass of NGC 3252 from Table 8.4, we estimated its halo mass to be 1.9 $\times 10^{11}$ $M_{\odot}$ from the stellar mass to halo mass relation using Equation 2 from Moster et al. (2013) and the NFW profile halo concentration factor = 9.4 using Equation 24 from Klypin et al. (2016). At a projected offset of 14 kpc, using the method described Chapter 5, we estimate the DM contribution of the NGC 3252 halo $\approx$ 15 or 30 pc cm^{-3} for baryon fractions 0.4 and 0.75, respectively, using the halo density profile from Maller and Bullock (2004) $-$ the profile that predicted the lowest M81 halo DM in Figure 5.4 of Chapter 5. The former baryon fraction value is the minimum that Hafen et al. (2019) found in the Feedback In Realistic Environments (FIRE) simulation for a halo of mass $\sim 10^{11}$ $M_{\odot}$). The latter value, i.e., 0.75, is estimated assuming $\approx$ 25% of the baryons exist in the galaxy as the interstellar medium (ISM), stars, and compact remnants (Fukugita et al., 1998). Moreover, NGC 3252 is a part of a galaxy group with the dynamic group mass = 1.2 $\times 10^{12}$ $M_{\odot}$ (Kourkchi and Tully, 2017). In addition to this, the FRB sight-line intersects several other galaxy groups that are located within z = $z_{\max}$ (Lim et al., 2017, Tempel et al., 2016). All these would contribute to the observed FRB DM and consequently, if accounted for, would reduce our maximum redshift estimate considerably.

Note that an FRB 20121102A-like star-forming dwarf galaxy ($M_{\rm r} = -17$ AB mag; Tendulkar et al., 2017), the faintest FRB host discovered to date, if located at $z_{\max}$, would have r-band magnitude $\approx$ 19.8 AB mag. Fortunately, the FRB field-of-view is imaged by the Dark Energy Spectroscopic Instrument (DESI) Legacy Imaging Survey (Dey et al., 2019) with an r-band depth $\approx$ 24 AB mag (5σ). Using the DESI data, Zou et al. (2019) estimated photometric redshifts of all the identified galaxies with a 5σ r-band completeness limit of 23.6 AB mag. However, this limit is likely not complete for low surface brightness (LSB) galaxies. For the DESI Legacy Imaging Survey, the average r-band surface brightness limit is $\sim$ 26 mag arcsec^{-2} (Arora et al., 2021, Dey et al., 2019, Tanoglidis et al., 2021). At z = $z_{\max}$, an $M_r = -17$ AB mag LSB galaxy of effective radius $\sim$ 1-3 kpc (Greco et al., 2018) and uniform surface brightness = 26 mag arcsec^{-2} should be detected in the DESI data as an $m_r \lesssim 22$ AB mag source. More importantly, the $m_r \lesssim 22$ AB mag limit is sensitive to detect a dwarf host 5 times less luminous than any FRB host discovered to date ($M_r = -15$ AB mag). Given this constraint, we selected seven galaxies from Zhou et al. (2020), including NGC 3252, which have $m_r \leq 22$ AB mag and are located within the FRB 90% confidence localization region (shown as a cyan ellipse in Figure 8.2) and estimated their spectroscopic redshifts using the 10.4-m Gran Telescopio Canarias (GTC) (see Section 3.4).

2.3 GTC observations and analysis

In this section, we describe our GTC observations of the seven plausible host candidates. As will be shown later, only NGC 3252 satisfies the z_{max} constraint, and hence, the most plausible host of the FRB.

Observations

Observations of the galaxies identified within the FRB 20181030A 90% localization region were performed with the the Optical System for Imaging and low-intermediate Resolution Integrated Spectroscopy (OSIRIS[4]) at the GTC. The OSIRIS detector consists of two CCDs and provides a field of view (FoV) of 7.8′× 7.8′ with a pixel scale of 0.254″. The data were obtained during four observing runs in October 2020 and May 2021. The observing blocks corresponding to the first two runs were executed under Director's Discretionary time. A summary of the observations is given in Table 6.4.

We obtained long-slit spectra of the NGC 3252 using the R1000B grism that covers the spectral range from 3700 to 7500 Å, with the 1.2″ slit width, providing a spectral resolution of about 9 Å. The slit was placed to pass through the major axis of the galaxy at a PA=37.31°, which is shown in Figure 6.5.

To perform simultaneous observations of the other six host galaxy candidates in the localization region (see Table 8.3), we utilized the OSIRIS MOS (multi-object spectroscopy) mode. The mask for the MOS observations was designed with the OSIRIS Mask Designer Tool (Gómez-Velarde et al., 2016, González-Serrano et al., 2004) using the catalogue coordinates of the galaxies and a set of five fiducial stars. The observations were performed with the R500B and R500R grisms that cover the spectral ranges 3600−7200 Å and 4800−10000 Å, respectively. For the target galaxies we designed rectangular slitlets with length varying between 4.5″ and 10″ and a width of 1.5″ each. Two additional slitlets covered source-free regions for sky subtraction. The spectral resolution of the R500B and R500R data is ∼21 Å and ∼27 Å, respectively.

[4] http://www.gtc.iac.es/instruments/osiris/

Table 6.4: Log of the GTC/OSIRIS long-slit and MOS spectroscopic observations of the FRB 20181030A 90% localization region.

Program	Date	Mode	Grism	Position Angle	Exposure Time	Seeing	Airmass	Night
GTC04-20BDDT	24/10/2020	long-slit	R1000B	37.31°	4×60 s	1.2″	1.59	Dark
GTC04-20BDDT	26/10/2020	MOS	R500R	0	8×700 s	1.5″	1.75	Dark
GTC18-21AMEX	04/05/2021	MOS	R500B	0	3×1200 s	0.9″	1.68	Dark
GTC18-21AMEX	15/05/2021	MOS	R500B	0	3×1200 s	1.0″	1.56	Dark

Data reduction

The OSIRIS MOS and long-slit spectra were reduced using the GTCMOS pipeline (Gómez-González et al., 2016) and standard IRAF routines (Tody, 1986, 1993). All spectra were bias-subtracted, and flat-fielded using the set of corresponding images taken during the same observing nights. For flux calibration we used spectrophotometric standards Feige 110, GD153 and Ross 640 (Bohlin et al., 1995, Oke, 1974, 1990) observed during the same nights as the targets. A set of arc-lamp spectra of Ne, Hg and Ar was used for wavelength calibration. The rms errors of the resulting solutions were <0.5Å for the R1000B grating and <2 Å for the R500R and R500B gratings.

Table 6.5: Galaxies identified within the FRB localization region with $M_r < -15$ AB mag at z_{max} = 0.05.

Number	R.A. J2000	Dec. J2000	DESI(r-band)[a] AB mag.	Identified lines	z_{spec}
1	$10^h34^m24.^s81$	$73^\circ45'12.''81$	19.69	[OII], Ca doublet, G-band	0.460(1)
2	$10^h34^m11.^s23$	$73^\circ45'49.''23$	19.89	Ca doublet, G-band, Mg, Na	0.455(2)
3	$10^h34^m9.^s33$	$73^\circ45'42.''33$	19.41	[OII], Ca doublet, [OIII] doublet	0.276(2)
4[b]	$\mathbf{10^h34^m22.^s56}$	$\mathbf{73^\circ45'49.''56}$	**12.58**	see text	**0.00385(2)**
5	$10^h34^m26.^s20$	$73^\circ44'57.''20$	21.61	Ca doublet, G-band, Mg, Na	0.645(1)
6	$10^h33^m58.^s36$	$73^\circ45'21.''36$	20.76	Ca doublet, G-band	0.647(1)
7	$10^h34^m6.^s12$	$73^\circ45'28.''12$	21.67	[OII], Ca doublet	0.563(2)

[a] The r-band magnitudes are corrected for the Milky Way extinction.
[b] Source 4 is NGC 3252, and at a spectroscopic redshift = 0.0039 (20 Mpc), it is the only galaxy in our list with the redshift < z_{max}.

Multi-object Spectroscopy

The resulting product of the pipeline contained 2-D calibrated spectra collected in all of the slitlets. We extracted each spectrum and subtracted the sky using the IRAF task *apall*. We utilized background from the source-free regions to subtract sky from the spectra obtained in the shortest slitlets. The lines identified for each galaxy and the corresponding average redshifts are presented in Table 8.3. To confirm our redshift estimations, we used the Manual and Automatic Redshifting Software (MARZ, Hinton et al., 2016) and compared the extracted spectra with the galaxy templates. In all cases the identified spectral lines (see Table 8.3) have shown an agreement with the spectral features corresponding to early type absorption and intermediate type galaxy templates, confirming our estimations.

Among the identified host galaxy candidates, only NGC 3252 has a spectroscopic redshift $< z_{max}$. This makes NGC 3252 the only viable FRB host candidate among all the identified galaxies with $m_r \leq 22$ AB mag. Note that blue star-forming dwarf galaxies have been proposed to host FRB progenitors (Metzger et al., 2017) via “prompt"-formation-channels, such as superluminous supernovae and long gamma-ray bursts (Fruchter et al., 2006). However, because of their highly dynamic and rich ISM, these galaxies are expected to contribute significantly to the FRB DM (Li et al., 2019). For instance, Tendulkar et al. (2017) estimated that the DM contribution of the FRB 20121102A host, a dwarf irregular star-forming galaxy, is $\sim 60 - 220$ pc cm^{-3}. Hence, together with the inference from Section 2.2, the prospect of a host galaxy beyond NGC 3252 seems unlikely. Lastly, in Table 5, we have listed the three galaxies in the photometric redshift catalogue of DESI extragalactic sources (Zou et al., 2019) that are located within the FRB localization region and have r-band magnitude > 22 AB mag along with their estimated photometric redshifts. All three galaxies have 5σ lower limit on the redshift $> z_{\rm max}$. Therefore, we conclude that the association between FRB and NGC 3252 is real and robust.

Table 6.6: Galaxies with $m_r > 22$ AB mag in the FRB 90% confidence localization region.

Number	R.A. J2000	Dec. J2000	DESI(r-band) AB mag.	$z^a_{\rm photoz}$	$z^{a,b}_{\rm photoz-err}$
1	$10^h34^m16^s.01$	$73^\circ44'18''.60$	22.56	0.62	0.06
2	$10^h33^m59^s.30$	$73^\circ44'40''.56$	22.90	0.60	0.09
3	$10^h34^m35^s.06$	$73^\circ44'58''.56$	22.73	0.72	0.06

[a] From photometric redshift catalogue of galaxies detected in the DESI survey (Zou et al., 2019).
[b] For all three galaxies, $z_{\rm photz} - 5\sigma_{\rm photz-err} > z_{\rm max}$.

2.4 Physical properties of NGC 3252

Here we summarize major physical properties of NGC 3252. We obtained long-slit spectroscopy data from GTC, and its analysis is described below.

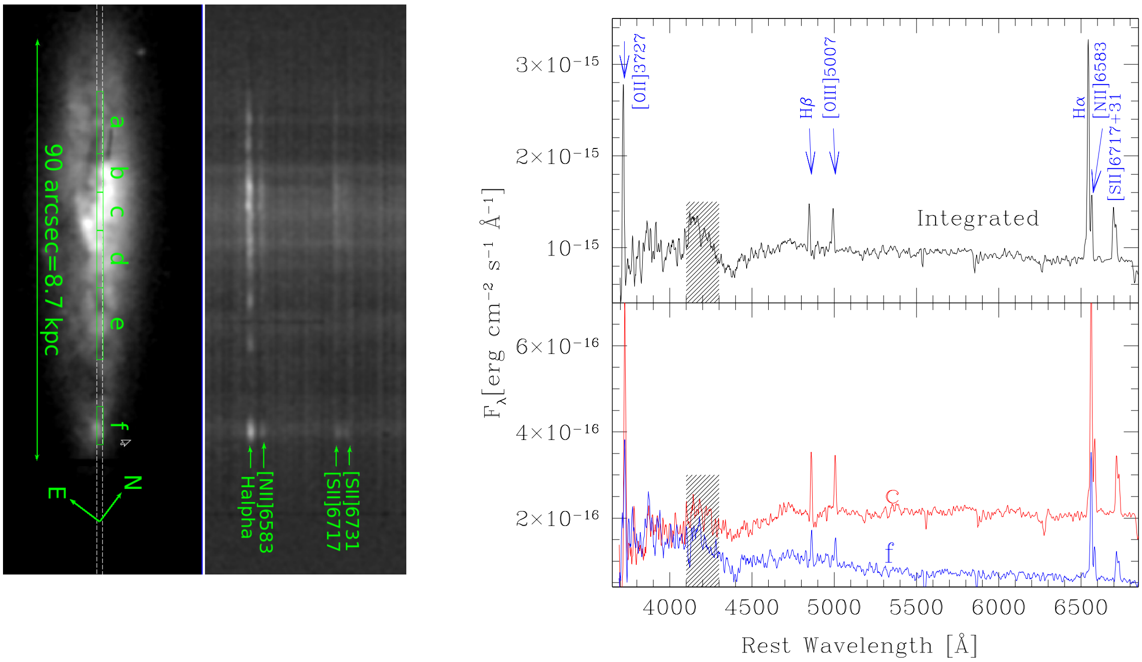

Figure 6.5: (Left) GTC/OSIRIS r-band acquisition image showing the position of the long-slit (white dashed rectangle; PA=37.31°) and the zones a–f selected for the spectral extraction (green rectangles). The image scale and orientation are shown. (Centre) Spectral image along the long-slit showing prominent emission lines in the red part of the spectrum. (Right) Rest frame spectra, where the top spectrum was obtained by summing the rest frame spectra of all the six zones denoted a–f. Spectra marked “c" and “f" correspond to the zone passing through the nucleus and a bright HII, respectively. Note that the latter region lies almost at the centre of the 90% localization ellipse of the FRB source shown (see Figure 8.2). A bump in the spectra between 4100 Å and 4300 Å is due to a detector artefact, which is shown by shaded box.

We acquired the long-slit data of NGC 3252 in order to estimate the physical properties of NGC 3252, such as nebular metallicity and dust extinction. Here we discuss the steps for reducing the NGC 3252 long-slit spectroscopy data. In Figure 6.5, we show the zones used for the extraction of spectra along the long-slit. Hα and other nebular lines are traced over a zone of ∼90” (8.7 kpc) which covers the entire bright optical extent of the galaxy. Several emission knots are seen along the slit, especially in the Hα spectral image. Each knot represents an HII region in the host galaxy. The presence of these HII regions allows us to obtain physical quantities along the slit using the physics of photoionized nebulae (Osterbrock and Ferland, 2006). In order to maximize the S/N ratio of the extracted spectra, we defined six zones, identified by letters a–f, in such a way that each zone contains at least one of the emission knots. The zone c spectrum contains the nucleus, and the zone f spectrum corresponds to a bright HII region to the south-west of the nucleus. This HII region lies almost at the centre of the 90% localization ellipse of the FRB source shown in Figure 8.2. In the right panel, we show the extracted spectrum for these two regions. Each extracted spectrum was analyzed to measure the fluxes of bright nebular lines using the Gaussian fitting technique of the *splot* task in IRAF, which also performs a measurement and subtraction of continuum flux. The prominent lines in the spectrum were identified and are shown in the top panel. A deblending algorithm was used to extract accurate fluxes of [NII]λ6548 and [NII]λ6583 lines in the presence of the bright Hα line and also to resolve the [SII] doublet.

The measured line fluxes in each spectrum are given in Table 6.7. The spectra were first corrected for Doppler shift using a mean of the recessional velocities measured using the Hβ, Hα and [OIII]λ5007 lines in each spectrum. The measured velocities are also given in Table 6.7. All the six rest frame spectra were summed to get an integrated spectrum of the galaxy, which is shown in the top-right panel in Figure 6.5. Values measured for the integrated spectrum are given in the last column of Table 6.7. The mean of the velocities of the six extracted spectra was taken as the velocity of the integrated spectrum, which agrees very well with the systemic velocity of 1156$\pm$6 km s^{-1} reported in NED (Schneider et al., 1992). The Hα and Hβ emission line fluxes stated in Table 6.7 are used to obtain the visual extinction A_V experienced in each zone, shown in Figure 6.5, following the Balmer decrement method for case B recombination of a typical photo-ionized nebula ($T_{\rm e}$ =10000 K, $n_{\rm e}$=100 cm^{-3}; Osterbrock and Ferland, 2006) and the reddening curve of Cardelli et al. (1989). We corrected the observed Hα and Hβ fluxes for the effects of the underlying stellar absorption by assuming an absorption equivalent width of 2 Å following McCall et al. (1985). The resulting A_V values vary between 0.8–1.6 mag in the zones along the slit. The line fluxes were corrected for the measured extinction and are given as ratios with respect to the flux of the Hβ line, which is multiplied by 100 following the normal convention.

Electron temperature-sensitive Auroral lines were not detected in any of the extracted spectra. However, nebular lines for the determination of the oxygen and nitrogen abundances using the strong-line method are detected with S/N >10. We used the calibrations of Pilyugin and Grebel (2016) for this purpose (their Equations 4 and 13). The resulting values of 12+log(O/H) are given in Table 6.7 for each zone as well as that measured in the integrated spectrum.

Table 6.7: Physical quantities from long-slit spectra of NGC 3252.

Quantity[a]	a	b	c	d	e	f	Integrated
R.A.(J2000)	10:34:25.50	10:34:23.94	10:34:22.73	10:34:21.27	10:34:19.26	10:34:16.11	
Dec.(J2000)	+73:46:05.0	+73:45:56.4	+73:45:49.7	+73:45:41.6	+73:45:30.5	+73:45:13.1	
Area[$''\times''$]	13.3×1.2	8.2×1.2	8.2×1.2	12.3×1.2	15.3×1.2	8.2×1.2	65.5×1.2
I([OII]3727)	38.5 ± 4.6	556.7 ± 3.7	498.2 ± 11.1	769.8 ± 9.5	412.4 ± 8.2	168.7 ± 0.3	437.0 ± 4.5
I(Hβ)	100.0	100.0	100.0	100.0	100.0	100.0	100.0
I([OIII]5007)	79.8 ± 0.1	51.7 ± 4.0	84.2 ± 2.8	89.3 ± 1.3	51.4 ± 5.6	74.0 ± 0.5	77.4 ± 1.0
I(Hα)	287.0 ± 53.1	287.0 ± 66.3	287.0 ± 29.8	287.0 ± 38.8	287.0 ± 75.0	287.0 ± 37.4	287.0 ± 32.2
I([NII]6583)	96.1 ± 14.1	82.7 ± 16.1	89.9 ± 7.6	87.7 ± 9.3	69.0 ± 8.2	61.9 ± 4.1	80.6 ± 7.0
I([SII]6717)	53.8 ± 5.9	61.7 ± 9.5	62.2 ± 4.1	67.8 ± 6.7	58.2 ± 2.9	63.5 ± 3.0	60.6 ± 3.7
I([SII]6731)	25.1 ± 0.1	42.5 ± 4.6	47.4 ± 2.1	45.9 ± 3.2	44.9 ± 1.2	41.6 ± 0.1	45.0 ± 0.3
logF(Hβ_0)[erg cm^{-2} s^{-1}]	−14.50±0.20	−14.25± 0.19	−14.25± 0.11	−14.02±0.14	−14.28± 0.29	−14.62± 0.16	−13.50 ±0.11
A_V[mag]	0.9 ±0.4	1.4 ± 0.4	0.9 ± 0.2	1.6 ± 0.2	1.6 ± 0.4	0.8 ± 0.3	1.3 ± 0.2
EW(Hβ)[Å]	12.4	11.1	7.3	3.3	2.9	8.6	5.8
Velocity [km s^{-1}]	1073 ±43	1105 ±49	1056 ± 35	1125 ± 15	1166 ± 57	1274± 50	1133 ± 79
12+log(O/H)	8.64 ± 0.05	8.38± 0.05	8.46 ±0.05	8.38 ±0.05	8.37 ±0.05	8.49 ±0.05	8.44 ± 0.05

[a] In the first block, centre coordinates of the rectangular zones (named a to f; see Figure 6.3) chosen for the extraction of spectra are given. The next block contains the extinction corrected fluxes of prominent nebular lines relative to the flux of the Hβ line, i.e. I(λ)=100× F(λ)/F(Hβ). The last block contains the extinction-corrected Hβ flux and physical quantities derived from the diagnostics of the nebular lines.

From the integrated optical spectrum of the galaxy, we estimate the oxygen abundance 12+log(O/H) = 8.44±0.06 (or nebular metallicity $\log(Z_{\rm gas}/Z_{\odot}) = -0.25 \pm 0.07$), which is ∼60% of the solar value (Asplund et al., 2009). We also derive dust extinction at the V-band, $A_v = 1.3 \pm 0.2$ (E(B−V)= 0.42 ± 0.06 using $R_v = 3.1$), using Hα/Hβ ratio (i.e. Balmer decrement), assuming the standard Milky Way extinction curve (Cardelli et al., 1989). Finally, using SFR(Hα) = 7.9×10^{-42} $M_\odot$ yr^{-1}× L(Hα/erg s^{-1}) (Kennicutt et al., 1994), we get SFR(Hα)=0.033 $M_\odot$ yr^{-1} using the extinction corrected total Hα luminosity of L(Hα) = 4.12×10^{39} erg s^{-1}.

However, as the slits only cover a small fraction of the surface area of NGC 3252, it is expected that the above star formation rate is significantly underestimated. Therefore, we estimate the total star formation rate (SFR_{total}) by combining the total infrared (TIR) luminosity and far-UV (FUV)-derived SFR as described in Iglesias-Páramo et al. (2006), which is found to be a robust estimate for the disk galaxies (Buat et al., 2007). We estimated the TIR luminosity of NGC 3252 using the prescription of Dale and Helou (2002) which uses the Infrared Astronomical Satellite (IRAS) filters' fluxes (Fullmer and Londsale, 1995), and got L(TIR) = 2.13 $\times 10^9$ $L_\odot$. Using Equation 5 from Iglesias-Páramo et al. (2006), SFR(TIR) = 0.38 $M_\odot$ yr^{-1}. Similarly, for the FUV luminosity, we use the Galex NUV filter flux and estimated the SFR(FUV) = 0.13 $M_\odot$ yr^{-1} using the extinction uncorrected L(FUV) of NGC 3252 = 2.7 $\times$ 10^8 $L_\odot$. Finally, the total recent star formation rate was calculated using the relation from Iglesias-Páramo et al. (2006): SFR_{total} = SFR(NUV) + (1-η) $\times$ SFR(TIR) = 0.36 $M_\odot$ yr^{-1} where $\eta = 0.4$ for disk galaxies in the local Universe (Iglesias-Páramo et al., 2004), which accounts for the fraction of the total IR luminosity heated by old stars. This relation has a calibrated uncertainty of about 20%.

To estimate stellar mass, metallicity and mass-weighted age of NGC 3252, we use a Bayesian inference spectral energy distribution (SED) fitting code, `Prospector` (Johnson et al., 2019, Leja et al., 2017) , which estimates galaxy properties using stellar population synthesis models defined within the framework of the Flexible Stellar Populations Synthesis (FSPS) stellar populations code (Conroy et al., 2009). `Prospector` provides an MCMC framework via `emcee` to fit observed spectral energy distributions (SEDs) and estimate posterior distribution for each free-parameters. In this paper, we use `Prospector` to estimate the stellar mass, metallicity, and mass-weighted stellar population age of NGC 3252. We use 17 broadband filters from the GALEX FUV filter at 1549 Å through the Herschel telescope bands that provide coverage at far-infrared wavelengths as shown in Figure 7.5 and Table 7.7.

Table 6.8: 17 broadband filters used to model the SED of NGC 3252.

Instrument[c]	Filter	Effective Wavelength Å	Flux density[a,b] maggies
GALEX	FUV	1549	4.38×10^{-7}
	NUV	2304	5.56×10^{-7}
DESI[d]	g	4670	4.98×10^{-6}
	r	6156	9.26×10^{-6}
	z	8917	1.41×10^{-5}
2MASS	J	12319	1.75×10^{-5}
	H	16420	1.79×10^{-5}
	Ks	21567	1.67×10^{-5}
WISE	W1	33461	9.75×10^{-6}
	W2	45952	6.33×10^{-6}
	W3	115526	1.99×10^{-5}
	W4	220783	2.50×10^{-5}
Herschel	PACS(Green)	979036	8.40×10^{-4}
	PACS(RED)	1539451	1.13×10^{-3}
	SPIRE(PSW)	2428393	5.87×10^{-4}
	SPIRE(PMW)	3408992	3.00×10^{-4}
	SPIRE(PLW)	4822635	1.27×10^{-4}

[a] Note that 1 maggie is defined as the flux density in Janskys divided by 3631. Fluxes at $\lambda < 100000$ Å are corrected for Galactic extinction according to the prescription of Schlafly and Finkbeiner (2011).
[b] All broadband fluxes are assigned a 20% fractional uncertainty.
[c] Except for the DESI survey, all instruments' flux densities are obtained from the aperture-matched photometry catalogue of nearby galaxies by Clark et al. (2018).
[d] For DESI filter magnitudes, we used the photometric redshift catalogue by Zhou et al. (2020).

Table 6.9: Free parameters and their associated priors for the Prospector 'delayed-τ' model.

Parameter	Description	Prior
$\log(M/M_{\odot})$	total stellar mass formed	uniform: min=8, max=11
$\log(Z/Z_{\odot})$	stellar metallicity	Gaussian: mean=-0.25, σ=0.21
dust2	diffuse V-band dust optical depth	top-hat: min=0.0, max=3.0
t_{age} [Gyrs]	stellar population age of NGC 3252	top-hat: min=0.01, max=13.6
τ [Gyrs]	e-folding time of the SFH	uniform: min=0.1, max=30

All flux densities are estimated after correcting for the Milky Way extinction. We fit a delayed-τ star formation history model (Carnall et al., 2019, Simha et al., 2014) with five free parameters – metallicity, mass-weighted stellar population age, star formation timescale, and V-band optical extinction (= 1.086 $\times$ dust2), which are described in Table 7.8. In this model, the star-formation history is proportional to $\mathrm{t}\times\exp(-\mathrm{t}/\tau)$, where t is the time since the formation epoch of the galaxy, and τ is the characteristic decay time of our star-formation history. Additionally, we enabled nebular emission (Byler et al., 2017) and dust emission (Draine and Li, 2007) models in the FSPS framework along with a standard dust attenuation model from Calzetti et al. (2000). Finally, all five parameters are given standard Prospector priors, except $\log(Z/Z_{\odot})$, which is informed by the constraints derived in Section 4. This is included to reduce the effect of the age-metallicity degeneracy (Worthey, 1994). We used a Gaussian prior to model $\log(Z/Z_{\odot})$ with mean $= -0.25$ derived in Section 4 using optical spectral lines. However, we increased the σ value by a factor of three to account for any potential bias in converting the oxygen abundance to nebular metallicity, a conservative choice given that the conversion error is typically ~ 0.02 (Serenelli et al., 2009), which is less than one sigma error on the $\log(\mathrm{Z_{gas}}/\mathrm{Z_{\odot}})$, i.e. 0.07 (see Table 8.4).

Using this framework, we derived a metallicity fraction, $\log(\mathrm{Z}/\mathrm{Z}_{\odot}) = -0.21^{+0.18}_{-0.19}$, and the present-day stellar mass of the galaxy = $5.8^{+1.6}_{-2.0} \times 10^{9}\mathrm{M}_{\odot}$. To estimate the best-fitted mass-weighted stellar population age value, we used Equation 5 of Carnall et al. (2019) and found it to be $4.8^{+1.6}_{-1.8}$ Gyr. All these values are provided in Table 8.4. Note that the quoted uncertainties in all cases are 1σ values.

The best-fit spectral energy distribution (SED) profile of NGC 3252 is shown in Figure 7.5.

Table 6.10: Notable properties of NGC 3252.

Property	Value	Reference
log[SFR] ($M_\odot$ yr^{-1})	-0.45 ± 0.1	this work
Stellar Metallicity ($\log(Z/Z_\odot)$)[a]	$-0.21^{+0.18}_{-0.19}$	this work
Nebular Metallicity ($\log(Z_{gas}/Z_\odot)$)	$-0.25\pm$ 0.07	this work
Oxygen abundance [O/H]	8.44 $\pm$ 0.06	this work
Stellar mass ($M_\odot$)	$5.8^{+1.6}_{-2.0} \times 10^9$	this work
Effective radius (R_{eff}; kpc)	2.6	Salo et al. (2015)
Mass-weighted age (Gyr)[a]	$4.8^{+1.6}_{-1.8}$	this work
E(B-V) (mag)	0.42 $\pm$ 0.06	this work
Absolute r-band mag. (AB)	-19.1 ± 0.5	–
Luminosity distance (Mpc)	20 $\pm$ 5	Tully et al. (2016)

[a] Estimated using `Prospector`; See Section 4.

2.5 Search for a multi-wavelength counterpart to FRB 20181030A

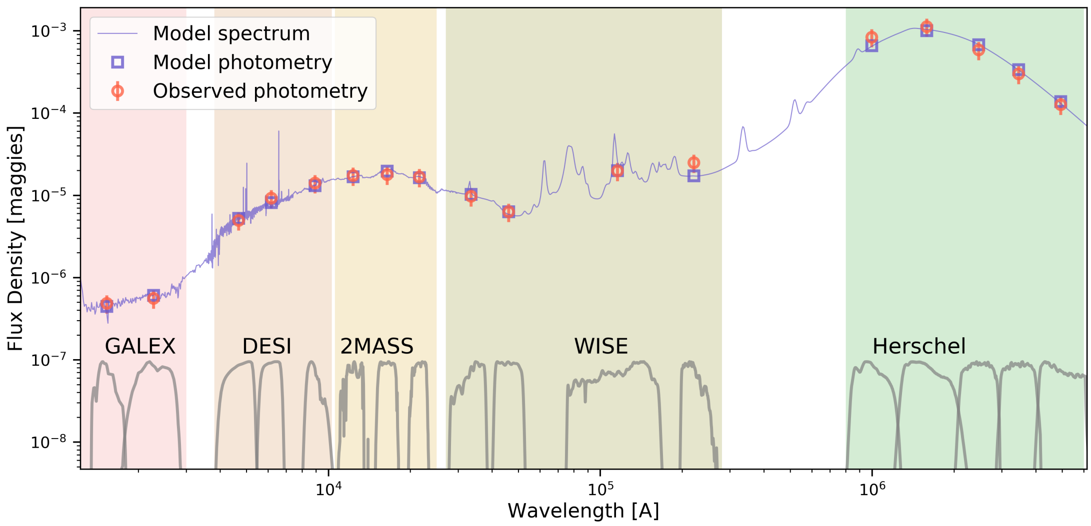

Figure 6.6: Modelling the SED of NGC 3252. The flux density of NGC 3252 in different wavelength bands are plotted along with the best-fit `Prospector` model spectrum. To assess the quality of the `Prospector` model, the modelled and actual photometry data are also shown. The shown model profile is used to estimate different physical properties of NGC 3252. For more information, see Section 4. The modelled SED of NGC 3252 shown in Figure 7.5 is in excellent agreement with that of a typical star-forming galaxy (Leitherer, 2005).

Persistent radio source search

We searched archival radio data of the following surveys to check for the presence of a persistent radio source within the FRB uncertainty region: the NRAO VLA Sky Survey (NVSS; Condon et al., 1998), the VLA Sky Survey (Lacy et al., 2016, VLASS;), the Westerbork Northern Sky Survey (WENSS; Rengelink et al., 1997), and the Tata Institute of Fundamental Research Giant Metrewave Radio Telescope Sky Survey (TGSS) Alternative Data Release (Intema et al., 2017). We found only one radio source, NVSS J103422+734554. The radio source is only detected in NVSS and is either unresolved or marginally extended. Moreover, it is spatially coincident with the centre of NGC 3252. Table 8.5 lists 5σ upper limits on the source's integrated flux density derived from the archival radio images of all other surveys. The NVSS radio source is likely resolved out and hence, undetected in the VLASS 2.1 data. In VLASS 1.1 data, we detected an irregular-shape source spatially coincident with the NVSS radio source. However, due to the lack of detection in the VLASS 2.1 data despite similar sensitivity, and known calibration and imaging artefacts in the VLASS 1.1 data (Lacy et al., 2016), the radio source is likely spurious (M. Lacy, private communication). From the non-detection in the TGSS data and assuming a power-law dependence of the NVSS radio source flux density i.e., $S_\nu \propto S^\alpha$, we estimated a lower limit on $\alpha > -0.43$. This agrees well with the observed radio continuum spectral index of local star-forming galaxies (between -0.1 and -0.7; Marvil et al., 2015).

While searching the VLA archive, we also found raw EVLA data (project ID = AK752) that cover the FRB localization region. Observations were conducted on 2010 June 19 (MJD 55366) with the array in D-configuration in two 128-MHz bandwidth sub-bands with central frequencies 4.495 GHz and 7.852 GHz, and about 40 minutes of time on source. The absolute flux density calibrator 3C147 and the phase calibrator J1048+7143 were used. The data were calibrated and flagged using `CASA` software (McMullin et al., 2007). Additional RFI flagging and self-calibration were done resulting in a final primary-beam corrected image with a local rms noise of $\sigma \approx 30$ μJy beam^{-1}. Within the FRB localization region, we detect only the NVSS radio source extended in both the EVLA observations (See Figure 6.7). The integrated flux density of the NVSS source at 4.495 GHz and 7.852 GHz is estimated using the `Aegean` package (Hancock et al., 2012, Hancock et al., 2018) and is stated in Table 8.5. Using the EVLA flux densities at 4.495 GHz and 7.852 GHz, we estimated α to be -0.94 ± 0.16, which is steeper than the lower-limit on α estimated using the flux densities at 150 MHz and 1.4 GHz (> -0.43). This is not unusual as the radio spectra of star-forming galaxies are known to show a break (or an exponential decline) in the frequency range of $1-12$ GHz (Klein et al., 2018).

The NVSS source is likely to be produced via ongoing star formation in NGC 3252. To test this, we estimate the SFR using the NVSS 1.4 GHz continuum emission and compare it with the value estimated in Section 4. Using the 1.4 GHz–SFR relation from Davies et al. (2017), $\log(\mathrm{SFR_{UV+TIR}}/\mathrm{M_\odot yr^{-1}}) = 0.66 \pm 0.02 \times \log(\mathrm{L_{1.4}(W/Hz)}) - 14.02 \pm 0.39$, we estimate $\log(\mathrm{SFR_{UV+TIR}}/\mathrm{M_\odot yr^{-1}}) = -0.6 \pm 0.5$ which agrees with the SFR estimate in Table 8.4. Though it is difficult to rule out the presence of a low-luminosity active galactic nucleus (AGN) at the centre of NGC 3252 (Maoz, 2007), the extended nature of the radio source and agreement of its 1.4 GHz flux density with the SFR of NGC 3252 suggest that an AGN is unlikely to be the dominant source of the observed persistent radio emission. Moreover, from the non-detection of a persistent compact radio source (< 0.3 kpc at 20 Mpc) in the FRB 20181030A localization region in the VLASS 2.1 data (which has the best angular resolution among all the radio surveys considered here), we estimate a 3σ upper limit of 480 μJy at 3 GHz which at 20 Mpc implies an isotropic spectral luminosity $\approx 2 \times 10^{26}$ erg/s/Hz, at least 1500 times fainter than that the persistent radio source detected spatially coincident to FRB 20121102A (Chatterjee et al., 2017, Resmi et al., 2020).

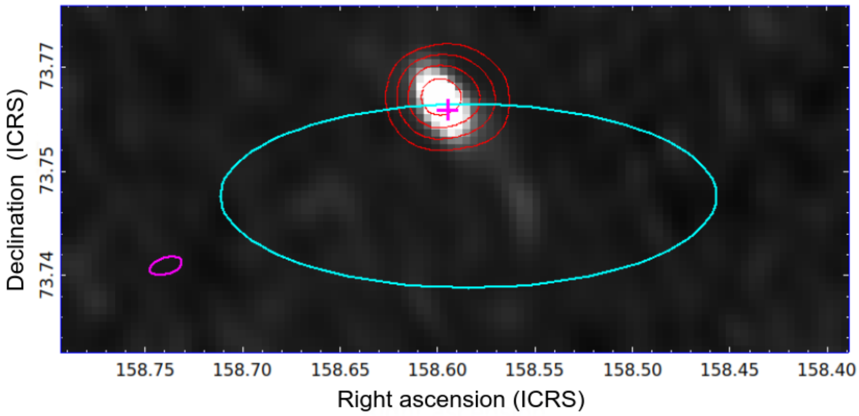

Figure 6.7: The EVLA 4.5 GHz image of the FRB 20181030A 90% localization region (cyan ellipse). NVSS contours (3 mJy, 2.5 mJy, 2 mJy, and 1.5 mJy) of the radio source are shown in red. The centre of NGC 3252 (see Table 8.3) is represented by a magenta cross. Finally, the EVLA beam is shown as magenta ellipse on the bottom left side of the image.

Table 6.11: Summary of radio observations of NGC 3252.

Survey	Frequency GHz	Date UT	Image Resolution[a] $''$	Integrated Flux Density mJy
TGSS	0.15	2016 March 15	25	$<10^b$
WENSS	0.326	1997 October 22	56	$< 18^b$
NVSS[c]	1.4	1993 December 18	45	3.8 ± 0.5
VLASS 2.1	3.0	2020 October 13	2.5	$< 0.6^b$
EVLA[c]	4.495	2010 June 19	12.8	1.35 ± 0.06
	7.852	2010 June 19	9.1	0.80 ± 0.06

[a] For each survey, average of major and minor axes of the formed beam is quoted.
[b] 5× local rms noise.
[c] The lone radio source in the FRB uncertainty region is extended and spatially coincident with the centre of NGC 3252 in the NVSS and two EVLA observations.

Archival search for X-ray counterparts

We searched the Transient Name Server (TNS)[5] for any archival transient event that is spatially and temporally coincident with any of the nine recorded FRB 20181030A bursts and found none. We also checked if the FRB was visible to the *Swift*/Burst Alert Telescope (BAT) and *Fermi*/GBM at the time of the bursts. Unfortunately, *Swift*/BAT was either not operational (transiting through the South Atlantic Anomaly region) or the FRB location was not within the BAT's field-of-view. Similarly, for all except FRB 20200122A , the FRB location was not visible to *Fermi*/GBM. If FRB 20200122A was associated with a giant magnetar flare like the one detected from SGR 1806−20 on 2004 December 27 (Palmer et al., 2005), *Fermi*/GBM with a flux sensitivity of $\sim 10^{-7}$ erg cm^{-2} s^{-1} in the 50–300 keV band (von Kienlin et al., 2020) would have marginally detected it. This places an upper limit on the coincident X-ray flare energy $\approx 10^{46}$ erg s^{-1} at 20 Mpc (without correcting for the attenuation by the host). There is an X-ray source RX J1034.3.3+7345 (or 1AXG J103422+7344 in the *ASCA* medium sensitivity survey by Ueda et al., 2001) in the vicinity of NGC 3252. This source was discovered in the *ROSAT* all-sky survey (Truemper, 1982) and was initially associated with NGC 3252 by Bade et al. (1998), Condon et al. (1998) and Bauer et al. (2000). However, with the availability of higher resolution X-ray images,

[5] https://www.wis-tns.org/

this association has been argued to be incorrect (Haakonsen and Rutledge, 2009). More interesting, the X-ray source was found to be spatially coincident with an optical transient PTF10hjz discovered by the Palomar Transient Factory (PTF) on 2010 May 16 (Kasliwal, 2011). Based on its high optical and radio flux variability and estimated broadband spectral energy distribution, PTF10hjz was later classified as a background blazar (S. Kulkarni, private communication). Therefore, we conclude that the X-ray source RX J103423.1+734525 (or PTF10hjz) is unrelated to FRB 20181030A.

3 Discussion

3.1 Constraints on the Milky Way halo DM contribution

With NGC 3252 as its host, we can use FRB 20181030A and its low DM-excess, to constrain the Milky Way halo DM along the FRB sight-line. At 20 Mpc, using the average Macquart relation, we estimate $\mathrm{DM_{IGM}} \approx 5$ pc cm^{-3}.[6] Assuming negligible host DM contribution, we find an upper limit on the $\mathrm{DM_{MW,halo}}$ to be 58 and 66 pc cm^{-3} using the $\mathrm{DM_{MW}}$ estimate from the NE2001 and YMW16 models, respectively (See Table 8.2). However, a negligible host contribution is likely an overly conservative assumption as even in the extreme scenario where the FRB has a very large offset from the host, the host's circumgalactic medium would still contribute to the FRB DM. Therefore, we use the MCMC analysis discussed in Section 2.2, but this time, fix the redshift of the FRB to that of NGC 3252. From this analysis, we estimate the $\mathrm{DM_{MW,halo}}$ 90% Bayesian credible interval to be (19 pc cm^{-3}, 55 pc cm^{-3}). This, along with a similar constraint derived in Chapter 5, suggests that the Milky Way halo DM contribution could be relatively small. This in turn would help in constraining the state and composition of the Milky Way circumgalactic medium (Tumlinson et al., 2017). However, to constrain the average $\mathrm{DM_{MW,halo}}$ estimate, we need more low-DM FRBs.

[6]$\mathrm{DM_{IGM}}$ is expected to be considerable as the FRB sight-line intersects several foreground groups, including that of M81 (Tully, 2015) making $\mathrm{DM_{IGM}}$ = 5 pc cm^{-3} a conservative estimate.

3.2 Comparison with SGR 1935+2154 radio bursts

From Table 2 of CHIME/FRB Collaboration et al. (2019c), the peak 400–800-MHz flux densities of the two published bursts from this source, FRBs 20181030A and 20181030B, are 3.2 ± 1.7 Jy and 3.1 ± 1.4 Jy, respectively. At a distance of 20 Mpc, the isotropic radio luminosity of these two bursts would be $\sim 9{\times}10^{38}$ erg s^{-1}, around six times larger than those of the very bright SGR 1935+2154 radio bursts recently detected by CHIME/FRB and STARE2 (Bochenek et al., 2020, CHIME/FRB Collaboration et al., 2020a).[7] This suggests a continuum of FRB luminosities, at least at low values. Bochenek et al. (2020) estimated the volumetric rate of SGR 1935+2154-like bursts to be $7^{+9}_{-6} \times 10^{7}\ \mathrm{Gpc^{-3}yr^{-1}}$, assuming that the FRB luminosity function follows a power law and the FRB rate is proportional to the star-formation rate. As at least the two FRB bursts in the first CHIME/FRB catalogue (The CHIME/FRB Collaboration et al., 2021) have isotropic luminosity $\geq 10^{38}$ erg s^{-1}, we estimate a lower limit on the volumetric rate of FRBs ($\geq 10^{38}$ erg s^{-1}) to be $1.5^{+1.6}_{-0.7} \times 10^{7}\ \mathrm{Gpc^{-3}yr^{-1}}$. This lower limit is in agreement with the estimate by Bochenek et al. (2020), which supports their conclusion that magnetars like those observed in the Milky Way could be a dominant channel of FRB production, at least at the lower end of the FRB luminosity function.

Moreover, the estimated CHIME/FRB volumetric rate agrees with the rate calculated by extrapolating the luminosity function derived from a sample of bright FRBs observed at 1.4 GHz by the Australian Square Kilometre Array Pathfinder (ASKAP) and Parkes down to the luminosity of FRB 20181030A's bursts (Lu and Piro, 2019, Luo et al., 2020). Lastly, the estimated FRB volumetric rate at low luminosities is at least 100 times higher than the observed volumetric rate of core-collapse supernovae in the local Universe (Taylor et al., 2014, $\sim 10^{5}$ Gpc^{-3} yr^{-1}). Assuming core-collapse supernovae are the most common way to produce compact objects, FRBs detected at low luminosities ($\sim 10^{38}$ erg s^{-1}) are therefore more likely to be repeating sources.

[7] Assuming the distance to SGR 1935+2154 is 10 kpc, but note that Zhou et al. (2020), Mereghetti et al. (2020) and Bailes et al. (2021) argue for a significantly smaller distance to the magnetar, $\approx$ 2-7 kpc.

3.3 Implications for different progenitor models

Three repeating FRB sources within a comoving volume out to a distance of 20 Mpc (Bochenek et al., 2020, CHIME/FRB Collaboration et al., 2020a, Chapter 5) have now been discovered. Using these discoveries, we estimate a lower limit on the comoving number density ($\mathrm{n_{FRB}}$) of repeating FRB sources to be $9^{+7}_{-4} \times 10^4$ Gpc^{-3}. We can also express $\mathrm{n_{FRB}} = \mathrm{R_{FRB}}\tau\eta\zeta$, where $\mathrm{R_{FRB}}$ is the local Universe volumetric birth rate of repeating FRB sources, τ and ζ are the average lifetime and active duty cycle of repeating FRBs, respectively, and η is the beaming fraction. Taking the fiducial values of $\eta = 0.1$ and $\zeta = 0.3$ from Lu and Kumar (2016) and Nicholl et al. (2017), we estimate $\mathrm{R_{FRB}}\tau = 3^{+2}_{-1}\times10^6 \left(\frac{0.1}{\eta}\right)\times\left(\frac{0.3}{\zeta}\right) \mathrm{Gpc}^{-3}$. One of the popular proposed repeating FRB models is a highly magnetized ($> 10^{15}$ G) young neutron star with period $\sim$ ms. Nicholl et al. (2017) estimated the volumetric birth-rate of millisecond magnetars ($\mathrm{R_{ms}}$) to be $\sim$ few $10 - 100\ \mathrm{Gpc^{-3}yr^{-1}}$. Using this $\mathrm{R_{ms}}$ value as $\mathrm{R_{FRB}}$, we estimate $\tau \sim 10^4 - 10^5$ yr. This is around two orders of magnitude greater than the expected typical lifetime of a repeating FRB in the models that invoke millisecond magnetars ($\sim 30 - 300$ yrs; Metzger et al., 2017, Metzger et al., 2019). Therefore, it is unlikely that all repeating FRBs are produced by millisecond magnetars formed primarily via cataclysmic events, like superluminous supernovae, or long and short gamma-ray bursts. Note that Nicholl et al. (2017) did not include accretion induced collapse (AIC) as a channel for forming millisecond magnetars in their calculation due to the high uncertainty in the AIC rates. However, theoretically estimated rates of AIC are found to be comparable to that of binary neutron star mergers (Kwiatkowski, 2015, Tauris et al., 2013). If these estimates are correct, including them would not change our conclusion significantly.

3.4 Comparison with other repeating FRB hosts

With the inclusion of FRB 20181030A, likely localized to the star-forming galaxy NGC 3252, in the sample of five repeating FRBs, 20121102A, 20180916B, 20190711A, 20200120E, and FRB 20201124A (CHIME/FRB Collaboration, 2021, Fong et al., 2021, Ravi et al., 2021), it is evident that the repeating FRB hosts exhibit a continuum of properties in terms of their luminosities, stellar masses, metallicity, and SFRs, ranging from FRB 20121102A, a metal-poor, high-star forming dwarf irregular galaxy, to FRB 20200120E, a metal-rich massive early-type spiral galaxy. However, it is interesting to note that all five localized repeating FRBs discovered thus far are in either spiral or irregular galaxies (Mannings et al., 2020), where practically all core-collapse supernovae (SN II, IIn, IIb, and Ib/c) occur (van den Bergh et al., 2005). However, FRB 20200120E is localized to an M81 globular cluster (see Chapter 5) where core-collapse supernovae are not expected to occur. Therefore, we need a larger sample of FRB hosts to decipher the nature of FRB progenitors. Lastly, we note that all three local Universe repeating FRBs have thus far been observed to produce only low-energy bursts ($\lesssim 10^{35}$ erg), unlike, for example, the FRB 20121102A bursts, which have shown a range of burst energies ($10^{36} - 10^{40}$ erg; e.g., Chatterjee et al., 2005, Gourdji et al., 2019). More bursts, particularly high-energy ones, from these FRBs would aid in constraining the emission mechanism of the local Universe FRBs (Lyubarsky, 2021).

4 Summary & conclusions

We have reported on the likely association of the repeating FRB 20181030A discovered by CHIME/FRB Collaboration et al. (2019c) with a nearby star-forming spiral galaxy, NGC 3252, at a distance of 20 Mpc. The chance coincidence probability of finding NGC 3252 within the FRB localization region is $< 2.5 \times 10^{-3}$. Moreover, we searched for plausible host galaxies within the 90% confidence localization region of the FRB, and found no galaxy except NGC 3252 with $\mathrm{M_r} < -15$, a limit in luminosity over five times smaller than for any FRB hosts identified to date.

NGC 3252 is a star-forming spiral galaxy (see Figure 7.5). We found no archival transient event spatially or temporally coincident with any of the reported FRB 20181030A bursts to date. For one FRB burst, FRB 20200122A, that was detected on 2020 January 22 by CHIME/FRB and was also visible to *Fermi*/GBM, we estimated an upper limit on the coincident X-ray flare energy to be $\approx 10^{46}$ erg s^{-1}. We also searched for a compact, persistent radio continuum source within the FRB localization region and found none. We then estimated a 3σ upper limit at 3 GHz $= 4.3 \times 10^{25}$ erg s^{-1}Hz^{-1}, at least 1500 times fainter than the persistent source associated with FRB 20121102A. Due to its low DM-excess, we constrain the Milky Way halo DM contribution to be 19−55 pc cm^{-3} (90% confidence interval) along the FRB sight-line. We also compared the two published FRB 20181030A bursts with those of SGR 1935+2154. The FRB bursts' isotropic luminosity is ~ 6 times larger than those of SGR 1935+2154; using this, we have estimated a lower limit on the volumetric rate of FRBs with luminosities $\geq 10^{38}$ erg s^{-1}. We found this to be in good agreement with the rate estimated by Bochenek et al. (2020) using the SGR 1935+2154 radio burst, suggesting that many low-luminosity FRBs could be produced by magnetars. Lastly, we also showed that it is unlikely that most of the repeating FRB progenitors are young millisecond magnetars, and that if we expect millisecond magnetars to be a source of repeating FRBs, we need multiple repeating FRB formation channels.

At a distance of 20 Mpc, FRB 20181030A is one of the closest FRBs discovered to date. In principle, it should be possible to detect prompt multi-wavelength counterparts as predicted by several FRB models (Burke-Spolaor, 2018, Chen et al., 2020, Nicastro et al., 2021, Yi et al., 2014). Therefore, we strongly encourage multi-wavelength follow-up of FRB 20181030A.

Chapter 7

A Search for the Host Galaxy of FRB 20180814A

1 Introduction

Here we report on the search for the host galaxy of FRB 20180814A[1], the first repeating FRB discovered by the CHIME/FRB Collaboration in August 2018 (CHIME/FRB Collaboration et al., 2019a) and the second one ever discovered. Its DM is 189.4 ± 0.4 pc cm^{-3}, which is significantly larger than the expected contribution in this direction from the Milky Way interstellar medium (87 and 108 pc cm^{-3}; Cordes and Lazio, 2002, Yao et al., 2017, respectively). Moreover, CHIME/FRB Collaboration et al. (2019b) did not find any Galactic ionized and/or star-forming region within the 99% confidence localization region of FRB 20180814A that could provide the observed excess DM. Therefore, they asserted that the FRB has an extragalactic origin. However, the large localization region of the FRB reported by CHIME/FRB Collaboration et al. (2019b) prevented the identification of the FRB host.

In this chapter, we combined baseband localizations of four bursts from FRB 20180814A that were detected before 2021 March 9, our cutoff date for this analysis. The combined region enabled localization of the FRB to a sky-region of 3.8 sq. arcmin (2σ), over 500 times

[1] Formerly named FRB 180814.J0422+73, or internally to the CHIME/FRB team, R2.

more precise localization compared to the one reported by CHIME/FRB Collaboration et al. (2019b). Within this new localization region, we identify only one plausible host in archival PanSTARRS-DR1 data, a passive red spiral, PanSTARRS-DR1 J042256.01+733940.7 (Chambers et al., 2016). If this is the host, it would make the FRB the only source thus far to be associated with a spectroscopically identified quiescent host.

The chapter is organized as follows: in Section 2, we describe the basic physical properties of the FRB bursts along with the baseband localization region used in this analysis. Section 2.1 details our search for the host galaxy of FRB 20180814A. From the absence of any other viable host candidate in the FRB localization region other than PanSTARRS-DR1 J042256.01+733940.7 that is described in Section 3.4, we argue that it is a promising host for the FRB. However, we note that the chance coincidence probability of PanSTARRS-DR1 galaxy (Section 3) is not small enough to conclusively argue for it to be the host of FRB 20180814A. But as it is the only host candidate we found in our search, we estimate its notable physical properties in Section 4. For completeness, we also discuss the nature of the FRB host if PanSTARRS-DR1 J042256.01+733940.7 is not the host in Section 6. We then discuss our archival multi-wavelength data search to identify any plausible FRB counterpart in Section 6. Finally, we discuss the implications of the association of the FRB with the PanSTARRS galaxy in Section 7 and conclude in Section 8.

2 Observations

CHIME/FRB reported six repeat bursts of FRB 20180814A between 2018 August 14 and October 28 (CHIME/FRB Collaboration et al., 2019a). Unfortunately, the baseband pipeline did not exist then. Therefore, the raw voltage data were not saved for any of those six bursts. In this chapter, we use four bursts from FRB 20180814A that successfully triggered baseband callback data (Michilli et al., 2020) over a 5 month period between 2019 June 25 and 2019 November 11.

The source's DM is larger than the predicted Galactic contribution in the FRB sight-line (see Table 8.2). After subtracting DM contributions from the Milky Way disk and halo, as shown in Table 8.2, the DM-excess of the FRB is $\sim 50 - 70$ pc cm^{-3}. Using the average Macquart relation (Equation 2 in Macquart et al., 2020), we estimate the redshift of the

FRB to be $\sim 0.05 - 0.07$ assuming negligible host DM contribution. This suggests close proximity of the FRB host ($\lesssim$ 330 Mpc). As of 2022 July 27, CHIME/FRB has detected 22 bursts from the FRB[2] and some of them have saved baseband data that can be used to get a more precise localization.

There are five bursts of FRB 20180814A that have baseband data saved by the CHIME/FRB baseband system (bursts with reported $\mathrm{DM_{bb}}$ values in Table 8.1), and were detected before our cut-off date of 2021 March 9. However, the first FRB (see Table 8.1) cannot be localized despite the fact that we saved its baseband data due to some unidentified pipeline-related issues. Therefore, in this chapter, we consider events 2-5 in Table 8.1 that have saved baseband data.

The CHIME/FRB baseband system stores $\sim$ 100 ms of channelized raw voltage data around signals of interest (CHIME/FRB Collaboration et al., 2018). Michilli et al. (2020) have developed a pipeline to automatically process such baseband data and localize a burst on the sky with a precision of $\sim \frac{8}{\mathrm{S/N}}$ arcmin, which is described in Chapter 3. We used the baseband data of four detected bursts from FRB 20180814A to estimate the localization region of the FRB. The dedispersed baseband data waterfall plots and major characteristics of all the five FRB bursts with saved baseband data are shown in Figure 7.1 and Table 8.1, respectively. As the reported baseband localization uncertainties are statistical in nature (Michilli et al., 2020), we combined the localization regions of the four FRB bursts using a weighted average with inverse variance weights and localized the FRB to a sky area of $\approx$ 3.8 arcmin^2 (2σ localization region; see Table 8.2). Next, we use the baseband localization region of FRB 20180814A to search for a potential host galaxy.

3 Host galaxy search

3.1 Prospects of a Milky Way origin of the FRB

First, we argue below that the FRB is unlikely to be Galactic in origin. As noted by CHIME/FRB Collaboration et al. (2019c), there is no catalogued Galactic ionized region,

[2] For a complete list, check https://www.chime-frb.ca/repeaters/FRB20180814A (visited on 29/06/2022).

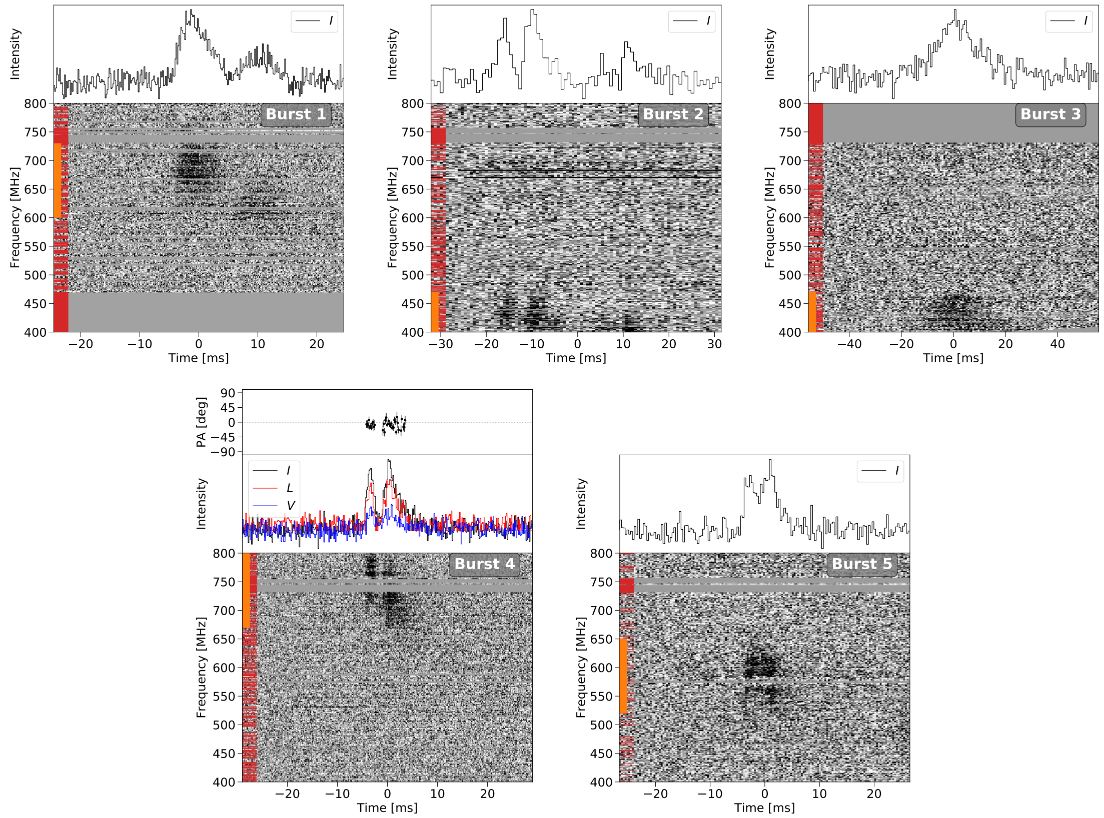

Figure 7.1: Frequency versus time (“waterfall") plots of the five dedispersed bursts detected from FRB 20180814A with saved baseband data. See Table 8.1 for their major burst properties. The waterfall plots are binned to have temporal resolution 0.655 ms and spectral resolution 0.391 MHz. Dark grey lines represent bad frequency channels that were flagged in this analysis. In addition, we show linear polarization (red) and circular polarization (blue) intensity profiles (peak normalized) as well as polarization angle (PA) curves for Burst 4 which shows significant RM detection. Signal is added over the spectral limits of the burst, denoted by orange lines along the frequency axis, to obtain the burst profile. Masked frequency channels are indicated by red lines along the vertical axis. Each panel is labeled with the corresponding burst number from Table 8.1. Figure from Mckinven et al. (submitted to ApJ).

Table 7.1: Properties of the bursts from FRB 20180814A.

Burst number	Arrival Time[a] (MJD)	S/N[b]	$\mathrm{DM_{struct}}$[c] (pc $\mathrm{cm^{-3}}$)	$\mathrm{RM_{QU}}$[d] (rad $\mathrm{m^{-2}}$)
1	58645.78660	43.8	190.13(84)	–
2	58659.73874	22.4	188.743(70)	–
3	58660.77631	26.8	191.62(73)	–
4	58785.40415	46.3	189.02(35)	+699.8(1.0)
5	58798.37171	33.0	188.552(35)	–

[a] All burst times of arrival are topocentric. The arrival times of the bursts are estimated by the baseband pipeline (Michilli et al., 2020).
[b] The reported signal-to-noise (S/N) ratios are band-averaged as estimated by the baseband pipeline.
[c] S/N-optimized DM for the bursts detected in the baseband data.
[d] Rotation measure (RM) is determined by Mckinven et. al (submitted to ApJ).

satellite galaxy, or globular cluster in the direction of the FRB that could contribute to the FRB DM. In the absence of any star-forming and ionizing regions, the source of Galactic dispersion measure is likely coming from the Warm Ionized Medium. Ocker et al. (2020) estimated the mean DM through the Milky Way's Warm Ionized Medium at large distances from the Galactic plane ($z > 2$ kpc), $\overline{\mathrm{DM}\sin|\mathrm{b}|}$ = 23.0 $\pm$ 2.5 pc cm^{-3}. At the FRB's Galactic latitude ($\mathrm{b} = 16°$), the implied mean Galactic DM is $= 82.1 \pm 8.7$ pc cm^{-3}. This is in agreement with the Galactic DM prediction of the NE2001 model (Cordes and Lazio, 2002), 87 pc cm^{-3}, and is considerably smaller than that of the YMW16 model (108 pc cm^{-3}; Yao et al., 2017). The Milky Way halo DM contribution, $\mathrm{DM_{Halo}}$, on the other hand, is poorly constrained. Recently, Kirsten et al. (2021) estimated the Milky Way halo contribution in the direction of FRB 20200120E to be $\lesssim$ 40 pc cm^{-3}. Moreover, two widely used halo DM models predict $\mathrm{DM_{Halo}} \approx$ 50-80 pc cm^{-3} (Prochaska and Zheng, 2019) and $\mathrm{DM_{Halo}} \approx$ 30 pc cm^{-3} (Yamasaki and Totani, 2020), hence, also classify FRB as extragalactic. Finally, as discussed in Chapter 5, if the source is indeed Galactic, then it must be an exotic neutron star wandering at the outskirts of the Milky Way halo. Therefore, it is more plausible that the FRB has an extragalactic origin. In next section, we estimate the maximum redshift of the FRB, which is important in identifying plausible sources.

Table 7.2: Major Observables of FRB 20180814A.

Parameter	**Value**
R.A.(J2000)[a]	$4^{\rm h}22^{\rm m}43^{\rm s}.4 \pm 13^{\rm s}.2$
Dec. (J2000)[a]	$73°39'55'' \pm 20''$
l, b	136.°46, +16.°64
DM[b]	189.4 ± 0.4 pc cm^{-3}
$\mathrm{DM}^c_{\mathrm{MW,NE2001}}$	87 pc cm^{-3}
$\mathrm{DM}^c_{\mathrm{MW,YMW16}}$	108 pc cm^{-3}
$\mathrm{DM}^c_{\mathrm{MW,WIM}}$	82.1 ± 8.7 pc cm^{-3}
$\mathrm{DM}^d_{\mathrm{MW,halo}}$	30 pc cm^{-3}
Max. distance[e]	$\lesssim 415$ Mpc

[a] Baseband localization with 1σ error.
[b] From CHIME/FRB Collaboration et al. (2019c).
[c] Maximum DM model prediction along this line-of-sight for the NE2001 (Cordes and Lazio, 2002) and YMW16 (Yao et al., 2017) Galactic electron density distribution models. The $\mathrm{DM}_{\mathrm{MW,WIM}}$ is estimated using the relation from Ocker et al. (2020): DM = 23.5 ± 2.5 pc cm^{-3}/sin(|b|) = 82.1 ± 8.7 pc cm^{-3}.
[d] Fiducial Milky Way halo prediction from the Yamasaki and Totani (2020) Milky Way Halo model.
[e] Corresponds to the maximum redshift of 0.091 (see Section 3.2).

3.2 Maximum redshift of the FRB

We estimated the maximum redshift of FRB 20180814A using a Bayesian formalism described in Chapter 4. We summarized individual DM components and their respective priors in Table 7.3. The rationale of our prior choices is described in Chapter 4. We note that due to the absence of any ionized region and/or star-forming region in the vicinity of the FRB localization region, the main contributor to the Milky Way disk DM is the Warm Ionized Medium. Therefore, in our MCMC simulation, we used a Gaussian prior with a mean = 82.1 pc cm^{-3}, the minimum of the three Galactic DM estimates, and a standard deviation (σ) = 8.7 pc cm^{-3} (see Table 8.2).

For the MCMC sampling, we used the `emcee` package (Foreman-Mackey et al., 2013), which implements an affine-invariant sampling algorithm proposed by Goodman and Weare (2010). We use 256 walkers of 20,000 samples after discarding 1000 burn-in samples from

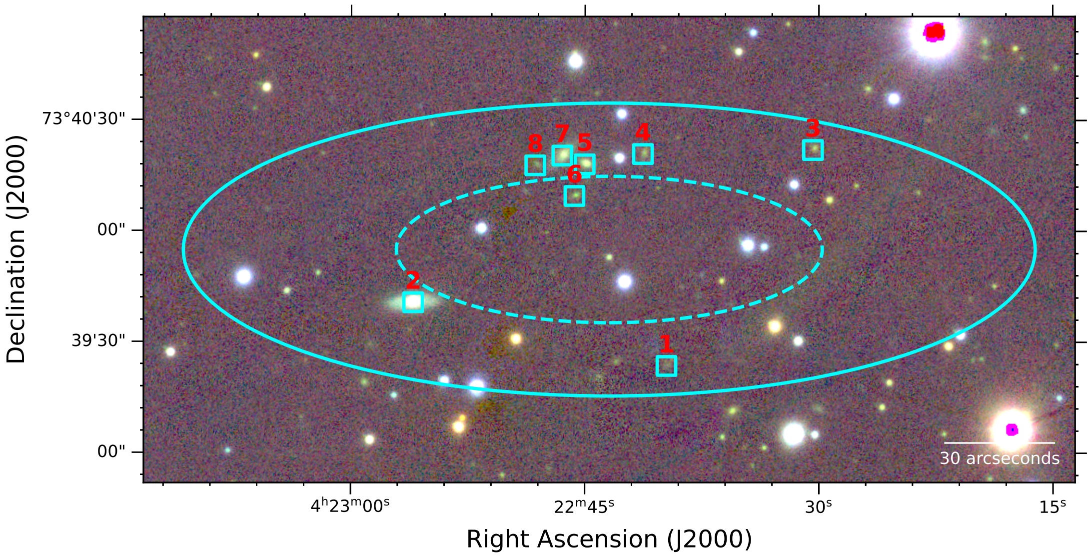

Figure 7.2: PanSTARRS RGB-image of the FRB 20180814A 1σ (dotted cyan ellipse) and 2σ localization region (solid cyan ellipse). Cyan boxes show the locations of 8 host galaxy candidates within the localization region (see Table 8.3) identified in the PanSTARRS data; Source 2 is PanSTARRS-DR1 J042256.01+733940.7, the only host candidate that satisfies the maximum redshift constraint derived in Section 3.2.

each walker, and thinned the samples by a factor of 100. To assess the convergence of the samplings, we noted that the mean proposal acceptance fraction = 38%, and the chain auto-correlation length ≈ 1.13. Both of the estimates are within the acceptable range (Gelman et al., 2013). Lastly, we also estimated convergence criterion for the redshift parameter $\hat{R} \approx 1.02$ which implies good convergence of the MCMC (Gelman et al., 2013).

From the MCMC analysis, we marginalized the redshift posterior over all other priors and calculated a one-sided 95% Bayesian credible upper limit = $z_{\rm max} = 0.091$. This is the maximum redshift of FRB 20180814A used in our analysis. Next, we show that this is likely a conservative upper limit.

The FRB intersects the halos of several galaxy groups as noted by Li et al. (2019). These authors estimated the DM contribution of the intersecting galaxy groups using a Navarro–Frenk–White baryon density profile and galaxy group masses and concentration indexes from Lim et al. (2017). They estimated the maximum redshift of the FRB to be ~ 0.02. However if we instead use the halo density profile from Maller and Bullock (2004), that provided the smallest DM contribution of the M81 halo in Chapter 4, we estimate the DM contribution of the galaxy groups $\approx$ 20 pc cm^{-3}. Including this contribution in the MCMC analysis discussed in Section 3.2, we get $z_{max} \approx 0.07$. Therefore, it is unlikely that the FRB host lies beyond z_{max} = 0.091. In next section, we use this maximum redshift value to identify plausible galaxy candidates.

Table 7.3: Parameters used in the MCMC analysis described in Section 3.2.

Parameter	**Symbol**	**Units**	**Prior**[a]
Host galaxy redshift	z	–	U(10^{-4},1)
Host galaxy DM	DM_{host}	pc cm^{-3}	LN(96.4,0.9)[b]
Milky way DM	DM_{MW}	pc cm^{-3}	N(82.1, 8.7)
Milky way halo DM	$DM_{MW,halo}$	pc cm^{-3}	N(40,33.33%$\times$40)
IGM DM	DM_{IGM}	pc cm^{-3}	Equation 4 from Macquart et al. (2020)

[a]

Here 'U(lower limit, upper limit)' is a uniform distribution, 'LN(mean, standard deviation)' is a lognormal distribution, and 'N(mean, standard deviation)' is a normal distribution.
[b] It is the repeating FRB host prior (based on FRB 20180916A-like hosts) at z = 0.1 estimated by Zhang et al..

3.3 Extragalactic host of the FRB

We searched the PanSTARRS1 (PS1) catalogue (Chambers et al., 2016) for host candidates within the 2σ localization region of the FRB, and found 8 sources which are listed in Table 8.3. In Figure 8.2, we plotted the FRB localization region over a PanSTARRS RGB image made using PanSTARRS's g-band (B:blue), r-band (G:green), and z-band (R:red) data.

At z_{max} = 0.091, an FRB 20121102-like host, the faintest FRB host known to date at z=0.19273(8) with estimated $M_r = -17$ AB mag Tendulkar et al. (2017), would have an apparent r-band magnitude of 21.45 AB mag (uncorrected for Galactic extinction). If such a galaxy were present within the FRB localization region, it would have been detected in PanSTARRS DR1 data, which are sufficiently sensitive to detect point sources of 5σ r-band depth $\lesssim 22$. Note that out of 8 candidate galaxies, only one source, Source 8, does not satisfy this criterion (rKmag $>$ 21.45 AB mag; See Table 8.3), but its photometric redshift from the PanSTARRS 3π Data Release 1 photometric redshift catalogue is 0.5 ± 0.1, which is greater than z_{max} by 4σ. We estimate the spectroscopic redshift of other seven sources

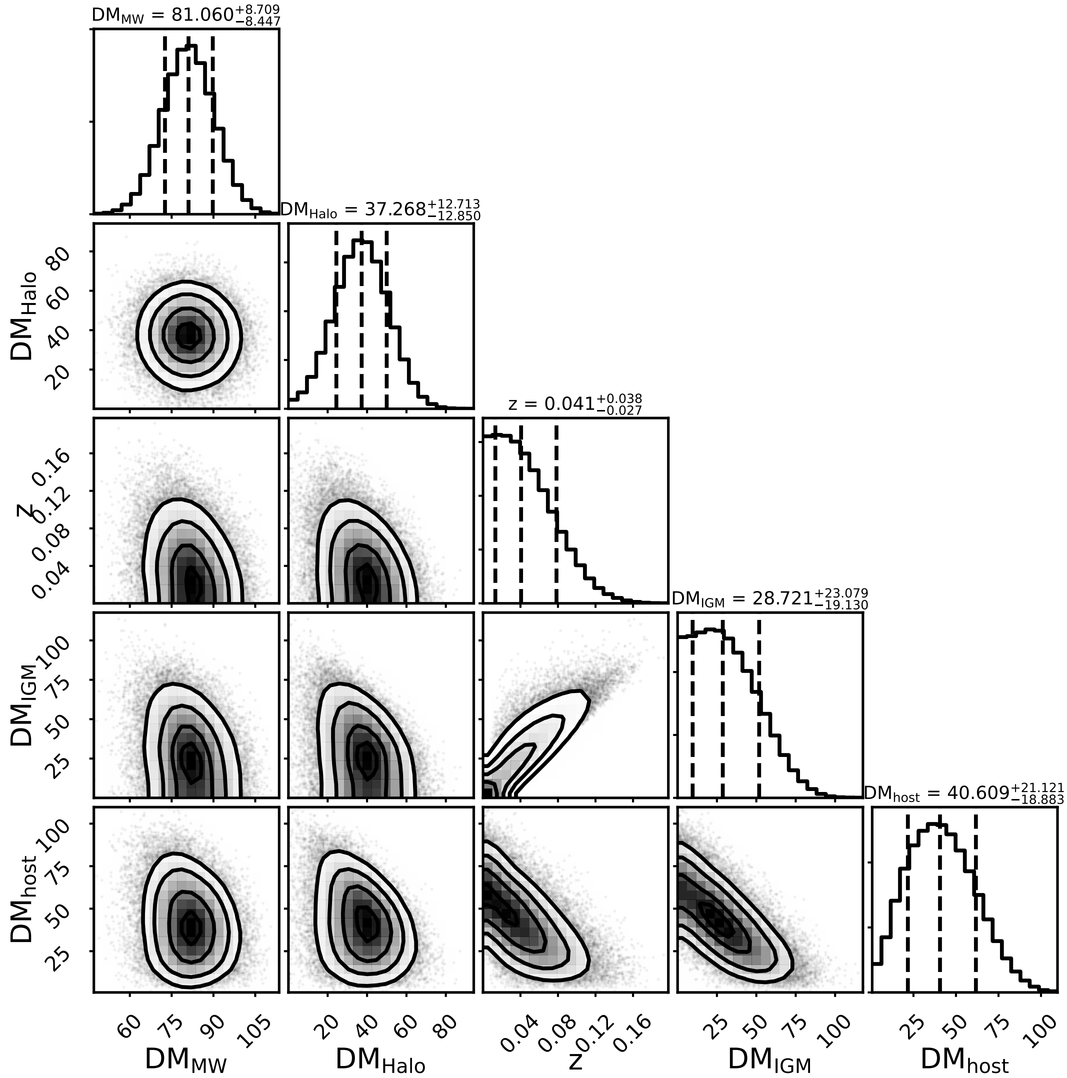

Figure 7.3: The corner plot of the Markov-Chain Monte Carlo (MCMC) analysis to constrain the maximum redshift of FRB 20180814A. The marginalized distribution for each DM component is shown along the diagonal of the corner plot. All DM units are in pc cm^{-3}. Using the marginalized posterior of the host galaxy redshift, we estimated a one-sided 95% Bayesian credible upper limit = $z_{\max}$ = 0.091.

using GTC multi-object spectroscopy observations.

3.4 GTC observations and analysis

In this Section, we describe the GTC multi-object spectroscopy observations that we use to estimate redshifts of the seven plausible host candidates. This is required because most galaxies in the field did not have a spectroscopic redshift reported in the literature. As we will show later, only Source 2 satisfies the z_{max} constraint, which makes it the only plausible host of the FRB among seven sources.

Observations of seven galaxies identified within the FRB 20180814A 2σ localization region were performed with the the Optical System for Imaging and low-intermediate Resolution Integrated Spectroscopy (OSIRIS[3]) at the GTC. The OSIRIS detector consists of two CCDs and provides a field of view (FoV) of $7.8' \times 7.8'$ with a pixel scale of $0.254''$. The observations were performed on February 12, 2021 under clear sky conditions. The log of observations is given in Table 7.4.

To obtain the spectra of all the host galaxy candidates simultaneously, we utilized the OSIRIS multi-object spectroscopy (MOS) mode. The mask was designed with the OSIRIS Mask Designer Tool (Gómez-Velarde et al., 2016, González-Serrano et al., 2004), a set of five fiducial stars and catalogue coordinates of the host galaxy candidates. The observations were performed with the R500B grism covering the spectral range 3600−7200 Å. For the target galaxies we used slitlets with length varying between 4.5”and 10”and a width of 1.5”.

The spectra were reduced using the GTCMOS pipeline (Gómez-González et al., 2016) and standard IRAF routines (Tody, 1986, 1993). All spectra were bias-subtracted, and flat-fielded using the set of corresponding images taken during the same observing nights. For flux calibration we used spectrophotometric standards Feige 110, GD153 and Ross 640 (Bohlin et al., 1995, Oke, 1974, 1990) observed during the same night as the targets. A set of arc-lamp spectra of Ne, Hg and Ar was used for wavelength calibration. The rms errors of the resulting solutions were <2 Å for the R500B grating.

Table 8.3 reports the redshift measured for the identified PanSTARRS galaxies. As only

[3] http://www.gtc.iac.es/instruments/osiris/

Source 2 has a spectroscopic redshift $< z_{max}$ = 0.091, this makes Source 2 the only viable FRB host candidate among all the identified galaxies with $m_r \leq 21.45$ AB mag.

Table 7.4: Log of the GTC/OSIRIS long-slit and MOS spectroscopic observations.

Program	Date	Mode	Grism	Position Angle	Exposure Time	Seeing	Airmass	Night
GTCMULTIPLE3B-20BMEX	12/02/2021	MOS	R500B	0	3 × 1200 s	0.7″	1.47-1.52	Dark

Table 7.5: Galaxies identified within the FRB localization region.

Number	**R.A.** J2000	**Dec.** J2000	**rKmag(PanSTARRS)**[a] AB mag.	**Identified lines**	$\mathbf{z_{spec}}$
1	$4^h22^m39.^s77$	4°39′23.″6	21.28	[OII], [OIII] doublet	0.412(1)
2[b]	$4^h22^m56.^s01$	4°39′40.″7	17.15	Ca doublet, G-band, Mg, Na, Hβ, Hδ	0.06835(1)
3	$4^h22^m30.^s38$	73°40′22.″0	20.75	Ca doublet, G-band, Mg	0.409(1)
4	$4^h22^m41.^s29$	73°40′20.″9	20.65	Ca doublet, G-band, Mg, Na	0.376(1)
5	$4^h22^m45.^s02$	73°40′18.″1	19.26	Ca doublet, G-band, Mg, Na	0.235(1)
6	$4^h22^m45.^s68$	73°40′9.″5	21.01	Ca doublet, G-band, Mg	0.410(1)
7	$4^h22^m46.^s46$	73°40′20.″5	18.75	[OII], Ca doublet, G-band, Mg, Na	0.238(1)
8	$4^h22^m48.^s19$	73°40′17.″8	21.81	–	0.5(1)[c]

[a] Kron r-band magnitudes estimated by the PanSTARRS DR1 photometry pipeline (Tonry et al.). [b] Source 2 is PanSTARRS-DR1 J042256.01+733940.7, and at a spectroscopic redshift = 0.06835, it is the only galaxy in our list with the redshift $< z_{max} = 0.091$.
[c] The stated value is the photometric redshift. As the rKmag of Source 8 is greater than our r-band magnitude limit, we did not estimate its spectroscopic redshift.

3.5 Chance coincidence probability of Source 2

We now estimate the chance coincidence probability (P_{cc}) of finding Source 2-like galaxy within the FRB's 2σ localization region. Briefly, we assume a Poisson distribution of galaxies across the sky and calculate the probability of finding one or more galaxies by chance with $m_r \leq 17.15$ AB mag, the r-band Kron magnitude of Source 2 without correcting for the Galactic extinction, within the FRB 2σ localization region (3.8 arcmin^2). Using the areal number density of Source 2-like or brighter galaxies, $n(m_r \leq 17.15)$ = 0.02 arcmin^{-2} from Driver et al. (2016), we estimate $P_{cc} = 7.6 \times 10^{-2}$. However, as the presence of

Source 2 is inferred post-hoc, the look-elsewhere effect corrected P_{cc} would be > 0.1 after accounting for all CHIME FRBs using the method described in Chapter 4. Therefore, using the P_{cc} argument alone, we cannot conclusively establish Source 2 as the host of FRB 20180814A. However, it is still the most plausible host within the FRB localization region as discussed in Section 3.4.

4 Physical properties of Source 2

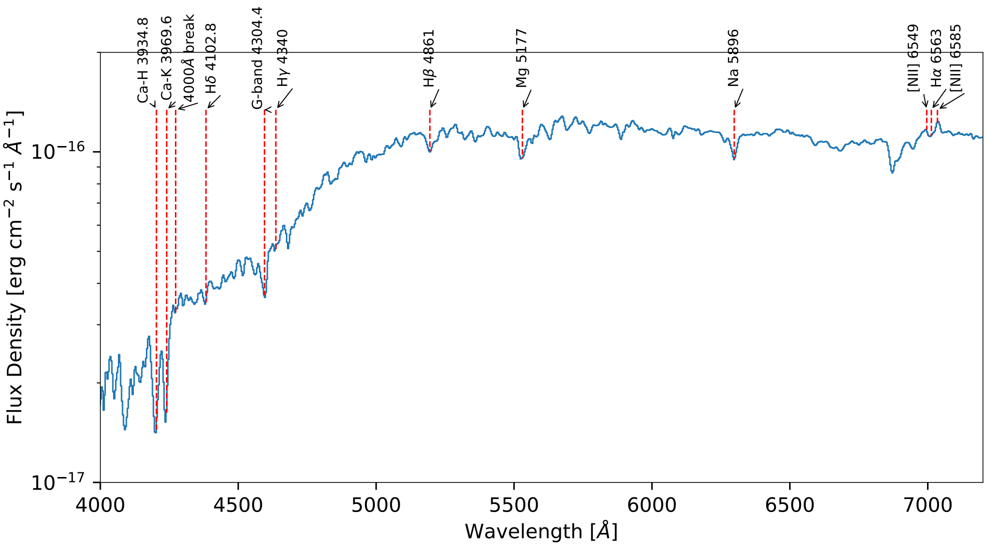

Figure 7.4: GTC optical spectrum of Source 2.

As Source 2 is the only plausible galaxy we found within the FRB localization region, we discuss its major physical properties in this section. First, based on its rest-frame (g-r) colour = 0.74 AB mag and absolute r-band magnitude = -20.75 AB mag, Source 2 can be classified as a red sequence (early-type) galaxy using the colour–magnitude relation identified by Bell et al.. Additionally, based on the WISE colour-colour classification (Wright et al., 2010), Source 2's WISE colour, i.e., W1 (3.4 μm) - W2 (4.6 μm) = 0.13 ± 0.04 and W2 (4.6 μm) - W3 (12 μm) = 2.45 ± 0.12, classifies it to be a spiral galaxy with no actively accreting massive black hole in its centre. Based on these classifications, Source 2 is likely a passive red spiral, a very old spiral galaxy that has already used up its reserves of gas, and hence, stopped forming new stars for $\gtrsim 1$ Gyr (Masters et al.).

We show the calibrated GTC optical spectrum of Source 2 in Figure 7.4 (see Section 3.4 for data reduction steps). In the spectrum, we clearly see many Balmer and metal absorption lines, including Calcium H and K lines (found at 3934A and 3969A), the G-band (λ4304), Mg I (λ5175), and Na I (λ5894). These absorption features are indicative of an evolved stellar population. Additionally, the spectrum also lacks prominent emission lines, except weak [NII] lines, which suggests that the galaxy lacks young stars and gas. Hence, spectroscopically as well, Source 2 is likely a passive galaxy.

Finally, we estimate the D4000 index which is the ratio of the flux in the red continuum $(4000-4100)$ to that in the blue continuum $(3850-3950)$, both in the rest frame, and found it to be ≈ 1.7. As it is greater than the passive and star-forming galaxy separation cutoff of 1.45 (Balogh et al.), this too corroborates the conclusion that Source 2 is an early-type spiral galaxy that is not forming stars and is currently in the quenched/passive phase.

Now we summarize major physical properties of Source 2. To estimate its stellar mass, stellar metallicity, mass-weighted stellar population age, and extinction, we use a Bayesian inference spectral energy distribution (SED) fitting code, `Prospector` (Johnson et al., 2019, Leja et al., 2017). Appendix 5 describes the SED fitting analysis in detail. Briefly, we use 11 broadband optical, near-, and mid-IR filters fluxes (see Table 7.7) of Source 2 and fit a nine free-parameter delayed-τ model (Carnall et al., 2019, Simha et al., 2014). The model and assumed priors of the free-parameters are discussed in Appendix 5. The best-fit spectral energy distribution (SED) profile of Source 2 is shown in Figure 7.5. `Prospector` also supports for Markov Chain Monte Carlo (MCMC) posterior sampling to calculate uncertainty in the best-fit values of the model parameters, which are stated in Table 8.4. Although the absence of the Hα line prevents us to estimate its recent star formation rate, we still estimate a 95% upper-limit on the total star formation rate of Source 2 via `Prospector` and found it to be $< 0.32 \mathrm{M}_{\odot}\ \mathrm{yr}^{-1}$.

5 Stellar population synthesis using `Prospector`

We estimated major physical properties of PanSTARRS-DR1 J042256.01+733940.7 aka Source 2 at z = 0.06835 using a python-based Bayesian inference code, `Prospector`

Table 7.6: Notable properties of Source 2.

Property	**Value**	**Reference**
log[SFR] ($M_\odot$ yr^{-1})	$< -0.5^a$	this work
Stellar Metallicity ($\log(Z/Z_\odot)$)^a	$-0.61^{+0.43}_{-0.53}$	this work
$(u\text{-}r)_0$	$2.57^{+0.17}_{-0.20}$	this work
log[stellar mass] ($M_\odot$)	$10.78^{+0.12}_{-0.18}$	this work
Effective radius ($R_{\rm eff}$; kpc)	3.2	this work
Mass-weighted age (Gyr)^a	$7.6^{3.3}_{-3.4}$	this work
A_v(young) (mag)	$0.43^{+0.33}_{-0.20}$	this work
A_v(old) (mag)	$0.45^{+0.32}_{-0.18}$	this work
Absolute r-band mag. (AB)	-20.78 ± 0.02	–

[a] Estimated using Prospector; See Section 5.

(Johnson et al., 2019, Leja et al., 2017). It computes galaxy attributes using stellar population synthesis models provided in the Flexible Stellar Populations Synthesis (FSPS) stellar populations code (Conroy et al., 2009). We used the MCMC framework (via emcee) of Prospector to fit the observed spectral energy distributions (SEDs) and to compute posterior distribution for all free-parameters. In this paper, we use Prospector to estimate the stellar mass, star-formation rate (95% confidence upper limit), stellar metallicity, and mass-weighted stellar population age of Source 2, and dust attenuation due to birth cloud and diffuse dust screens. We used 11 broadband filters which are listed in Table 7.7.

All flux densities are estimated after correcting for the Milky Way extinction. We fit a delayed-τ star formation history model (Carnall et al., 2019, Simha et al., 2014) that has nine free parameters described in Table 7.8. In this model, the star-formation history is proportional to $\mathrm{t}\times\exp(-\mathrm{t}/\tau)$, where t is the time since the formation epoch of the galaxy, and τ is the characteristic decay time of our star-formation history. Additionally, we enabled the dust emission model by Draine and Li (2007) in the FSPS framework which has three free parameters which regulate the shape of the IR SED: duste($U_{\rm min}$), duste($Q_{\rm PAH}$), and duste(γ). Specifically, duste($U_{\rm min}$) represents the minimum starlight intensity to which the dust mass is exposed, duste(γ) represents the fraction of dust mass which is exposed to this minimum starlight intensity, and duste($Q_{\rm PAH}$) quantifies the fraction of total dust mass that is in polycyclic aromatic hydrocarbons (PAHs).

Table 7.7: 17 broadband filters used to model the SED of Source 2.

Instrument	Filter	Effective Wavelength Å	Flux density[a,b] maggies
PanSTARRS	g	4810	9.98×10^{-8}
	r	6170	1.98×10^{-7}
	i	7520	2.88×10^{-7}
	z	8660	3.14×10^{-7}
	y	9620	3.28×10^{-7}
2MASS	J	12319	4.79×10^{-7}
	H	16420	5.98×10^{-7}
	Ks	21567	5.52×10^{-7}
WISE	W1	33461	2.77×10^{-7}
	W2	45952	1.73×10^{-7}
	W3	115526	2.74×10^{-7}

[a] Note that 1 maggie = Flux density (in Jansky)/3631. Fluxes at $\lambda < 100000$ Å are corrected for Galactic extinction according to the prescription of Schlafly and Finkbeiner (2011).
[b] All broadband fluxes are assigned a 20% fractional uncertainty, which is larger than the catalogued error.

Finally, to account for dust attenuation, we use the two-component (Charlot and Fall, 2000) dust attenuation model, which postulates separate birth-cloud (dust1) and diffuse dust (dust2) screens. In order to estimate 'dust1' parameter, we used an in-built prospector function `models.transforms.dustratio_to_dust1`. Finally, all ten parameters are given standard `Prospector` priors (see Table 7.8).

Under this approach, we derived a metallicity fraction, $\log(Z/Z_{\odot}) = -0.61^{+43}_{-0.18}$, and the present-day stellar mass of the galaxy, $\log(M/M_{\odot}) = 10.78^{+0.12}_{-0.18}$. To estimate the best-fitted mass-weighted stellar population age value, we used an in-built prospector function `parametric_mwa` and found it to be $7.6^{3.3}_{-3.4}$ Gyr. We estimated separately internal dust extinction due to young stars ($A_{V,young}$) and old stars ($A_{V,old}$) to be $0.43^0.33\_0.2$ and $0.45^0.32\_0.18$, respectively. Finally, we used the SED templates produced via MCMC simulation and estimate the rest frame u-r colour to be $2.57^{+0.17}_{-0.20}$. The major physical properties

Table 7.8: Free parameters and their associated priors for the `Prospector` 'delayed-τ' model.

Parameter	Description	Prior
$\log(M/M_\odot)$	total stellar mass formed	log-uniform: min=8, max=12
$\log(Z/Z_\odot)$	stellar metallicity	top-hat: min=-2, max=0.20
dust2	diffuse V-band dust optical depth	top-hat: min=0.0, max=3.0
dust-ratio	ratio of additional optical depth in the direction of young stars to diffuse optical depth in all stars	clipped-normal: mean=1.0, sigma=0.3, min=0.0, max=2.0
t_{age} [Gyrs]	stellar population age of Source 2	top-hat: min=0.001, max=13.6
τ [Gyrs]	e-folding time of the SFH	log-uniform: min=0.1, max=30
duste(U_{min})	From (Draine and Li, 2007) dust attenuation model	top-hat: min=0.1, max=25.0
duste(Q_{PAH})	From (Draine and Li, 2007) dust attenuation model	top-hat: min=0.5, max=7.0
duste(γ)	From (Draine and Li, 2007) dust attenuation model	log-uniform: min=0.001, max=0.15

of Source 2 are provided in Table 8.4. Note that the quoted uncertainties in all cases are 1σ values.

6 What if Source 2 is not the host?

It is also possible that Source 2 is not the host of the FRB. In that scenario, we expect the host of the FRB to be fainter than the faintest FRB host known to date (FRB 20121102A host; $M_r < -17$ AB mag). That would make the host of FRB 20180814A the faintest one known to date. We note that long gamma ray bursts (LGRBs) and Hydrogen-poor superluminous supernovae (SLSNe), which are proposed to host FRB progenitors (Metzger et al., 2017) via “prompt" formation channels, are preferentially found in blue star-forming dwarf galaxies (Fruchter et al., 2006). Note that FRB progenitors formed via “delayed" formation channels, like short gamma ray bursts and accretion induced collapses of white dwarfs, are expected to be found in massive galaxies (Artale et al.). As the ISM of blue star-forming dwarf galaxies are rich and dynamic, these galaxies are expected to contribute considerably to the FRB DM (Li et al., 2019). For instance, Tendulkar et al. (2017) estimated that the DM contribution of the FRB 20121102A host, a dwarf irregular star-forming galaxy, is $\sim 60 - 220$ pc cm^{-3}. If the FRB 20180814A source is located in a similar environment, the FRB host galaxy would be very nearby ($<$ 100 Mpc) and hence, intrinsically very faint ($M_r < -14$ AB mag). Moreover, if the contribution from the intersecting galaxy groups (see Section 3.2) is significant as claimed by Connor and Ravi, the DM contribution of the host would be very small, and the FRB host is unlikely to be similar to those of the known sample of SLSNe and LGRBs as noted by Li and Zhang (2020).

7 Search for a multi-wavelength counterpart to FRB 20180814A

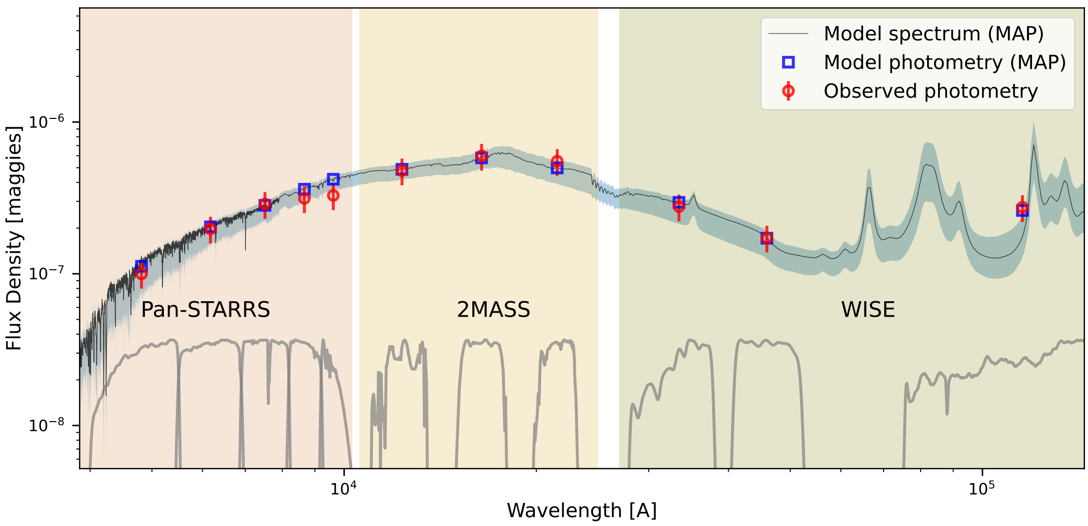

Figure 7.5: SED of Source 2. The flux densities of Source 2 in different optical and infrared bands are plotted along with the best-fit `Prospector` model spectrum. To assess the quality of the `Prospector` model, the modelled (blue square) and observed photometry (red circle) data are also shown. For more information, see Section 5

.

Persistent radio source search

We searched archival radio data of the following surveys to check for the presence of a persistent radio source within the FRB uncertainty region: the NRAO VLA Sky Survey

(NVSS; Condon et al., 1998), the VLA Sky Survey (Lacy et al., 2016, VLASS;), the Westerbork Northern Sky Survey (WENSS; Rengelink et al., 1997), and the Tata Institute of Fundamental Research Giant Metrewave Radio Telescope Sky Survey (TGSS) Alternative Data Release (Intema et al., 2017), and we found no radio source within the 2σ baseband localization of the FRB. From the non-detection of a persistent compact radio source in the VLASS 2.1 data (which has angular resolution of $2.5''$ – the best among all the radio surveys considered here), we estimate a 3σ upper limit of 480 μJy at 3 GHz which at $\approx$ 318 Mpc, the luminosity distance of Source 2, implies an isotropic spectral luminosity $\approx 4.6 \times 10^{27}$ erg/s/Hz, at least four and six times fainter than that the persistent radio source detected spatially coincident to FRB 20121102A and FRB 20190520A, respectively (Chatterjee et al., 2017, Niu et al., 2022).

8 Discussion

8.1 Milky Way Halo DM contribution

We can estimate an upper limit on the DM contribution of the Milky Way halo in the direction of FRB 20180814A using the Bayesian formalism discussed in Section 3.2 under the presumption that Source 2 is the host of the FRB. After fixing the redshift of the FRB to that of Source 2, we estimate the $\mathrm{DM}_{\mathrm{MW,halo}}$ 90% Bayesian credible interval to be (16 pc cm^{-3}, 54 pc cm^{-3}). This and similar constraints derived using low-DM FRBs discussed in Chapters 4 and 5, suggest that the Milky Way halo DM contribution could be considerably smaller than what several Milky Way halo DM models predict (Keating and Pen, 2020). We note that as the Milky Way halo is possibly clumpy (Kaaret et al., 2020), therefore, considerable spatial variation in $\mathrm{DM}_{\mathrm{Halo}}$ may still be possible. With more such localized low-DM FRBs, the structure and dynamics of the MW halo can eventually be modelled with greater precision.

8.2 Implications for different progenitor models

The sample of hosts of localized FRBs exhibits remarkable diversity. With each new addition, the distinction between repeating and non-repeating FRB host populations appears to be becoming less clear. If Source 2 is indeed the FRB host, it would be the first one to date to be associated to a massive passive and red spiral galaxy. Such galaxies offer an ideal environment to form proposed “delayed"-channel FRB progenitors, such as binary neutron star mergers and accretion-induced white dwarf collapses (Giacomazzo and Perna, 2013, Ruiter et al.).

Additionally, one of FRB 20180814A bursts (Burst 4; See Table 8.1) is found to have a high rotation measure = 699.8 ± 1.0 rad m^{-2} with estimated extragalactic contribution to the RM $= 745 \pm 18$ rad m^{-2} (Mckinven et al., submitted to ApJ). This excess is likely contributed by the FRB host and/or its local environment as neither the IGM nor the outskirts of galaxy groups is expected to have sufficiently high magnetic field (> 10 μG) to produce the observed Faraday rotation (Govoni and Feretti). Now, if Source 2 is the FRB host, the MCMC analysis discussed in Section 8.1 gives median $\mathrm{DM_{host}} \approx 20$ pc cm^{-3} (after fixing the FRB redshift = 0.06835; see Figure 8.3). Using this host DM contribution and the observed extragalactic RM, we estimate the average line-of-sight component of the magnetic field $< \mathrm{B}_{||} >$ in the path to the FRB source through the host ISM to be RM/(0.812 DM) $\approx 46\mu$G. This $< \mathrm{B}_{||} >$ is larger than the magnetic field estimated in the ISM around the Sun (1-5 μG; Wielebinski and Beck) and in the Galactic centre region (20-40 μG; Wielebinski and Beck). Therefore, the observed extragalactic RM is likely contributed by the circumburst medium.

Piro and Gaensler showed that if the extragalactic rotation measure is provided by the circumburst medium dominated by magnetized stellar winds, for example, like what we see in pulsar wind nebula, we expect a much larger dispersion measure contribution (> 500 pc cm^{-3}), which is not permitted in the case of FRB 20180814A (DM-excess < 100 pc cm^{-3}). On the other hand, if the FRB source is young and the observed extragalactic rotation measure is provided by a supernova remnant or post-merger ejecta which is expanding in a constant density host ISM, then the ambient electron number density must be small ($\lesssim 0.1$ pc cm^{-3}). Such a low-density ambient environment is expected to be around progenitors formed via “delayed"-formation channel models, such as binary neutron star mergers and accretion-induced collapse of white dwarfs (Liu, Moriya, Piro and Kulkarni). A more precise localization, followed by multi-wavelength studies of the local environment, will shed light on the origin of the large extragalactic RM.

8.3 Comparison with the FRB 20200120E source

If Source 2 is the host of FRB 20180814A, it is more plausible that the progenitor of the FRB is formed via “delayed" channel (see Section 4). This suggests that the FRB source might be similar to that of FRB 20200120E (see Chapter 4), which is found to be located in a globular cluster of the Messier 81 galaxy at 3.6 Mpc (Kirsten et al., 2021). However, the brightest burst from the repeating FRB 20180814A in the first CHIME/FRB catalogue (The CHIME/FRB Collaboration et al., 2021), FRB 20181028A has fluence $\approx$ 23 Jy ms, is over seven times brighter than that of the published CHIME FRB bursts of FRB 20200120E (see Chapter 4). After correcting for different luminosity distances, FRB 20181028A has isotropic energy $\sim 10^{39}$ ergs, close to the median isotropic burst energy seen from other FRBs (Petroff et al., 2019) and around 56,000 times more energetic than that of FRB 20200120E bursts. If both FRBs have the same formation channel, it suggests that “delayed"-formation channels can produce FRB sources with wide range of energies.

9 Summary & conclusions

We have reported on the search for the host of the repeating FRB 20180814A discovered by CHIME/FRB Collaboration et al. (2019c). From our search, we found PanSTARRS-DR1 J042256.01+733940.7 aka Source 2, a nearby (z= 0.06835) passive and red spiral galaxy, as the only plausible host within the 2σ baseband localization region. Our search is sensitive to detected the faintest FRB host known to date to the estimated maximum FRB redshift, $z_{\max} = 0.091$. However, the chance coincidence probability of finding Source 2-like or brighter galaxies within the FRB localization region is $> 10\%$. Alternatively, if Source 2 is not the host of the FRB, then the FRB 20180814A host would be the faintest FRB host known to date and would likely contribute insignificantly to the FRB dispersion measure. In either scenario, the FRB 20180814A host would be an outlier amongst the sample of known FRB hosts. This argues that more FRB host localizations are required to uncover global properties of FRB host population.

We found no archival transient event spatially or temporally coincident with any of the reported FRB 20180814A bursts to date. We also searched for a compact, persistent radio continuum source within the FRB localization region and found none. We then estimated a 3σ upper limit at 3 GHz $= 4.6 \times 10^{27}$ erg s^{-1}Hz^{-1}, at least four times and six times fainter than that the persistent radio source detected spatially coincident to FRB 20121102A and FRB 20190520A, respectively. Due to its low DM-excess, we constrain the Milky Way halo DM contribution to be $16-54$ pc cm^{-3} (90% confidence interval) along the FRB sight-line. We also compared the host of FRB 20180814A with that of FRB 20200120E and found that both FRBs might share the same formation channel. However, to identify the source of FRB 20180814A, we need a more precise localization ($\lesssim$ arcsecond precision).

Chapter 8

A Search for the Host Galaxy of FRB 20190303A

1 Introduction

In this chapter, we present the search for the host galaxy of FRB 20190303A[1], one of the nine repeating FRBs reported by the CHIME/FRB Collaboration in 2020 March (Fonseca et al., 2020). Its DM is 222.4 ± 0.7 pc cm^{-3}, which is significantly larger than the expected Galactic contribution in the FRB direction (~ 25 pc cm^{-3}; Cordes and Lazio, 2002, Yao et al., 2017). As of 2022 October 18, CHIME/FRB has detected 27 bursts from the FRB (see Table 8.1).[2]

Additionally, Fonseca et al. (2020) reported the large extragalactic RM of the FRB ($\approx$ 490 rad m^{-2}). Compared to the predicted Galactic contribution, the FRB's low excess-DM and high extragalactic RM suggested the possibility of a nearby host galaxy. They found a pair of face-on star-forming merging galaxies, SDSS J135159.17+480729.0 and SDSS J135159.87+480714.2, at a spectroscopic redshift = 0.064 as a promising host. However, the reported localization region was not small enough to conclusively establish the merging pair as the FRB host. In this chapter, we used the combined baseband localization of 17

[1]Formerly named as FRB 190303.J1353+48, or internally to the CHIME/FRB team, R17.

[2]For a complete list, check `https://www.chime-frb.ca/repeaters/FRB20190303A` (visited on 18/10/2022).

bursts detected before 2021 March 9 that constrained the uncertainty region of the FRB to a sky-region of 0.13 sq. arcmin (2σ), an improvement of over a factor of 16,000 in localization area (Michilli et al., in prep). Within the localization region, we identify the merging pair as the only viable host with a low-chance association probability, making it the likely host of the FRB.

The chapter is organized as follows: in Section 2, we describe our search for the FRB host. From the low chance coincidence probability (Section 3), we argue that the merging pair is the likely host for the FRB. In Section 4, we list major physical properties of SDSS J135159.17+480729.0 and SDSS J135159.87+480714.2. In Section 5, we show that, besides the merging pair, there is no other viable host candidate detected within the 2σ localization region of the FRB that is detected in archival optical data. We discuss our archival multi-wavelength data search to identify any plausible FRB counterpart in Section 6. In Section 7, we discuss implications of the host association and conclude in Section 8.

2 Observations

CHIME/FRB (CHIME/FRB Collaboration et al., 2018) first reported the discovery of the repeating FRB 20190303A in 2020 (Fonseca et al., 2020). Till 2021 March 9, the CHIME/FRB baseband system triggered on 17 bursts of FRB 20190303A. The dedispersed waterfall plots and major observables of the 17 bursts using baseband data are shown in Figure 8.1 and Table 8.1. The baseband data were processed by an automatic pipeline (Michilli et al., 2020). The baseband localization pipeline is described in Chapter 3. Very briefly, the pipeline maps the FRB bursts' S/N using a grid of overlapping beams around an initial position guess for each FRB. A mathematical model of CHIME's formed beam is used to fit the resultant S/N measurements in each beam. By using a sample of sources with known locations, systematic uncertainties have been quantified. The pipeline facilitates the localization of bursts on the sky with a precision of $\sim \frac{8}{\mathrm{S/N}}$ arcmin. As the reported baseband localization uncertainties are dominated by statistical errors (Michilli et al., 2020). We combined the localization regions of the 17 FRB bursts using a weighted average with inverse variance weights and localized the FRB to a sky area of ≈ 0.13 arcmin^2 (2σ; see Table 8.2). Next, we use the combined FRB baseband localization region to look for a plausible host galaxy.

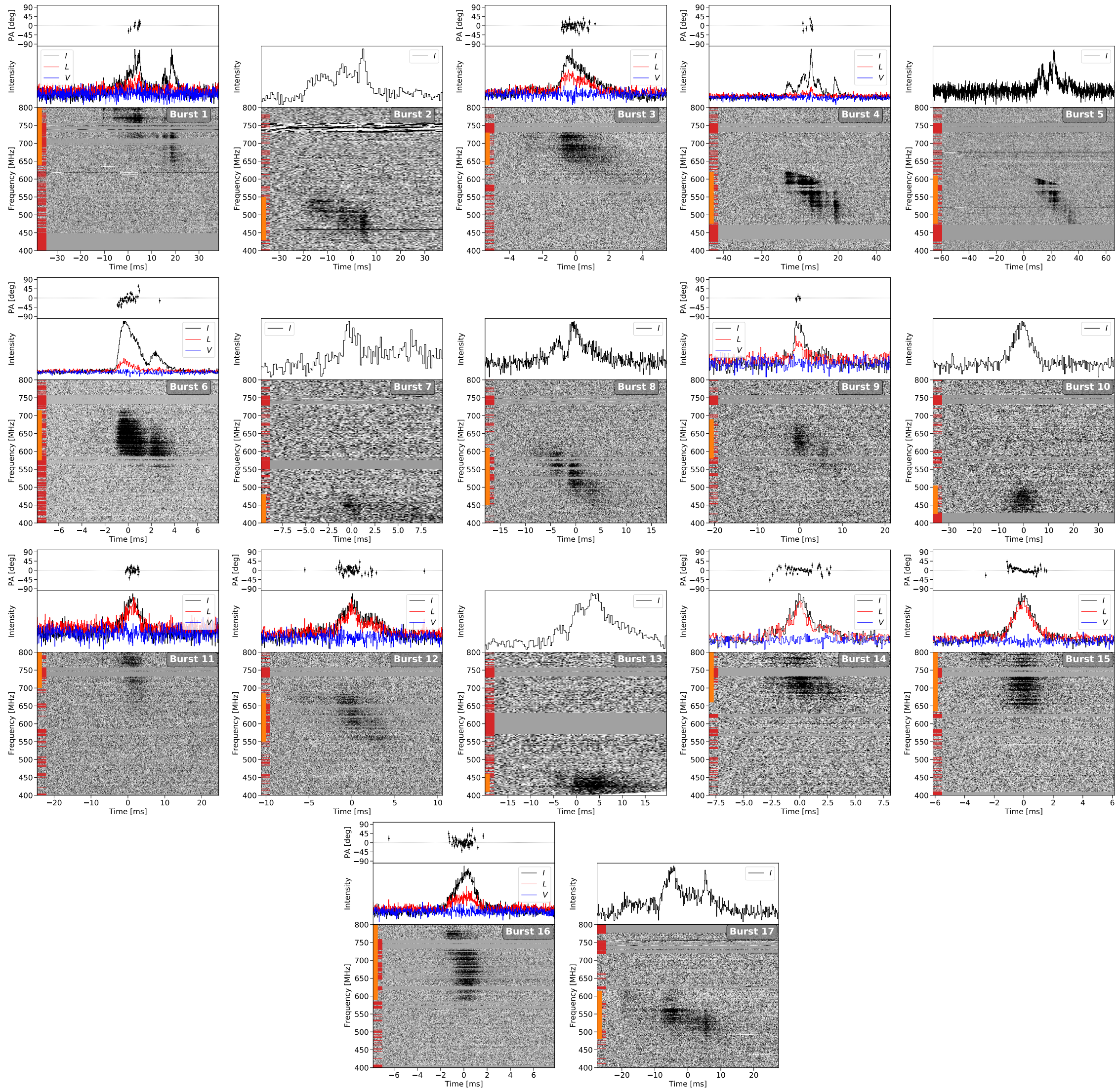

Figure 8.1: Waterfall plots using Stokes I data of 17 FRB 20190303A bursts dedispersed to their structure optimized DMs (DM_{struct}; listed in Table 8.1). The total intensity burst profiles are shown in panels above the spectra (black). For bursts with substantial RM detections, we provide both the linear polarization (red) and circular polarization (blue) intensity profiles (peak normalized) along with the polarization angle (PA) curves. Signal is added over the spectral limits of the burst, shown by orange lines along the frequency axis, to obtain the burst profile. Red lines show masked frequency channels along the vertical axis. Each panel is labelled with the corresponding burst number from Table 8.1. Figure from Mckinven et al. (submitted to ApJ).

Table 8.1: Properties of the bursts from FRB 20190303A using the baseband data.

Burst number	Arrival Time[a] (MJD)	S/N	$\mathrm{DM}^{b}_{\mathrm{struct}}$ (pc cm^{-3})
1	58666.13522	76.8	221.43(21)
2	58769.85517	45.0	221.233(11)
3	58776.82559	82.1	221.579(97)
4	58797.77293	113.7	221.354(59)
5	58800.75865	54.8	221.353(82)
6	58803.75684	208.9	221.473(62)
7	58804.76286	33.5	221.264(61)
8	58832.67612	46.8	221.55(16)
9	58848.63738	27.2	221.64(57)
10	58860.60178	38.8	221.70(25)
11	59022.16102	36.8	222.04(29)
12	59070.02806	57.8	221.39(38)
13	59101.93754	68.7	221.71(15)
14	59248.53543	57.7	221.333(43)
15	59252.52666	80.2	221.78(24)
16	59254.52323	102.2	221.72(12)
17	59275.46633	31.3	221.387(90)

[a] All burst times of arrival are topocentric. The arrival times are estimated by the baseband pipeline (Michilli et al., 2020).
[b] S/N-optimized DM for the bursts detected in the baseband data.

Table 8.2: Major Observables of FRB 20190303A.

Parameter	Value
R.A.(J2000)[a]	$13^{\mathrm{h}}51^{\mathrm{m}}59^{\mathrm{s}}.1 \pm 1^{\mathrm{s}}.3$
Dec. (J2000)[a]	$48°7'15'' \pm 10''$
l, b	97.°635, +65.°925
DM[b]	222.4 ± 0.7 pc cm^{-3}
$\mathrm{DM}^{c}_{\mathrm{MW,NE2001}}$	29 pc cm^{-3}
$\mathrm{DM}^{c}_{\mathrm{MW,YMW16}}$	22 pc cm^{-3}
$\mathrm{DM}^{d}_{\mathrm{MW,WIM}}$	26 ± 3 pc cm^{-3}
$\mathrm{DM}^{e}_{\mathrm{MW,halo}}$	30 pc cm^{-3}
Max. distance[f]	$\lesssim 640$ Mpc

[a] 1σ uncertainty (from Michilli et al. in prep).
[b] From Fonseca et al. (2020).
[c] Maximum DM model prediction along this line-of-sight for the NE2001 (Cordes and Lazio, 2002) and YMW16 (Yao et al., 2017) Galactic electron density distribution models.
[d] Using the $\overline{\mathrm{DM}\sin|\mathrm{b}|}$ estimate from Ocker et al. (2020).
[e]Milky Way halo DM prediction from the Dolag et al. (2015) hydrodynamic simulation and Yamasaki and Totani (2020) Milky Way Halo model.
[f] Corresponds to $z_{\mathrm{max}} = 0.16$ (Fonseca et al., 2020).

2.1 Host galaxy search

As the FRB field-of-view is covered by the Sloan Digital Sky Survey (SDSS; Gunn et al., 2006), we queried the SDSS DR12 catalogue (Alam et al., 2015) to identify plausible host candidates, and found three galaxies within the FRB's 2σ localization region. These sources are listed in Table 8.3. More interesting, out of three sources, Sources 1 and 2 are the pair of face-on star-forming merging galaxies, SDSS J135159.17+480729.0 and SDSS J135159.87+480714.2, that were noted by Fonseca et al. (2020) as a promising FRB host. In Figure 8.2, we plotted the identified sources, and 1σ and 2σ baseband localization regions over an SDSS RGB image made using SDSS's u-band (B:blue), r-band (G:green), and z-band (R:red) data. Clearly, the merging pair at the redshift of z = 0.064 is the most prominent host candidate. We note that SDSS with an r-band depth $\approx$ 22.5 AB mag is sensitive to detect a FRB 20121102A-like host – a star-forming dwarf galaxy ($\mathrm{M_r} = -17$

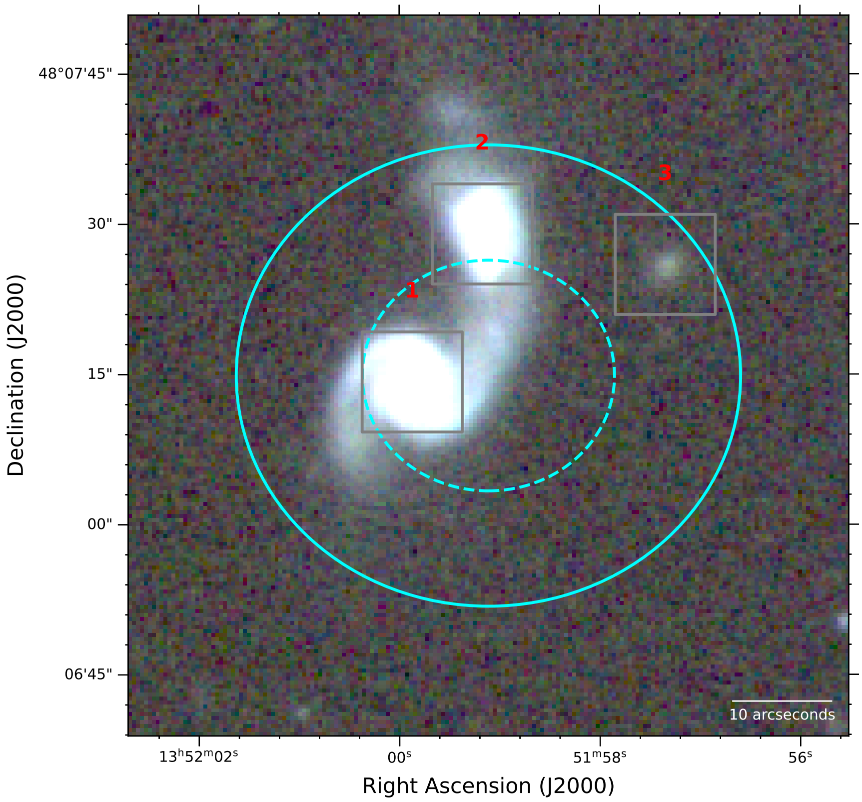

Figure 8.2: SDSS RGB-image of the FRB 20190303A localization regions (dashed ellipse - 1σ; solid ellipse - 2σ). Grey boxes show the locations of 3 host galaxy candidates within the localization region (see Table 8.3); Sources 1 and 2 are a part of the merging pair at z = 0.064, the most promising host galaxy of the FRB.

AB mag; Tendulkar et al., 2017) – the faintest FRB host discovered to date, to the maximum redshift (z_{max}) of the FRB estimated by Fonseca et al. (2020) = 0.16. Additionally, the FRB field-of-view is also covered by the Dark Energy Spectroscopic Instrument (DESI) Legacy Imaging Survey (Dey et al., 2019). Its r-band depth $\approx$ 24 AB mag (5σ). In the DESI data as well, we found the same three SDSS sources that are listed in Table 8.3.

Although the spectroscopic redshift of Source 3 is not catalogued in literature, its photometric redshift $\sim$ 0.20 (Alam et al., 2015, Zhou et al., 2020) places it beyond the maximum redshift limit z_{max} = 0.16. The optical follow-up for estimating the spectroscopic redshift of Source 3 is underway.

Table 8.3: Galaxies identified within the FRB localization region with $M_r \lesssim -16$ AB mag at $z_{max} = 0.16$.

Number	R.A. J2000	Dec. J2000	r-band (SDSS)[a] AB mag.	z_{spec}
1	$13^h51^m59.^s87$	$48°7'14.''2$	15.50(2)	0.06387
2	$13^h51^m59.^s17$	$48°7'29.''0$	15.99(4)	0.06438
3	$13^h51^m57.^s34$	$48°7'25.''9$	20.12(6)	0.20(4)[b]

[a] Petrosian r-band magnitudes from the SDSS DR12 photometric catalogue (Alam et al., 2015).
[b] Photometric redshift estimated for Source 3 by the SDSS collaboration (see Section 2.1).

3 Chance coincidence probability of the merging pair

As the most plausible host candidate of FRB 20190303A is a pair of face-on star-forming merging galaxies, SDSS J135159.17+480729.0 and SDSS J135159.87+480714.2, we first estimate the likelihood of finding a such a merging pair by pure coincidence with the FRB localization. We use the same formalism that is discussed in Section 4.4 of Fonseca et al. (2020). Briefly, we estimate the density of galaxies with $M_B \leq -20$ AB mag, using the luminosity function of low-redshift galaxies from Faber et al. (2007), to be ≈ 0.0015 Mpc^{-3}. We then estimate the probability of finding a pair of massive merging galaxies by chance assuming a Poisson spatial distribution of galaxies in the Universe and a number of companions per galaxy (N_c) = 0.02 (Patton and Atfield, 2008) to be $\approx 1.2 \times 10^{-4}$ for $z_{max} = 0.16$. Even when considering all the baseband localized CHIME FRBs with unknown hosts reported thus far ($= 13$; Michilli et al., in prep) as a trial factor to account for the look-elsewhere effect, the P_{cc} would be 1.6 $\times 10^{-3}$ suggesting a robust host association. However, though several repeating FRBs are found to be spatially associated with merging systems (see Section 7.2), there is no *a priori* reason to have expected a merging pair as the host of FRB 20190303A. Therefore, we next use the Bayesian formalism PATH (Probabilistic Association of Transients to their Hosts; Aggarwal et al., 2021) to calculate the true host association probability of FRB with either of the merging pair galaxies.

For that, we employ a Bayesian framework, Probabilistic Association of Transients to their Hosts (PATH; Aggarwal et al., 2021), for estimating the probability of chance coincidence between the FRB and either of the merging galaxies. We examine all the galaxies detected within the FRB localization region by both SDSS and DESI (see Table 8.3) to obtain a posterior probability of true association with either of the merging galaxies, P(O|merging pair). > 0.99 (where $P(O|x) > 0.90$ is generally considered a secure association; Bhandari et al., 2022). Here, as recommended by Aggarwal et al. (2021), we assume a 10% prior probability that the host galaxy of the FRB is not detected either in the SDSS or in the DESI survey. The estimates discussed above (P_{cc} and true host association probability) strengthen the host association of FRB 201903030A with the merging pair.

4 Physical properties of Sources 1 and 2

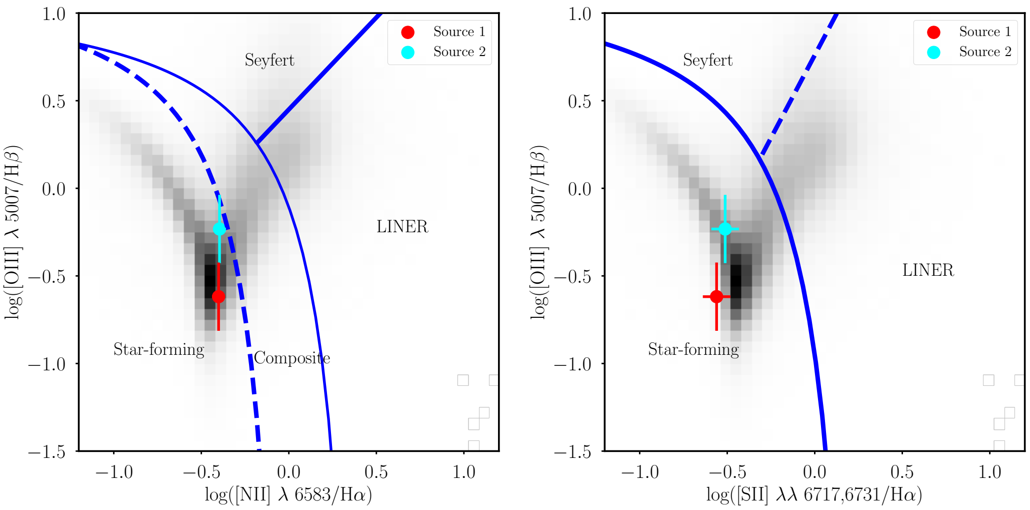

Figure 8.3: The two "Baldwin, Phillips & Terlevich" (BPT) diagrams used to classify the emission-line galaxies as: Star-forming, Seyfert, LINER, and Composite galaxies. Left: dashed line shows the Kauffmann et al. (2003) classification criteria. The Kewley et al. (2006) classification is shown as the solid line. Right:Kauffmann et al. (2003) criteria is shown as the solid line which separates star-forming galaxies from active galaxies and the dashed lines represent the Seyfert–LINER demarcation from Schawinski et al. (2007). Both SDSS J135159.87+480714.2 (Source 1) and SDSS J135159.17+480729.0 (Source 2) are classified as starforming galaxies using the BPT diagrams

Here we summarize the major physical properties of the face-on star-forming merging galaxies, SDSS J135159.87+480714.2 (Source 1) and SDSS J135159.17+480729.0 (Source 2). The SDSS collaboration (Alam et al., 2015) acquired optical spectra along with calibrated photometry (ugriz) for both the galaxies. They used those datasets to calculate redshifts and major physical parameters of the two sources, which are presented in Table 8.4. Additionally, we estimated the nebular metallicity of the merging pair via Oxygen abundance, 12 + log (O/H), using the O3N2 calibration formula from Hirschauer et al. (2018), and the effective radii of both the galaxies using the catalogued Petrosian radii (R_{50}, R_{90}) provided by SDSS Data Release 12 and Equation 7 of Graham et al. (2005), which are also listed in Table 8.4. Note that as only a small fraction of the two galaxies (including the central region) is covered by the SDSS spectragraph, we did not estimate the current star-formation rate of Sources 1 and 2 via the Hα line.

We now briefly outline the approach employed by the SDSS collaboration (Granada group[3]) to estimate the listed physical properties of the two galaxies. The parameters are based on the publicly available Flexible Stellar Population Synthesis code (FSPS; Conroy et al., 2009). With the assumption that star formation occurs over a wide range of redshifts which allows an extended star-formation history, the model fits extinction corrected SDSS photometry (SDSS ugriz band magnitudes). Additionally, it also fits for dust extinction using the two component model of dust attenuation by Charlot and Fall (2000). In this extinction model, radiation from all stars is attenuated $(\mathrm{Av, old})$ by a diffuse (and well mixed) dust component, but young stars' light ($\lesssim$ 10 Myr) experiences an extra source of attenuation $(\mathrm{Av, young})$ via a parental birth-cloud.

As the galaxies' optical spectrum shows all the major emission lines, we used The "Baldwin, Philips & Terlevich" (BPT) diagrams of [O III]/Hβ versus [N II]/Hα and [O III]/Hβ versus [S II]/Hα to classify the dominant source of ionizing radiation in the two galaxies. The plots are shown in Figure 8.3. Both Sources 1 and 2 are classified as predominantly star-forming galaxies by both the BPT diagrams.

[3]Refer this web-page for more information:https://www.sdss.org/dr12/spectro/galaxy_granada/

Table 8.4: Notable properties of Sources 1 and 2.

Property	**Source 1**	**Source 2**
log[SFR] ($M_\odot$ yr^{-1})	0.99 ± 0.03	0.84 ± 0.04
Stellar Metallicity ($\log(Z/Z_\odot)$)	-0.39 ± 0.01	-0.31 ± 0.07
Oxygen abundance [O/H]	9.04 ± 0.19	8.94 ± 0.07
Stellar mass ($\log(M/M_\odot)$)	10.63 ± 0.03	10.75 ± 0.03
Effective radius (R_{eff}; kpc)	4.9	4.7
Mass-weighted age (Gyr)[a]	1.72 ± 0.18	4.2 ± 0.8
$(u\text{-}r)_o$ (mag)	1.79 ± 0.01	1.93 ± 0.02
$A_{V,old}$ (mag)	0.76 ± 0.04	0.81 ± 0.01
$A_{V,young}$ (mag)	2.27 ± 0.13	2.44 ± 0.03
Absolute r-band mag. (AB)	-20.49	-19.94
Redshift (z)	0.06386 ± 0.00001	0.06437 ± 0.00001

5 Source 3 - The FRB host?

This section discusses the likelihood of Source 3 to be the host of FRB 20190303A. Unsurprisingly, $P_{cc,\text{ Source 3}} \approx 1$ and P(O|Source 3) < 0.01 if we use the methods discussed in Section 3 suggesting that it is unlikely to be the FRB host. However, we note that as fainter galaxies are more common in the Universe and thus more likely to be discovered in the FRB localization region, our chance coincidence analysis favours brighter galaxies over fainter ones. Therefore, in this section, we discuss the prospects of Source 3 to be the FRB host based on other arguments.

If Source 3 is indeed the FRB host, the interstellar medium (ISM) and circumgalactic medium (CGM) of Sources 1 and 2 would also contribute to the DM of the FRB. At z = 0.064, the FRB's projected offset from Sources 1 and 2 would be 26 kpc and 16 kpc, respectively, which is less than the typically observed radial extent of massive star-forming galaxies ($\sim 10^{11}$ $M_\odot$) ($\gtrsim$ 30 kpc; Genel et al., 2018, Paulino-Afonso et al., 2017, Schulz, 2017). To be conservative, we only consider here the contribution of the CGM of the two galaxies. For that, we follow the formalism used in Chapter 5 to estimate the halo contribution of M81. Briefly, we first estimate the halo mass of Sources 1 and 2 to be $1.5 \times 10^{12} M_\odot$ and $2.5 \times 10^{12} M_\odot$ using the relation between the stellar mass of a galaxy and the mass of its dark matter halo from Moster et al. (2013). The stellar masses of the merging galaxies that are used to estimate their halo masses are listed in Table 8.4. Next, using the calculated dark matter halo mass of the two galaxies, we estimate concentration factors of Sources 1 and 2 − dimensionless shape parameters that characterize dark matter halo profiles − to be 7.4 and 6.9, respectively, using a relation between halo mass and concentration factor from Klypin et al. (2016). To estimate a conservative DM contribution of the merging pair's CGM, we employ the MB04 density profile, which provided the most conservative (smallest) $DM_{M81,halo}$ estimate in Section 3.4 of Chapter 5. Using all these parameters, we calculate the DM contribution of the CGM to be 60 pc cm^{-3}. Here we use the fraction of baryons in the halos of the Sources 1 and 2 = $f_{b,halo}$ = 0.4, the minimum value that Hafen et al. (2019) found in the FIRE simulation for a $\sim 10^{12}$ $M_{\odot}$ halo. This is a conservative assumption, since zoom-in cosmology hydrodynamical simulations of massive mergers (Hani et al., 2018) showed that the density of baryons in the CGM was greatly enhanced by the merger event and would only begin to decrease approximately $\sim$ 3 Gyr after the merger. Therefore, we conclude that if Source 3 is the FRB host, the DM contribution of the merging pair would be significant. If we only include this conservative DM contribution of the foreground merging pair in the DM budget, we estimate the maximum redshift of the FRB to be 0.13 (95% upper limit) assuming negligible contribution from the FRB host, which is considerably smaller than the photometric redshift of Source 3 $= 0.20$. Therefore, this analysis also suggests that Source 3 is unlikely to be the FRB host.

6 Search for a multi-wavelength counterpart to FRB 20190303A

6.1 Persistent radio source search

As at least two localized FRBs are found to be associated with a persistent compact radio source, FRBs 20121102A (Chatterjee et al., 2005) and 20190520A (Niu et al., 2022), we search for a similar radio counterpart within the FRB localization region. For that, we check the following archival radio data: the VLA Sky Survey (VLASS - 3 GHz; Lacy et al., 2016), the Faint Images of the Radio Sky at Twenty-centimeters Survey (FIRST Survey - 1.5

GHz; Becker et al., 1995), the NRAO VLA Sky Survey (NVSS - 1.4 GHz; Condon et al., 1998), the Westerbork Northern Sky Survey (WENSS - 330 MHz; Rengelink et al., 1997), the Tata Institute of Fundamental Research Giant Metrewave Radio Telescope Sky Survey Alternative Data Release (TGSS - 150 MHz; Intema et al., 2017), and the LOFAR Two-metre Sky Survey (IoTSS - 144 MHz ; Shimwell et al., 2022). Among these surveys, we do not find any radio counterpart in VLASS, WENSS, and TGSS, and one barely resolved radio source coincident with the merging pair in the NVSS image, NVSS J103422+734554. However, the NVSS source is resolved in FIRST and IoTSS images as two sources that spatially coincide with the merging pair and have the same morphology as the galaxies in the SDSS images. Finally, the FIRST and IoTSS radio sources are likely resolved out and therefore undetectable in the VLASS 1.1 and 2.1 data, which have $\sim$ three times higher angular resolution than FIRST and IoTSS. This shows that the two radio sources are of an extended nature and are the outcome of ongoing star formation in the galaxies. This is in agreement with the conclusions made using BPT diagrams in Section 4.

We estimate the integrated flux density of the radio counterparts of Sources 1 and 2 detected in the FIRST and IoTSS images using the `Aegean` package (Hancock et al., 2012, Hancock et al., 2018) and is stated in Table 8.5. Using the IoTSS and FIRST flux densities and assuming a power-law dependence of the flux density of the radio counterparts of Sources 1 and 2 i.e., $S_\nu \propto S^\alpha$, we estimate α to be 0.63 ± 0.15 for Source 1 and 0.88 ± 0.15 for Source 2. These spectral indexes agree well with the observed radio continuum spectral index of local star-forming galaxies (between -0.1 and -0.8; Klein et al., 2018, Marvil et al., 2015).

We also estimate the SFR of both the galaxies using the FIRST 1.4 GHz flux density and compare it with the value estimated in Section 4. Using the 1.4 GHz–SFR relation from Davies et al. (2017),

$$\log(\mathrm{SFR_{UV+TIR}/M_\odot yr^{-1}}) = 0.66 \pm 0.02 \times \log(\mathrm{L_{1.4}(W/Hz)}) - 14.02 \pm 0.39, \quad (8.1)$$

we estimate,

$$\log(\mathrm{SFR_{UV+TIR}/M_\odot yr^{-1}, Source1}) = 0.7 \pm 0.4 \quad (8.2)$$

and,

$$\log(\mathrm{SFR_{UV+TIR}/M_\odot yr^{-1}, Source2}) = 0.5 \pm 0.4. \tag{8.3}$$

The SFRs of Sources 1 and 2 computed using the FIRST 1.4 GHz data are consistent with the values presented in Table 8.4.

From the non-detection of a persistent compact radio source in the FRB 20190303A localization region in the VLASS 2.1 data, the best angular resolution data among all the included radio surveys, we estimate a 3σ upper limit of 480 μJy at 3 GHz which at z = 0.064 implies an isotropic spectral luminosity $\approx$ 5 $\times$ 10^{28} erg/s/Hz, which is smaller than the spectral luminosity of the persistent radio source detected spatially coincident to FRB 20121102A and FRB 20190520A, respectively ($L_\nu > 10^{29}$ erg/s/Hz; Chatterjee et al., 2017, Niu et al., 2022).

Table 8.5: Summary of radio observations of FRB 20190303A

Survey	Frequency GHz	Date UT	Image Resolution[a] ″	Source 1 flux[b] mJy	Source 2 flux[b] mJy
IoTSS	0.144	2018 August 1[c]	6	8.27 ± 0.18	6.43 ± 0.09
FIRST	1.5	1997 April 05	5	1.9 ± 0.3	0.79 ± 0.12

[a] For each survey, average of major and minor axes of the formed beam is quoted.
[b] Integrated flux density estimated using `Aegean`.
[c] There are three mosaic images obtained between 2018 July 25 and 2018 August 8. The flux estimates for the two sources in each of the three images are consistent within 1σ error.

7 Discussion

7.1 Constraints in the progenitor of the FRB

Mckinven et al. (submitted to ApJ) noted that the bursts from FRB 20190303A detected between 2019 July and 2021 November (17 of those are displayed in Figure 8.1) showed a wide range of linear polarization fractions. More surprising, over a six-day period from 2019 November 10 to 2019 November 16, the $|\mathrm{RM}|$ of FRB 20190303A increased by more

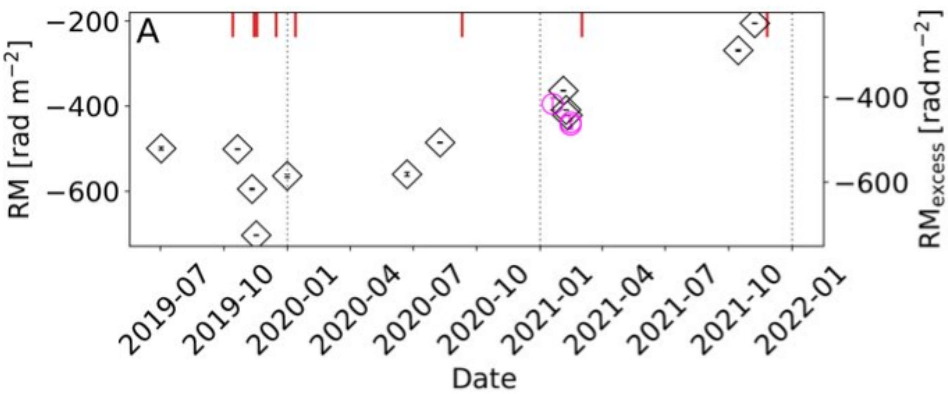

Figure 8.4: RM as a function of time for baseband data recorded from FRB 20190303A, displaying the ionospheric corrected RM (black diamonds); The RMs are uncorrected for the non-uniform bandpass of CHIME. Times are in Coordinated Universal Time (UTC) format with vertical dotted lines indicating the start of each calendar year. The RMs represented as black points are displayed alongside previously published RMs obtained from FAST observations (magenta points; Feng et al., 2022). The extent of the error bars appear invisible for some data points due to the the large RM variations displayed from this source. The times of arrival (TOA) of the unpolarized bursts are indicated as lines along the top horizontal axis. Figure from Mckinven et al. (submitted to ApJ)

than $\sim 100\ \mathrm{rad\,m^{-2}}$. This implies a temporal RM gradient of $|\nabla\mathrm{RM}| \gtrsim -17\ \mathrm{rad\,m^{-2}\,day^{-1}}$, which is followed by an interval of over a year where $|\mathrm{RM}|$ steadily decreased to its minimum near $\mathrm{RM} \sim -200\ \mathrm{rad\,m^{-2}}$. Using these observations, the authors estimated an average gradient of $|\nabla\mathrm{RM}| \gtrsim 0.7\ \mathrm{rad\,m^{-2}\,day^{-1}}$. Figure 8.4 summarizes this remarkable behaviour of the FRB bursts. It suggests a dynamic and highly evolving local environment, which one can expect from a merging pair. It is interesting to note that the two galaxies are about to merge (Patton and Atfield, 2008), which often causes enhanced star formation in and at the outskirts of the merging galaxies, making them a promising site of transients associated with young progenitors formed via prompt channels, like core-collapse supernovae, long gamma ray bursts (LGRBs) and hydrogen poor superluminous supernovae (SLSNe). However, it seems less likely that these two galaxies can host a LGRB or hydrogen poor SLSNe progenitor due to the following reasons: the host galaxies of LGRBs in the low-redshift Universe are typically at the faint, low-mass end of the population of star-forming galaxies (Lunnan et al., 2014, Perley et al., 2016, Savaglio et al., 2009, Vergani et al., 2015). In contrast, both Sources 1 and 2 are massive galaxies ($\sim 10^{11}$ $\mathrm{M_{\odot}}$). Moreover, the low-redshift host galaxies of LGRBs and hydrogen poor SLSNe are predominantly metal-poor with 12 + [O/H] $<$ 8.60 (Graham and Fruchter, 2013, Perley et al., 2016, Vergani et al., 2017), contrary to what is observed in this case. Therefore, it seems less likely that the FRB progenitors is a remnant formed via Hydrogen-poor SLSNe or LGRBs.

7.2 Comparison with other repeating FRB hosts

It would be interesting to investigate whether the FRB source is associated with the merger system. However, this is not the first FRB that is reported to be associated with a merging pair. Law et al. (2020) reported the discovery of an apparently non-repeating FRB, FRB 20190614D, and suggested that the galaxy pair J042017.71+734222.9 and J042017.87+734224.4 at a photometric redshift of ~ 0.6 as its plausible host. The merging pair has an angular separation of $\sim 1.5''$ from the FRB central position. However, the chance association probability of this galaxy pair is not small enough to make a robust association, i.e., 7% (Heintz et al., 2020). Moreover, Heintz et al. (2020) noted that FRB 191001 host is also likely in the process of merging with another galaxy at a projected separation of ≈ 25 kpc, though it is not clear if it has any impact on the formation of the FRB progenitor. Additionally, Kaur et al. (2022) analyzed the neutral atomic hydrogen distribution in the host galaxy of FRB20180916B (Marcote et al., 2020) and claimed that the FRB host recently underwent a small merger, resulting in a burst of star formation at the galaxy's outskirts that gave rise to the FRB progenitor. Finally, Ryder et al. (2022) reported the discovery of FRB 20220610A in a complex (likely merging) galaxy system at a redshift of $z = 1.016 \pm 0.002$. These associations of FRBs with merging systems suggest that merger events can facilitate conditions conducive to the formation of FRB progenitors. However, due to the diverse activity of the localized FRBs (only FRBs 20180916B and 20190303A thus far have been found to repeat) and the small sample size, we refrain for drawing any meaningful conclusion here.

With the inclusion of FRB 20190303A in the sample of seven repeating FRBs, 20121102A, 20180916B, 20181030A, 20190520A, 20190711A, 20200120E, and FRB 20201124A (Chatterjee et al., 2017, Heintz et al., 2020, Lanman et al., 2022, Marcote et al., 2020, Niu et al., 2022, ; Chapters 5 and 6), it is evident that the known repeating FRB hosts exhibit a continuum of properties in terms of their luminosities, stellar masses, metallicity, and SFRs. However, the association of FRB 20190303A with a pair of massive spiral star-forming galaxies along with the plausible association of FRB 20180814A with a passive red spiral (see Chapter 7) seem to contradict the tentative evidence found by Bhandari et al. (2022) for the hosts of repeating FRBs being less massive and less luminous on average, compared to the hosts of apparently non-repeating FRBs. Therefore, it is crucial to get more host associations to do meaningful statistical studies of the FRB host population.

8 Summary & conclusions

We have reported on the likely association of the repeating FRB 20190303A discovered by Fonseca et al. (2020) with a local Universe merging pair of two star-forming galaxies at a redshift of 0.064, SDSS J135159.17+480729.0 and SDSS J135159.87+480714.2. On the basis of a Bayesian framework for estimating the probability of chance coincidence between transients and host galaxies, we estimated that the probability of correctly associating the FRB with either of the merging galaxies is greater than 99 % and thus concluded that the association is robust.

We searched the Transient Name Server (TNS)[4] for any archival transient event that is spatially and temporally coincident with any of the 17 recorded FRB 20190303A bursts and find none. We also searched for a compact persistent radio source within the FRB localization region and found none. We then estimated a 3σ upper limit at 3 GHz $= 5 \times 10^{28}\,\mathrm{erg\,s^{-1}Hz^{-1}}$, smaller than spectral luminosity of the persistent sources associated with FRBs 20121102A and 20190520A.

At a distance of ≈ 300 Mpc, FRB 20190303A is one of the closest and most active repeating FRBs discovered to date. Hence, it is a promising candidate for VLBI follow-ups and for the detection of prompt multi-wavelength counterparts as predicted by several FRB models (Nicastro et al., 2021). Therefore, we strongly encourage multi-wavelength follow-up of FRB 20190303A.

[4] https://www.wis-tns.org/

Chapter 9

Final Conclusion & Future Work

This thesis outlines the framework developed to identify host galaxies of local Universe FRBs discovered by the CHIME telescope. In addition, we describe the automated pipeline that promptly identifies faulty hardware components. Given that CHIME is a highly sophisticated radio interferometer with 2048 signal chains processing sky signals at a data rate of $\sim 4.6\,\mathrm{Tb\,s^{-1}}$, early detection of malfunctioning hardware components is crucial to maintain the data integrity.

In order to identify plausible host galaxies of CHIME FRBs in the local universe, we develop a pipeline with which we found the likely hosts of many low excess-DM FRBs (some of the relevant publications are currently in preparation). In this dissertation, we report on the discovery and host association of four low excess-DM FRBs, two of which, FRBs 20181030A and 20200120E, are the closest known extragalactic FRBs to date. The low-DM or local Universe FRBs described in this thesis have constrained FRB emission mechanisms and progenitor models and disfavoured a number of previously held beliefs regarding the FRB population. For instance, the hosts of the four repeating FRBs have strikingly distinct physical properties, which raises questions about the kinds of conditions that could produce FRBs in galaxies with significantly different properties. Furthermore, FRB 20200120E was later localized to the M81 globular cluster by Kirsten et al. (2021) that we reported in our work. The most popular FRB model evokes young strongly magnetized compact objects. It is highly unlikely that FRB 20200120E source was formed through this channel. Therefore, the association provides the strongest evidence yet for the existence of multiple FRB formation channels.

In this chapter, we summarize the most significant findings from the works provided in this dissertation:

In Chapter 3, we present the pipeline designed to identify bad analog channels that are crucial to be removed to maintain data integrity. We describe the underlying framework of the pipeline, adaptive thresholding and cross-correlation techniques, to identify bad channels. We then demonstrate the pipeline's utility for finding channels with various hardware-related defects. In fact, the pipeline was the first to identify a sudden increasing in bad channels at the time of rain, which was later found to be caused by rain water interfering with CHIME feed electronics. We also evaluate the pipeline's fundamental assumptions and conclude that they are applicable to CHIME and other similar radio interferometric array, such as such as Murchison Widefield Array (MWA; Lonsdale et al., 2009), LOw Frequency ARray (LOFAR; Butcher, 2004), Hydrogen Epoch of Reionization Array (HERA; DeBoer et al., 2017), Hydrogen Intensity and Real-time Analysis eXperiment (HIREX; Newburgh et al., 2016), DSA-2000 (Hallinan et al., 2019), and Square Kilometer Array (SKA; Ellingson, 2005). For completeness, we investigate various scenarios where the pipeline is not designed to work optimally due to the limitations of the underlying assumptions. Finally, we discuss possible approaches to increase the pipeline's efficiency while dealing with those scenarios.

In Chapter 4, we describe the FRB$-\lambda$ pipeline, a `Python`-based fully automated pipeline that identifies plausible host galaxy candidates of CHIME FRBs, particularly those with low excess-DM. The pipeline searches archival optical survey data to identify catalogued galaxies within the FRB localization region and then searches for their possible infrared counterparts in WISE and 2MASS. It saves the identified galaxies' flux catalogue, which includes their coordinates, extinction-corrected flux magnitudes, and flux densities, as well as their spectroscopic or photometric redshifts. In addition, it estimates the maximum redshift of the FRB and the chance association probability of discovering (1) a galaxy of a particular apparent r-band magnitude and (2) a galaxy similar to the faintest FRB host discovered to date in the comoving volume in the FRB localization region to the estimated maximum FRB redshift. Lastly, it generates FRB localization plots utilizing Pan-STARRS g-, r-, and z-band data, that also show the location of discovered galaxies. Since its inception, the pipeline has consistently been used to identify plausible host candidates of low excess-DM CHIME FRBs, and many of them will be published soon. Due to its modular structure, the pipeline

In Chapter 5, we have reported on the discovery of the repeating fast radio burst source FRB 20200120E discovered with CHIME/FRB. This source has very low DM, 87.82 pc cm^{-3}, though greater than what is expected from models of the Milky Way ISM along its line-of-sight. We identified M81, a nearby grand-design spiral galaxy at a distance of $\sim$ 3.6 Mpc, with an angular offset $\approx 19'$ and chance coincidence probability $< 10^{-2}$, as its promising host candidate. We have shown that the observed extragalactic DM component of the FRB is significantly lower than the model-predicted DM contribution from the M81 halo as a foreground galaxy. This suggests that the FRB host galaxy is unlikely to be located beyond M81, though the FRB may exist within the extended disk of M81. Therefore, if extragalactic, FRB 20200120E is most likely associated with M81. We also found that the FRB localization region contains the extended M81 HI-disk and a number of interesting M81 sources including an H II region ([PWK2012] 31), an X-ray binary ([SPZ2011] 8), a VLASS source, VLASS1QLCIR J095756.10+684833.3 and a globular cluster At a distance of 3.6 Mpc, it should be possible to detect prompt multi-wavelength counterparts of FRB 20200120E predicted by several FRB models, including the magnetar model. Some FRB models anticipate even greater luminosities in high energy bands than in the radio band (Burke-Spolaor, 2018, Chen et al., 2020, Yi et al., 2014). For example, in the synchrotron maser model of Metzger et al. (2019), shock-heated electrons gyrate to produce synchrotron radiation that sweeps through the γ-ray and X-ray bands, and in some cases, even extends to the optical band on sub-second timescales. Additionally, if radio bursts from FRB 20200120E are accompanied by X-ray bursts, as was seen in SGR 1935+2154 (Bochenek et al., 2020, CHIME/FRB Collaboration et al., 2020a, Li et al., 2020, Mereghetti et al., 2020, Ridnaia et al., 2020), detecting a coincident X-ray counterpart seems feasible, and would be a strong test of the magnetar origin of FRBs. Therefore, we encourage multi-wavelength follow-up of FRB 20200120E.

Chapter 6 reports on the association of the repeating FRB 20181030A discovered by CHIME/FRB Collaboration et al. (2019c) with a nearby star-forming spiral galaxy, NGC 3252, at a distance of 20 Mpc. This makes the FRB the second closest extragalactic FRB known to date. We estimate the chance coincidence probability of finding NGC 3252 within the FRB localization region is $< 2.5 \times 10^{-3}$. Regardless, we searched for plausible host galaxies within the FRB's 90% confidence localization region, and found no galaxy except NGC 3252 with $\mathrm{M_r} < -15$, a limit in luminosity over five times smaller than for any FRB hosts identified to date. This further strengthens the association of FRB with NGC 3252. We found no archival transient event that coincided spatially or temporally with any of the reported FRB 20181030A bursts to date. For one FRB burst, FRB 20200122A, that was detected on 2020 January 22 by CHIME/FRB and was also visible to *Fermi*/GBM, we estimated an upper limit on the coincident X-ray flare energy to be $\approx 10^{46}$ erg s^{-1}. From our radio follow-up analysis, we noted that NGC 3252 does not harbour an actively accreting super-massive black hole at its center. We also searched for a compact, persistent radio continuum source within the FRB localization region and found none. We then estimated a 3σ upper limit at 3 GHz $= 4.3 \times 10^{25}$ erg s^{-1}Hz^{-1}, at least 1500 times fainter than the persistent source associated with FRB 20121102A. Due to its low DM-excess, we constrain the Milky Way halo DM contribution to be $19-55$ pc cm^{-3} (90% confidence interval) along the FRB sight-line. Additionally, we compared the two published FRB 20181030A bursts with those of SGR 1935+2154. The FRB bursts' isotropic luminosity is ~ 6 times larger than those of SGR 1935+2154; using this, we have estimated a lower limit on the volumetric rate of FRBs with luminosities $\geq 10^{38}$ erg s^{-1}. We found this to be in good agreement with the rate estimated by Bochenek et al. (2020) using the SGR 1935+2154 radio burst, suggesting that many low-luminosity FRBs could be produced by magnetars. Lastly, we also showed that it is unlikely that most of the repeating FRB progenitors are young millisecond magnetars, and that if we expect millisecond magnetars to be a source of repeating FRBs, we need multiple repeating FRB formation channels. At a distance of 20 Mpc, it is a promising candidate for detecting predicted prompt and afterglow emission at other wavelengths. Therefore, we strongly encourage multi-wavelength follow-up of FRB 20181030A.

Chapter 7 reports on the search for the host of the repeating FRB 20180814A discovered by CHIME/FRB Collaboration et al. (2019c). From our search, we found PanSTARRS-DR1 J042256.01+733940.7, a nearby (z= 0.06835) passive red spiral galaxy, as the only plausible host within the 2σ baseband localization region. Our search is sensitive to detected the faintest FRB host known to date to the estimated maximum FRB redshift, $z_{\rm max} = 0.091$. However, the chance coincidence probability of finding Source 2-like or brighter galaxies within the FRB localization region is $> 10\%$. Alternatively, if Source 2 is not the host of the FRB, then the FRB 20180814A host would be the faintest FRB host known to date and would likely contribute insignificantly to the FRB dispersion measure. In either scenario, the FRB 20180814A host would be an outlier amongst the sample of known FRB hosts. This argues that more FRB host localizations are required to uncover global properties of FRB host population. We found no archival transient event spatially or temporally coincident with any of the reported FRB 20180814A bursts to date. We also searched for a compact, persistent radio continuum source within the FRB localization region and found none. We then estimated a 3σ upper limit at 3 GHz $= 4.6 \times 10^{27}$ erg s^{-1}Hz^{-1}, at least four times and six times fainter than that the persistent radio source detected spatially coincident to FRB 20121102A and FRB 20190520A, respectively. Due to its low DM-excess, we constrain the Milky Way halo DM contribution to be $16-54$ pc cm^{-3} (90% confidence interval) along the FRB sight-line. We also compared the host of FRB 20180814A with that of FRB 20200120E and found that both FRBs might share the same formation channel. However, to identify the source of FRB 20180814A, we need a more precise localization ($\lesssim$ arcsecond precision).

Chapter 8 reports on the likely association of the repeating FRB 20190303A discovered by Fonseca et al. (2020) with a local Universe merging pair of two star-forming galaxies at a redshift of 0.064, SDSS J135159.17+480729.0 and SDSS J135159.87+480714.2. On the basis of a Bayesian framework for estimating the probability of chance coincidence between transients and host galaxies, we estimated that the probability of correctly associating the FRB with either of the merging galaxies is greater than 99 % and thus concluded that the association is robust. We searched the Transient Name Server (TNS)[1] for any archival transient event that is spatially and temporally coincident with any of the 17 recorded FRB 20190303A bursts and find none. We also searched for a compact persistent

[1] https://www.wis-tns.org/

radio source within the FRB localization region and found none. We then estimated a 3σ upper limit at 3 GHz $= 5 \times 10^{28}$ erg $\mathrm{s}^{-1}\mathrm{Hz}^{-1}$, smaller than spectral luminosity of the persistent sources associated with FRBs 20121102A and 20190520A. At a distance of ≈ 300 Mpc, FRB 20190303A is one of the closest and most active repeating FRBs discovered to date. Hence, it is a promising candidate for VLBI follow-ups and for the detection of prompt multi-wavelength counterparts as predicted by several FRB models (Nicastro et al., 2021). Therefore, we strongly encourage multi-wavelength follow-up of FRB 20190303A.

Fast radio bursts are an exciting new frontier for astrophysics. These millisecond radio transients, as described in Astro2020 Decadal Survey (National Academies of Sciences and Medicine, 2021), "have the potential to become a powerful new probe of the distribution of baryons throughout cosmic ecosystems". However, despite the fact that research on FRBs has progressed at an extraordinary pace since the first FRB was discovered in 2007, its nature remains a source of great debate, owing in part to a limited sample of localized FRBs. Expanding the FRB host sample is therefore a pressing scientific priority for FRB research, and the Canadian Hydrogen Intensity Mapping Experiment CHIME/FRB project (CHIME/FRB Collaboration et al., 2018) is destined to make tremendous strides in this direction. Moreover, it is noted that multi-wavelength follow-up analyses, which, for instance, were crucial in establishing the existence of two distinct classes of gamma ray bursts in the past (Kulkarni, 2018), are most promising for nearby FRBs ($<$ 100 Mpc; Scholz et al., 2020). Therefore, local Universe FRBs are unquestionably the most promising candidates for detecting hypothesized prompt and afterglow emission, for bridging the gap between known Galactic pulsed sources and FRBs, and perhaps for assessing whether all FRBs are repeating sources. The work described in this thesis is a stepping stone in direction of exploring the true potential of local Universe FRBs. When the CHIME/FRB outrigger project begins localizing all CHIME FRBs to a precision of ~ 50 milli-arcseconds in next few years (Cassanelli et al., 2022), we will use the described methodology and the FRB-λ pipeline as one of our tools for all of our FRBs. With such an enormous sample size of localized FRBs, robust statistical analyses of FRB hosts and their local environments will be possible. In addition, the large FRB host sample will allow us to determine whether repeating and non-repeating FRBs are fundamentally distinct sub-classes of FRBs. All in all, FRBs will no longer be as mysterious as they are at present.

Bibliography

K. N. Abazajian, J. K. Adelman-McCarthy, M. A. Agüeros, S. S. Allam, C. Allende Prieto, D. An, K. S. J. Anderson, S. F. Anderson, J. Annis, N. A. Bahcall, C. A. L. Bailer-Jones, J. C. Barentine, B. A. Bassett, A. C. Becker, T. C. Beers, E. F. Bell, V. Belokurov, A. A. Berlind, E. F. Berman, M. Bernardi, S. J. Bickerton, D. Bizyaev, J. P. Blakeslee, M. R. Blanton, J. J. Bochanski, W. N. Boroski, H. J. Brewington, J. Brinchmann, J. Brinkmann, R. J. Brunner, T. Budavári, L. N. Carey, S. Carliles, M. A. Carr, F. J. Castander, D. Cinabro, A. J. Connolly, I. Csabai, C. E. Cunha, P. C. Czarapata, J. R. A. Davenport, E. de Haas, B. Dilday, M. Doi, D. J. Eisenstein, M. L. Evans, N. W. Evans, X. Fan, S. D. Friedman, J. A. Frieman, M. Fukugita, B. T. Gänsicke, E. Gates, B. Gillespie, G. Gilmore, B. Gonzalez, C. F. Gonzalez, E. K. Grebel, J. E. Gunn, Z. Györy, P. B. Hall, P. Harding, F. H. Harris, M. Harvanek, S. L. Hawley, J. J. E. Hayes, T. M. Heckman, J. S. Hendry, G. S. Hennessy, R. B. Hindsley, J. Hoblitt, C. J. Hogan, D. W. Hogg, J. A. Holtzman, J. B. Hyde, S.-i. Ichikawa, T. Ichikawa, M. Im, Ž. Ivezić, S. Jester, L. Jiang, J. A. Johnson, A. M. Jorgensen, M. Jurić, S. M. Kent, R. Kessler, S. J. Kleinman, G. R. Knapp, K. Konishi, R. G. Kron, J. Krzesinski, N. Kuropatkin, H. Lampeitl, S. Lebedeva, M. G. Lee, Y. S. Lee, R. French Leger, S. Lépine, N. Li, M. Lima, H. Lin, D. C. Long, C. P. Loomis, J. Loveday, R. H. Lupton, E. Magnier, O. Malanushenko, V. Malanushenko, R. Mand elbaum, B. Margon, J. P. Marriner, D. Martínez-Delgado, T. Matsubara, P. M. McGehee, T. A. McKay, A. Meiksin, H. L. Morrison, F. Mullally, J. A. Munn, T. Murphy, T. Nash, A. Nebot, J. Neilsen, Eric H., H. J. Newberg, P. R. Newman, R. C. Nichol, T. Nicinski, M. Nieto-Santisteban, A. Nitta, S. Okamura, D. J. Oravetz, J. P. Ostriker, R. Owen, N. Padmanabhan, K. Pan, C. Park, G. Pauls, J. Peoples, John, W. J. Percival, J. R. Pier, A. C. Pope, D. Pourbaix, P. A. Price, N. Purger,

T. Quinn, M. J. Raddick, P. Re Fiorentin, G. T. Richards, M. W. Richmond, A. G. Riess, H.-W. Rix, C. M. Rockosi, M. Sako, D. J. Schlegel, D. P. Schneider, R.-D. Scholz, M. R. Schreiber, A. D. Schwope, U. Seljak, B. Sesar, E. Sheldon, K. Shimasaku, V. C. Sibley, A. E. Simmons, T. Sivarani, J. Allyn Smith, M. C. Smith, V. Smolčić, S. A. Snedden, A. Stebbins, M. Steinmetz, C. Stoughton, M. A. Strauss, M. SubbaRao, Y. Suto, A. S. Szalay, I. Szapudi, P. Szkody, M. Tanaka, M. Tegmark, L. F. A. Teodoro, A. R. Thakar, C. A. Tremonti, D. L. Tucker, A. Uomoto, D. E. Vanden Berk, J. Vandenberg, S. Vidrih, M. S. Vogeley, W. Voges, N. P. Vogt, Y. Wadadekar, S. Watters, D. H. Weinberg, A. A. West, S. D. M. White, B. C. Wilhite, A. C. Wonders, B. Yanny, D. R. Yocum, D. G. York, I. Zehavi, S. Zibetti, and D. B. Zucker. The Seventh Data Release of the Sloan Digital Sky Survey. ApJS, 182(2):543–558, June 2009. doi: 10.1088/0067-0049/182/2/543.

T. M. C. Abbott, F. B. Abdalla, S. Allam, A. Amara, J. Annis, J. Asorey, S. Avila, O. Ballester, M. Banerji, W. Barkhouse, L. Baruah, M. Baumer, K. Bechtol, M. R. Becker, A. Benoit-Lévy, G. M. Bernstein, E. Bertin, J. Blazek, S. Bocquet, D. Brooks, D. Brout, E. Buckley-Geer, D. L. Burke, V. Busti, R. Campisano, L. Cardiel-Sas, A. Carnero Rosell, M. Carrasco Kind, J. Carretero, F. J. Castander, R. Cawthon, C. Chang, X. Chen, C. Conselice, G. Costa, M. Crocce, C. E. Cunha, C. B. D'Andrea, L. N. da Costa, R. Das, G. Daues, T. M. Davis, C. Davis, J. De Vicente, D. L. DePoy, J. DeRose, S. Desai, H. T. Diehl, J. P. Dietrich, S. Dodelson, P. Doel, A. Drlica-Wagner, T. F. Eifler, A. E. Elliott, A. E. Evrard, A. Farahi, A. Fausti Neto, E. Fernandez, D. A. Finley, B. Flaugher, R. J. Foley, P. Fosalba, D. N. Friedel, J. Frieman, J. García-Bellido, E. Gaztanaga, D. W. Gerdes, T. Giannantonio, M. S. S. Gill, K. Glazebrook, D. A. Goldstein, M. Gower, D. Gruen, R. A. Gruendl, J. Gschwend, R. R. Gupta, G. Gutierrez, S. Hamilton, W. G. Hartley, S. R. Hinton, J. M. Hislop, D. Hollowood, K. Honscheid, B. Hoyle, D. Huterer, B. Jain, D. J. James, T. Jeltema, M. W. G. Johnson, M. D. Johnson, T. Kacprzak, S. Kent, G. Khullar, M. Klein, A. Kovacs, A. M. G. Koziol, E. Krause, A. Kremin, R. Kron, K. Kuehn, S. Kuhlmann, N. Kuropatkin, O. Lahav, J. Lasker, T. S. Li, R. T. Li, A. R. Liddle, M. Lima, H. Lin, P. López-Reyes, N. MacCrann, M. A. G. Maia, J. D. Maloney, M. Manera, M. March, J. Marriner, J. L. Marshall, P. Martini, T. McClintock, T. McKay, R. G. McMahon, P. Melchior, F. Menanteau, C. J. Miller, R. Miquel, J. J. Mohr, E. Morganson, J. Mould, E. Neilsen, R. C.

Nichol, F. Nogueira, B. Nord, P. Nugent, L. Nunes, R. L. C. Ogando, L. Old, A. B. Pace, A. Palmese, F. Paz-Chinchón, H. V. Peiris, W. J. Percival, D. Petravick, A. A. Plazas, J. Poh, C. Pond, A. Porredon, A. Pujol, A. Refregier, K. Reil, P. M. Ricker, R. P. Rollins, A. K. Romer, A. Roodman, P. Rooney, A. J. Ross, E. S. Rykoff, M. Sako, M. L. Sanchez, E. Sanchez, B. Santiago, A. Saro, V. Scarpine, D. Scolnic, S. Serrano, I. Sevilla-Noarbe, E. Sheldon, N. Shipp, M. L. Silveira, M. Smith, R. C. Smith, J. A. Smith, M. Soares-Santos, F. Sobreira, J. Song, A. Stebbins, E. Suchyta, M. Sullivan, M. E. C. Swanson, G. Tarle, J. Thaler, D. Thomas, R. C. Thomas, M. A. Troxel, D. L. Tucker, V. Vikram, A. K. Vivas, A. R. Walker, R. H. Wechsler, J. Weller, W. Wester, R. C. Wolf, H. Wu, B. Yanny, A. Zenteno, Y. Zhang, J. Zuntz, DES Collaboration, S. Juneau, M. Fitzpatrick, R. Nikutta, D. Nidever, K. Olsen, A. Scott, and NOAO Data Lab. The Dark Energy Survey: Data Release 1. ApJS, 239(2):18, Dec. 2018. doi: 10.3847/1538-4365/aae9f0.

Abdurro'uf, K. Accetta, C. Aerts, V. Silva Aguirre, R. Ahumada, N. Ajgaonkar, N. Filiz Ak, S. Alam, C. Allende Prieto, A. Almeida, F. Anders, S. F. Anderson, B. H. Andrews, B. Anguiano, E. Aquino-Ortíz, A. Aragón-Salamanca, M. Argudo-Fernández, M. Ata, M. Aubert, V. Avila-Reese, C. Badenes, R. H. Barbá, K. Barger, J. K. Barrera-Ballesteros, R. L. Beaton, T. C. Beers, F. Belfiore, C. F. Bender, M. Bernardi, M. A. Bershady, F. Beutler, C. M. Bidin, J. C. Bird, D. Bizyaev, G. A. Blanc, M. R. Blanton, N. F. Boardman, A. S. Bolton, M. Boquien, J. Borissova, J. Bovy, W. N. Brandt, J. Brown, J. R. Brownstein, M. Brusa, J. Buchner, K. Bundy, J. N. Burchett, M. Bureau, A. Burgasser, T. K. Cabang, S. Campbell, M. Cappellari, J. K. Carlberg, F. C. Wanderley, R. Carrera, J. Cash, Y.-P. Chen, W.-H. Chen, B. Cherinka, C. Chiappini, P. D. Choi, S. D. Chojnowski, H. Chung, N. Clerc, R. E. Cohen, J. M. Comerford, J. Comparat, L. da Costa, K. Covey, J. D. Crane, I. Cruz-Gonzalez, C. Culhane, K. Cunha, Y. S. Dai, G. Damke, J. Darling, J. Davidson, James W., R. Davies, K. Dawson, N. De Lee, A. M. Diamond-Stanic, M. Cano-Díaz, H. D. Sánchez, J. Donor, C. Duckworth, T. Dwelly, D. J. Eisenstein, Y. P. Elsworth, E. Emsellem, M. Eracleous, S. Escoffier, X. Fan, E. Farr, S. Feng, J. G. Fernández-Trincado, D. Feuillet, A. Filipp, S. P. Fillingham, P. M. Frinchaboy, S. Fromenteau, L. Galbany, R. A. García, D. A. García-Hernández, J. Ge, D. Geisler, J. Gelfand, T. Géron, B. J. Gibson, J. Goddy, D. Godoy-Rivera, K. Grabowski, P. J. Green, M. Greener, C. J. Grier, E. Griffith, H. Guo, J. Guy,

M. Hadjara, P. Harding, S. Hasselquist, C. R. Hayes, F. Hearty, J. Hernández, L. Hill, D. W. Hogg, J. A. Holtzman, D. Horta, B.-C. Hsieh, C.-H. Hsu, Y.-H. Hsu, D. Huber, M. Huertas-Company, B. Hutchinson, H. S. Hwang, H. J. Ibarra-Medel, J. I. Chitham, G. S. Ilha, J. Imig, W. Jaekle, T. Jayasinghe, X. Ji, J. A. Johnson, A. Jones, H. Jönsson, I. Katkov, D. Khalatyan, Arman, K. Kinemuchi, S. Kisku, J. H. Knapen, J.-P. Kneib, J. A. Kollmeier, M. Kong, M. Kounkel, K. Kreckel, D. Krishnarao, I. Lacerna, R. R. Lane, R. Langgin, R. Lavender, D. R. Law, D. Lazarz, H. W. Leung, H.-H. Leung, H. M. Lewis, C. Li, R. Li, J. Lian, F.-H. Liang, L. Lin, Y.-T. Lin, S. Lin, C. Lintott, D. Long, P. Longa-Peña, C. López-Cobá, S. Lu, B. F. Lundgren, Y. Luo, J. T. Mackereth, A. de la Macorra, S. Mahadevan, S. R. Majewski, A. Manchado, T. Mandeville, C. Maraston, B. Margalef-Bentabol, T. Masseron, K. L. Masters, S. Mathur, R. M. McDermid, M. Mckay, A. Merloni, M. Merrifield, S. Meszaros, A. Miglio, F. Di Mille, D. Minniti, R. Minsley, A. Monachesi, J. Moon, B. Mosser, J. Mulchaey, D. Muna, R. R. Muñoz, A. D. Myers, N. Myers, S. Nadathur, P. Nair, K. Nandra, J. Neumann, J. A. Newman, D. L. Nidever, F. Nikakhtar, C. Nitschelm, J. E. O'Connell, L. Garma-Oehmichen, G. Luan Souza de Oliveira, R. Olney, D. Oravetz, M. Ortigoza-Urdaneta, Y. Osorio, J. Otter, Z. J. Pace, N. Padilla, K. Pan, H.-A. Pan, T. Parikh, J. Parker, S. Peirani, K. Peña Ramírez, S. Penny, W. J. Percival, I. Perez-Fournon, M. Pinsonneault, F. Poidevin, V. J. Poovelil, A. M. Price-Whelan, A. Bárbara de Andrade Queiroz, M. J. Raddick, A. Ray, S. B. Rembold, N. Riddle, R. A. Riffel, R. Riffel, H.-W. Rix, A. C. Robin, A. Rodríguez-Puebla, A. Roman-Lopes, C. Román-Zúñiga, B. Rose, A. J. Ross, G. Rossi, K. H. R. Rubin, M. Salvato, S. F. Sánchez, J. R. Sánchez-Gallego, R. Sanderson, F. A. Santana Rojas, E. Sarceno, R. Sarmiento, C. Sayres, E. Sazonova, A. L. Schaefer, R. Schiavon, D. J. Schlegel, D. P. Schneider, M. Schultheis, A. Schwope, A. Serenelli, J. Serna, Z. Shao, G. Shapiro, A. Sharma, Y. Shen, M. Shetrone, Y. Shu, J. D. Simon, M. F. Skrutskie, R. Smethurst, V. Smith, J. Sobeck, T. Spoo, D. Sprague, D. V. Stark, K. G. Stassun, M. Steinmetz, D. Stello, A. Stone-Martinez, T. Storchi-Bergmann, G. S. Stringfellow, A. Stutz, Y.-C. Su, M. Taghizadeh-Popp, M. S. Talbot, J. Tayar, E. Telles, J. Teske, A. Thakar, C. Theissen, A. Tkachenko, D. Thomas, R. Tojeiro, H. Hernandez Toledo, N. W. Troup, J. R. Trump, J. Trussler, J. Turner, S. Tuttle, E. Unda-Sanzana, J. A. Vázquez-Mata, M. Valentini, O. Valenzuela, J. Vargas-González, M. Vargas-Magaña, P. V. Alfaro, S. Villanova, F. Vincenzo, D. Wake, J. T. Warfield, J. D.

Washington, B. A. Weaver, A.-M. Weijmans, D. H. Weinberg, A. Weiss, K. B. Westfall, V. Wild, M. C. Wilde, J. C. Wilson, R. F. Wilson, M. Wilson, J. Wolf, W. M. Wood-Vasey, R. Yan, O. Zamora, G. Zasowski, K. Zhang, C. Zhao, Z. Zheng, Z. Zheng, and K. Zhu. The Seventeenth Data Release of the Sloan Digital Sky Surveys: Complete Release of MaNGA, MaStar, and APOGEE-2 Data. ApJS, 259(2):35, Apr. 2022. doi: 10.3847/1538-4365/ac4414.

R. Adam, P. A. Ade, N. Aghanim, M. Alves, M. Arnaud, M. Ashdown, J. Aumont, C. Baccigalupi, A. Banday, R. Barreiro, et al. Planck 2015 results-x. diffuse component separation: Foreground maps. *Astronomy & Astrophysics*, 594:A10, 2016.

P. A. Ade, N. Aghanim, M. Arnaud, M. Ashdown, J. Aumont, C. Baccigalupi, A. Banday, R. Barreiro, J. Bartlett, N. Bartolo, et al. Planck 2015 results-xiii. cosmological parameters. *Astronomy & Astrophysics*, 594:A13, 2016.

K. Aggarwal, T. Budavári, A. T. Deller, T. Eftekhari, C. W. James, J. X. Prochaska, and S. P. Tendulkar. Probabilistic Association of Transients to their Hosts (PATH). ApJ, 911 (2):95, Apr. 2021. doi: 10.3847/1538-4357/abe8d2.

D. S. Aguado, R. Ahumada, A. Almeida, S. F. Anderson, B. H. Andrews, B. Anguiano, E. Aquino Ortíz, A. Aragón-Salamanca, M. Argudo-Fernández, M. Aubert, V. Avila-Reese, C. Badenes, S. Barboza Rembold, K. Barger, J. Barrera-Ballesteros, D. Bates, J. Bautista, R. L. Beaton, T. C. Beers, F. Belfiore, M. Bernardi, M. Bershady, F. Beutler, J. Bird, D. Bizyaev, G. A. Blanc, M. R. Blanton, M. Blomqvist, A. S. Bolton, M. Boquien, J. Borissova, J. Bovy, W. N. Brandt, J. Brinkmann, J. R. Brownstein, K. Bundy, A. Burgasser, N. Byler, M. Cano Diaz, M. Cappellari, R. Carrera, B. Cervantes Sodi, Y. Chen, B. Cherinka, P. D. Choi, H. Chung, D. Coffey, J. M. Comerford, J. Comparat, K. Covey, G. da Silva Ilha, L. da Costa, Y. S. Dai, G. Damke, J. Darling, R. Davies, K. Dawson, V. de Sainte Agathe, A. Deconto Machado, A. Del Moro, N. De Lee, A. M. Diamond-Stanic, H. Domínguez Sánchez, J. Donor, N. Drory, H. du Mas des Bourboux, C. Duckworth, T. Dwelly, G. Ebelke, E. Emsellem, S. Escoffier, J. G. Fernández-Trincado, D. Feuillet, J.-L. Fischer, S. W. Fleming, A. Fraser-McKelvie, G. Freischlad, P. M. Frinchaboy, H. Fu, L. Galbany, R. Garcia-Dias, D. A. García-Hernández, L. A. Garma Oehmichen, M. A. Geimba Maia, H. Gil-Marín, K. Grabowski, M. Gu, H. Guo,

J. Ha, E. Harrington, S. Hasselquist, C. R. Hayes, F. Hearty, H. Hernandez Toledo, H. Hicks, D. W. Hogg, K. Holley-Bockelmann, J. A. Holtzman, B.-C. Hsieh, J. A. S. Hunt, H. S. Hwang, H. J. Ibarra-Medel, C. E. Jimenez Angel, J. Johnson, A. Jones, H. Jönsson, K. Kinemuchi, J. Kollmeier, C. Krawczyk, K. Kreckel, S. Kruk, I. Lacerna, T.-W. Lan, R. R. Lane, D. R. Law, Y.-B. Lee, C. Li, J. Lian, L. Lin, Y.-T. Lin, C. Lintott, D. Long, P. Longa-Peña, J. T. Mackereth, A. de la Macorra, S. R. Majewski, O. Malanushenko, A. Manchado, C. Maraston, V. Mariappan, M. Marinelli, R. Marques-Chaves, T. Masseron, K. L. Masters, R. M. McDermid, N. Medina Peña, S. Meneses-Goytia, A. Merloni, M. Merrifield, S. Meszaros, D. Minniti, R. Minsley, D. Muna, A. D. Myers, P. Nair, J. Correa do Nascimento, J. A. Newman, C. Nitschelm, M. D. Olmstead, A. Oravetz, D. Oravetz, R. A. Ortega Minakata, Z. Pace, N. Padilla, P. A. Palicio, K. Pan, H.-A. Pan, T. Parikh, I. Parker, James, S. Peirani, S. Penny, W. J. Percival, I. Perez-Fournon, T. Peterken, M. H. Pinsonneault, A. Prakash, M. J. Raddick, A. Raichoor, R. A. Riffel, R. Riffel, H.-W. Rix, A. C. Robin, A. Roman-Lopes, B. Rose, A. J. Ross, G. Rossi, K. Rowlands, K. H. R. Rubin, S. F. Sánchez, J. R. Sánchez-Gallego, C. Sayres, A. Schaefer, R. P. Schiavon, J. S. Schimoia, E. Schlafly, D. Schlegel, D. P. Schneider, M. Schultheis, H.-J. Seo, S. J. Shamsi, Z. Shao, S. Shen, S. Shetty, G. Simonian, R. J. Smethurst, J. Sobeck, B. J. Souter, A. Spindler, D. V. Stark, K. G. Stassun, M. Steinmetz, T. Storchi-Bergmann, G. S. Stringfellow, G. Suárez, J. Sun, M. Taghizadeh-Popp, M. S. Talbot, J. Tayar, A. R. Thakar, D. Thomas, P. Tissera, R. Tojeiro, N. W. Troup, E. Unda-Sanzana, O. Valenzuela, M. Vargas-Magaña, J. A. Vázquez-Mata, D. Wake, B. A. Weaver, A.-M. Weijmans, K. B. Westfall, V. Wild, J. Wilson, E. Woods, R. Yan, M. Yang, O. Zamora, G. Zasowski, K. Zhang, Z. Zheng, Z. Zheng, G. Zhu, J. C. Zinn, and H. Zou. The Fifteenth Data Release of the Sloan Digital Sky Surveys: First Release of MaNGA-derived Quantities, Data Visualization Tools, and Stellar Library. ApJS, 240 (2):23, Feb. 2019. doi: 10.3847/1538-4365/aaf651.

S. Ai, H. Gao, and B. Zhang. On the True Fractions of Repeating and Nonrepeating Fast Radio Burst Sources. ApJ, 906(1):L5, Jan. 2021. doi: 10.3847/2041-8213/abcec9.

M. Al Najm, O. Polikarpova, and Y. A. Shchekinov. Ionized gas in the circumgalactic vicinity of the m81 galaxy group. *Astronomy Reports*, 60(4):389–396, 2016.

S. Alam, F. D. Albareti, C. Allende Prieto, F. Anders, S. F. Anderson, T. Anderton, B. H.

Andrews, E. Armengaud, É. Aubourg, S. Bailey, S. Basu, J. E. Bautista, R. L. Beaton, T. C. Beers, C. F. Bender, A. A. Berlind, F. Beutler, V. Bhardwaj, J. C. Bird, D. Bizyaev, C. H. Blake, M. R. Blanton, M. Blomqvist, J. J. Bochanski, A. S. Bolton, J. Bovy, A. Shelden Bradley, W. N. Brandt, D. E. Brauer, J. Brinkmann, P. J. Brown, J. R. Brownstein, A. Burden, E. Burtin, N. G. Busca, Z. Cai, D. Capozzi, A. Carnero Rosell, M. A. Carr, R. Carrera, K. C. Chambers, W. J. Chaplin, Y.-C. Chen, C. Chiappini, S. D. Chojnowski, C.-H. Chuang, N. Clerc, J. Comparat, K. Covey, R. A. C. Croft, A. J. Cuesta, K. Cunha, L. N. da Costa, N. Da Rio, J. R. A. Davenport, K. S. Dawson, N. De Lee, T. Delubac, R. Deshpande, S. Dhital, L. Dutra-Ferreira, T. Dwelly, A. Ealet, G. L. Ebelke, E. M. Edmondson, D. J. Eisenstein, T. Ellsworth, Y. Elsworth, C. R. Epstein, M. Eracleous, S. Escoffier, M. Esposito, M. L. Evans, X. Fan, E. Fernández-Alvar, D. Feuillet, N. Filiz Ak, H. Finley, A. Finoguenov, K. Flaherty, S. W. Fleming, A. Font-Ribera, J. Foster, P. M. Frinchaboy, J. G. Galbraith-Frew, R. A. García, D. A. García-Hernández, A. E. García Pérez, P. Gaulme, J. Ge, R. Génova-Santos, A. Georgakakis, L. Ghezzi, B. A. Gillespie, L. Girardi, D. Goddard, S. G. A. Gontcho, J. I. González Hernández, E. K. Grebel, P. J. Green, J. N. Grieb, N. Grieves, J. E. Gunn, H. Guo, P. Harding, S. Hasselquist, S. L. Hawley, M. Hayden, F. R. Hearty, S. Hekker, S. Ho, D. W. Hogg, K. Holley-Bockelmann, J. A. Holtzman, K. Honscheid, D. Huber, J. Huehnerhoff, I. I. Ivans, L. Jiang, J. A. Johnson, K. Kinemuchi, D. Kirkby, F. Kitaura, M. A. Klaene, G. R. Knapp, J.-P. Kneib, X. P. Koenig, C. R. Lam, T.-W. Lan, D. Lang, P. Laurent, J.-M. Le Goff, A. Leauthaud, K.-G. Lee, Y. S. Lee, T. C. Licquia, J. Liu, D. C. Long, M. López-Corredoira, D. Lorenzo-Oliveira, S. Lucatello, B. Lundgren, R. H. Lupton, I. Mack, Claude E., S. Mahadevan, M. A. G. Maia, S. R. Majewski, E. Malanushenko, V. Malanushenko, A. Manchado, M. Manera, Q. Mao, C. Maraston, R. C. Marchwinski, D. Margala, S. L. Martell, M. Martig, K. L. Masters, S. Mathur, C. K. McBride, P. M. McGehee, I. D. McGreer, R. G. McMahon, B. Ménard, M.-L. Menzel, A. Merloni, S. Mészáros, A. A. Miller, J. Miralda-Escudé, H. Miyatake, A. D. Montero-Dorta, S. More, E. Morganson, X. Morice-Atkinson, H. L. Morrison, B. Mosser, D. Muna, A. D. Myers, K. Nandra, J. A. Newman, M. Neyrinck, D. C. Nguyen, R. C. Nichol, D. L. Nidever, P. Noterdaeme, S. E. Nuza, J. E. O'Connell, R. W. O'Connell, R. O'Connell, R. L. C. Ogando, M. D. Olmstead, A. E. Oravetz, D. J. Oravetz, K. Osumi, R. Owen, D. L. Padgett, N. Padmanabhan, M. Paegert, N. Palanque-Delabrouille, K. Pan, J. K.

Parejko, I. Pâris, C. Park, P. Pattarakijwanich, M. Pellejero-Ibanez, J. Pepper, W. J. Percival, I. Pérez-Fournon, I. Pérez-Ràfols, P. Petitjean, M. M. Pieri, M. H. Pinsonneault, G. F. Porto de Mello, F. Prada, A. Prakash, A. M. Price-Whelan, P. Protopapas, M. J. Raddick, M. Rahman, B. A. Reid, J. Rich, H.-W. Rix, A. C. Robin, C. M. Rockosi, T. S. Rodrigues, S. Rodríguez-Torres, N. A. Roe, A. J. Ross, N. P. Ross, G. Rossi, J. J. Ruan, J. A. Rubiño-Martín, E. S. Rykoff, S. Salazar-Albornoz, M. Salvato, L. Samushia, A. G. Sánchez, B. Santiago, C. Sayres, R. P. Schiavon, D. J. Schlegel, S. J. Schmidt, D. P. Schneider, M. Schultheis, A. D. Schwope, C. G. Scóccola, C. Scott, K. Sellgren, H.-J. Seo, A. Serenelli, N. Shane, Y. Shen, M. Shetrone, Y. Shu, V. Silva Aguirre, T. Sivarani, M. F. Skrutskie, A. Slosar, V. V. Smith, F. Sobreira, D. Souto, K. G. Stassun, M. Steinmetz, D. Stello, M. A. Strauss, A. Streblyanska, N. Suzuki, M. E. C. Swanson, J. C. Tan, J. Tayar, R. C. Terrien, A. R. Thakar, D. Thomas, N. Thomas, B. A. Thompson, J. L. Tinker, R. Tojeiro, N. W. Troup, M. Vargas-Magaña, J. A. Vazquez, L. Verde, M. Viel, N. P. Vogt, D. A. Wake, J. Wang, B. A. Weaver, D. H. Weinberg, B. J. Weiner, M. White, J. C. Wilson, J. P. Wisniewski, W. M. Wood-Vasey, C. Ye‘che, D. G. York, N. L. Zakamska, O. Zamora, G. Zasowski, I. Zehavi, G.-B. Zhao, Z. Zheng, X. Zhou, Z. Zhou, H. Zou, and G. Zhu. The Eleventh and Twelfth Data Releases of the Sloan Digital Sky Survey: Final Data from SDSS-III. ApJS, 219(1):12, July 2015. doi: 10.1088/0067-0049/219/1/12.

M. Amiri, K. Bandura, P. Berger, M. Bhardwaj, M. Boyce, P. Boyle, C. Brar, M. Burhanpurkar, P. Chawla, J. Chowdhury, et al. The chime fast radio burst project: System overview. *The Astrophysical Journal*, 863(1):48, 2018.

L. D. Anderson, T. Bania, D. S. Balser, V. Cunningham, T. Wenger, B. Johnstone, and W. Armentrout. The wise catalog of galactic h ii regions. *The Astrophysical Journal Supplement Series*, 212(1):1, 2014.

R. Anna-Thomas, L. Connor, S. Burke-Spolaor, P. Beniamini, K. Aggarwal, C. J. Law, R. S. Lynch, D. Li, Y. Feng, S. K. Ocker, M. Cruces, S. Chatterjee, W. Yu, C. Niu, and M. Xue. A Highly Variable Magnetized Environment in a Fast Radio Burst Source. *arXiv e-prints*, art. arXiv:2202.11112, Feb. 2022.

A. Anumarlapudi, V. Bhalerao, S. P. Tendulkar, and A. Balasubramanian. Prompt X-Ray

Emission from Fast Radio Bursts—Upper Limits with AstroSat. ApJ, 888(1):40, Jan. 2020. doi: 10.3847/1538-4357/ab5363.

W. R. Arcus, J. P. Macquart, M. W. Sammons, C. W. James, and R. D. Ekers. The fast radio burst dispersion measure distribution. MNRAS, 501(4):5319–5329, Mar. 2021. doi: 10.1093/mnras/staa3948.

R. A. Armstrong. When to use the b onferroni correction. *Ophthalmic and Physiological Optics*, 34(5):502–508, 2014.

N. Arora, C. Stone, S. Courteau, and T. H. Jarrett. MaNGA Galaxy Properties. I: An Extensive Optical, Mid-Infrared Photometric, and Environmental Catalog. *arXiv e-prints*, art. arXiv:2105.01660, May 2021.

M. C. Artale, M. Mapelli, Y. Bouffanais, N. Giacobbo, M. Pasquato, and M. Spera. Mass and star formation rate of the host galaxies of compact binary mergers across cosmic time. 491(3):3419–3434. doi: 10.1093/mnras/stz3190.

M. Asplund, N. Grevesse, A. J. Sauval, and P. Scott. The Chemical Composition of the Sun. ARA&A, 47(1):481–522, Sept. 2009. doi: 10.1146/annurev.astro.46.060407.145222.

A.-N. Babul and L. Sironi. The synchrotron maser emission from relativistic magnetized shocks: dependence on the pre-shock temperature. MNRAS, 499(2):2884–2895, Dec. 2020. doi: 10.1093/mnras/staa2612.

N. Bade, D. Engels, W. Voges, V. Beckmann, T. Boller, L. Cordis, M. Dahlem, J. Englhauser, K. Molthagen, P. Nass, et al. The hamburg/rass catalogue of optical identifications. *Astronomy and Astrophysics Supplement Series*, 127(2):145–152, 1998.

M. Bailes, C. G. Bassa, G. Bernardi, S. Buchner, M. Burgay, M. Caleb, A. J. Cooper, G. Desvignes, P. J. Groot, I. Heywood, F. Jankowski, R. Karuppusamy, M. Kramer, M. Malenta, G. Naldi, M. Pilia, G. Pupillo, K. M. Rajwade, L. Spitler, M. Surnis, B. W. Stappers, A. Addis, S. Bloemen, M. C. Bezuidenhout, G. Bianchi, D. J. Champion, W. Chen, L. N. Driessen, M. Geyer, K. Gourdji, J. W. T. Hessels, V. I. Kondratiev, M. Klein-Wolt, E. Körding, R. Le Poole, K. Liu, M. E. Lower, A. G. Lyne, A. Magro, V. McBride, M. B. Mickaliger, V. Morello, A. Parthasarathy, K. Paterson, B. B. P. Perera,

D. L. A. Pieterse, Z. Pleunis, A. Possenti, A. Rowlinson, M. Serylak, G. Setti, M. Tavani, R. A. M. J. Wijers, S. ter Veen, V. Venkatraman Krishnan, P. Vreeswijk, and P. A. Woudt. Multifrequency observations of SGR J1935+2154. MNRAS, 503(4):5367–5384, June 2021. doi: 10.1093/mnras/stab749.

M. L. Balogh, S. L. Morris, H. K. C. Yee, R. G. Carlberg, and E. Ellingson. Differential Galaxy Evolution in Cluster and Field Galaxies at z~0.3. 527(1):54–79. doi: 10.1086/308056.

K. Bandura, G. E. Addison, M. Amiri, J. R. Bond, D. Campbell-Wilson, L. Connor, J.-F. Cliche, G. Davis, M. Deng, N. Denman, et al. Canadian hydrogen intensity mapping experiment (chime) pathfinder. In *Ground-based and Airborne Telescopes V*, volume 9145, page 914522. International Society for Optics and Photonics, 2014.

K. Bandura, J. F. Cliche, M. A. Dobbs, A. J. Gilbert, D. Ittah, J. Mena Parra, and G. Smecher. ICE-Based Custom Full-Mesh Network for the CHIME High Bandwidth Radio Astronomy Correlator. *Journal of Astronomical Instrumentation*, 5(4):1641004, Dec. 2016. doi: 10.1142/S225117171641004X.

K. W. Bannister, A. T. Deller, C. Phillips, J.-P. Macquart, J. X. Prochaska, N. Tejos, S. D. Ryder, E. M. Sadler, R. M. Shannon, S. Simha, et al. A single fast radio burst localized to a massive galaxy at cosmological distance. *Science*, 365(6453):565–570, 2019.

A. Barrau, C. Rovelli, and F. Vidotto. Fast radio bursts and white hole signals. Phys. Rev. D, 90(12):127503, Dec. 2014. doi: 10.1103/PhysRevD.90.127503.

C. G. Bassa, S. P. Tendulkar, E. A. K. Adams, N. Maddox, S. Bogdanov, G. C. Bower, S. Burke-Spolaor, B. J. Butler, S. Chatterjee, J. M. Cordes, J. W. T. Hessels, V. M. Kaspi, C. J. Law, B. Marcote, Z. Paragi, S. M. Ransom, P. Scholz, L. G. Spitler, and H. J. van Langevelde. FRB 121102 Is Coincident with a Star-forming Region in Its Host Galaxy. ApJ, 843(1):L8, July 2017. doi: 10.3847/2041-8213/aa7a0c.

F. E. Bauer, J. J. Condon, T. X. Thuan, and J. J. Broderick. RBSC-NVSS Sample. I. Radio and Optical Identifications of a Complete Sample of 1556 Bright X-Ray Sources. ApJS, 129(2):547–562, Aug. 2000. doi: 10.1086/313425.

R. Beck, I. Szapudi, H. Flewelling, C. Holmberg, E. Magnier, and K. C. Chambers. PS1-STRM: neural network source classification and photometric redshift catalogue for PS1 3π DR1. 500(2):1633–1644. doi: 10.1093/mnras/staa2587.

R. H. Becker, R. L. White, and D. J. Helfand. The FIRST Survey: Faint Images of the Radio Sky at Twenty Centimeters. ApJ, 450:559, Sept. 1995. doi: 10.1086/176166.

E. F. Bell, D. H. McIntosh, N. Katz, and M. D. Weinberg. The Optical and Near-Infrared Properties of Galaxies. I. Luminosity and Stellar Mass Functions. 149(2):289–312. doi: 10.1086/378847.

A. M. Beloborodov. A Flaring Magnetar in FRB 121102? ApJ, 843(2):L26, July 2017. doi: 10.3847/2041-8213/aa78f3.

A. M. Beloborodov. Blast Waves from Magnetar Flares and Fast Radio Bursts. ApJ, 896 (2):142, June 2020. doi: 10.3847/1538-4357/ab83eb.

R. Bender and S. Lange. Adjusting for multiple testing—when and how? *Journal of Clinical Epidemiology*, 54(4):343–349, 2001. ISSN 0895-4356. doi: https://doi.org/10.1016/S0895-4356(00)00314-0. URL https://www.sciencedirect.com/science/article/pii/S0895435600003140.

P. Beniamini, P. Kumar, and R. Narayan. Faraday depolarization and induced circular polarization by multipath propagation with application to FRBs. MNRAS, 510(3):4654–4668, Mar. 2022. doi: 10.1093/mnras/stab3730.

N. Benítez. Bayesian Photometric Redshift Estimation. ApJ, 536(2):571–583, June 2000. doi: 10.1086/308947.

G. B. Berriman and J. C. Good. The Application of the Montage Image Mosaic Engine To The Visualization Of Astronomical Images. PASP, 129(975):058006, May 2017. doi: 10.1088/1538-3873/aa5456.

S. Bhandari, K. W. Bannister, E. Lenc, H. Cho, R. Ekers, C. K. Day, A. T. Deller, C. Flynn, C. W. James, J.-P. Macquart, E. K. Mahony, L. Marnoch, V. A. Moss, C. Phillips, J. X. Prochaska, H. Qiu, S. D. Ryder, R. M. Shannon, N. Tejos, and O. I. Wong. Limits on Precursor and Afterglow Radio Emission from a Fast Radio Burst in a Star-forming Galaxy. ApJ, 901(2):L20, Oct. 2020. doi: 10.3847/2041-8213/abb462.

S. Bhandari, K. E. Heintz, K. Aggarwal, L. Marnoch, C. K. Day, J. Sydnor, S. Burke-Spolaor, C. J. Law, J. Xavier Prochaska, N. Tejos, K. W. Bannister, B. J. Butler, A. T. Deller, R. D. Ekers, C. Flynn, W.-f. Fong, C. W. James, T. J. W. Lazio, R. Luo, E. K. Mahony, S. D. Ryder, E. M. Sadler, R. M. Shannon, J. Han, K. Lee, and B. Zhang. Characterizing the Fast Radio Burst Host Galaxy Population and its Connection to Transients in the Local and Extragalactic Universe. AJ, 163(2):69, Feb. 2022. doi: 10.3847/1538-3881/ac3aec.

M. Bhardwaj, B. M. Gaensler, V. M. Kaspi, T. L. Landecker, R. Mckinven, D. Michilli, Z. Pleunis, S. P. Tendulkar, B. C. Andersen, P. J. Boyle, T. Cassanelli, P. Chawla, A. Cook, M. Dobbs, E. Fonseca, J. Kaczmarek, C. Leung, K. Masui, M. Mnchmeyer, C. Ng, M. Rafiei-Ravandi, P. Scholz, K. Shin, K. M. Smith, I. H. Stairs, and A. V. Zwaniga. A Nearby Repeating Fast Radio Burst in the Direction of M81. ApJ, 910 (2):L18, Apr. 2021a. doi: 10.3847/2041-8213/abeaa6.

M. Bhardwaj, A. Y. Kirichenko, D. Michilli, Y. D. Mayya, V. M. Kaspi, B. M. Gaensler, M. Rahman, S. P. Tendulkar, E. Fonseca, A. Josephy, C. Leung, M. Merryfield, E. Petroff, Z. Pleunis, P. Sanghavi, P. Scholz, K. Shin, K. M. Smith, and I. H. Stairs. A Local Universe Host for the Repeating Fast Radio Burst FRB 20181030A. ApJ, 919 (2):L24, Oct. 2021b. doi: 10.3847/2041-8213/ac223b.

P. K. Blanchard, E. Berger, and W.-f. Fong. The offset and host light distributions of long gamma-ray bursts: a new view from hst observations of swift bursts. *The Astrophysical Journal*, 817(2):144, 2016.

J. S. Bloom, S. R. Kulkarni, and S. G. Djorgovski. The Observed Offset Distribution of Gamma-Ray Bursts from Their Host Galaxies: A Robust Clue to the Nature of the Progenitors. AJ, 123(3):1111–1148, Mar. 2002. doi: 10.1086/338893.

J. S. Bloom, S. R. Kulkarni, and S. G. Djorgovski. The observed offset distribution of gamma-ray bursts from their host galaxies: a robust clue to the nature of the progenitors. *The Astronomical Journal*, 123(3):1111, 2002.

C. D. Bochenek, V. Ravi, K. V. Belov, G. Hallinan, J. Kocz, S. R. Kulkarni, and D. L. McKenna. A fast radio burst associated with a Galactic magnetar. *arXiv e-prints*, art. arXiv:2005.10828, May 2020.

F. Boerngen and V. E. Karachentseva. New dwarf galaxies in M 81/ M 82 group. *Astronomische Nachrichten*, 303(3):189–192, Jan. 1982. doi: 10.1002/asna.2103030303.

R. C. Bohlin, L. Colina, and D. S. Finley. White Dwarf Standard Stars: G191-B2B, GD 71, GD 153, HZ 43. AJ, 110:1316, Sept. 1995. doi: 10.1086/117606.

T. Boller, M. J. Freyberg, J. Trümper, F. Haberl, W. Voges, and K. Nandra. Second ROSAT all-sky survey (2RXS) source catalogue. A&A, 588:A103, Apr. 2016. doi: 10.1051/0004-6361/201525648.

D. G. Bonett and T. A. Wright. Sample size requirements for estimating pearson, kendall and spearman correlations. *Psychometrika*, 65(1):23–28, 2000.

A. Bosma. 21-cm line studies of spiral galaxies. ii. the distribution and kinematics of neutral hydrogen in spiral galaxies of various morphological types. *The Astronomical Journal*, 86:1825–1846, 1981.

P. Boyce, R. Minchin, V. Kilborn, M. Disney, R. Lang, C. Jordan, M. Grossi, A. Lyne, R. Cohen, I. Morison, et al. A blind hi survey of the m81 group. *The Astrophysical Journal Letters*, 560(2):L127, 2001.

G. B. Brammer, P. G. van Dokkum, and P. Coppi. EAZY: A Fast, Public Photometric Redshift Code. ApJ, 686(2):1503–1513, Oct. 2008. doi: 10.1086/591786.

R. Brandenberger, B. Cyr, and A. Varna Iyer. Fast Radio Bursts from the Decay of Cosmic String Cusps. *arXiv e-prints*, art. arXiv:1707.02397, July 2017.

C. Brasseur and T. Donaldson. MAST APIs: Present to Future. In R. Pizzo, E. R. Deul, J. D. Mol, J. de Plaa, and H. Verkouter, editors, *Astronomical Data Analysis Software and Systems XXIX*, volume 527 of *Astronomical Society of the Pacific Conference Series*, page 347, Jan. 2020.

J. N. Bregman and E. J. Lloyd-Davies. X-Ray Absorption from the Milky Way Halo and the Local Group. ApJ, 669(2):990–1002, Nov. 2007. doi: 10.1086/521321.

J. N. Bregman, M. E. Anderson, M. J. Miller, E. Hodges-Kluck, X. Dai, J.-T. Li, Y. Li, and Z. Qu. The Extended Distribution of Baryons around Galaxies. ApJ, 862(1):3, July 2018. doi: 10.3847/1538-4357/aacafe.

M. A. Brentjens and A. G. de Bruyn. Faraday rotation measure synthesis. A&A, 441(3): 1217–1228, Oct. 2005. doi: 10.1051/0004-6361:20052990.

J. P. Brodie and J. Strader. Extragalactic Globular Clusters and Galaxy Formation. ARA&A, 44(1):193–267, Sept. 2006. doi: 10.1146/annurev.astro.44.051905.092441.

W. R. Brown. Hypervelocity stars. *Annual Review of Astronomy and Astrophysics*, 53 (1):15–49, 2015. doi: 10.1146/annurev-astro-082214-122230. URL `https://doi.org/10.1146/annurev-astro-082214-122230`.

V. Buat, T. T. Takeuchi, J. Iglesias-Páramo, C. K. Xu, D. Burgarella, A. Boselli, T. Barlow, L. Bianchi, J. Donas, K. Forster, P. G. Friedman, T. M. Heckman, Y. W. Lee, B. F. Madore, D. C. Martin, B. Milliard, P. Morissey, S. Neff, M. Rich, D. Schiminovich, M. Seibert, T. Small, A. S. Szalay, B. Welsh, T. Wyder, and S. K. Yi. The Local Universe as Seen in the Far-Infrared and Far-Ultraviolet: A Global Point of View of the Local Recent Star Formation. ApJS, 173(2):404–414, Dec. 2007. doi: 10.1086/516645.

S. Burke-Spolaor. Multiple messengers of fast radio bursts. *Nature Astronomy*, 2(11): 845–848, 2018.

S. Burke-Spolaor, M. Bailes, R. Ekers, J.-P. Macquart, and I. Crawford, Fronefield. Radio Bursts with Extragalactic Spectral Characteristics Show Terrestrial Origins. ApJ, 727 (1):18, Jan. 2011. doi: 10.1088/0004-637X/727/1/18.

B. J. Burn. On the depolarization of discrete radio sources by Faraday dispersion. MNRAS, 133:67, Jan. 1966. doi: 10.1093/mnras/133.1.67.

H. R. Butcher. Lofar: First of a new generation of radio telescopes. In *Ground-based Telescopes*, volume 5489, pages 537–544. International Society for Optics and Photonics, 2004.

N. Byler, J. J. Dalcanton, C. Conroy, and B. D. Johnson. Nebular Continuum and Line Emission in Stellar Population Synthesis Models. ApJ, 840(1):44, May 2017. doi: 10.3847/1538-4357/aa6c66.

N. Caldwell, T. E. Armandroff, G. Da Costa, and P. Seitzer. Dwarf elliptical galaxies in the m81 group: The structure and stellar populations of bk5n and f8d1. *The Astronomical Journal*, 115(2):535, 1998.

M. Caleb and E. Keane. A Decade and a Half of Fast Radio Burst Observations. *Universe*, 7(11):453, Nov. 2021. doi: 10.3390/universe7110453.

M. Caleb, B. W. Stappers, K. Rajwade, and C. Flynn. Are all fast radio bursts repeating sources? MNRAS, 484(4):5500–5508, Apr. 2019. doi: 10.1093/mnras/stz386.

D. Calzetti, L. Armus, R. C. Bohlin, A. L. Kinney, J. Koornneef, and T. Storchi-Bergmann. The Dust Content and Opacity of Actively Star-forming Galaxies. ApJ, 533(2):682–695, Apr. 2000. doi: 10.1086/308692.

X.-F. Cao, Y.-W. Yu, and Z.-G. Dai. Constraining the Age of a Magnetar Possibly Associated with FRB 121102. ApJ, 839(2):L20, Apr. 2017. doi: 10.3847/2041-8213/aa6af2.

J. A. Cardelli, G. C. Clayton, and J. S. Mathis. The Relationship between Infrared, Optical, and Ultraviolet Extinction. ApJ, 345:245, Oct. 1989. doi: 10.1086/167900.

A. C. Carnall, J. Leja, B. D. Johnson, R. J. McLure, J. S. Dunlop, and C. Conroy. How to Measure Galaxy Star Formation Histories. I. Parametric Models. ApJ, 873(1):44, Mar. 2019. doi: 10.3847/1538-4357/ab04a2.

S. Cary, J. Mena-Parra, C. Leung, K. Masui, J. F. Kaczmarek, T. Cassanelli, and Chime/Frb Collaboration. Evaluating and Enhancing Candidate Clocking Systems for CHIME/FRB VLBI Outriggers. *Research Notes of the American Astronomical Society*, 5(9):216, Sept. 2021. doi: 10.3847/2515-5172/ac289d.

C. Casentini, F. Verrecchia, M. Tavani, A. Ursi, L. A. Antonelli, A. Argan, G. Barbiellini, A. Bulgarelli, P. Caraveo, M. Cardillo, P. W. Cattaneo, A. Chen, E. Costa, I. Donnarumma, M. Feroci, A. Ferrari, F. Fuschino, M. Galli, A. Giuliani, C. Labanti,

F. Lazzarotto, P. Lipari, F. Longo, F. Lucarelli, M. Marisaldi, A. Morselli, F. Paoletti, N. Parmiggiani, A. Pellizzoni, G. Piano, M. Pilia, C. Pittori, and S. Vercellone. AGILE Observations of Two Repeating Fast Radio Bursts with Low Intrinsic Dispersion Measures. ApJ, 890(2):L32, Feb. 2020. doi: 10.3847/2041-8213/ab720a.

T. Cassanelli, C. Leung, M. Rahman, K. Vanderlinde, J. Mena-Parra, S. Cary, K. W. Masui, J. Luo, H. H. Lin, A. Bij, A. Gill, D. Baker, K. Bandura, S. Berger, P. J. Boyle, C. Brar, S. Chatterjee, D. Cubranic, M. Dobbs, E. Fonseca, D. C. Good, J. F. Kaczmarek, V. M. Kaspi, T. L. Landecker, A. E. Lanman, D. Li, J. W. McKee, B. W. Meyers, D. Michilli, A. Naidu, C. Ng, C. Patel, A. B. Pearlman, U. L. Pen, Z. Pleunis, B. Quine, A. Renard, P. Sanghavi, K. M. Smith, I. Stairs, and S. P. Tendulkar. Localizing FRBs through VLBI with the Algonquin Radio Observatory 10 m Telescope. AJ, 163(2):65, Feb. 2022. doi: 10.3847/1538-3881/ac3d2f.

K. C. Chambers, E. A. Magnier, N. Metcalfe, H. A. Flewelling, M. E. Huber, C. Z. Waters, L. Denneau, P. W. Draper, D. Farrow, D. P. Finkbeiner, C. Holmberg, J. Koppenhoefer, P. A. Price, A. Rest, R. P. Saglia, E. F. Schlafly, S. J. Smartt, W. Sweeney, R. J. Wainscoat, W. S. Burgett, S. Chastel, T. Grav, J. N. Heasley, K. W. Hodapp, R. Jedicke, N. Kaiser, R. P. Kudritzki, G. A. Luppino, R. H. Lupton, D. G. Monet, J. S. Morgan, P. M. Onaka, B. Shiao, C. W. Stubbs, J. L. Tonry, R. White, E. Bañados, E. F. Bell, R. Bender, E. J. Bernard, M. Boegner, F. Boffi, M. T. Botticella, A. Calamida, S. Casertano, W. P. Chen, X. Chen, S. Cole, N. Deacon, C. Frenk, A. Fitzsimmons, S. Gezari, V. Gibbs, C. Goessl, T. Goggia, R. Gourgue, B. Goldman, P. Grant, E. K. Grebel, N. C. Hambly, G. Hasinger, A. F. Heavens, T. M. Heckman, R. Henderson, T. Henning, M. Holman, U. Hopp, W. H. Ip, S. Isani, M. Jackson, C. D. Keyes, A. M. Koekemoer, R. Kotak, D. Le, D. Liska, K. S. Long, J. R. Lucey, M. Liu, N. F. Martin, G. Masci, B. McLean, E. Mindel, P. Misra, E. Morganson, D. N. A. Murphy, A. Obaika, G. Narayan, M. A. Nieto-Santisteban, P. Norberg, J. A. Peacock, E. A. Pier, M. Postman, N. Primak, C. Rae, A. Rai, A. Riess, A. Riffeser, H. W. Rix, S. Röser, R. Russel, L. Rutz, E. Schilbach, A. S. B. Schultz, D. Scolnic, L. Strolger, A. Szalay, S. Seitz, E. Small, K. W. Smith, D. R. Soderblom, P. Taylor, R. Thomson, A. N. Taylor, A. R. Thakar, J. Thiel, D. Thilker, D. Unger, Y. Urata, J. Valenti, J. Wagner, T. Walder, F. Walter, S. P. Watters, S. Werner,

W. M. Wood-Vasey, and R. Wyse. The Pan-STARRS1 Surveys. *arXiv e-prints*, art. arXiv:1612.05560, Dec. 2016.

S. Charlot and S. M. Fall. A Simple Model for the Absorption of Starlight by Dust in Galaxies. ApJ, 539(2):718–731, Aug. 2000. doi: 10.1086/309250.

S. Chatterjee, W. Vlemmings, W. Brisken, T. Lazio, J. Cordes, W. Goss, S. Thorsett, E. Fomalont, A. Lyne, and M. Kramer. Getting its kicks: a vlba parallax for the hyperfast pulsar b1508+ 55. *The Astrophysical Journal Letters*, 630(1):L61, 2005.

S. Chatterjee, C. Law, R. Wharton, S. Burke-Spolaor, J. Hessels, G. Bower, J. Cordes, S. Tendulkar, C. Bassa, P. Demorest, et al. A direct localization of a fast radio burst and its host. *Nature*, 541(7635):58–61, 2017.

P. Chawla, V. M. Kaspi, S. M. Ransom, M. Bhardwaj, P. J. Boyle, D. Breitman, T. Cassanelli, D. Cubranic, F. Q. Dong, E. Fonseca, B. M. Gaensler, U. Giri, A. Josephy, J. F. Kaczmarek, C. Leung, K. W. Masui, J. Mena-Parra, M. Merryfield, D. Michilli, M. Münchmeyer, C. Ng, C. Patel, A. B. Pearlman, E. Petroff, Z. Pleunis, M. Rahman, P. Sanghavi, K. Shin, K. M. Smith, I. Stairs, and S. P. Tendulkar. Modeling Fast Radio Burst Dispersion and Scattering Properties in the First CHIME/FRB Catalog. ApJ, 927 (1):35, Mar. 2022. doi: 10.3847/1538-4357/ac49e1.

G. Chen, V. Ravi, and W. Lu. The multiwavelength counterparts of fast radio bursts. *arXiv preprint arXiv:2004.10787*, 2020.

G. Chen, V. Ravi, and G. W. Hallinan. A comprehensive observational study of the FRB 121102 persistent radio source. *arXiv e-prints*, art. arXiv:2201.00999, Jan. 2022.

H.-W. Chen. Outskirts of distant galaxies in absorption. In *Outskirts of Galaxies*, pages 291–331. Springer, 2017.

J. N. Chengalur, Y. Gupta, and K. Dwarkanath. Low frequency radio astronomy 3rd edition, 2007.

K. Chiboucas, I. D. Karachentsev, and R. B. Tully. Discovery of New Dwarf Galaxies in the M81 Group. AJ, 137(2):3009–3037, Feb. 2009. doi: 10.1088/0004-6256/137/2/3009.

CHIME Collaboration, M. Amiri, K. Bandura, A. Boskovic, T. Chen, J.-F. Cliche, M. Deng, N. Denman, M. Dobbs, M. Fandino, S. Foreman, M. Halpern, D. Hanna, A. S. Hill, G. Hinshaw, C. Höfer, J. Kania, P. Klages, T. L. Landecker, J. MacEachern, K. Masui, J. Mena-Parra, N. Milutinovic, A. Mirhosseini, L. Newburgh, R. Nitsche, A. Ordog, U.-L. Pen, T. Pinsonneault-Marotte, A. Polzin, A. Reda, A. Renard, J. R. Shaw, S. R. Siegel, S. Singh, R. Smegal, I. Tretyakov, K. van Gassen, K. Vanderlinde, H. Wang, D. V. Wiebe, J. S. Willis, and D. Wulf. An Overview of CHIME, the Canadian Hydrogen Intensity Mapping Experiment. ApJS, 261(2):29, Aug. 2022. doi: 10.3847/1538-4365/ac6fd9.

CHIME/FRB Collaboration. Recent high activity from a repeating Fast Radio Burst discovered by CHIME/FRB. *The Astronomer's Telegram*, 14497:1, Mar. 2021.

CHIME/FRB Collaboration, M. Amiri, K. Bandura, P. Berger, M. Bhardwaj, M. M. Boyce, P. J. Boyle, C. Brar, M. Burhanpurkar, P. Chawla, J. Chowdhury, J. F. Cliche, M. D. Cranmer, D. Cubranic, M. Deng, N. Denman, M. Dobbs, M. Fandino, E. Fonseca, B. M. Gaensler, U. Giri, A. J. Gilbert, D. C. Good, S. Guliani, M. Halpern, G. Hinshaw, C. Höfer, A. Josephy, V. M. Kaspi, T. L. Landecker, D. Lang, H. Liao, K. W. Masui, J. Mena-Parra, A. Naidu, L. B. Newburgh, C. Ng, C. Patel, U. L. Pen, T. Pinsonneault-Marotte, Z. Pleunis, M. Rafiei Ravandi, S. M. Ransom, A. Renard, P. Scholz, K. Sigurdson, S. R. Siegel, K. M. Smith, I. H. Stairs, S. P. Tendulkar, K. Vand erlinde, and D. V. Wiebe. The CHIME Fast Radio Burst Project: System Overview. ApJ, 863(1):48, Aug. 2018. doi: 10.3847/1538-4357/aad188.

CHIME/FRB Collaboration, M. Amiri, K. Bandura, M. Bhardwaj, P. Boubel, M. M. Boyce, P. J. Boyle, C. . Brar, M. Burhanpurkar, T. Cassanelli, P. Chawla, J. F. Cliche, D. Cubranic, M. Deng, N. Denman, M. Dobbs, M. Fandino, E. Fonseca, B. M. Gaensler, A. J. Gilbert, A. Gill, U. Giri, D. C. Good, M. Halpern, D. S. Hanna, A. S. Hill, G. Hinshaw, C. Höfer, A. Josephy, V. M. Kaspi, T. L. Landecker, D. A. Lang, H. H. Lin, K. W. Masui, R. Mckinven, J. Mena-Parra, M. Merryfield, D. Michilli, N. Milutinovic, C. Moatti, A. Naidu, L. B. Newburgh, C. Ng, C. Patel, U. Pen, T. Pinsonneault-Marotte, Z. Pleunis, M. Rafiei-Ravandi, M. Rahman, S. M. Ransom, A. Renard, P. Scholz, J. R. Shaw, S. R. Siegel, K. M. Smith, I. H. Stairs, S. P. Tendulkar, I. Tretyakov, K. Vanderlinde, and P. Yadav. A second source of repeating fast radio bursts. Nature, 566(7743): 235–238, Jan. 2019a. doi: 10.1038/s41586-018-0864-x.

CHIME/FRB Collaboration, M. Amiri, K. Bandura, M. Bhardwaj, P. Boubel, M. M. Boyce, P. J. Boyle, C. Brar, M. Burhanpurkar, P. Chawla, J. F. Cliche, D. Cubranic, M. Deng, N. Denman, M. Dobbs, M. Fand ino, E. Fonseca, B. M. Gaensler, A. J. Gilbert, U. Giri, D. C. Good, M. Halpern, D. Hanna, A. S. Hill, G. Hinshaw, C. Höfer, A. Josephy, V. M. Kaspi, T. L. Landecker, D. A. Lang, K. W. Masui, R. Mckinven, J. Mena-Parra, M. Merryfield, N. Milutinovic, C. Moatti, A. Naidu, L. B. Newburgh, C. Ng, C. Patel, U. Pen, T. Pinsonneault-Marotte, Z. Pleunis, M. Rafiei-Ravandi, S. M. Ransom, A. Renard, P. Scholz, J. R. Shaw, S. R. Siegel, K. M. Smith, I. H. Stairs, S. P. Tendulkar, I. Tretyakov, K. Vand erlinde, and P. Yadav. Observations of fast radio bursts at frequencies down to 400 megahertz. Nature, 566(7743):230–234, Jan. 2019b. doi: 10.1038/s41586-018-0867-7.

CHIME/FRB Collaboration, B. C. Andersen, K. Band ura, M. Bhardwaj, P. Boubel, M. M. Boyce, P. J. Boyle, C. Brar, T. Cassanelli, P. Chawla, D. Cubranic, M. Deng, M. Dobbs, M. Fandino, E. Fonseca, B. M. Gaensler, A. J. Gilbert, U. Giri, D. C. Good, M. Halpern, C. Höfer, A. S. Hill, G. Hinshaw, A. Josephy, V. M. Kaspi, R. Kothes, T. L. Landecker, D. A. Lang, D. Z. Li, H. H. Lin, K. W. Masui, J. Mena-Parra, M. Merryfield, R. Mckinven, D. Michilli, N. Milutinovic, A. Naidu, L. B. Newburgh, C. Ng, C. Patel, U. Pen, T. Pinsonneault-Marotte, Z. Pleunis, M. Rafiei-Ravandi, M. Rahman, S. M. Ransom, A. Renard, P. Scholz, S. R. Siegel, S. Singh, K. M. Smith, I. H. Stairs, S. P. Tendulkar, I. Tretyakov, K. Vanderlinde, P. Yadav, and A. V. Zwaniga. CHIME/FRB Detection of Eight New Repeating Fast Radio Burst Sources. ApJ, 885(1):L24, Aug 2019c.

CHIME/FRB Collaboration, :, B. C. Andersen, K. M. Band ura, M. Bhardwaj, A. Bij, M. M. Boyce, P. J. Boyle, C. Brar, T. Cassanelli, P. Chawla, T. Chen, J. F. Cliche, A. Cook, D. Cubranic, A. P. Curtin, N. T. Denman, M. Dobbs, F. Q. Dong, M. Fandino, E. Fonseca, B. M. Gaensler, U. Giri, D. C. Good, M. Halpern, A. S. Hill, G. F. Hinshaw, C. Höfer, A. Josephy, J. W. Kania, V. M. Kaspi, T. L. Landecker, C. Leung, D. Z. Li, H. H. Lin, K. W. Masui, R. Mckinven, J. Mena-Parra, M. Merryfield, B. W. Meyers, D. Michilli, N. Milutinovic, A. Mirhosseini, M. Münchmeyer, A. Naidu, L. B. Newburgh, C. Ng, C. Patel, U. L. Pen, T. Pinsonneault-Marotte, Z. Pleunis, B. M. Quine, M. Rafiei-Ravandi, M. Rahman, S. M. Ransom, A. Renard, P. Sanghavi, P. Scholz, J. R. Shaw, K. Shin, S. R. Siegel, S. Singh, R. J. Smegal, K. M. Smith, I. H. Stairs, C. M. Tan,

S. P. Tendulkar, I. Tretyakov, K. Vanderlinde, H. Wang, D. Wulf, and A. V. Zwaniga. A bright millisecond-duration radio burst from a Galactic magnetar. *arXiv e-prints*, art. arXiv:2005.10324, May 2020a.

CHIME/FRB Collaboration, M. Amiri, B. C. Andersen, K. M. Bandura, M. Bhardwaj, P. J. Boyle, C. Brar, P. Chawla, T. Chen, J. F. Cliche, D. Cubranic, M. Deng, N. T. Denman, M. Dobbs, F. Q. Dong, M. Fandino, E. Fonseca, B. M. Gaensler, U. Giri, D. C. Good, M. Halpern, J. W. T. Hessels, A. S. Hill, C. Höfer, A. Josephy, J. W. Kania, R. Karuppusamy, V. M. Kaspi, A. Keimpema, F. Kirsten, T. L. Landecker, D. A. Lang, C. Leung, D. Z. Li, H. H. Lin, B. Marcote, K. W. Masui, R. McKinven, J. Mena-Parra, M. Merryfield, D. Michilli, N. Milutinovic, A. Mirhosseini, A. Naidu, L. B. Newburgh, C. Ng, K. Nimmo, Z. Paragi, C. Patel, U. L. Pen, T. Pinsonneault-Marotte, Z. Pleunis, M. Rafiei-Ravandi, M. Rahman, S. M. Ransom, A. Renard, P. Sanghavi, P. Scholz, J. R. Shaw, K. Shin, S. R. Siegel, S. Singh, R. J. Smegal, K. M. Smith, I. H. Stairs, S. P. Tendulkar, I. Tretyakov, K. Vanderlinde, H. Wang, X. Wang, D. Wulf, P. Yadav, and A. V. Zwaniga. Periodic activity from a fast radio burst source. Nature, 582(7812): 351–355, June 2020b. doi: 10.1038/s41586-020-2398-2.

B. C. CHIME/FRB Collaboration, Andersen, K. Bandura, M. Bhardwaj, P. J. Boyle, C. Brar, D. Breitman, T. Cassanelli, S. Chatterjee, P. Chawla, J.-F. Cliche, D. Cubranic, A. P. Curtin, M. Deng, M. Dobbs, F. A. Dong, E. Fonseca, B. M. Gaensler, U. Giri, D. C. Good, A. S. Hill, A. Josephy, J. F. Kaczmarek, Z. Kader, J. Kania, V. M. Kaspi, C. Leung, D. Z. Li, H.-H. Lin, K. W. Masui, R. McKinven, J. Mena-Parra, M. Merryfield, B. W. Meyers, D. Michilli, A. Naidu, L. Newburgh, C. Ng, A. Ordog, C. Patel, A. B. Pearlman, U.-L. Pen, E. Petroff, Z. Pleunis, M. Rafiei-Ravandi, M. Rahman, S. Ransom, A. Renard, P. Sanghavi, P. Scholz, J. R. Shaw, K. Shin, S. R. Siegel, S. Singh, K. Smith, I. Stairs, C. M. Tan, S. P. Tendulkar, K. Vanderlinde, D. V. Wiebe, D. Wulf, and A. Zwaniga. Subsecond periodicity in a fast radio burst. Nature, 607(7918):256–259, July 2022. doi: 10.1038/s41586-022-04841-8.

CHIME/Pulsar Collaboration, M. Amiri, K. M. Bandura, P. J. Boyle, C. Brar, J. F. Cliche, K. Crowter, D. Cubranic, P. B. Demorest, N. T. Denman, M. Dobbs, F. Q. Dong, M. Fandino, E. Fonseca, D. C. Good, M. Halpern, A. S. Hill, C. Höfer, V. M. Kaspi,

T. L. Landecker, C. Leung, H. H. Lin, J. Luo, K. W. Masui, J. W. McKee, J. Mena-Parra, B. W. Meyers, D. Michilli, A. Naidu, L. Newburgh, C. Ng, C. Patel, T. Pinsonneault-Marotte, S. M. Ransom, A. Renard, P. Scholz, J. R. Shaw, A. E. Sikora, I. H. Stairs, C. M. Tan, S. P. Tendulkar, I. Tretyakov, K. Vanderlinde, H. Wang, and X. Wang. The CHIME Pulsar Project: System Overview. ApJS, 255(1):5, July 2021. doi: 10.3847/1538-4365/abfdcb.

H. Cho, J.-P. Macquart, R. M. Shannon, A. T. Deller, I. S. Morrison, R. D. Ekers, K. W. Bannister, W. Farah, H. Qiu, M. W. Sammons, M. Bailes, S. Bhandari, C. K. Day, C. W. James, C. J. Phillips, J. X. Prochaska, and J. Tuthill. Spectropolarimetric Analysis of FRB 181112 at Microsecond Resolution: Implications for Fast Radio Burst Emission Mechanism. ApJ, 891(2):L38, Mar. 2020. doi: 10.3847/2041-8213/ab7824.

K. M. Chynoweth, G. I. Langston, M. S. Yun, F. J. Lockman, K. Rubin, and S. A. Scoles. Neutral hydrogen clouds in the m81/m82 group. *The Astronomical Journal*, 135(6): 1983, 2008.

C. J. R. Clark, S. Verstocken, S. Bianchi, J. Fritz, S. Viaene, M. W. L. Smith, M. Baes, V. Casasola, L. P. Cassara, J. I. Davies, I. De Looze, P. De Vis, R. Evans, M. Galametz, A. P. Jones, S. Lianou, S. Madden, A. V. Mosenkov, and M. Xilouris. DustPedia: Multi-wavelength photometry and imagery of 875 nearby galaxies in 42 ultraviolet-microwave bands. A&A, 609:A37, Jan. 2018. doi: 10.1051/0004-6361/201731419.

I. Cognard, J. A. Shrauner, J. H. Taylor, and S. E. Thorsett. Giant Radio Pulses from a Millisecond Pulsar. ApJ, 457:L81, Feb. 1996. doi: 10.1086/309894.

J. J. Condon, W. Cotton, E. Greisen, Q. Yin, R. A. Perley, G. Taylor, and J. Broderick. The nrao vla sky survey. *The Astronomical Journal*, 115(5):1693, 1998.

J. J. Condon, Q. F. Yin, T. X. Thuan, and T. Boller. The ROSAT/IRAS Galaxy Sample Revisited. AJ, 116(6):2682–2716, Dec. 1998. doi: 10.1086/300624.

L. Connor and V. Ravi. The observed impact of galaxy halo gas on fast radio bursts. ISSN 2397-3366. doi: 10.1038/s41550-022-01719-7. URL https://doi.org/10.1038/s41550-022-01719-7.

C. Conroy, J. E. Gunn, and M. White. The Propagation of Uncertainties in Stellar Population Synthesis Modeling. I. The Relevance of Uncertain Aspects of Stellar Evolution and the Initial Mass Function to the Derived Physical Properties of Galaxies. ApJ, 699 (1):486–506, July 2009. doi: 10.1088/0004-637X/699/1/486.

F. Contenta, M. Gieles, E. Balbinot, and M. L. M. Collins. The contribution of dissolving star clusters to the population of ultra faint objects in the outer halo of the Milky Way. MNRAS, 466(2):1741–1756, Apr. 2017. doi: 10.1093/mnras/stw3178.

J. M. Cordes and T. J. W. Lazio. NE2001.I. A New Model for the Galactic Distribution of Free Electrons and its Fluctuations. *arXiv e-prints*, art. astro-ph/0207156, July 2002.

J. M. Cordes and T. J. W. Lazio. Ne2001. i. a new model for the galactic distribution of free electrons and its fluctuations. *arXiv preprint astro-ph/0207156*, 2002.

J. M. Cordes and M. A. McLaughlin. Searches for Fast Radio Transients. ApJ, 596(2): 1142–1154, Oct. 2003. doi: 10.1086/378231.

J. M. Cordes and I. Wasserman. Supergiant pulses from extragalactic neutron stars. MNRAS, 457(1):232–257, Mar. 2016. doi: 10.1093/mnras/stv2948.

J. M. Cordes, R. S. Wharton, L. G. Spitler, S. Chatterjee, and I. Wasserman. Radio Wave Propagation and the Provenance of Fast Radio Bursts. *arXiv e-prints*, art. arXiv:1605.05890, May 2016.

A. H. Costa and S. R. Spangler. A faraday rotation study of the stellar bubble and h ii region associated with the w4 complex. *The Astrophysical Journal*, 865(1):65, 2018.

B. P. Crill, M. Werner, R. Akeson, M. Ashby, L. Bleem, J. J. Bock, S. Bryan, J. Burnham, J. Byunh, T.-C. Chang, Y.-K. Chiang, W. Cook, A. Cooray, A. Davis, O. Doré, C. D. Dowell, G. Dubois-Felsmann, T. Eifler, A. Faisst, S. Habib, C. Heinrich, K. Heitmann, G. Heaton, C. Hirata, V. Hristov, H. Hui, W.-S. Jeong, J. H. Kang, B. Kecman, J. D. Kirkpatrick, P. M. Korngut, E. Krause, B. Lee, C. Lisse, D. Masters, P. Mauskopf, G. Melnick, H. Miyasaka, H. Nayyeri, H. Nguyen, K. Öberg, S. Padin, R. Paladini, M. Pourrahmani, J. Pyo, R. Smith, Y.-S. Song, T. Symons, H. Teplitz, V. Tolls, S. Unwin, R. Windhorst,

Y. Yang, and M. Zemcov. SPHEREx: NASA's near-infrared spectrophotometric all-sky survey. In *Society of Photo-Optical Instrumentation Engineers (SPIE) Conference Series*, volume 11443 of *Society of Photo-Optical Instrumentation Engineers (SPIE) Conference Series*, page 114430I, Dec. 2020. doi: 10.1117/12.2567224.

P. Crowther. Birth, life and death of massive stars. *Astronomy & Geophysics*, 53(4): 4.30–4.36, 08 2012. ISSN 1366-8781. doi: 10.1111/j.1468-4004.2012.53430.x. URL https://doi.org/10.1111/j.1468-4004.2012.53430.x.

M. Cruces, L. G. Spitler, P. Scholz, R. Lynch, A. Seymour, J. W. T. Hessels, C. Gouiffés, G. H. Hilmarsson, M. Kramer, and S. Munjal. Repeating behaviour of FRB 121102: periodicity, waiting times, and energy distribution. MNRAS, 500(1):448–463, Jan. 2020. doi: 10.1093/mnras/staa3223.

V. Cunningham, S. B. Cenko, E. Burns, A. Goldstein, A. Lien, D. Kocevski, M. Briggs, V. Connaughton, M. C. Miller, J. Racusin, and M. Stanbro. A Search for High-energy Counterparts to Fast Radio Bursts. ApJ, 879(1):40, July 2019. doi: 10.3847/1538-4357/ab2235.

A. P. Curtin, S. P. Tendulkar, A. Josephy, P. Chawla, B. Andersen, V. M. Kaspi, M. Bhardwaj, T. Cassanelli, A. Cook, F. A. Dong, E. Fonseca, B. M. Gaensler, J. F. Kaczmarek, A. E. Lanmnan, C. Leung, A. B. Pearlman, E. Petroff, Z. Pleunis, M. Rafiei-Ravandi, S. M. Ransom, K. Shin, P. Scholz, K. Smith, and I. Stairs. Limits on Fast Radio Burst-like Counterparts to Gamma-ray Bursts using CHIME/FRB. *arXiv e-prints*, art. arXiv:2208.00803, Aug. 2022.

R. M. Cutri, E. L. Wright, T. Conrow, J. W. Fowler, P. R. M. Eisenhardt, C. Grillmair, J. D. Kirkpatrick, F. Masci, H. L. McCallon, S. L. Wheelock, S. Fajardo-Acosta, L. Yan, D. Benford, M. Harbut, T. Jarrett, S. Lake, D. Leisawitz, M. E. Ressler, S. A. Stanford, C. W. Tsai, F. Liu, G. Helou, A. Mainzer, D. Gettngs, A. Gonzalez, D. Hoffman, K. A. Marsh, D. Padgett, M. F. Skrutskie, R. Beck, M. Papin, and M. Wittman. VizieR Online Data Catalog: AllWISE Data Release (Cutri+ 2013). *VizieR Online Data Catalog*, art. II/328, Feb. 2021.

R. D'Agostino and E. S. Pearson. Tests for departure from normality. empirical results for the distributions of b_2 and $\sqrt{b}$. *Biometrika*, 60(3):613–622, 1973.

R. B. d'Agostino. An omnibus test of normality for moderate and large size samples. *Biometrika*, 58(2):341–348, 1971.

Z. G. Dai and S. Q. Zhong. Periodic Fast Radio Bursts as a Probe of Extragalactic Asteroid Belts. ApJ, 895(1):L1, May 2020. doi: 10.3847/2041-8213/ab8f2d.

Z. G. Dai, J. S. Wang, X. F. Wu, and Y. F. Huang. Repeating Fast Radio Bursts from Highly Magnetized Pulsars Traveling through Asteroid Belts. ApJ, 829(1):27, Sept. 2016. doi: 10.3847/0004-637X/829/1/27.

Z. G. Dai, J. S. Wang, and Y. W. Yu. Radio Emission from Pulsar Wind Nebulae without Surrounding Supernova Ejecta: Application to FRB 121102. ApJ, 838(1):L7, Mar. 2017. doi: 10.3847/2041-8213/aa6745.

D. A. Dale and G. Helou. The Infrared Spectral Energy Distribution of Normal Star-forming Galaxies: Calibration at Far-Infrared and Submillimeter Wavelengths. ApJ, 576 (1):159–168, Sept. 2002. doi: 10.1086/341632.

T. M. Dame, D. Hartmann, and P. Thaddeus. The Milky Way in Molecular Clouds: A New Complete CO Survey. ApJ, 547(2):792–813, Feb. 2001. doi: 10.1086/318388.

L. J. M. Davies, M. T. Huynh, A. M. Hopkins, N. Seymour, S. P. Driver, A. G. R. Robotham, I. K. Baldry, J. Bland-Hawthorn, N. Bourne, M. N. Bremer, M. J. I. Brown, S. Brough, M. Cluver, M. W. Grootes, M. Jarvis, J. Loveday, A. Moffet, M. Owers, S. Phillipps, E. Sadler, L. Wang, S. Wilkins, and A. Wright. Galaxy And Mass Assembly: the 1.4 GHz SFR indicator, SFR-M_* relation and predictions for ASKAP-GAMA. MNRAS, 466(2):2312–2324, Apr. 2017. doi: 10.1093/mnras/stw3080.

C. K. Day, A. T. Deller, R. M. Shannon, H. Qiu, K. W. Bannister, S. Bhandari, R. Ekers, C. Flynn, C. W. James, J.-P. Macquart, E. K. Mahony, C. J. Phillips, and J. Xavier Prochaska. High time resolution and polarization properties of ASKAP-localized fast radio bursts. MNRAS, 497(3):3335–3350, Sept. 2020. doi: 10.1093/mnras/staa2138.

W. J. G. de Blok, F. Walter, E. Brinks, C. Trachternach, S. H. Oh, and J. Kennicutt, R. C. High-Resolution Rotation Curves and Galaxy Mass Models from THINGS. AJ, 136(6): 2648–2719, Dec. 2008. doi: 10.1088/0004-6256/136/6/2648.

W. J. G. de Blok, F. Walter, A. M. N. Ferguson, E. J. Bernard, J. M. van der Hulst, M. Neeleman, A. K. Leroy, J. Ott, L. K. Zschaechner, M. A. Zwaan, M. S. Yun, G. Langston, and K. M. Keating. A High-resolution Mosaic of the Neutral Hydrogen in the M81 Triplet. ApJ, 865(1):26, Sept. 2018. doi: 10.3847/1538-4357/aad557.

R. de Heide and P. D. Grünwald. Why optional stopping can be a problem for bayesians. *Psychonomic Bulletin & Review*, pages 1–18, 2020.

G. de Vaucouleurs, A. de Vaucouleurs, J. Corwin, Herold G., R. J. Buta, G. Paturel, and P. Fouque. *Third Reference Catalogue of Bright Galaxies*. Springer, 1991.

D. R. DeBoer, A. R. Parsons, J. E. Aguirre, P. Alexander, Z. S. Ali, A. P. Beardsley, G. Bernardi, J. D. Bowman, R. F. Bradley, C. L. Carilli, et al. Hydrogen epoch of reionization array (hera). *Publications of the Astronomical Society of the Pacific*, 129 (974):045001, 2017.

W. Dehnen, D. E. McLaughlin, and J. Sachania. The velocity dispersion and mass profile of the Milky Way. MNRAS, 369(4):1688–1692, July 2006. doi: 10.1111/j.1365-2966. 2006.10404.x.

J. J. DeLaunay, D. B. Fox, K. Murase, P. Mészáros, A. Keivani, C. Messick, M. A. Mostafá, F. Oikonomou, G. Tešić, and C. F. Turley. Discovery of a Transient Gamma-Ray Counterpart to FRB 131104. ApJ, 832(1):L1, Nov. 2016. doi: 10.3847/2041-8205/832/1/L1.

C.-M. Deng, Y. Cai, X.-F. Wu, and E.-W. Liang. Fast radio bursts from primordial black hole binaries coalescence. Phys. Rev. D, 98(12):123016, Dec. 2018. doi: 10.1103/ PhysRevD.98.123016.

M. Deng and D. Campbell-Wilson. The cloverleaf antenna: A compact wide-bandwidth dual-polarization feed for chime. In *2014 16th International Symposium on Antenna Technology and Applied Electromagnetics (ANTEM)*, pages 1–2. IEEE, 2014.

N. Denman, A. Renard, K. Vanderlinde, P. Berger, K. Masui, and I. Tretyakov. A GPU Spatial Processing System for CHIME. *Journal of Astronomical Instrumentation*, 9(3): 2050014-2, Jan. 2020. doi: 10.1142/S2251171720500142.

DESI Collaboration, A. Aghamousa, J. Aguilar, S. Ahlen, S. Alam, L. E. Allen, C. Allende Prieto, J. Annis, S. Bailey, C. Balland, O. Ballester, C. Baltay, L. Beaufore, C. Bebek, T. C. Beers, E. F. Bell, J. L. Bernal, R. Besuner, F. Beutler, C. Blake, H. Bleuler, M. Blomqvist, R. Blum, A. S. Bolton, C. Briceno, D. Brooks, J. R. Brownstein, E. Buckley-Geer, A. Burden, E. Burtin, N. G. Busca, R. N. Cahn, Y.-C. Cai, L. Cardiel-Sas, R. G. Carlberg, P.-H. Carton, R. Casas, F. J. Castander, J. L. Cervantes-Cota, T. M. Claybaugh, M. Close, C. T. Coker, S. Cole, J. Comparat, A. P. Cooper, M. C. Cousinou, M. Crocce, J.-G. Cuby, D. P. Cunningham, T. M. Davis, K. S. Dawson, A. de la Macorra, J. De Vicente, T. Delubac, M. Derwent, A. Dey, G. Dhungana, Z. Ding, P. Doel, Y. T. Duan, A. Ealet, J. Edelstein, S. Eftekharzadeh, D. J. Eisenstein, A. Elliott, S. Escoffier, M. Evatt, P. Fagrelius, X. Fan, K. Fanning, A. Farahi, J. Farihi, G. Favole, Y. Feng, E. Fernandez, J. R. Findlay, D. P. Finkbeiner, M. J. Fitzpatrick, B. Flaugher, S. Flender, A. Font-Ribera, J. E. Forero-Romero, P. Fosalba, C. S. Frenk, M. Fumagalli, B. T. Gaensicke, G. Gallo, J. Garcia-Bellido, E. Gaztanaga, N. Pietro Gentile Fusillo, T. Gerard, I. Gershkovich, T. Giannantonio, D. Gillet, G. Gonzalez-de-Rivera, V. Gonzalez-Perez, S. Gott, O. Graur, G. Gutierrez, J. Guy, S. Habib, H. Heetderks, I. Heetderks, K. Heitmann, W. A. Hellwing, D. A. Herrera, S. Ho, S. Holland, K. Honscheid, E. Huff, T. A. Hutchinson, D. Huterer, H. S. Hwang, J. M. Illa Laguna, Y. Ishikawa, D. Jacobs, N. Jeffrey, P. Jelinsky, E. Jennings, L. Jiang, J. Jimenez, J. Johnson, R. Joyce, E. Jullo, S. Juneau, S. Kama, A. Karcher, S. Karkar, R. Kehoe, N. Kennamer, S. Kent, M. Kilbinger, A. G. Kim, D. Kirkby, T. Kisner, E. Kitanidis, J.-P. Kneib, S. Koposov, E. Kovacs, K. Koyama, A. Kremin, R. Kron, L. Kronig, A. Kueter-Young, C. G. Lacey, R. Lafever, O. Lahav, A. Lambert, M. Lampton, M. Landriau, D. Lang, T. R. Lauer, J.-M. Le Goff, L. Le Guillou, A. Le Van Suu, J. H. Lee, S.-J. Lee, D. Leitner, M. Lesser, M. E. Levi, B. L'Huillier, B. Li, M. Liang, H. Lin, E. Linder, S. R. Loebman, Z. Lukić, J. Ma, N. MacCrann, C. Magneville, L. Makarem, M. Manera, C. J. Manser, R. Marshall, P. Martini, R. Massey, T. Matheson, J. McCauley, P. McDonald, I. D. McGreer, A. Meisner, N. Metcalfe, T. N. Miller, R. Miquel, J. Moustakas, A. Myers, M. Naik, J. A. Newman, R. C. Nichol, A. Nicola, L. Nicolati da Costa, J. Nie, G. Niz, P. Norberg, B. Nord, D. Norman, P. Nugent, T. O'Brien, M. Oh, K. A. G. Olsen, C. Padilla, H. Padmanabhan, N. Padmanabhan, N. Palanque-Delabrouille, A. Palmese, D. Pappalardo, I. Pâris, C. Park, A. Patej, J. A. Peacock, H. V. Peiris, X. Peng, W. J. Percival, S. Perruchot, M. M. Pieri, R. Pogge, J. E. Pollack, C. Poppett, F. Prada, A. Prakash, R. G. Probst, D. Rabinowitz, A. Raichoor, C. H. Ree, A. Refregier, X. Regal, B. Reid, K. Reil, M. Rezaie, C. M. Rockosi, N. Roe, S. Ronayette, A. Roodman, A. J. Ross, N. P. Ross, G. Rossi, E. Rozo, V. Ruhlmann-Kleider, E. S. Rykoff, C. Sabiu, L. Samushia, E. Sanchez, J. Sanchez, D. J. Schlegel, M. Schneider, M. Schubnell, A. Secroun, U. Seljak, H.-J. Seo, S. Serrano, A. Shafieloo, H. Shan, R. Sharples, M. J. Sholl, W. V. Shourt, J. H. Silber, D. R. Silva, M. M. Sirk, A. Slosar, A. Smith, G. F. Smoot, D. Som, Y.-S. Song, D. Sprayberry, R. Staten, A. Stefanik, G. Tarle, S. Sien Tie, J. L. Tinker, R. Tojeiro, F. Valdes, O. Valenzuela, M. Valluri, M. Vargas-Magana, L. Verde, A. R. Walker, J. Wang, Y. Wang, B. A. Weaver, C. Weaverdyck, R. H. Wechsler, D. H. Weinberg, M. White, Q. Yang, C. Yeche, T. Zhang, G.-B. Zhao, Y. Zheng, X. Zhou, Z. Zhou, Y. Zhu, H. Zou, and Y. Zu. The DESI Experiment Part I: Science,Targeting, and Survey Design. *arXiv e-prints*, art. arXiv:1611.00036, Oct. 2016.

A. Dey, D. J. Schlegel, D. Lang, R. Blum, K. Burleigh, X. Fan, J. R. Findlay, D. Finkbeiner, D. Herrera, S. Juneau, M. Landriau, M. Levi, I. McGreer, A. Meisner, A. D. Myers, J. Moustakas, P. Nugent, A. Patej, E. F. Schlafly, A. R. Walker, F. Valdes, B. A. Weaver, C. Yèche, H. Zou, X. Zhou, B. Abareshi, T. M. C. Abbott, B. Abolfathi, C. Aguilera, S. Alam, L. Allen, A. Alvarez, J. Annis, B. Ansarinejad, M. Aubert, J. Beechert, E. F. Bell, S. Y. BenZvi, F. Beutler, R. M. Bielby, A. S. Bolton, C. Briceño, E. J. Buckley-Geer, K. Butler, A. Calamida, R. G. Carlberg, P. Carter, R. Casas, F. J. Castander, Y. Choi, J. Comparat, E. Cukanovaite, T. Delubac, K. DeVries, S. Dey, G. Dhungana, M. Dickinson, Z. Ding, J. B. Donaldson, Y. Duan, C. J. Duckworth, S. Eftekharzadeh, D. J. Eisenstein, T. Etourneau, P. A. Fagrelius, J. Farihi, M. Fitzpatrick, A. Font-Ribera, L. Fulmer, B. T. Gänsicke, E. Gaztanaga, K. George, D. W. Gerdes, S. G. A. Gontcho, C. Gorgoni, G. Green, J. Guy, D. Harmer, M. Hernand ez, K. Honscheid, L. W. Huang, D. J. James, B. T. Jannuzi, L. Jiang, R. Joyce, A. Karcher, S. Karkar, R. Kehoe, J.-P. Kneib, A. Kueter-Young, T.-W. Lan, T. R. Lauer, L. Le Guillou, A. Le Van Suu, J. H.

Lee, M. Lesser, L. Perreault Levasseur, T. S. Li, J. L. Mann, R. Marshall, C. E. Martínez-Vázquez, P. Martini, H. du Mas des Bourboux, S. McManus, T. G. Meier, B. Ménard, N. Metcalfe, A. Muñoz-Gutiérrez, J. Najita, K. Napier, G. Narayan, J. A. Newman, J. Nie, B. Nord, D. J. Norman, K. A. G. Olsen, A. Paat, N. Palanque-Delabrouille, X. Peng, C. L. Poppett, M. R. Poremba, A. Prakash, D. Rabinowitz, A. Raichoor, M. Rezaie, A. N. Robertson, N. A. Roe, A. J. Ross, N. P. Ross, G. Rudnick, S. Safonova, A. Saha, F. J. Sánchez, E. Savary, H. Schweiker, A. Scott, H.-J. Seo, H. Shan, D. R. Silva, Z. Slepian, C. Soto, D. Sprayberry, R. Staten, C. M. Stillman, R. J. Stupak, D. L. Summers, S. Sien Tie, H. Tirado, M. Vargas-Magaña, A. K. Vivas, R. H. Wechsler, D. Williams, J. Yang, Q. Yang, T. Yapici, D. Zaritsky, A. Zenteno, K. Zhang, T. Zhang, R. Zhou, and Z. Zhou. Overview of the DESI Legacy Imaging Surveys. AJ, 157(5):168, May 2019. doi: 10.3847/1538-3881/ab089d.

K. Dolag, B. M. Gaensler, A. M. Beck, and M. C. Beck. Constraints on the distribution and energetics of fast radio bursts using cosmological hydrodynamic simulations. *Monthly Notices of the Royal Astronomical Society*, 451(4):4277–4289, 2015.

R. Dong, J. Gunn, G. Knapp, C. Rockosi, and M. Blanton. Investigation of the Errors in Sloan Digital Sky Survey Proper-motion Measurements Using Samples of Quasars. AJ, 142(4):116, Oct. 2011. doi: 10.1088/0004-6256/142/4/116.

B. T. Draine and A. Li. Infrared Emission from Interstellar Dust. IV. The Silicate-Graphite-PAH Model in the Post-Spitzer Era. ApJ, 657(2):810–837, Mar. 2007. doi: 10.1086/511055.

S. P. Driver, S. K. Andrews, L. J. Davies, A. S. Robotham, A. H. Wright, R. A. Windhorst, S. Cohen, K. Emig, R. A. Jansen, and L. Dunne. Measurements of extragalactic background light from the far uv to the far ir from deep ground-and space-based galaxy counts. *The Astrophysical Journal*, 827(2):108, 2016.

C. Du, H. Li, S. Liu, T. Donlon, and H. J. Newberg. The High-velocity Stars in the Local Stellar Halo from Gaia and LAMOST. ApJ, 863(1):87, Aug. 2018. doi: 10.3847/1538-4357/aad088.

R. C. Duncan and C. Thompson. Formation of Very Strongly Magnetized Neutron Stars: Implications for Gamma-Ray Bursts. ApJ, 392:L9, June 1992. doi: 10.1086/186413.

T. Eftekhari and E. Berger. Associating Fast Radio Bursts with Their Host Galaxies. ApJ, 849(2):162, Nov. 2017. doi: 10.3847/1538-4357/aa90b9.

T. Eftekhari, E. Berger, P. K. G. Williams, and P. K. Blanchard. Associating Fast Radio Bursts with Extragalactic Radio Sources: General Methodology and a Search for a Counterpart to FRB 170107. ApJ, 860(1):73, June 2018. doi: 10.3847/1538-4357/aac270.

T. Eifler, H. Miyatake, E. Krause, C. Heinrich, V. Miranda, C. Hirata, J. Xu, S. Hemmati, M. Simet, P. Capak, A. Choi, O. Doré, C. Doux, X. Fang, R. Hounsell, E. Huff, H.-J. Huang, M. Jarvis, J. Kruk, D. Masters, E. Rozo, D. Scolnic, D. N. Spergel, M. Troxel, A. von der Linden, Y. Wang, D. H. Weinberg, L. Wenzl, and H.-Y. Wu. Cosmology with the Roman Space Telescope - multiprobe strategies. MNRAS, 507(2):1746–1761, Oct. 2021. doi: 10.1093/mnras/stab1762.

S. W. Ellingson. Rfi mitigation and the ska. In *The Square Kilometre Array: An Engineering Perspective*, pages 261–267. Springer, 2005.

M. Ester, H.-P. Kriegel, J. Sander, and X. Xu. A density-based algorithm for discovering clusters in large spatial databases with noise. In *Proceedings of the Second International Conference on Knowledge Discovery and Data Mining*, KDD'96, page 226â€“231, Portland, Oregon, 1996. AAAI Press.

Euclid Collaboration, R. Scaramella, J. Amiaux, Y. Mellier, C. Burigana, C. S. Carvalho, J. C. Cuillandre, A. Da Silva, A. Derosa, J. Dinis, E. Maiorano, M. Maris, I. Tereno, R. Laureijs, T. Boenke, G. Buenadicha, X. Dupac, L. M. Gaspar Venancio, P. Gómez-Álvarez, J. Hoar, J. Lorenzo Alvarez, G. D. Racca, G. Saavedra-Criado, J. Schwartz, R. Vavrek, M. Schirmer, H. Aussel, R. Azzollini, V. F. Cardone, M. Cropper, A. Ealet, B. Garilli, W. Gillard, B. R. Granett, L. Guzzo, H. Hoekstra, K. Jahnke, T. Kitching, T. Maciaszek, M. Meneghetti, L. Miller, R. Nakajima, S. M. Niemi, F. Pasian, W. J. Percival, S. Pottinger, M. Sauvage, M. Scodeggio, S. Wachter, A. Zacchei, N. Aghanim, A. Amara, T. Auphan, N. Auricchio, S. Awan, A. Balestra, R. Bender, C. Bodendorf, D. Bonino, E. Branchini, S. Brau-Nogue, M. Brescia, G. P. Candini, V. Capobianco, C. Carbone, R. G. Carlberg, J. Carretero, R. Casas, F. J. Castander, M. Castellano, S. Cavuoti, A. Cimatti, R. Cledassou, G. Congedo, C. J. Conselice, L. Conversi, Y. Copin, L. Corcione, A. Costille, F. Courbin, H. Degaudenzi, M. Douspis, F. Dubath, C. A. J. Duncan, S. Dusini, S. Farrens, S. Ferriol, P. Fosalba, N. Fourmanoit, M. Frailis, E. Franceschi, P. Franzetti, M. Fumana, B. Gillis, C. Giocoli, A. Grazian, F. Grupp, S. V. H. Haugan, W. Holmes, F. Hormuth, P. Hudelot, S. Kermiche, A. Kiessling, M. Kilbinger, R. Kohley, B. Kubik, M. Kümmel, M. Kunz, H. Kurki-Suonio, O. Lahav, S. Ligori, P. B. Lilje, I. Lloro, O. Mansutti, O. Marggraf, K. Markovic, F. Marulli, R. Massey, S. Maurogordato, M. Melchior, E. Merlin, G. Meylan, J. J. Mohr, M. Moresco, B. Morin, L. Moscardini, E. Munari, R. C. Nichol, C. Padilla, S. Paltani, J. Peacock, K. Pedersen, V. Pettorino, S. Pires, M. Poncet, L. Popa, L. Pozzetti, F. Raison, R. Rebolo, J. Rhodes, H. W. Rix, M. Roncarelli, E. Rossetti, R. Saglia, P. Schneider, T. Schrabback, A. Secroun, G. Seidel, S. Serrano, C. Sirignano, G. Sirri, J. Skottfelt, L. Stanco, J. L. Starck, P. Tallada-Crespí, D. Tavagnacco, A. N. Taylor, H. I. Teplitz, R. Toledo-Moreo, F. Torradeflot, M. Trifoglio, E. A. Valentijn, L. Valenziano, G. A. Verdoes Kleijn, Y. Wang, N. Welikala, J. Weller, M. Wetzstein, G. Zamorani, J. Zoubian, S. Andreon, M. Baldi, S. Bardelli, A. Boucaud, S. Camera, D. Di Ferdinando, G. Fabbian, R. Farinelli, S. Galeotta, J. Graciá-Carpio, D. Maino, E. Medinaceli, S. Mei, C. Neissner, G. Polenta, A. Renzi, E. Romelli, C. Rosset, F. Sureau, M. Tenti, T. Vassallo, E. Zucca, C. Baccigalupi, A. Balaguera-Antolínez, P. Battaglia, A. Biviano, S. Borgani, E. Bozzo, R. Cabanac, A. Cappi, S. Casas, G. Castignani, C. Colodro-Conde, J. Coupon, H. M. Courtois, J. Cuby, S. de la Torre, S. Desai, H. Dole, M. Fabricius, M. Farina, P. G. Ferreira, F. Finelli, P. Flose-Reimberg, S. Fotopoulou, K. Ganga, G. Gozaliasl, I. M. Hook, E. Keihanen, C. C. Kirkpatrick, P. Liebing, V. Lindholm, G. Mainetti, M. Martinelli, N. Martinet, M. Maturi, H. J. McCracken, R. B. Metcalf, G. Morgante, J. Nightingale, A. Nucita, L. Patrizii, D. Potter, G. Riccio, A. G. Sánchez, D. Sapone, J. A. Schewtschenko, M. Schultheis, V. Scottez, R. Teyssier, I. Tutusaus, J. Valiviita, M. Viel, W. Vriend, and L. Whittaker. Euclid preparation. I. The Euclid Wide Survey. A&A, 662: A112, June 2022. doi: 10.1051/0004-6361/202141938.

S. M. Faber, C. N. A. Willmer, C. Wolf, D. C. Koo, B. J. Weiner, J. A. Newman, M. Im, A. L. Coil, C. Conroy, M. C. Cooper, M. Davis, D. P. Finkbeiner, B. F. Gerke, K. Gebhardt, E. J. Groth, P. Guhathakurta, J. Harker, N. Kaiser, S. Kassin, M. Kleinheinrich, N. P. Konidaris, R. G. Kron, L. Lin, G. Luppino, D. S. Madgwick, K. Meisenheimer, K. G. Noeske, A. C. Phillips, V. L. Sarajedini, R. P. Schiavon, L. Simard, A. S. Szalay, N. P. Vogt, and R. Yan. Galaxy Luminosity Functions to z$\sim$1 from DEEP2 and COMBO-17: Implications for Red Galaxy Formation. ApJ, 665(1):265–294, Aug. 2007. doi: 10.1086/519294.

H. Falcke and L. Rezzolla. Fast radio bursts: the last sign of supramassive neutron stars. A&A, 562:A137, Feb. 2014. doi: 10.1051/0004-6361/201321996.

N. J. Fantin, P. Côté, A. W. McConnachie, P. Bergeron, J.-C. Cuillandre, S. D. J. Gwyn, R. A. Ibata, G. F. Thomas, R. G. Carlberg, S. Fabbro, M. Haywood, A. Lançon, G. F. Lewis, K. Malhan, N. F. Martin, J. F. Navarro, D. Scott, and E. Starkenburg. The Canada-France Imaging Survey: Reconstructing the Milky Way Star Formation History from Its White Dwarf Population. ApJ, 887(2):148, Dec. 2019. doi: 10.3847/1538-4357/ab5521.

W. Farah, C. Flynn, M. Bailes, A. Jameson, K. W. Bannister, E. D. Barr, T. Bateman, S. Bhandari, M. Caleb, D. Campbell-Wilson, S. W. Chang, A. Deller, A. J. Green, R. Hunstead, F. Jankowski, E. Keane, J. P. Macquart, A. Möller, C. A. Onken, S. Osłowski, A. Parthasarathy, K. Plant, V. Ravi, R. M. Shannon, B. E. Tucker, V. Venkatraman Krishnan, and C. Wolf. FRB microstructure revealed by the real-time detection of FRB170827. MNRAS, 478(1):1209–1217, July 2018. doi: 10.1093/mnras/sty1122.

D. J. Farrow, S. Cole, N. Metcalfe, P. W. Draper, P. Norberg, S. Foucaud, W. S. Burgett, K. C. Chambers, N. Kaiser, R. P. Kudritzki, E. A. Magnier, P. A. Price, J. L. Tonry, and C. Waters. Pan-STARRS1: Galaxy clustering in the Small Area Survey 2. MNRAS, 437 (1):748–770, Jan. 2014. doi: 10.1093/mnras/stt1933.

Y. Feng, D. Li, Y.-P. Yang, Y. Zhang, W. Zhu, B. Zhang, W. Lu, P. Wang, S. Dai, R. S. Lynch, J. Yao, J. Jiang, J. Niu, D. Zhou, H. Xu, C. Miao, C. Niu, L. Meng, L. Qian, C.-W. Tsai, B. Wang, M. Xue, Y. Yue, M. Yuan, S. Zhang, and L. Zhang. Frequency-dependent polarization of repeating fast radio bursts—implications for their origin. *Science*, 375 (6586):1266–1270, Mar. 2022. doi: 10.1126/science.abl7759.

R. A. Fisher. Statistical methods for research workers. In *Breakthroughs in statistics*, pages 66–70. Springer, 1992.

W.-f. Fong, Y. Dong, J. Leja, S. Bhandari, C. K. Day, A. T. Deller, P. Kumar, J. X. Prochaska, D. R. Scott, K. W. Bannister, T. Eftekhari, A. C. Gordon, K. E. Heintz, C. W. James, C. D. Kilpatrick, E. K. Mahony, A. Rouco Escorial, S. D. Ryder, R. M. Shannon, and N. Tejos. Chronicling the Host Galaxy Properties of the Remarkable Repeating FRB 20201124A. *arXiv e-prints*, art. arXiv:2106.11993, June 2021.

E. Fonseca, B. C. Andersen, M. Bhardwaj, P. Chawla, D. C. Good, A. Josephy, V. M. Kaspi, K. W. Masui, R. Mckinven, D. Michilli, Z. Pleunis, K. Shin, S. P. Tendulkar, K. M. Bandura, P. J. Boyle, C. Brar, T. Cassanelli, D. Cubranic, M. Dobbs, F. Q. Dong, B. M. Gaensler, G. Hinshaw, T. L. Land ecker, C. Leung, D. Z. Li, H. H. Lin, J. Mena-Parra, M. Merryfield, A. Naidu, C. Ng, C. Patel, U. Pen, M. Rafiei-Ravandi, M. Rahman, S. M. Ransom, P. Scholz, K. M. Smith, I. H. Stairs, K. Vanderlinde, P. Yadav, and A. V. Zwaniga. Nine New Repeating Fast Radio Burst Sources from CHIME/FRB. ApJ, art. arXiv:2001.03595, Jan. 2020.

D. Foreman-Mackey, D. W. Hogg, D. Lang, and J. Goodman. emcee: The MCMC Hammer. PASP, 125(925):306, Mar. 2013. doi: 10.1086/670067.

D. Frederiks, V. Palshin, R. Aptekar, S. Golenetskii, T. Cline, and E. Mazets. On the possibility of identifying the short hard burst grb 051103 with a giant flare from a soft gamma repeater in the m81 group of galaxies. *Astronomy Letters*, 33(1):19–24, 2007.

W. L. Freedman, S. M. Hughes, B. F. Madore, J. R. Mould, M. G. Lee, P. Stetson, R. C. Kennicutt, A. Turner, L. Ferrarese, H. Ford, et al. The hubble space telescope extragalactic distance scale key project. 1: The discovery of cepheids and a new distance to m81. *The Astrophysical Journal*, 427:628–655, 1994.

D. Froebrich and H. Meusinger. A search for lsb dwarf galaxies in the m 81 group on digitally stacked schmidt plates. *Astronomy and Astrophysics Supplement Series*, 145 (2):229–242, 2000.

A. S. Fruchter, A. J. Levan, L. Strolger, P. M. Vreeswijk, S. E. Thorsett, D. Bersier, I. Burud, J. M. Castro Cerón, A. J. Castro-Tirado, C. Conselice, T. Dahlen, H. C. Ferguson,

J. P. U. Fynbo, P. M. Garnavich, R. A. Gibbons, J. Gorosabel, T. R. Gull, J. Hjorth, S. T. Holland, C. Kouveliotou, Z. Levay, M. Livio, M. R. Metzger, P. E. Nugent, L. Petro, E. Pian, J. E. Rhoads, A. G. Riess, K. C. Sahu, A. Smette, N. R. Tanvir, R. A. M. J. Wijers, and S. E. Woosley. Long γ-ray bursts and core-collapse supernovae have different environments. Nature, 441(7092):463–468, May 2006. doi: 10.1038/nature04787.

M. Fukugita, C. Hogan, and P. Peebles. The cosmic baryon budget. *The Astrophysical Journal*, 503(2):518, 1998.

M. Fukugita, C. J. Hogan, and P. J. E. Peebles. The Cosmic Baryon Budget. ApJ, 503(2): 518–530, Aug. 1998. doi: 10.1086/306025.

L. Fullmer and C. J. Londsale. VizieR Online Data Catalog: Catalogued Galaxies + QSOs observed in IRAS Survey, Vers.2 (IPAC 1989). *VizieR Online Data Catalog*, art. VII/113, Jan. 1995.

B. M. Gaensler, G. J. Madsen, S. Chatterjee, and S. A. Mao. The Vertical Structure of Warm Ionised Gas in the Milky Way. PASA, 25(4):184–200, Nov. 2008. doi: 10.1071/AS08004.

Gaia Collaboration, A. Helmi, F. van Leeuwen, P. J. Mc Millan, D. Massari, T. Antoja, A. C. Robin, L. Lindegren, U. Bastian, F. Arenou, C. Babusiaux, M. Biermann, M. A. Breddels, D. Hobbs, C. Jordi, E. Pancino, C. Reyle, J. Veljanoski, A. G. A. Brown, A. Vallenari, T. Prusti, J. H. J. de Bruijne, C. A. L. Bailer-Jones, D. W. Evans, L. Eyer, F. Jansen, S. A. Klioner, U. Lammers, X. Luri, F. Mignard, C. Panem, D. Pourbaix, S. Randich, P. Sartoretti, H. I. Siddiqui, C. Soubiran, N. A. Walton, M. Cropper, R. Drimmel, D. Katz, M. G. Lattanzi, J. Bakker, C. Cacciari, J. Castaneda, L. Chaoul, N. Cheek, F. de Angeli, C. Fabricius, R. Guerra, B. Holl, E. Masana, R. Messineo, N. Mowlavi, K. Nienartowicz, P. Panuzzo, J. Portell, M. Riello, G. M. Seabroke, P. Tanga, F. Thevenin, G. Gracia-Abril, G. Comoretto, M. Garcia-Reinaldos, D. Teyssier, M. Altmann, R. Andrae, M. Audard, I. Bellas-Velidis, K. Benson, J. Berthier, R. Blomme, P. Burgess, G. Busso, B. Carry, A. Cellino, G. Clementini, M. Clotet, O. ! Creevey, M. Davidson, J. De Ridder, L. Delchambre, A. Dell'Oro, C. Ducourant, J. Fernand ez-Hernandez, M. Fouesneau, Y. Fremat, L. Galluccio,

M. Garcia-Torres, J. Gonzalez-Nunez, J. J. Gonzalez-Vidal, E. Gosset, L. P. Guy, J. L. Halbwachs, N. C. Hambly, D. L. Harrison, J. Hernand ez, D. Hestroffer, S. T. Hodgkin, A. Hutton, G. Jasniewicz, A. Jean-Antoine-Piccolo, S. Jordan, A. J. Korn, A. Krone-Martins, A. C. Lanzafame, T. Lebzelter, W. Loeffler, M. Manteiga, P. M. Marrese, J. M. Martin-Fleitas, A. Moitinho, A. Mora, K. Muinonen, J. Osinde, T. Pauwels, J. M. Petit, A. Recio-Blanco, P. J. Richards, L. Rimoldini, L. M. Sarro, C. Siopis, M. Smith, A. Sozzetti, M. Sueveges, J. Torra, W. van Reeven, U. Abbas, A. Abreu Aramburu, S. Accart, C. Aerts, G. Altavilla, M. A. Alvarez, R. Alvarez, J. Alves, R. I. Anderson, A. H. Andrei, E. Anglada Varela, E. Antiche, B. Arcay, T. L. Astraatmadja, N. Bach, S. G. Baker, L. Balaguer-Nunez, P. Balm, C. Barache, C. Barata, D. Barbato, F. Barblan, P. S. Barklem, D. Barra! Do, M. Ba Rros, M. A. Barstow, S. Bartholome Munoz, J. L. Bassilana, U. Becciani, M. Bellazzini, A. Berihuete, S. Bertone, L. Bianchi, O. Bienayme, S. Blanco-Cuaresma, T. Boch, C. Boeche, A. Bombrun, R. Borrachero, D. Bossini, S. Bouquillon, G. Bourda, A. Bragaglia, L. Bramante, A. Bressan, N. Brouillet, T. Bruesemeister, E. Brugaletta, B. Bucciarelli, A. Burlacu, D. Busonero, A. G. Butkevich, R. Buzzi, E. Caffau, R. Cancelliere, G. Cannizzaro, T. Cantat-Gaudin, R. Carballo, T. Carlucci, J. M. Carrasco, L. Casamiquela, M. Castellani, A. Castro-Ginard, P. Charlot, L. Chemin, A. Chiavassa, G. Cocozza, G. Costigan, S. Cowell, F. Crifo, M. Crosta, C. Crowley, J. Cuypers, C. Dafonte, Y. Damerdji, A. Dapergolas, P. David, M. David, P. de Laverny, F. de Luise, R. de March, D. de Martino, R. de Souza, A. de Torres, J. Debosscher, E. Del Pozo, M. Delbo, A. Delgado, H. E. Delgado, P. Di Matteo, S. Diakite, C. Diener, E. Distefano, C. Dolding, P. Drazinos, J. Duran, B. Edvardsson, H. Enke, K. Eriks! Son, P. E Squej, G. Eynard Bontemps, C. Fabre, M. Fabrizio, S. Faigler, A. J. Falcao, M. Farras Casas, L. Federici, G. Fedorets, P. Fernique, F. Figueras, F. Filippi, K. Findeisen, A. Fonti, E. Fraile, M. Fraser, B. Frezouls, M. Gai, S. Galleti, D. Garabato, F. Garcia-Sedano, A. Garofalo, N. Garralda, A. Gavel, P. Gavras, J. Gerssen, R. Geyer, P. Giacobbe, G. Gilmore, S. Girona, G. Giuffrida, F. Glass, M. Gomes, M. Granvik, A. Gueguen, A. Guerrier, J. Guiraud, R. Gutierrez-Sanchez, W. Hofmann, G. Holland, H. E. Huckle, A. Hypki, V. Icardi, K. Janssen, G. Jevardat de Fombelle, P. G. Jonker, A. L. Juhasz, F. Julbe, A. Karampelas, A. Kewley, J. Klar, A. Kochoska, R. Kohley, K. Kolenberg, M. Kontizas, E. Kontizas, S. E. Koposov, G. Kordopatis, Z. Kostrzewa-Rutkowska, P. Koubsky, S. Lambert, A. F. Lanza,

Y. Lasne, J. B. Lavigne, Y. Le Fustec, C. Le Poncin-Lafitte, Y. Lebreton, S. Leccia, N. Leclerc, I. Lecoeur-Taibi, H. Lenhardt, F. Leroux, S. Liao, E. Licata, H. E. P. Lindstrom, T. A. Lister, E. ! Livanou, A. Lobel, M. Lopez, S. Managau, R. G. Mann, G. Mantelet, O. Marchal, J. M. Marchant, M. Marconi, S. Marinoni, G. Marschalko, D. J. Marshall, M. Martino, G. Marton, N. Mary, G. Matijevic, T. Mazeh, S. Messina, D. Michalik, N. R. Millar, D. Molina, R. Molinaro, L. Molnar, P. Montegriffo, R. Mor, R. Morbidelli, T. Morel, D. Morris, A. F. Mulone, T. Muraveva, I. Musella, G. Nelemans, L. Nicastro, L. Noval, W. O'Mullane, C. Ordenovic, D. Ordonez-Blanco, P. Osborne, C. Pagani, I. Pagano, F. Pailler, H. Palacin, L. Palaversa, A. Panahi, M. Pawlak, A. M. Piersimoni, F. X. Pineau, E. Plachy, G. Plum, E. Poggio, E. Poujoulet, A. Prsa, L. Pulone, E. Racero, S. Ragaini, N. Rambaux, M. Ramos-Lerate, S. Regibo, F. Riclet, V. Ripepi, A. Riva, A. Rivard, G. Rixon, T. Roegiers, M. Roelens, M. Romero-Gomez, N. Rowell, F. Royer, L. Ruiz-Dern, G. Sadowski, T. Sagrista Selles, J. Sahlmann, J. Salgado, E. Salguero, N. Sanna, T. Santana-Ros, M. Sarasso, H. Savietto, M. Schultheis, E. Sciacca, M. Segol !, I. J. C. Segov, D. Segransan, I. C. Shih, L. Siltala, A. F. Silva, R. L. Smart, K. W. Smith, E. Solano, F. Solitro, R. Sordo, S. Soria Nieto, J. Souchay, A. Spagna, F. Spoto, U. Stampa, I. A. Steele, H. Steidelmueller, C. A. Stephenson, H. Stoev, F. F. Suess, J. Surdej, L. Szabados, E. Szegedi-Elek, D. Tapiador, F. Taris, G. Tauran, M. B. Taylor, R. Teixeira, D. Terrett, P. Teyssand ier, W. Thuillot, A. Titarenko, F. Torra Clotet, C. Turon, A. Ulla, E. Utrilla, S. Uzzi, M. Vaillant, G. Valentini, V. Valette, A. van Elteren, E. van Hemelryck, M. van Leeuwen, M. Vaschetto, A. Vecchiato, Y. Viala, D. Vicente, S. Vogt, C. von Essen, H. Voss, V. Votruba, S. Voutsinas, G. Walmsley, M. Weiler, O. Wertz, T. Wevems, L. Wyrzykowski, A. Yoldas, M. Zerjal, H. Ziaeepour, J. Zorec, S. Zschocke, S. Zucker, C. Zurbach, and T. Zwitter. VizieR Online Data Catalog: Gaia DR2 sources in GC and dSph (Gaia Collaboration+, 2018). *VizieR Online Data Catalog*, art. J/A+A/616/A12, Apr. 2018.

E. Gallo, N. Degenaar, and J. van den Eijnden. Hard state neutron star and black hole x-ray binaries in the radio: X-ray luminosity plane. *Monthly Notices of the Royal Astronomical Society: Letters*, 478(1):L132–L136, 2018.

A. Gelman, J. Hill, and M. Yajima. Why we (usually) don't have to worry about multiple comparisons. *Journal of Research on Educational Effectiveness*, 5(2):189–211, 2012.

A. Gelman, J. B. Carlin, H. S. Stern, D. B. Dunson, A. Vehtari, and D. B. Rubin. *Bayesian data analysis*. CRC press, 2013.

S. Genel, D. Nelson, A. Pillepich, V. Springel, R. Pakmor, R. Weinberger, L. Hernquist, J. Naiman, M. Vogelsberger, F. Marinacci, and P. Torrey. The size evolution of star-forming and quenched galaxies in the IllustrisTNG simulation. MNRAS, 474(3):3976–3996, Mar. 2018. doi: 10.1093/mnras/stx3078.

J. Geng, B. Li, and Y. Huang. Repeating fast radio bursts from collapses of the crust of a strange star. *The Innovation*, 2:100152, Nov. 2021. doi: 10.1016/j.xinn.2021.100152.

A. Ghasemi and S. Zahediasl. Normality tests for statistical analysis: a guide for non-statisticians. *International journal of endocrinology and metabolism*, 10(2):486, 2012.

G. Ghisellini and N. Locatelli. Coherent curvature radiation and fast radio bursts. A&A, 613:A61, June 2018. doi: 10.1051/0004-6361/201731820.

B. Giacomazzo and R. Perna. Formation of stable magnetars from binary neutron star mergers. *The Astrophysical Journal Letters*, 771(2):L26, 2013.

A. Gil de Paz, S. Boissier, B. F. Madore, M. Seibert, Y. H. Joe, A. Boselli, T. K. Wyder, D. Thilker, L. Bianchi, S.-C. Rey, R. M. Rich, T. A. Barlow, T. Conrow, K. Forster, P. G. Friedman, D. C. Martin, P. Morrissey, S. G. Neff, D. Schiminovich, T. Small, J. Donas, T. M. Heckman, Y.-W. Lee, B. Milliard, A. S. Szalay, and S. Yi. The GALEX Ultraviolet Atlas of Nearby Galaxies. ApJS, 173(2):185–255, Dec. 2007. doi: 10.1086/516636.

V. M. A. Gómez-González, Y. D. Mayya, and D. Rosa-González. Wolf-Rayet stars in M81: detection and characterization using GTC/OSIRIS spectra and HST/ACS images. MNRAS, 460(2):1555–1566, Aug. 2016. doi: 10.1093/mnras/stw1118.

G. Gómez-Velarde, D. García-Alvarez, and A. Cabrerra-Lavers. OSIRIS Multi-Object Spectroscopy: Mask Design Process. In I. Skillen, M. Balcells, and S. Trager, editors, *Multi-Object Spectroscopy in the Next Decade: Big Questions, Large Surveys, and Wide Fields*, volume 507 of *Astronomical Society of the Pacific Conference Series*, page 191, Oct. 2016.

J. I. González-Serrano, M. Sánchez-Portal, H. Castañeda, R. Quirk, E. D. de Miguel, M. Aguiar, and J. Cepa. OSIRIS software: the Mask Designer Tool. *Experimental Astronomy*, 18(1-3):65–75, Apr. 2004. doi: 10.1007/s10686-005-9003-4.

J. Goodman and J. Weare. Ensemble samplers with affine invariance. *Communications in Applied Mathematics and Computational Science*, 5(1):65–80, Jan. 2010. doi: 10.2140/camcos.2010.5.65.

K. Gordon, P. Pérez-González, K. Misselt, E. Murphy, G. Bendo, F. Walter, M. Thornley, R. Kennicutt Jr, G. H. Rieke, C. Engelbracht, et al. Spatially resolved ultraviolet, hα, infrared, and radio star formation in m81. *The Astrophysical Journal Supplement Series*, 154(1):215, 2004.

Y. A. Gordon, M. M. Boyce, C. P. O'Dea, L. Rudnick, H. Andernach, A. N. Vantyghem, S. A. Baum, J.-P. Bui, and M. Dionyssiou. A Catalog of Very Large Array Sky Survey Epoch 1 Quick Look Components, Sources, and Host Identifications. *Research Notes of the American Astronomical Society*, 4(10):175, Oct. 2020. doi: 10.3847/2515-5172/abbe23.

K. Gourdji, D. Michilli, L. G. Spitler, J. W. T. Hessels, A. Seymour, J. M. Cordes, and S. Chatterjee. A Sample of Low-energy Bursts from FRB 121102. ApJ, 877(2):L19, June 2019. doi: 10.3847/2041-8213/ab1f8a.

F. Govoni and L. Feretti. Magnetic Fields in Clusters of Galaxies. 13(8):1549–1594. doi: 10.1142/S0218271804005080.

A. W. Graham, S. P. Driver, V. Petrosian, C. J. Conselice, M. A. Bershady, S. M. Crawford, and T. Goto. Total galaxy magnitudes and effective radii from petrosian magnitudes and radii. *The Astronomical Journal*, 130(4):1535–1544, 10 2005. ISSN 1538-3881. doi: 10.1086/444475. URL `http://dx.doi.org/10.1086/444475`.

J. F. Graham and A. S. Fruchter. The Metal Aversion of Long-duration Gamma-Ray Bursts. ApJ, 774(2):119, Sept. 2013. doi: 10.1088/0004-637X/774/2/119.

J. P. Greco, J. E. Greene, M. A. Strauss, L. A. Macarthur, X. Flowers, A. D. Goulding, S. Huang, J. H. Kim, Y. Komiyama, A. Leauthaud, L. Leisman, R. H. Lupton, C. Sifón, and S.-Y. Wang. Illuminating Low Surface Brightness Galaxies with the Hyper Suprime-Cam Survey. ApJ, 857(2):104, Apr. 2018. doi: 10.3847/1538-4357/aab842.

G. Green. dustmaps: A Python interface for maps of interstellar dust. *The Journal of Open Source Software*, 3(26):695, Jun 2018. doi: 10.21105/joss.00695.

A. Gruzinov and E. Waxman. Masers and Other Instabilities in a Weakly Magnetized Relativistic Plasma: Theory and the Astrophysical Relevance of the Maser. ApJ, 875(2): 126, Apr. 2019. doi: 10.3847/1538-4357/ab0f9b.

J. E. Gunn, W. A. Siegmund, E. J. Mannery, R. E. Owen, C. L. Hull, R. F. Leger, L. N. Carey, G. R. Knapp, D. G. York, W. N. Boroski, S. M. Kent, R. H. Lupton, C. M. Rockosi, M. L. Evans, P. Waddell, J. E. Anderson, J. Annis, J. C. Barentine, L. M. Bartoszek, S. Bastian, S. B. Bracker, H. J. Brewington, C. I. Briegel, J. Brinkmann, Y. J. Brown, M. A. Carr, P. C. Czarapata, C. C. Drennan, T. Dombeck, G. R. Federwitz, B. A. Gillespie, C. Gonzales, S. U. Hansen, M. Harvanek, J. Hayes, W. Jordan, E. Kinney, M. Klaene, S. J. Kleinman, R. G. Kron, J. Kresinski, G. Lee, S. Limmongkol, C. W. Lindenmeyer, D. C. Long, C. L. Loomis, P. M. McGehee, P. M. Mantsch, J. Neilsen, Eric H., R. M. Neswold, P. R. Newman, A. Nitta, J. Peoples, John, J. R. Pier, P. S. Prieto, A. Prosapio, C. Rivetta, D. P. Schneider, S. Snedden, and S.-i. Wang. The 2.5 m Telescope of the Sloan Digital Sky Survey. AJ, 131(4):2332–2359, Apr. 2006. doi: 10.1086/500975.

C. B. Haakonsen and R. E. Rutledge. XID II: Statistical Cross-Association of ROSAT Bright Source Catalog X-ray Sources with 2MASS Point Source Catalog Near-Infrared Sources. ApJS, 184(1):138–151, Sept. 2009. doi: 10.1088/0067-0049/184/1/138.

Z. Hafen, C.-A. Faucher-Giguère, D. Anglés-Alcázar, J. Stern, D. Kereš, C. Hummels, C. Esmerian, S. Garrison-Kimmel, K. El-Badry, A. Wetzel, et al. The origins of the circumgalactic medium in the fire simulations. *Monthly Notices of the Royal Astronomical Society*, 488(1):1248–1272, 2019.

L. Haffner, R. Reynolds, S. Tufte, G. Madsen, K. Jaehnig, and J. Percival. The wisconsin hα mapper northern sky survey. *The Astrophysical Journal Supplement Series*, 149(2): 405, 2003.

G. Hallinan, V. Ravi, S. Weinreb, J. Kocz, Y. Huang, D. Woody, J. Lamb, L. D'Addario, M. Catha, J. Shi, et al. The dsa-2000–a radio survey camera. *arXiv preprint arXiv:1907.07648*, 2019.

G. Hallinan, V. Ravi, S. Weinreb, J. Kocz, Y. Huang, D. P. Woody, J. Lamb, L. D'Addario, M. Catha, C. Law, S. R. Kulkarni, E. S. Phinney, M. W. Eastwood, K. Bouman, M. McLaughlin, S. Ransom, X. Siemens, J. Cordes, R. Lynch, D. Kaplan, A. Brazier, S. Bhatnagar, S. Myers, F. Walter, and B. Gaensler. The DSA-2000 — A Radio Survey Camera. In *Bulletin of the American Astronomical Society*, volume 51, page 255, Sept. 2019.

P. J. Hancock, T. Murphy, B. M. Gaensler, A. Hopkins, and J. R. Curran. Compact continuum source finding for next generation radio surveys. *Monthly Notices of the Royal Astronomical Society*, 422(2):1812–1824, 2012.

P. J. Hancock, C. M. Trott, and N. Hurley-Walker. Source Finding in the Era of the SKA (Precursors): Aegean 2.0. PASA, 35:e011, Mar. 2018. doi: 10.1017/pasa.2018.3.

M. H. Hani, M. Sparre, S. L. Ellison, P. Torrey, and M. Vogelsberger. Galaxy mergers moulding the circum-galactic medium - I. The impact of a major merger. MNRAS, 475 (1):1160–1176, Mar. 2018. doi: 10.1093/mnras/stx3252.

T. H. Hankins and J. A. Eilek. Radio Emission Signatures in the Crab Pulsar. ApJ, 670(1): 693–701, Nov. 2007. doi: 10.1086/522362.

T. H. Hankins and B. J. Rickett. Pulsar signal processing. *Methods in Computational Physics*, 14:55–129, Jan. 1975. doi: 10.1016/B978-0-12-460814-6.50007-3.

C. Harris and K. Haines. A mathematical review of polyphase filterbank implementations for radio astronomy. *Publications of the Astronomical Society of Australia*, 28(4):317–322, 2011.

W. E. Harris. A New Catalog of Globular Clusters in the Milky Way. *arXiv e-prints*, art. arXiv:1012.3224, Dec. 2010.

T. Hashimoto, T. Goto, A. Y. L. On, T.-Y. Lu, D. J. D. Santos, S. C. C. Ho, S. J. Kim, T.-W. Wang, and T. Y. Y. Hsiao. No redshift evolution of non-repeating fast radio burst rates. MNRAS, 498(3):3927–3945, Nov. 2020a. doi: 10.1093/mnras/staa2490.

T. Hashimoto, T. Goto, T.-W. Wang, S. J. Kim, S. C. C. Ho, A. Y. L. On, T.-Y. Lu, and D. J. D. Santos. Luminosity-duration relations and luminosity functions of repeating and non-repeating fast radio bursts. MNRAS, 494(2):2886–2904, May 2020b. doi: 10.1093/mnras/staa895.

T. Hashimoto, T. Goto, B. H. Chen, S. C. C. Ho, T. Y. Y. Hsiao, Y. H. V. Wong, A. Y. L. On, S. J. Kim, E. Kilerci-Eser, K.-C. Huang, D. J. D. Santos, and S. Yamasaki. Energy functions of fast radio bursts derived from the first CHIME/FRB catalogue. MNRAS, 511(2):1961–1976, Apr. 2022. doi: 10.1093/mnras/stac065.

M. Haverkorn. Magnetic fields in the milky way. In *Magnetic fields in diffuse media*, pages 483–506. Springer, 2015.

C. He, C.-Y. Ng, and V. Kaspi. The correlation between dispersion measure and x-ray column density from radio pulsars. *The Astrophysical Journal*, 768(1):64, 2013.

K. E. Heintz, J. X. Prochaska, S. Simha, E. Platts, W.-f. Fong, N. Tejos, S. D. Ryder, K. Aggerwal, S. Bhandari, C. K. Day, A. T. Deller, C. D. Kilpatrick, C. J. Law, J.-P. Macquart, A. Mannings, L. J. Marnoch, E. M. Sadler, and R. M. Shannon. Host Galaxy Properties and Offset Distributions of Fast Radio Bursts: Implications for Their Progenitors. ApJ, 903(2):152, Nov. 2020. doi: 10.3847/1538-4357/abb6fb.

K. E. Heintz, J. X. Prochaska, S. Simha, E. Platts, W.-f. Fong, N. Tejos, S. D. Ryder, K. Aggerwal, S. Bhandari, C. K. Day, et al. Host galaxy properties and offset distributions of fast radio bursts: Implications for their progenitors. *arXiv preprint arXiv:2009.10747*, 2020.

D. B. Henley and R. L. Shelton. An XMM-Newton Survey of the Soft X-Ray Background. III. The Galactic Halo X-Ray Emission. ApJ, 773(2):92, Aug. 2013. doi: 10.1088/0004-637X/773/2/92.

J. W. T. Hessels, L. G. Spitler, A. D. Seymour, J. M. Cordes, D. Michilli, R. S. Lynch, K. Gourdji, A. M. Archibald, C. G. Bassa, G. C. Bower, S. Chatterjee, L. Connor, F. Crawford, J. S. Deneva, V. Gajjar, V. M. Kaspi, A. Keimpema, C. J. Law, B. Marcote, M. A. McLaughlin, Z. Paragi, E. Petroff, S. M. Ransom, P. Scholz, B. W. Stappers, and S. P. Tendulkar. FRB 121102 Bursts Show Complex Time-Frequency Structure. ApJ, 876(2):L23, May 2019. doi: 10.3847/2041-8213/ab13ae.

HI4PI Collaboration, N. Ben Bekhti, L. Flöer, R. Keller, J. Kerp, D. Lenz, B. Winkel, J. Bailin, M. R. Calabretta, L. Dedes, H. A. Ford, B. K. Gibson, U. Haud, S. Janowiecki, P. M. W. Kalberla, F. J. Lockman, N. M. McClure-Griffiths, T. Murphy, H. Nakanishi, D. J. Pisano, and L. Staveley-Smith. HI4PI: A full-sky H I survey based on EBHIS and GASS. A&A, 594:A116, Oct. 2016. doi: 10.1051/0004-6361/201629178.

A. Hill, R. Reynolds, L. Haffner, K. Wood, and G. Madsen. Modern view of the warm ionized medium. *Highlights of Astronomy*, 16:574–575, Mar. 2015. doi: 10.1017/S1743921314012228.

A. S. Hill, R. J. Reynolds, R. A. Benjamin, and L. M. Haffner. Density Distribution of the Warm Ionized Medium. In M. Haverkorn and W. M. Goss, editors, *SINS - Small Ionized and Neutral Structures in the Diffuse Interstellar Medium*, volume 365 of *Astronomical Society of the Pacific Conference Series*, page 250, July 2007.

G. H. Hilmarsson, L. G. Spitler, R. A. Main, and D. Z. Li. Polarization properties of FRB 20201124A from detections with the Effelsberg 100-m radio telescope. MNRAS, 508 (4):5354–5361, Dec. 2021. doi: 10.1093/mnras/stab2936.

S. R. Hinton, T. M. Davis, C. Lidman, K. Glazebrook, and G. F. Lewis. MARZ: Manual and automatic redshifting software. *Astronomy and Computing*, 15:61–71, Apr. 2016. doi: 10.1016/j.ascom.2016.03.001.

A. S. Hirschauer, J. J. Salzer, S. Janowiecki, and G. A. Wegner. Metal Abundances of KISS Galaxies. VI. New Metallicity Relations for the KISS Sample of Star-forming Galaxies. AJ, 155(2):82, Feb. 2018. doi: 10.3847/1538-3881/aaa4ba.

L. C. Ho, A. V. Filippenko, and W. L. Sargent. New insights into the physical nature of liners from a multiwavelength analysis of the nucleus of m81. *The Astrophysical Journal*, 462:183, 1996.

P. F. Hopkins, D. Kereš, J. Oñorbe, C.-A. Faucher-Giguère, E. Quataert, N. Murray, and J. S. Bullock. Galaxies on FIRE (Feedback In Realistic Environments): stellar feedback explains cosmologically inefficient star formation. *Monthly Notices of the Royal Astronomical Society*, 445(1):581–603, 09 2014. ISSN 0035-8711. doi: 10.1093/mnras/stu1738. URL https://doi.org/10.1093/mnras/stu1738.

P. F. Hopkins, A. Wetzel, D. Kereš, C.-A. Faucher-Giguère, E. Quataert, M. Boylan-Kolchin, N. Murray, C. C. Hayward, S. Garrison-Kimmel, C. Hummels, R. Feldmann, P. Torrey, X. Ma, D. Anglés-Alcázar, K.-Y. Su, M. Orr, D. Schmitz, I. Escala, R. Sanderson, M. Y. Grudić, Z. Hafen, J.-H. Kim, A. Fitts, J. S. Bullock, C. Wheeler, T. K. Chan, O. D. Elbert, and D. Narayanan. FIRE-2 simulations: physics versus numerics in galaxy formation. *Monthly Notices of the Royal Astronomical Society*, 480(1): 800–863, 06 2018. ISSN 0035-8711. doi: 10.1093/mnras/sty1690. URL https://doi.org/10.1093/mnras/sty1690.

J. Huchra, M. Davis, D. Latham, and J. Tonry. A survey of galaxy redshifts. IV - The data. ApJS, 52:89–119, June 1983. doi: 10.1086/190860.

J. P. Huchra, L. M. Macri, K. L. Masters, T. H. Jarrett, P. Berlind, M. Calkins, A. C. Crook, R. Cutri, P. Erdoğdu, E. Falco, T. George, C. M. Hutcheson, O. Lahav, J. Mader, J. D. Mink, N. Martimbeau, S. Schneider, M. Skrutskie, S. Tokarz, and M. Westover. THE 2mass REDSHIFT SURVEY—DESCRIPTION AND DATA RELEASE. *The Astrophysical Journal Supplement Series*, 199(2):26, mar 2012. doi: 10.1088/0067-0049/199/2/26. URL https://doi.org/10.1088%2F0067-0049%2F199%2F2%2F26.

K. Hurley, A. Rowlinson, E. Bellm, D. Perley, I. G. Mitrofanov, D. V. Golovin, A. S. Kozyrev, M. L. Litvak, A. B. Sanin, W. Boynton, C. Fellows, K. Harshmann, M. Ohno, K. Yamaoka, Y. E. Nakagawa, D. M. Smith, T. Cline, N. R. Tanvir, P. T. O'Brien, K. Wiersema, E. Rol, A. Levan, J. Rhoads, A. Fruchter, D. Bersier, J. J. Kavelaars, N. Gehrels, H. Krimm, D. M. Palmer, R. C. Duncan, C. Wigger, W. Hajdas, J. L. Atteia,

G. Ricker, R. Vanderspek, A. Rau, and A. von Kienlin. A new analysis of the short-duration, hard-spectrum GRB 051103, a possible extragalactic soft gamma repeater giant flare. MNRAS, 403(1):342–352, Mar. 2010. doi: 10.1111/j.1365-2966.2009.16118.x.

J. Iglesias-Páramo, V. Buat, J. Donas, A. Boselli, and B. Milliard. UV and FIR selected samples of galaxies in the local Universe. Dust extinction and star formation rates. A&A, 419:109–126, May 2004. doi: 10.1051/0004-6361:20034049.

J. Iglesias-Páramo, V. Buat, T. T. Takeuchi, K. Xu, S. Boissier, A. Boselli, D. Burgarella, B. F. Madore, A. Gil de Paz, L. Bianchi, T. A. Barlow, Y. I. Byun, J. Donas, K. Forster, P. G. Friedman, T. M. Heckman, P. N. Jelinski, Y. W. Lee, R. F. Malina, D. C. Martin, B. Milliard, P. F. Morrissey, S. G. Neff, R. M. Rich, D. Schiminovich, M. Seibert, O. H. W. Siegmund, T. Small, A. S. Szalay, B. Y. Welsh, and T. K. Wyder. Star Formation in the Nearby Universe: The Ultraviolet and Infrared Points of View. ApJS, 164(1): 38–51, May 2006. doi: 10.1086/502628.

H. Intema, P. Jagannathan, K. Mooley, and D. Frail. The gmrt 150 mhz all-sky radio survey-first alternative data release tgss adr1. *Astronomy & Astrophysics*, 598:A78, 2017.

K. Ioka and B. Zhang. A Binary Comb Model for Periodic Fast Radio Bursts. ApJ, 893 (1):L26, Apr. 2020. doi: 10.3847/2041-8213/ab83fb.

Ž. Ivezić, S. M. Kahn, J. A. Tyson, B. Abel, E. Acosta, R. Allsman, D. Alonso, Y. AlSayyad, S. F. Anderson, J. Andrew, J. R. P. Angel, G. Z. Angeli, R. Ansari, P. Antilogus, C. Araujo, R. Armstrong, K. T. Arndt, P. Astier, É. Aubourg, N. Auza, T. S. Axelrod, D. J. Bard, J. D. Barr, A. Barrau, J. G. Bartlett, A. E. Bauer, B. J. Bauman, S. Baumont, E. Bechtol, K. Bechtol, A. C. Becker, J. Becla, C. Beldica, S. Bellavia, F. B. Bianco, R. Biswas, G. Blanc, J. Blazek, R. D. Blandford, J. S. Bloom, J. Bogart, T. W. Bond, M. T. Booth, A. W. Borgland, K. Borne, J. F. Bosch, D. Boutigny, C. A. Brackett, A. Bradshaw, W. N. Brandt, M. E. Brown, J. S. Bullock, P. Burchat, D. L. Burke, G. Cagnoli, D. Calabrese, S. Callahan, A. L. Callen, J. L. Carlin, E. L. Carlson, S. Chandrasekharan, G. Charles-Emerson, S. Chesley, E. C. Cheu, H.-F. Chiang, J. Chiang, C. Chirino, D. Chow, D. R. Ciardi, C. F. Claver, J. Cohen-Tanugi, J. J. Cockrum, R. Coles, A. J. Connolly, K. H. Cook, A. Cooray, K. R. Covey, C. Cribbs,

W. Cui, R. Cutri, P. N. Daly, S. F. Daniel, F. Daruich, G. Daubard, G. Daues, W. Dawson, F. Delgado, A. Dellapenna, R. de Peyster, M. de Val-Borro, S. W. Digel, P. Doherty, R. Dubois, G. P. Dubois-Felsmann, J. Durech, F. Economou, T. Eifler, M. Eracleous, B. L. Emmons, A. Fausti Neto, H. Ferguson, E. Figueroa, M. Fisher-Levine, W. Focke, M. D. Foss, J. Frank, M. D. Freemon, E. Gangler, E. Gawiser, J. C. Geary, P. Gee, M. Geha, C. J. B. Gessner, R. R. Gibson, D. K. Gilmore, T. Glanzman, W. Glick, T. Goldina, D. A. Goldstein, I. Goodenow, M. L. Graham, W. J. Gressler, P. Gris, L. P. Guy, A. Guyonnet, G. Haller, R. Harris, P. A. Hascall, J. Haupt, F. Hernandez, S. Hermann, E. Hileman, J. Hoblitt, J. A. Hodgson, C. Hogan, J. D. Howard, D. Huang, M. E. Huffer, P. Ingraham, W. R. Innes, S. H. Jacoby, B. Jain, F. Jammes, M. J. Jee, T. Jenness, G. Jernigan, D. Jevremović, K. Johns, A. S. Johnson, M. W. G. Johnson, R. L. Jones, C. Juramy-Gilles, M. Jurić, J. S. Kalirai, N. J. Kallivayalil, B. Kalmbach, J. P. Kantor, P. Karst, M. M. Kasliwal, H. Kelly, R. Kessler, V. Kinnison, D. Kirkby, L. Knox, I. V. Kotov, V. L. Krabbendam, K. S. Krughoff, P. Kubánek, J. Kuczewski, S. Kulkarni, J. Ku, N. R. Kurita, C. S. Lage, R. Lambert, T. Lange, J. B. Langton, L. Le Guillou, D. Levine, M. Liang, K.-T. Lim, C. J. Lintott, K. E. Long, M. Lopez, P. J. Lotz, R. H. Lupton, N. B. Lust, L. A. MacArthur, A. Mahabal, R. Mandelbaum, T. W. Markiewicz, D. S. Marsh, P. J. Marshall, S. Marshall, M. May, R. McKercher, M. McQueen, J. Meyers, M. Migliore, M. Miller, D. J. Mills, C. Miraval, J. Moeyens, F. E. Moolekamp, D. G. Monet, M. Moniez, S. Monkewitz, C. Montgomery, C. B. Morrison, F. Mueller, G. P. Muller, F. Muñoz Arancibia, D. R. Neill, S. P. Newbry, J.-Y. Nief, A. Nomerotski, M. Nordby, P. O'Connor, J. Oliver, S. S. Olivier, K. Olsen, W. O'Mullane, S. Ortiz, S. Osier, R. E. Owen, R. Pain, P. E. Palecek, J. K. Parejko, J. B. Parsons, N. M. Pease, J. M. Peterson, J. R. Peterson, D. L. Petravick, M. E. Libby Petrick, C. E. Petry, F. Pierfederici, S. Pietrowicz, R. Pike, P. A. Pinto, R. Plante, S. Plate, J. P. Plutchak, P. A. Price, M. Prouza, V. Radeka, J. Rajagopal, A. P. Rasmussen, N. Regnault, K. A. Reil, D. J. Reiss, M. A. Reuter, S. T. Ridgway, V. J. Riot, S. Ritz, S. Robinson, W. Roby, A. Roodman, W. Rosing, C. Roucelle, M. R. Rumore, S. Russo, A. Saha, B. Sassolas, T. L. Schalk, P. Schellart, R. H. Schindler, S. Schmidt, D. P. Schneider, M. D. Schneider, W. Schoening, G. Schumacher, M. E. Schwamb, J. Sebag, B. Selvy, G. H. Sembroski, L. G. Seppala, A. Serio, E. Serrano, R. A. Shaw, I. Shipsey, J. Sick, N. Silvestri, C. T. Slater, J. A. Smith, R. C. Smith, S. Sobhani, C. Soldahl, L. Storrie-Lombardi, E. Stover,

M. A. Strauss, R. A. Street, C. W. Stubbs, I. S. Sullivan, D. Sweeney, J. D. Swinbank, A. Szalay, P. Takacs, S. A. Tether, J. J. Thaler, J. G. Thayer, S. Thomas, A. J. Thornton, V. Thukral, J. Tice, D. E. Trilling, M. Turri, R. Van Berg, D. Vanden Berk, K. Vetter, F. Virieux, T. Vucina, W. Wahl, L. Walkowicz, B. Walsh, C. W. Walter, D. L. Wang, S.-Y. Wang, M. Warner, O. Wiecha, B. Willman, S. E. Winters, D. Wittman, S. C. Wolff, W. M. Wood-Vasey, X. Wu, B. Xin, P. Yoachim, and H. Zhan. LSST: From Science Drivers to Reference Design and Anticipated Data Products. ApJ, 873(2):111, Mar. 2019. doi: 10.3847/1538-4357/ab042c.

A. Iwazaki. Axion Stars and Repeating Fast Radio Bursts with Finite Bandwidths. *arXiv e-prints*, art. arXiv:1707.04827, July 2017.

C. W. James. Limits on the population of repeating fast radio bursts from the ASKAP/CRAFT lat50 survey. MNRAS, 486(4):5934–5950, July 2019. doi: 10.1093/mnras/stz1224.

C. W. James, S. Osłowski, C. Flynn, P. Kumar, K. Bannister, S. Bhandari, W. Farah, M. Kerr, D. R. Lorimer, J. P. Macquart, C. Ng, C. Phillips, D. C. Price, H. Qiu, R. M. Shannon, and R. Spiewak. Which bright fast radio bursts repeat? MNRAS, 495(2): 2416–2427, June 2020. doi: 10.1093/mnras/staa1361.

C. W. James, J. X. Prochaska, J. P. Macquart, F. O. North-Hickey, K. W. Bannister, and A. Dunning. The z-DM distribution of fast radio bursts. MNRAS, 509(4):4775–4802, Feb. 2022. doi: 10.1093/mnras/stab3051.

A. Jessner, M. V. Popov, V. I. Kondratiev, Y. Y. Kovalev, D. Graham, A. Zensus, V. A. Soglasnov, A. V. Bilous, and O. A. Moshkina. Giant pulses with nanosecond time resolution detected from the Crab pulsar at 8.5 and 15.1 GHz. A&A, 524:A60, Dec. 2010. doi: 10.1051/0004-6361/201014806.

B. D. Johnson, J. L. Leja, C. Conroy, and J. S. Speagle. Prospector: Stellar population inference from spectra and SEDs, May 2019.

T. J. Johnson, L. Guillemot, M. Kerr, I. Cognard, P. S. Ray, M. T. Wolff, S. Bégin, G. H. Janssen, R. W. Romani, C. Venter, J. E. Grove, P. C. C. Freire, M. Wood, C. C. Cheung,

J. M. Casandjian, I. H. Stairs, F. Camilo, C. M. Espinoza, E. C. Ferrara, A. K. Harding, S. Johnston, M. Kramer, A. G. Lyne, P. F. Michelson, S. M. Ransom, R. Shannon, D. A. Smith, B. W. Stappers, G. Theureau, and S. E. Thorsett. Broadband Pulsations from PSR B1821-24: Implications for Emission Models and the Pulsar Population of M28. ApJ, 778(2):106, Dec. 2013. doi: 10.1088/0004-637X/778/2/106.

S. Johnston and R. W. Romani. Giant Pulses - A Brief Review. In F. Camilo and B. M. Gaensler, editors, *Young Neutron Stars and Their Environments*, volume 218, page 315, Jan. 2004.

A. Josephy, P. Chawla, A. P. Curtin, V. M. Kaspi, M. Bhardwaj, P. J. Boyle, C. Brar, T. Cassanelli, E. Fonseca, B. M. Gaensler, C. Leung, H. H. Lin, K. W. Masui, R. Mckinven, J. Mena-Parra, D. Michilli, C. Ng, Z. Pleunis, M. Rafiei-Ravandi, M. Rahman, P. Sanghavi, P. Scholz, K. Shin, K. M. Smith, I. H. Stairs, S. P. Tendulkar, and A. V. Zwaniga. No Evidence for Galactic Latitude Dependence of the Fast Radio Burst Sky Distribution. ApJ, 923(1):2, Dec. 2021. doi: 10.3847/1538-4357/ac33ad.

P. Kaaret, D. Koutroumpa, K. D. Kuntz, K. Jahoda, J. Bluem, H. Gulick, E. Hodges-Kluck, D. M. LaRocca, R. Ringuette, and A. Zajczyk. A disk-dominated and clumpy circumgalactic medium of the Milky Way seen in X-ray emission. *Nature Astronomy*, 2020. ISSN 23973366. doi: 10.1038/s41550-020-01215-w. URL https://doi.org/10.1038/s41550-020-01215-w.

Z. Kader, C. Leung, M. Dobbs, K. W. Masui, D. Michilli, J. Mena-Parra, R. McKinven, C. Ng, K. Bandura, M. Bhardwaj, C. Brar, T. Cassanelli, P. Chawla, F. A. Dong, D. Good, V. Kaspi, A. E. Lanman, H.-H. Lin, B. W. Meyers, A. B. Pearlman, U.-L. Pen, E. Petroff, Z. Pleunis, M. Rafiei-Ravandi, M. Rahman, P. Sanghavi, P. Scholz, K. Shin, S. Siegel, K. M. Smith, I. Stairs, S. P. Tendulkar, K. Vanderlinde, D. Wulf, and Chime/Frb Collaboration. High-time resolution search for compact objects using fast radio burst gravitational lens interferometry with CHIME/FRB. Phys. Rev. D, 106(4):043016, Aug. 2022. doi: 10.1103/PhysRevD.106.043016.

E. I. Kaisina, I. D. Karachentsev, D. I. Makarov, and S. S. Kaisin. Catalog & atlas of the LV galaxies. In K. B. W. McQuinn and S. Stierwalt, editors, *Dwarf Galaxies: From* *the Deep Universe to the Present*, volume 344 of *IAU Symposium*, pages 377–380, Oct. 2019. doi: 10.1017/S1743921318005987.

I. Karachentsev and V. Karachentseva. New dwarf galaxy candidates in the leo-i group. *Astronomy Reports*, 48(4):267–274, 2004.

I. Karachentsev, A. Dolphin, D. Geisler, E. Grebel, P. Guhathakurta, P. Hodge, V. Karachentseva, A. Sarajedini, P. Seitzer, and M. Sharina. The m 81 group of galaxies: New distances, kinematics and structure. *Astronomy & Astrophysics*, 383(1):125–136, 2002.

I. D. Karachentsev and E. I. Kaisina. Dwarf Galaxies in the Local Volume. In K. B. W. McQuinn and S. Stierwalt, editors, *Dwarf Galaxies: From the Deep Universe to the Present*, volume 344 of *IAU Symposium*, pages 381–383, Oct. 2019. doi: 10.1017/S1743921318005975.

I. D. Karachentsev, D. I. Makarov, and E. I. Kaisina. Updated nearby galaxy catalog. *The Astronomical Journal*, 145(4):101, 2013.

V. E. Karachentseva. The distribution of Sculptor-type dwarf galaxies. *Communications of the Byurakan Astrophysical Observatory*, 39:61–75, Jan. 1968.

V. E. Karachentseva, I. D. Karachentsev, and F. Boerngen. Atlas of dwarf galaxies in the region of M 81 group. A&AS, 60:213–227, May 1985.

K. Kashiyama and K. Murase. Testing the Young Neutron Star Scenario with Persistent Radio Emission Associated with FRB 121102. ApJ, 839(1):L3, Apr. 2017. doi: 10.3847/2041-8213/aa68e1.

K. Kashiyama, K. Ioka, and P. Mészáros. Cosmological Fast Radio Bursts from Binary White Dwarf Mergers. ApJ, 776(2):L39, Oct. 2013. doi: 10.1088/2041-8205/776/2/L39.

M. Kasliwal. Transients in the local universe. The Gravitational-wave Physics and Astronomy Workshop,January 26-29, 2011, 2011. URL http://www.gravity.phys.uwm.edu/conferences/gwpaw/program/talks.html.

V. M. Kaspi and A. M. Beloborodov. Magnetars. ARA&A, 55(1):261–301, Aug. 2017. doi: 10.1146/annurev-astro-081915-023329.

J. I. Katz. Coherent plasma-curvature radiation in FRB. MNRAS, 481(3):2946–2950, Dec. 2018. doi: 10.1093/mnras/sty2459.

G. Kauffmann, T. M. Heckman, C. Tremonti, J. Brinchmann, S. Charlot, S. D. M. White, S. E. Ridgway, J. Brinkmann, M. Fukugita, P. B. Hall, Ž. Ivezić, G. T. Richards, and D. P. Schneider. The host galaxies of active galactic nuclei. MNRAS, 346(4):1055–1077, Dec. 2003. doi: 10.1111/j.1365-2966.2003.07154.x.

B. Kaur, N. Kanekar, and J. X. Prochaska. A fast radio burst progenitor born in a galaxy merger. ApJ, 925(2):L20, Feb. 2022. doi: 10.3847/2041-8213/ac4ca8.

E. F. Keane, B. W. Stappers, M. Kramer, and A. G. Lyne. On the origin of a highly dispersed coherent radio burst. MNRAS, 425(1):L71–L75, Sept. 2012. doi: 10.1111/j.1745-3933.2012.01306.x.

E. F. Keane, S. Johnston, S. Bhandari, E. Barr, N. D. R. Bhat, M. Burgay, M. Caleb, C. Flynn, A. Jameson, M. Kramer, E. Petroff, A. Possenti, W. van Straten, M. Bailes, S. Burke-Spolaor, R. P. Eatough, B. W. Stappers, T. Totani, M. Honma, H. Furusawa, T. Hattori, T. Morokuma, Y. Niino, H. Sugai, T. Terai, N. Tominaga, S. Yamasaki, N. Yasuda, R. Allen, J. Cooke, J. Jencson, M. M. Kasliwal, D. L. Kaplan, S. J. Tingay, A. Williams, R. Wayth, P. Chandra, D. Perrodin, M. Berezina, M. Mickaliger, and C. Bassa. The host galaxy of a fast radio burst. Nature, 530(7591):453–456, Feb. 2016. doi: 10.1038/nature17140.

L. C. Keating and U.-L. Pen. Exploring the dispersion measure of the Milky Way halo. MNRAS, 496(1):L106–L110, July 2020. doi: 10.1093/mnrasl/slaa095.

J. Kennicutt, Robert C., P. Tamblyn, and C. E. Congdon. Past and Future Star Formation in Disk Galaxies. ApJ, 435:22, Nov. 1994. doi: 10.1086/174790.

L. J. Kewley, B. Groves, G. Kauffmann, and T. Heckman. The host galaxies and classification of active galactic nuclei. MNRAS, 372(3):961–976, Nov. 2006. doi: 10.1111/j.1365-2966.2006.10859.x.

F. Kirsten, B. Marcote, K. Nimmo, J. W. T. Hessels, M. Bhardwaj, S. P. Tendulkar, A. Keimpema, J. Yang, M. P. Snelders, P. Scholz, A. B. Pearlman, C. J. Law, W. M. Peters, M. Giroletti, D. M. Hewitt, U. Bach, V. Bezukovs, M. Burgay, S. T. Buttaccio, J. E. Conway, A. Corongiu, R. Feiler, O. Forssén, M. P. Gawroński, R. Karuppusamy, M. A. Kharinov, M. Lindqvist, G. Maccaferri, A. Melnikov, O. S. Ould-Boukattine, Z. Paragi, A. Possenti, G. Surcis, N. Wang, J. Yuan, K. Aggarwal, R. Anna-Thomas, G. C. Bower, R. Blaauw, S. Burke-Spolaor, T. Cassanelli, T. E. Clarke, E. Fonseca, B. M. Gaensler, A. Gopinath, V. M. Kaspi, N. Kassim, T. J. W. Lazio, C. Leung, D. Li, H. H. Lin, K. W. Masui, R. Mckinven, D. Michilli, A. Mikhailov, C. Ng, A. Orbidans, U. L. Pen, E. Petroff, M. Rahman, S. M. Ransom, K. Shin, K. M. Smith, I. H. Stairs, and W. Vlemmings. A repeating fast radio burst source in a globular cluster. *arXiv e-prints*, art. arXiv:2105.11445, May 2021.

U. Klein, U. Lisenfeld, and S. Verley. Radio synchrotron spectra of star-forming galaxies. A&A, 611:A55, Mar. 2018. doi: 10.1051/0004-6361/201731673.

A. Klypin, G. Yepes, S. Gottlöber, F. Prada, and S. Heß. MultiDark simulations: the story of dark matter halo concentrations and density profiles. MNRAS, 457(4):4340–4359, Apr. 2016. doi: 10.1093/mnras/stw248.

K. I. I. Koljonen and D. M. Russell. The Radio/X-Ray Correlation in X-Ray Binaries—Insights from a Hard X-Ray Perspective. ApJ, 871(1):26, Jan. 2019. doi: 10.3847/1538-4357/aaf38f.

X. Kong, X. Zhou, J. Chen, F. Cheng, Z. Jiang, J. Zhu, Z. Zheng, S. Mao, Z. Shang, X. Fan, Y.-I. Byun, R. Chen, W.-p. Chen, L. Deng, J. J. Hester, Y. Li, W. Lin, H. Su, W.-h. Sun, W.-s. Tsay, R. A. Windhorst, H. Wu, X. Xia, W. Xu, S. Xue, H. Yan, Z. Zheng, and Z. Zou. Spatially Resolved Spectrophotometry of M81: Age, Metallicity, and Reddening Maps. AJ, 119(6):2745–2756, June 2000. doi: 10.1086/301396.

E. Kourkchi and R. B. Tully. Galaxy Groups Within 3500 km s^{-1}. ApJ, 843(1):16, July 2017. doi: 10.3847/1538-4357/aa76db.

M. Krause. Magnetic fields and star formation in spiral galaxies. *arXiv preprint arXiv:0806.2060*, 2008.

A. V. Kravtsov, A. A. Berlind, R. H. Wechsler, A. A. Klypin, S. Gottlöber, B. Allgood, and J. R. Primack. The Dark Side of the Halo Occupation Distribution. ApJ, 609(1):35–49, July 2004. doi: 10.1086/420959.

M. Kriek, P. G. van Dokkum, I. Labbé, M. Franx, G. D. Illingworth, D. Marchesini, and R. F. Quadri. An Ultra-Deep Near-Infrared Spectrum of a Compact Quiescent Galaxy at z = 2.2. ApJ, 700(1):221–231, July 2009. doi: 10.1088/0004-637X/700/1/221.

R.-P. Kudritzki, M. A. Urbaneja, Z. Gazak, F. Bresolin, N. Przybilla, W. Gieren, and G. Pietrzyński. Quantitative spectroscopy of blue supergiant stars in the disk of m81: metallicity, metallicity gradient, and distance. *The Astrophysical Journal*, 747(1):15, 2012.

S. R. Kulkarni. From gamma-ray bursts to fast radio bursts. *Nature Astronomy*, 2:832–835, Oct. 2018. doi: 10.1038/s41550-018-0621-y.

P. Kumar and Ž. Bošnjak. FRB coherent emission from decay of Alfvén waves. MNRAS, 494(2):2385–2395, May 2020. doi: 10.1093/mnras/staa774.

P. Kumar and E. V. Linder. Use of fast radio burst dispersion measures as distance measures. Phys. Rev. D, 100(8):083533, Oct. 2019. doi: 10.1103/PhysRevD.100.083533.

P. Kumar, W. Lu, and M. Bhattacharya. Fast radio burst source properties and curvature radiation model. MNRAS, 468(3):2726–2739, July 2017. doi: 10.1093/mnras/stx665.

P. Kumar, R. M. Shannon, S. Osłowski, H. Qiu, S. Bhandari, W. Farah, C. Flynn, M. Kerr, D. R. Lorimer, J.-P. Macquart, C. Ng, C. J. Phillips, D. C. Price, and R. Spiewak. Faint repetitions from a bright fast radio burst source. *The Astrophysical Journal Letters*, 887(2):l30, 2019. doi: 10.3847/2041-8213/ab5b08. URL `https://app.dimensions.ai/details/publication/pub.1123496441andhttp://arxiv.org/pdf/1908.10026`.

A. Kurcz, M. Bilicki, A. Solarz, M. Krupa, A. Pollo, and K. Małek. Towards automatic classification of all WISE sources. A&A, 592:A25, July 2016. doi: 10.1051/0004-6361/201628142.

D. Kwiatkowski. Progenitors of the Accretion-Induced Collapse of White Dwarfs. *arXiv e-prints*, art. arXiv:1512.00678, Dec. 2015.

M. Lacy, S. A. Baum, C. J. Chandler, S. Chatterjee, E. J. Murphy, S. T. Myers, et al. The vla sky survey (vlass): Description and science goals. *AAS*, 227:324–09, 2016.

D. Lang, D. W. Hogg, and D. J. Schlegel. WISE Photometry for 400 Million SDSS Sources. AJ, 151(2):36, Feb. 2016. doi: 10.3847/0004-6256/151/2/36.

A. E. Lanman, B. C. Andersen, P. Chawla, A. Josephy, G. Noble, V. M. Kaspi, K. Bandura, M. Bhardwaj, P. J. Boyle, C. Brar, D. Breitman, T. Cassanelli, F. A. Dong, E. Fonseca, B. M. Gaensler, D. Good, J. Kaczmarek, C. Leung, K. W. Masui, B. W. Meyers, C. Ng, C. Patel, A. B. Pearlman, E. Petroff, Z. Pleunis, M. Rafiei-Ravandi, M. Rahman, P. Sanghavi, P. Scholz, K. Shin, I. Stairs, S. Tendulkar, and A. Zwaniga. A Sudden Period of High Activity from Repeating Fast Radio Burst 20201124A. ApJ, 927(1):59, Mar. 2022. doi: 10.3847/1538-4357/ac4bc7.

C. J. Law, B. J. Butler, J. X. Prochaska, B. Zackay, S. Burke-Spolaor, A. Mannings, N. Tejos, A. Josephy, B. Andersen, P. Chawla, K. E. Heintz, K. Aggarwal, G. C. Bower, P. B. Demorest, C. D. Kilpatrick, T. J. W. Lazio, J. Linford, R. Mckinven, S. Tendulkar, and S. Simha. A Distant Fast Radio Burst Associated with Its Host Galaxy by the Very Large Array. ApJ, 899(2):161, Aug. 2020. doi: 10.3847/1538-4357/aba4ac.

C. J. Law, L. Connor, and K. Aggarwal. On the Fast Radio Burst and Persistent Radio Source Populations. ApJ, 927(1):55, Mar. 2022. doi: 10.3847/1538-4357/ac4c42.

C. Leitherer. Modeling the Stellar Spectral Energy Distributions of Star-Forming Galaxies. In C. C. Popescu and R. J. Tuffs, editors, *The Spectral Energy Distributions of Gas-Rich Galaxies: Confronting Models with Data*, volume 761 of *American Institute of Physics Conference Series*, pages 39–58, Apr. 2005. doi: 10.1063/1.1913914.

J. Leja, B. D. Johnson, C. Conroy, P. G. van Dokkum, and N. Byler. Deriving Physical Properties from Broadband Photometry with Prospector: Description of the Model and a Demonstration of its Accuracy Using 129 Galaxies in the Local Universe. ApJ, 837: 170, 2017. doi: 10.3847/1538-4357/aa5ffe.

C. Leung, J. Mena-Parra, K. Masui, K. Bandura, M. Bhardwaj, P. J. Boyle, C. Brar, M. Bruneault, T. Cassanelli, D. Cubranic, J. F. Kaczmarek, V. Kaspi, T. Landecker, D. Michilli, N. Milutinovic, C. Patel, Z. Pleunis, M. Rahman, A. Renard, P. Sanghavi, I. H. Stairs, P. Scholz, K. Vanderlinde, and Chime/Frb Collaboration. A Synoptic VLBI Technique for Localizing Nonrepeating Fast Radio Bursts with CHIME/FRB. AJ, 161 (2):81, Feb. 2021. doi: 10.3847/1538-3881/abd174.

C. Leung, Z. Kader, K. W. Masui, M. Dobbs, D. Michilli, J. Mena-Parra, R. Mckinven, C. Ng, K. Bandura, M. Bhardwaj, C. Brar, T. Cassanelli, P. Chawla, F. A. Dong, D. Good, V. Kaspi, A. E. Lanman, H.-H. Lin, B. W. Meyers, A. B. Pearlman, U.-L. Pen, E. Petroff, Z. Pleunis, M. Rafiei-Ravandi, M. Rahman, P. Sanghavi, P. Scholz, K. Shin, S. Siegel, K. M. Smith, I. Stairs, S. P. Tendulkar, and K. Vanderlinde. Constraining primordial black holes using fast radio burst gravitational-lens interferometry with CHIME/FRB. Phys. Rev. D, 106(4):043017, Aug. 2022. doi: 10.1103/PhysRevD.106.043017.

Y. Levin, A. M. Beloborodov, and A. Bransgrove. Precessing Flaring Magnetar as a Source of Repeating FRB 180916.J0158+65. ApJ, 895(2):L30, June 2020. doi: 10.3847/2041-8213/ab8c4c.

C. Li, L. Lin, S. Xiong, M. Ge, X. Li, T. Li, F. Lu, S. Zhang, Y. Tuo, Y. Nang, et al. Identification of a non-thermal x-ray burst with the galactic magnetar sgr 1935+ 2154 and a fast radio burst with insight-hxmt. *arXiv preprint arXiv:2005.11071*, 2020.

D. Li, P. Wang, W. W. Zhu, B. Zhang, X. X. Zhang, R. Duan, Y. K. Zhang, Y. Feng, N. Y. Tang, S. Chatterjee, J. M. Cordes, M. Cruces, S. Dai, V. Gajjar, G. Hobbs, C. Jin, M. Kramer, D. R. Lorimer, C. C. Miao, C. H. Niu, J. R. Niu, Z. C. Pan, L. Qian, L. Spitler, D. Werthimer, G. Q. Zhang, F. Y. Wang, X. Y. Xie, Y. L. Yue, L. Zhang, Q. J. Zhi, and Y. Zhu. A bimodal burst energy distribution of a repeating fast radio burst source. Nature, 598(7880):267–271, Oct. 2021. doi: 10.1038/s41586-021-03878-5.

Y. Li and B. Zhang. A Comparative Study of Host Galaxy Properties between Fast Radio Bursts and Stellar Transients. ApJ, 899(1):L6, Aug. 2020. doi: 10.3847/2041-8213/aba907.

Y. Li, B. Zhang, K. Nagamine, and J. Shi. The FRB 121102 Host Is Atypical among Nearby Fast Radio Bursts. ApJ, 884(1):L26, Oct. 2019. doi: 10.3847/2041-8213/ab3e41.

S. H. Lim, H. J. Mo, Y. Lu, H. Wang, and X. Yang. Galaxy groups in the low-redshift Universe. MNRAS, 470(3):2982–3005, Sept. 2017. doi: 10.1093/mnras/stx1462.

X. Liu. The Remnant of Neutron Star-White Dwarf Merger and the Repeating Fast Radio Bursts. 10(1):28–38. doi: 10.4236/ijaa.2020.101003.

X. Liu. A model of neutron-star-white-dwarf collision for fast radio bursts. Ap&SS, 363 (11):242, Nov. 2018. doi: 10.1007/s10509-018-3462-3.

N. Locatelli, M. Ronchi, G. Ghirlanda, and G. Ghisellini. The luminosity-volume test for cosmological fast radio bursts. A&A, 625:A109, May 2019. doi: 10.1051/0004-6361/201834722.

C. J. Lonsdale, R. J. Cappallo, M. F. Morales, F. H. Briggs, L. Benkevitch, J. D. Bowman, J. D. Bunton, S. Burns, B. E. Corey, L. DeSouza, et al. The murchison widefield array: Design overview. *Proceedings of the IEEE*, 97(8):1497–1506, 2009.

D. R. Lorimer and M. Kramer. *Handbook of Pulsar Astronomy*, volume 4. 2004.

D. R. Lorimer, M. Bailes, M. A. McLaughlin, D. J. Narkevic, and F. Crawford. A Bright Millisecond Radio Burst of Extragalactic Origin. *Science*, 318:777, Nov. 2007.

W. Lu and P. Kumar. A universal EDF for repeating fast radio bursts? MNRAS, 461(1): L122–L126, Sept. 2016. doi: 10.1093/mnrasl/slw113.

W. Lu and P. Kumar. On the radiation mechanism of repeating fast radio bursts. MNRAS, 477(2):2470–2493, June 2018. doi: 10.1093/mnras/sty716.

W. Lu and A. L. Piro. Implications from ASKAP Fast Radio Burst Statistics. ApJ, 883(1): 40, Sept. 2019. doi: 10.3847/1538-4357/ab3796.

W. Lu, P. Kumar, and B. Zhang. A unified picture of Galactic and cosmological fast radio bursts. MNRAS, 498(1):1397–1405, Oct. 2020a. doi: 10.1093/mnras/staa2450.

W. Lu, A. L. Piro, and E. Waxman. Implications of Canadian Hydrogen Intensity Mapping Experiment repeating fast radio bursts. MNRAS, 498(2):1973–1982, Oct. 2020b. doi: 10.1093/mnras/staa2397.

P. W. Lucas, M. G. Hoare, A. Longmore, A. C. Schröder, C. J. Davis, A. Adamson, R. M. Bandyopadhyay, R. de Grijs, M. Smith, A. Gosling, S. Mitchison, A. Gáspár, M. Coe, M. Tamura, Q. Parker, M. Irwin, N. Hambly, J. Bryant, R. S. Collins, N. Cross, D. W. Evans, E. Gonzalez-Solares, S. Hodgkin, J. Lewis, M. Read, M. Riello, E. T. W. Sutorius, A. Lawrence, J. E. Drew, S. Dye, and M. A. Thompson. The UKIDSS Galactic Plane Survey. MNRAS, 391(1):136–163, Nov. 2008. doi: 10.1111/j.1365-2966.2008.13924.x.

R. Lunnan, R. Chornock, E. Berger, T. Laskar, W. Fong, A. Rest, N. E. Sanders, P. M. Challis, M. R. Drout, R. J. Foley, M. E. Huber, R. P. Kirshner, C. Leibler, G. H. Marion, M. McCrum, D. Milisavljevic, G. Narayan, D. Scolnic, S. J. Smartt, K. W. Smith, A. M. Soderberg, J. L. Tonry, W. S. Burgett, K. C. Chambers, H. Flewelling, K. W. Hodapp, N. Kaiser, E. A. Magnier, P. A. Price, and R. J. Wainscoat. Hydrogen-poor Superluminous Supernovae and Long-duration Gamma-Ray Bursts Have Similar Host Galaxies. ApJ, 787(2):138, June 2014. doi: 10.1088/0004-637X/787/2/138.

R. Lunnan, R. Chornock, E. Berger, A. Rest, W.-f. Fong, D. Scolnic, D. Jones, A. M. Soderberg, P. M. Challis, M. R. Drout, et al. Zooming in on the progenitors of superluminous supernovae with the hst. *The Astrophysical Journal*, 804(2):90, 2015.

R. Luo, K. Lee, D. R. Lorimer, and B. Zhang. On the normalized FRB luminosity function. MNRAS, 481(2):2320–2337, Dec. 2018. doi: 10.1093/mnras/sty2364.

R. Luo, Y. Men, K. Lee, W. Wang, D. R. Lorimer, and B. Zhang. On the FRB luminosity function - - II. Event rate density. MNRAS, 494(1):665–679, May 2020. doi: 10.1093/mnras/staa704.

R. H. Lupton, J. E. Gunn, and A. S. Szalay. A Modified Magnitude System that Produces Well-Behaved Magnitudes, Colors, and Errors Even for Low Signal-to-Noise Ratio Measurements. AJ, 118(3):1406–1410, Sept. 1999. doi: 10.1086/301004.

Y. Lyubarsky. A model for fast extragalactic radio bursts. MNRAS, 442:L9–L13, July 2014. doi: 10.1093/mnrasl/slu046.

Y. Lyubarsky. Fast Radio Bursts from Reconnection in a Magnetar Magnetosphere. ApJ, 897(1):1, July 2020. doi: 10.3847/1538-4357/ab97b5.

Y. Lyubarsky. Emission Mechanisms of Fast Radio Bursts. *Universe*, 7(3):56, Mar. 2021. doi: 10.3390/universe7030056.

M. Lyutikov, M. V. Barkov, and D. Giannios. FRB Periodicity: Mild Pulsars in Tight O/B-star Binaries. ApJ, 893(2):L39, Apr. 2020. doi: 10.3847/2041-8213/ab87a4.

J. P. Macquart and R. Ekers. FRB event rate counts - II. Fluence, redshift, and dispersion measure distributions. MNRAS, 480(3):4211–4230, Nov. 2018. doi: 10.1093/mnras/sty2083.

J.-P. Macquart, M. Bailes, N. D. R. Bhat, G. C. Bower, J. D. Bunton, S. Chatterjee, T. Colegate, J. M. Cordes, L. D'Addario, A. Deller, R. Dodson, R. Fender, K. Haines, P. Halll, C. Harris, A. Hotan, S. Johnston, D. L. Jones, M. Keith, J. Y. Koay, T. J. W. Lazio, W. Majid, T. Murphy, R. Navarro, C. Phillips, P. Quinn, R. A. Preston, B. Stansby, I. Stairs, B. Stappers, L. Staveley-Smith, S. Tingay, D. Thompson, W. van Straten, K. Wagstaff, M. Warren, R. Wayth, L. Wen, and CRAFT Collaboration. The Commensal Real-Time ASKAP Fast-Transients (CRAFT) Survey. PASA, 27(3):272–282, June 2010. doi: 10.1071/AS09082.

J.-P. Macquart, J. Prochaska, M. McQuinn, K. Bannister, S. Bhandari, C. Day, A. Deller, R. Ekers, C. James, L. Marnoch, et al. A census of baryons in the universe from localized fast radio bursts. *Nature*, 581(7809):391–395, 2020.

D. R. Madison, D. Agarwal, K. Aggarwal, O. Young, H. T. Cromartie, M. T. Lam, S. Chatterjee, J. M. Cordes, N. Garver-Daniels, D. R. Lorimer, R. S. Lynch, M. A. McLaughlin, S. M. Ransom, and R. S. Wharton. A Deep Targeted Search for Fast Radio Bursts from the Sites of Low-redshift Short Gamma-Ray Bursts. ApJ, 887(2):252, Dec. 2019. doi: 10.3847/1538-4357/ab58c3.

E. A. Magnier, E. F. Schlafly, D. P. Finkbeiner, J. L. Tonry, B. Goldman, S. Röser, E. Schilbach, S. Casertano, K. C. Chambers, H. A. Flewelling, M. E. Huber, P. A. Price, W. E. Sweeney, C. Z. Waters, L. Denneau, P. W. Draper, K. W. Hodapp, R. Jedicke,

N. Kaiser, R. P. Kudritzki, N. Metcalfe, C. W. Stubbs, and R. J. Wainscoat. Pan-STARRS Photometric and Astrometric Calibration. ApJS, 251(1):6, Nov. 2020a. doi: 10.3847/1538-4365/abb82a.

E. A. Magnier, W. E. Sweeney, K. C. Chambers, H. A. Flewelling, M. E. Huber, P. A. Price, C. Z. Waters, L. Denneau, P. W. Draper, D. Farrow, R. Jedicke, K. W. Hodapp, N. Kaiser, R. P. Kudritzki, N. Metcalfe, C. W. Stubbs, and R. J. Wainscoat. Pan-STARRS Pixel Analysis: Source Detection and Characterization. ApJS, 251(1):5, Nov. 2020b. doi: 10.3847/1538-4365/abb82c.

R. A. Main, G. H. Hilmarsson, V. R. Marthi, L. G. Spitler, R. S. Wharton, S. Bethapudi, D. Z. Li, and H. H. Lin. Scintillation time-scale measurement of the highly active FRB20201124A. MNRAS, 509(3):3172–3180, Jan. 2022. doi: 10.1093/mnras/stab3218.

W. A. Majid, A. B. Pearlman, T. A. Prince, R. S. Wharton, C. J. Naudet, K. Bansal, L. Connor, M. Bhardwaj, and S. P. Tendulkar. A Bright Fast Radio Burst from FRB 20200120E with Sub-100 Nanosecond Structure. ApJ, 919(1):L6, Sept. 2021. doi: 10.3847/2041-8213/ac1921.

A. H. Maller and J. S. Bullock. Multiphase galaxy formation: high-velocity clouds and the missing baryon problem. *Monthly Notices of the Royal Astronomical Society*, 355(3): 694–712, 2004.

R. N. Manchester, G. B. Hobbs, A. Teoh, and M. Hobbs. The Australia Telescope National Facility Pulsar Catalogue. AJ, 129(4):1993–2006, Apr. 2005. doi: 10.1086/428488.

A. G. Mannings, W.-f. Fong, S. Simha, J. X. Prochaska, M. Rafelski, C. D. Kilpatrick, N. Tejos, K. E. Heintz, S. Bhandari, C. K. Day, A. T. Deller, S. D. Ryder, R. M. Shannon, and S. P. Tendulkar. A High-Resolution View of Fast Radio Burst Host Environments. *arXiv e-prints*, art. arXiv:2012.11617, Dec. 2020.

D. Maoz. Low-luminosity active galactic nuclei: are they UV faint and radio loud? MNRAS, 377(4):1696–1710, June 2007. doi: 10.1111/j.1365-2966.2007.11735.x.

B. Marcote, Z. Paragi, J. W. T. Hessels, A. Keimpema, H. J. van Langevelde, Y. Huang, C. G. Bassa, S. Bogdanov, G. C. Bower, S. Burke-Spolaor, B. J. Butler, R. M. Campbell,

S. Chatterjee, J. M. Cordes, P. Demorest, M. A. Garrett, T. Ghosh, V. M. Kaspi, C. J. Law, T. J. W. Lazio, M. A. McLaughlin, S. M. Ransom, C. J. Salter, P. Scholz, A. Seymour, A. Siemion, L. G. Spitler, S. P. Tendulkar, and R. S. Wharton. The Repeating Fast Radio Burst FRB 121102 as Seen on Milliarcsecond Angular Scales. ApJ, 834(2):L8, Jan. 2017. doi: 10.3847/2041-8213/834/2/L8.

B. Marcote, K. Nimmo, J. Hessels, S. Tendulkar, C. Bassa, Z. Paragi, A. Keimpema, M. Bhardwaj, R. Karuppusamy, V. Kaspi, et al. A repeating fast radio burst source localized to a nearby spiral galaxy. *Nature*, 577(7789):190–194, 2020.

B. Margalit and B. D. Metzger. A Concordance Picture of FRB 121102 as a Flaring Magnetar Embedded in a Magnetized Ion-Electron Wind Nebula. ApJ, 868(1):L4, Nov. 2018. doi: 10.3847/2041-8213/aaedad.

B. Margalit, P. Beniamini, N. Sridhar, and B. D. Metzger. Implications of a Fast Radio Burst from a Galactic Magnetar. ApJ, 899(2):L27, Aug. 2020. doi: 10.3847/2041-8213/abac57.

S. Markoff, M. Nowak, A. Young, H. L. Marshall, C. R. Canizares, A. Peck, M. Krips, G. Petitpas, R. Schödel, G. C. Bower, et al. Results from an extensive simultaneous broadband campaign on the underluminous active nucleus m81*: Further evidence for mass-scaling accretion in black holes. *The Astrophysical Journal*, 681(2):905, 2008.

L. Marnoch, S. D. Ryder, K. W. Bannister, S. Bhandari, C. K. Day, A. T. Deller, J.-P. Macquart, R. M. McDermid, J. Xavier Prochaska, H. Qiu, E. M. Sadler, R. M. Shannon, and N. Tejos. A search for supernova-like optical counterparts to ASKAP-localised fast radio bursts. A&A, 639:A119, July 2020. doi: 10.1051/0004-6361/202038076.

R. Martone, C. Guidorzi, R. Margutti, L. Nicastro, L. Amati, F. Frontera, M. Marongiu, M. Orlandini, and E. Virgilli. A cumulative search for hard X/γ-ray emission associated with fast radio bursts in Fermi/GBM data. A&A, 631:A62, Nov. 2019. doi: 10.1051/0004-6361/201936284.

J. Marvil, F. Owen, and J. Eilek. Integrated Radio Continuum Spectra of Galaxies. AJ, 149(1):32, Jan. 2015. doi: 10.1088/0004-6256/149/1/32.

K. L. Masters, M. Mosleh, A. K. Romer, R. C. Nichol, S. P. Bamford, K. Schawinski, C. J. Lintott, D. Andreescu, H. C. Campbell, B. Crowcroft, I. Doyle, E. M. Edmondson, P. Murray, M. J. Raddick, A. Slosar, A. S. Szalay, and J. Vandenberg. Galaxy Zoo: passive red spirals. 405(2):783–799. doi: 10.1111/j.1365-2966.2010.16503.x.

K. L. Masters, A. Crook, T. Hong, T. H. Jarrett, B. S. Koribalski, L. Macri, C. M. Springob, and L. Staveley-Smith. 2MTF III. H I 21 cm observations of 1194 spiral galaxies with the Green Bank Telescope. MNRAS, 443(2):1044–1056, Sept. 2014. doi: 10.1093/mnras/stu1225.

K. Masui, H.-H. Lin, J. Sievers, C. J. Anderson, T.-C. Chang, X. Chen, A. Ganguly, M. Jarvis, C.-Y. Kuo, Y.-C. Li, Y.-W. Liao, M. McLaughlin, U.-L. Pen, J. B. Peterson, A. Roman, P. T. Timbie, T. Voytek, and J. K. Yadav. Dense magnetized plasma associated with a fast radio burst. Nature, 528(7583):523–525, Dec. 2015. doi: 10.1038/nature15769.

K. W. Masui, J. R. Shaw, C. Ng, K. M. Smith, K. Vanderlinde, and A. Paradise. Algorithms for FFT Beamforming Radio Interferometers. *arXiv e-prints*, art. arXiv:1710.08591, Oct. 2017.

K. W. Masui, J. R. Shaw, C. Ng, K. M. Smith, K. Vanderlinde, and A. Paradise. Algorithms for fft beamforming radio interferometers. *The Astrophysical Journal*, 879(1):16, 2019.

W. G. Mathews and J. X. Prochaska. Circumgalactic Oxygen Absorption and Feedback. ApJ, 846(2):L24, Sept. 2017. doi: 10.3847/2041-8213/aa8861.

S. E. Maxwell, H. D. Delaney, and K. Kelley. *Designing experiments and analyzing data: A model comparison perspective*. Routledge, 2017.

M. L. McCall, P. M. Rybski, and G. A. Shields. The chemistry of galaxies. I. The nature of giant extragalactic H II regions. ApJS, 57:1–62, Jan. 1985. doi: 10.1086/190994.

J. W. McKee, B. W. Stappers, C. G. Bassa, S. Chen, I. Cognard, M. Gaikwad, G. H. Janssen, R. Karuppusamy, M. Kramer, K. J. Lee, K. Liu, D. Perrodin, S. A. Sanidas, R. Smits, L. Wang, and W. W. Zhu. A detailed study of giant pulses from PSR B1937+21 using the Large European Array for Pulsars. MNRAS, 483(4):4784–4802, Mar. 2019. doi: 10.1093/mnras/sty3058.

R. Mckinven, D. Michilli, K. Masui, D. Cubranic, B. M. Gaensler, C. Ng, M. Bhardwaj, C. Leung, P. J. Boyle, C. Brar, T. Cassanelli, D. Li, J. Mena-Parra, M. Rahman, and I. H. Stairs. Polarization Pipeline for Fast Radio Bursts Detected by CHIME/FRB. ApJ, 920 (2):138, Oct. 2021. doi: 10.3847/1538-4357/ac126a.

J. P. McMullin, B. Waters, D. Schiebel, W. Young, and K. Golap. CASA Architecture and Applications. In R. A. Shaw, F. Hill, and D. J. Bell, editors, *Astronomical Data Analysis Software and Systems XVI*, volume 376 of *Astronomical Society of the Pacific Conference Series*, page 127, Oct. 2007.

M. McQuinn. Locating the "Missing" Baryons with Extragalactic Dispersion Measure Estimates. ApJ, 780(2):L33, Jan. 2014. doi: 10.1088/2041-8205/780/2/L33.

D. B. Melrose. Coherent emission mechanisms in astrophysical plasmas. *Reviews of Modern Plasma Physics*, 1(1):5, Dec. 2017. doi: 10.1007/s41614-017-0007-0.

Y. Men, K. Aggarwal, Y. Li, D. Palaniswamy, S. Burke-Spolaor, K. J. Lee, R. Luo, P. Demorest, S. Tendulkar, D. Agarwal, O. Young, and B. Zhang. Non-detection of fast radio bursts from six gamma-ray burst remnants with possible magnetar engines. MNRAS, 489(3):3643–3647, Nov. 2019. doi: 10.1093/mnras/stz2386.

J. Mena-Parra, K. Bandura, M. Dobbs, J. Shaw, and S. Siegel. Quantization bias for digital correlators. *Journal of Astronomical Instrumentation*, 7(02n03):1850008, 2018.

J. Mena-Parra, C. Leung, S. Cary, K. W. Masui, J. F. Kaczmarek, M. Amiri, K. Bandura, P. J. Boyle, T. Cassanelli, J. F. Cliche, M. Dobbs, V. M. Kaspi, T. L. Landecker, A. Lanman, J. L. Sievers, J. L. Sievers, and Chime/Frb Collaboration. A Clock Stabilization System for CHIME/FRB Outriggers. AJ, 163(2):48, Feb. 2022. doi: 10.3847/1538-3881/ac397a.

S. Mereghetti, V. Savchenko, C. Ferrigno, D. Götz, M. Rigoselli, A. Tiengo, A. Bazzano, E. Bozzo, A. Coleiro, T.-L. Courvoisier, et al. Integral discovery of a burst with associated radio emission from the magnetar sgr 1935+ 2154. *arXiv preprint arXiv:2005.06335*, 2020.

S. Mereghetti, M. Topinka, M. Rigoselli, and D. Götz. INTEGRAL Limits on Past High-energy Activity from FRB 20200120E in M81. ApJ, 921(1):L3, Nov. 2021. doi: 10.3847/2041-8213/ac2ee7.

D. Merritt, J. F. Navarro, A. Ludlow, and A. Jenkins. A universal density profile for dark and luminous matter? *The Astrophysical Journal Letters*, 624(2):L85, 2005.

B. D. Metzger, E. Berger, and B. Margalit. Millisecond Magnetar Birth Connects FRB 121102 to Superluminous Supernovae and Long-duration Gamma-Ray Bursts. ApJ, 841 (1):14, May 2017. doi: 10.3847/1538-4357/aa633d.

B. D. Metzger, B. Margalit, and L. Sironi. Fast radio bursts as synchrotron maser emission from decelerating relativistic blast waves. *Monthly Notices of the Royal Astronomical Society*, 485(3):4091–4106, 2019.

D. Michilli, A. Seymour, J. W. T. Hessels, L. G. Spitler, V. Gajjar, A. M. Archibald, G. C. Bower, S. Chatterjee, J. M. Cordes, K. Gourdji, G. H. Heald, V. M. Kaspi, C. J. Law, C. Sobey, E. A. K. Adams, C. G. Bassa, S. Bogdanov, C. Brinkman, P. Demorest, F. Fernandez, G. Hellbourg, T. J. W. Lazio, R. S. Lynch, N. Maddox, B. Marcote, M. A. McLaughlin, Z. Paragi, S. M. Ransom, P. Scholz, A. P. V. Siemion, S. P. Tendulkar, P. van Rooy, R. S. Wharton, and D. Whitlow. An extreme magneto-ionic environment associated with the fast radio burst source FRB 121102. Nature, 553(7687):182–185, Jan. 2018. doi: 10.1038/nature25149.

D. Michilli, K. W. Masui, R. Mckinven, D. Cubranic, M. Bruneault, C. Brar, C. Patel, P. J. Boyle, I. H. Stairs, A. Renard, K. Bandura, S. Berger, D. Breitman, T. Cassanelli, M. Dobbs, V. M. Kaspi, C. Leung, J. Mena-Parra, Z. Pleunis, L. Russell, P. Scholz, S. R. Siegel, S. P. Tendulkar, and K. Vand erlinde. An analysis pipeline for CHIME/FRB full-array baseband data. *arXiv e-prints*, art. arXiv:2010.06748, Oct. 2020.

M. J. Miller and J. N. Bregman. Constraining the Milky Way's Hot Gas Halo with O VII and O VIII Emission Lines. ApJ, 800(1):14, Feb. 2015. doi: 10.1088/0004-637X/800/1/14.

C. M. F. Mingarelli, J. Levin, and T. J. W. Lazio. Fast Radio Bursts and Radio Transients from Black Hole Batteries. ApJ, 814(2):L20, Dec. 2015. doi: 10.1088/2041-8205/814/2/L20.

D. Mitra, R. Wielebinski, M. Kramer, and A. Jessner. The effect of hii regions on rotation measure of pulsars. *Astronomy & Astrophysics*, 398(3):993–1005, 2003.

H. Mo, S. Mao, and S. D. White. The formation of galactic discs. *Monthly Notices of the Royal Astronomical Society*, 295(2):319–336, 1998.

T. J. Moriya. Radio Transients from Accretion-induced Collapse of White Dwarfs. 830(2): L38. doi: 10.3847/2041-8205/830/2/L38.

D. Morris, S. Voutsinas, N. C. Hambly, and R. G. Mann. Use of Docker for deployment and testing of astronomy software. *Astronomy and Computing*, 20:105–119, July 2017. doi: 10.1016/j.ascom.2017.07.004.

D. Moss and A. Shukurov. Turbulence and magnetic fields in elliptical galaxies. *Monthly Notices of the Royal Astronomical Society*, 279(1):229–239, 1996.

B. P. Moster, T. Naab, and S. D. M. White. Galactic star formation and accretion histories from matching galaxies to dark matter haloes. MNRAS, 428(4):3121–3138, Feb. 2013. doi: 10.1093/mnras/sts261.

M. Mouhcine and R. Ibata. A panoramic view of M81: new stellar systems in the debris field. MNRAS, 399(2):737–743, Oct. 2009. doi: 10.1111/j.1365-2966.2009.15135.x.

M. P. Muno, J. S. Clark, P. A. Crowther, S. M. Dougherty, R. de Grijs, C. Law, S. L. W. McMillan, M. R. Morris, I. Negueruela, D. Pooley, S. Portegies Zwart, and F. Yusef-Zadeh. A Neutron Star with a Massive Progenitor in Westerlund 1. ApJ, 636(1):L41–L44, Jan. 2006. doi: 10.1086/499776.

S. Nakagawa. A farewell to bonferroni: the problems of low statistical power and publication bias. *Behavioral ecology*, 15(6):1044–1045, 2004.

J. B. Nantais and J. P. Huchra. Spectroscopy of M81 Globular Clusters. AJ, 139(6):2620–2638, June 2010. doi: 10.1088/0004-6256/139/6/2620.

E. National Academies of Sciences and Medicine. *Pathways to Discovery in Astronomy and Astrophysics for the 2020s*. 2021. doi: 10.17226/26141.

L. Newburgh, K. Bandura, M. Bucher, T.-C. Chang, H. Chiang, J. Cliche, R. Davé, M. Dobbs, C. Clarkson, K. Ganga, et al. Hirax: a probe of dark energy and radio transients. In *Ground-based and Airborne Telescopes VI*, volume 9906, page 99065X. International Society for Optics and Photonics, 2016.

L. B. Newburgh, G. E. Addison, M. Amiri, K. Bandura, J. R. Bond, L. Connor, J.-F. Cliche, G. Davis, M. Deng, N. Denman, et al. Calibrating chime: a new radio interferometer to probe dark energy. In *Ground-based and Airborne Telescopes V*, volume 9145, page 91454V. International Society for Optics and Photonics, 2014.

C. Ng, K. Vanderlinde, A. Paradise, P. Klages, K. Masui, K. Smith, K. Bandura, P. J. Boyle, M. Dobbs, V. Kaspi, A. Renard, J. R. Shaw, I. Stairs, and I. Tretyakov. CHIME FRB: An application of FFT beamforming for a radio telescope. In *XXXII International Union of Radio Science General Assembly & Scientific Symposium (URSI GASS) 2017*, page 4, Aug. 2017. doi: 10.23919/URSIGASS.2017.8105318.

C. Ng, K. Vanderlinde, A. Paradise, P. Klages, K. Masui, K. Smith, K. Bandura, P. J. Boyle, M. Dobbs, V. Kaspi, et al. Chime frb: An application of fft beamforming for a radio telescope. In *2017 XXXIInd General Assembly and Scientific Symposium of the International Union of Radio Science (URSI GASS)*, pages 1–4. IEEE, 2017.

L. Nicastro, C. Guidorzi, E. Palazzi, L. Zampieri, M. Turatto, and A. Gardini. Multi-wavelength Observations of Fast Radio Bursts. *Universe*, 7(3):76, Mar. 2021. doi: 10.3390/universe7030076.

M. Nicholl, P. K. G. Williams, E. Berger, V. A. Villar, K. D. Alexander, T. Eftekhari, and B. D. Metzger. Empirical Constraints on the Origin of Fast Radio Bursts: Volumetric Rates and Host Galaxy Demographics as a Test of Millisecond Magnetar Connection. ApJ, 843(2):84, July 2017. doi: 10.3847/1538-4357/aa794d.

R. Nikutta, N. Hunt-Walker, M. Nenkova, Ž. Ivezić, and M. Elitzur. The meaning of WISE colours - I. The Galaxy and its satellites. MNRAS, 442(4):3361–3379, Aug. 2014. doi: 10.1093/mnras/stu1087.

K. Nimmo, J. W. T. Hessels, A. Keimpema, A. M. Archibald, J. M. Cordes, R. Karuppusamy, F. Kirsten, D. Z. Li, B. Marcote, and Z. Paragi. Highly polarized microstructure from the repeating FRB 20180916B. *Nature Astronomy*, Mar. 2021. doi: 10.1038/s41550-021-01321-3.

K. Nimmo, J. W. T. Hessels, F. Kirsten, A. Keimpema, J. M. Cordes, M. P. Snelders, D. M. Hewitt, R. Karuppusamy, A. M. Archibald, V. Bezrukovs, M. Bhardwaj, R. Blaauw, S. T. Buttaccio, T. Cassanelli, J. E. Conway, A. Corongiu, R. Feiler, E. Fonseca, O. Forssén, M. Gawroński, M. Giroletti, M. A. Kharinov, C. Leung, M. Lindqvist, G. Maccaferri, B. Marcote, K. W. Masui, R. Mckinven, A. Melnikov, D. Michilli, A. G. Mikhailov, C. Ng, A. Orbidans, O. S. Ould-Boukattine, Z. Paragi, A. B. Pearlman, E. Petroff, M. Rahman, P. Scholz, K. Shin, K. M. Smith, I. H. Stairs, G. Surcis, S. P. Tendulkar, W. Vlemmings, N. Wang, J. Yang, and J. P. Yuan. Burst timescales and luminosities as links between young pulsars and fast radio bursts. *Nature Astronomy*, 6:393–401, Feb. 2022a. doi: 10.1038/s41550-021-01569-9.

K. Nimmo, D. M. Hewitt, J. W. T. Hessels, F. Kirsten, B. Marcote, U. Bach, R. Blaauw, M. Burgay, A. Corongiu, R. Feiler, M. P. Gawroński, M. Giroletti, R. Karuppusamy, A. Keimpema, M. A. Kharinov, M. Lindqvist, G. Maccaferri, A. Melnikov, A. Mikhailov, O. S. Ould-Boukattine, Z. Paragi, M. Pilia, A. Possenti, M. P. Snelders, G. Surcis, M. Trudu, T. Venturi, W. Vlemmings, N. Wang, J. Yang, and J. Yuan. Milliarcsecond Localization of the Repeating FRB 20201124A. ApJ, 927(1):L3, Mar. 2022b. doi: 10.3847/2041-8213/ac540f.

C. H. Niu, K. Aggarwal, D. Li, X. Zhang, S. Chatterjee, C. W. Tsai, W. Yu, C. J. Law, S. Burke-Spolaor, J. M. Cordes, Y. K. Zhang, S. K. Ocker, J. M. Yao, P. Wan, Y. Feng, Y. Niino, C. Bochenek, M. Cruces, L. Connor, J. A. Jiang, S. Dai, R. Luo, G. D. Li, C. C. Miao, J. R. Niu, R. Anna-Thomas, J. Sydnor, D. Stern, W. Y. Wang, M. Yuan, Y. L. Yue, D. J. Zhou, Z. Yan, W. W. Zhu, and B. Zhang. A repeating fast radio burst associated with a persistent radio source. Nature, 606(7916):873–877, June 2022. doi: 10.1038/s41586-022-04755-5.

C. Núñez, N. Tejos, G. Pignata, C. D. Kilpatrick, J. X. Prochaska, K. E. Heintz, K. W. Bannister, S. Bhandari, C. K. Day, A. T. Deller, C. Flynn, E. K. Mahony, D. Majewski, L. Marnoch, H. Qiu, S. D. Ryder, and R. M. Shannon. Constraining bright optical counterparts of fast radio bursts. A&A, 653:A119, Sept. 2021. doi: 10.1051/0004-6361/202141110.

S. K. Ocker, J. M. Cordes, and S. Chatterjee. Electron Density Structure of the Local Galactic Disk. ApJ, 897(2):124, July 2020. doi: 10.3847/1538-4357/ab98f9.

S. K. Ocker, J. M. Cordes, S. Chatterjee, C.-H. Niu, D. Li, J. W. McKee, C. J. Law, C.-W. Tsai, R. Anna-Thomas, J.-M. Yao, and M. Cruces. The Large Dispersion and Scattering of FRB 20190520B Are Dominated by the Host Galaxy. ApJ, 931(2):87, June 2022. doi: 10.3847/1538-4357/ac6504.

W. Oehm, I. Thies, and P. Kroupa. Constraints on the dynamical evolution of the galaxy group m81. *Monthly Notices of the Royal Astronomical Society*, 467(1):273–289, 2017.

S. Okamoto, N. Arimoto, A. M. Ferguson, M. J. Irwin, E. J. Bernard, and Y. Utsumi. Stellar population and structural properties of dwarf galaxies and young stellar systems in the m81 group. *The Astrophysical Journal*, 884(2):128, 2019.

J. B. Oke. Absolute Spectral Energy Distributions for White Dwarfs. ApJS, 27:21, Feb. 1974. doi: 10.1086/190287.

J. B. Oke. Faint Spectrophotometric Standard Stars. AJ, 99:1621, May 1990. doi: 10.1086/115444.

S. Olausen and V. Kaspi. The mcgill magnetar catalog. *The Astrophysical Journal Supplement Series*, 212(1):6, 2014.

W. OMullane, N. Li, M. Nieto-Santisteban, A. Szalay, A. Thakar, and J. Gray. Batch is back: CasJobs, serving multi-TB data on the Web. *arXiv e-prints*, art. cs/0502072, Feb. 2005.

N. Oppermann, H. Junklewitz, G. Robbers, M. R. Bell, T. Enßlin, A. Bonafede, R. Braun, J. Brown, T. E. Clarke, I. J. Feain, et al. An improved map of the galactic faraday sky. *Astronomy & Astrophysics*, 542:A93, 2012.

D. E. Osterbrock and G. J. Ferland. *Astrophysics of gaseous nebulae and active galactic nuclei*. University Science Books, 2006.

S. P. O'Sullivan, S. Brown, T. Robishaw, D. H. F. M. Schnitzeler, N. M. McClure-Griffiths, I. J. Feain, A. R. Taylor, B. M. Gaensler, T. L. Land ecker, L. Harvey-Smith, and E. Carretti. Complex Faraday depth structure of active galactic nuclei as revealed by broad-band radio polarimetry. MNRAS, 421(4):3300–3315, Apr. 2012. doi: 10.1111/j.1365-2966.2012.20554.x.

D. Palaniswamy, R. B. Wayth, C. M. Trott, J. N. McCallum, S. J. Tingay, and C. Reynolds. A Search for Fast Radio Bursts Associated with Gamma-Ray Bursts. ApJ, 790(1):63, July 2014. doi: 10.1088/0004-637X/790/1/63.

D. Palaniswamy, Y. Li, and B. Zhang. Are There Multiple Populations of Fast Radio Bursts? ApJ, 854(1):L12, Feb. 2018. doi: 10.3847/2041-8213/aaaa63.

D. M. Palmer, S. Barthelmy, N. Gehrels, R. Kippen, T. Cayton, C. Kouveliotou, D. Eichler, R. Wijers, P. Woods, J. Granot, et al. A giant γ-ray flare from the magnetar sgr 1806–20. *Nature*, 434(7037):1107–1109, 2005.

K. Parfrey, A. M. Beloborodov, and L. Hui. Dynamics of Strongly Twisted Relativistic Magnetospheres. ApJ, 774(2):92, Sept. 2013. doi: 10.1088/0004-637X/774/2/92.

I. Pastor-Marazuela, J. van Leeuwen, A. Bilous, L. Connor, Y. Maan, L. Oostrum, E. Petroff, S. Straal, D. Vohl, E. A. K. Adams, B. Adebahr, J. Attema, O. M. Boersma, R. van den Brink, W. A. van Cappellen, A. H. W. M. Coolen, S. Damstra, H. Dénes, K. M. Hess, J. M. van der Hulst, B. Hut, A. Kutkin, G. Marcel Loose, D. M. Lucero, Á. Mika, V. A. Moss, H. Mulder, M. J. Norden, T. A. Oosterloo, K. Rajwade, D. van der Schuur, A. Sclocco, R. Smits, and J. Ziemke. A fast radio burst with sub-millisecond quasi-periodic structure. *arXiv e-prints*, art. arXiv:2202.08002, Feb. 2022.

C. Patel, D. Agarwal, M. Bhardwaj, M. M. Boyce, A. Brazier, S. Chatterjee, P. Chawla, V. M. Kaspi, D. R. Lorimer, M. A. McLaughlin, E. Parent, Z. Pleunis, S. M. Ransom, P. Scholz, R. S. Wharton, W. W. Zhu, M. Alam, K. Caballero Valdez, F. Camilo, J. M. Cordes, F. Crawford, J. S. Deneva, R. D. Ferdman, P. C. C. Freire, J. W. T. Hessels,

B. Nguyen, I. Stairs, K. Stovall, and J. van Leeuwen. PALFA Single-pulse Pipeline: New Pulsars, Rotating Radio Transients, and a Candidate Fast Radio Burst. ApJ, 869 (2):181, Dec. 2018. doi: 10.3847/1538-4357/aaee65.

M. T. Patterson, R. A. M. Walterbos, R. C. Kennicutt, C. Chiappini, and D. A. Thilker. An oxygen abundance gradient into the outer disc of M81. MNRAS, 422(1):401–419, May 2012. doi: 10.1111/j.1365-2966.2012.20616.x.

D. R. Patton and J. E. Atfield. The Luminosity Dependence of the Galaxy Merger Rate. ApJ, 685(1):235–246, Sept. 2008. doi: 10.1086/590542.

A. Paulino-Afonso, D. Sobral, F. Buitrago, and J. Afonso. The structural and size evolution of star-forming galaxies over the last 11 Gyr. MNRAS, 465(3):2717–2733, Mar. 2017. doi: 10.1093/mnras/stw2933.

F. Pedregosa, G. Varoquaux, A. Gramfort, V. Michel, B. Thirion, O. Grisel, M. Blondel, P. Prettenhofer, R. Weiss, V. Dubourg, J. Vanderplas, A. Passos, D. Cournapeau, M. Brucher, M. Perrot, and E. Duchesnay. Scikit-learn: Machine learning in python. *J. Mach. Learn. Res.*, 12(null):2825â€“2830, nov 2011. ISSN 1532-4435.

U.-L. Pen. Heating of the intergalactic medium. *The Astrophysical Journal*, 510(1):L1–L5, jan 1999. doi: 10.1086/311799. URL `https://doi.org/10.1086%2F311799`.

D. A. Perley, N. R. Tanvir, J. Hjorth, T. Laskar, E. Berger, R. Chary, A. de Ugarte Postigo, J. P. U. Fynbo, T. Krühler, A. J. Levan, M. J. Michałowski, and S. Schulze. The Swift GRB Host Galaxy Legacy Survey. II. Rest-frame Near-IR Luminosity Distribution and Evidence for a Near-solar Metallicity Threshold. ApJ, 817(1):8, Jan. 2016. doi: 10.3847/0004-637X/817/1/8.

T. V. Perneger. What's wrong with bonferroni adjustments. *Bmj*, 316(7139):1236–1238, 1998.

E. Petroff, S. Johnston, E. F. Keane, W. van Straten, M. Bailes, E. D. Barr, B. R. Barsdell, S. Burke-Spolaor, M. Caleb, D. J. Champion, C. Flynn, A. Jameson, M. Kramer, C. Ng, A. Possenti, and B. W. Stappers. A survey of FRB fields: limits on repeatability. MNRAS, 454(1):457–462, Nov. 2015. doi: 10.1093/mnras/stv1953.

E. Petroff, L. Houben, K. Bannister, S. Burke-Spolaor, J. Cordes, H. Falcke, R. van Haren, A. Karastergiou, M. Kramer, C. Law, J. van Leeuwen, D. Lorimer, O. Martinez-Rubi, J. Rachen, L. Spitler, and A. Weltman. VOEvent Standard for Fast Radio Bursts. *arXiv e-prints*, art. arXiv:1710.08155, Oct. 2017.

E. Petroff, J. W. T. Hessels, and D. R. Lorimer. Fast radio bursts. A&A Rev., 27(1):4, May 2019. doi: 10.1007/s00159-019-0116-6.

E. Petroff, J. W. T. Hessels, and D. R. Lorimer. Fast radio bursts at the dawn of the 2020s. *arXiv e-prints*, art. arXiv:2107.10113, July 2021.

L. S. Pilyugin and E. K. Grebel. New calibrations for abundance determinations in H II regions. MNRAS, 457(4):3678–3692, Apr. 2016. doi: 10.1093/mnras/stw238.

A. L. Piro and B. M. Gaensler. The Dispersion and Rotation Measure of Supernova Remnants and Magnetized Stellar Winds: Application to Fast Radio Bursts. 861(2):150. doi: 10.3847/1538-4357/aac9bc.

A. L. Piro and S. R. Kulkarni. Radio Transients from the Accretion-induced Collapse of White Dwarfs. 762(2):L17. doi: 10.1088/2041-8205/762/2/L17.

Planck Collaboration, P. A. R. Ade, N. Aghanim, M. I. R. Alves, C. Armitage-Caplan, M. Arnaud, M. Ashdown, F. Atrio-Barandela, J. Aumont, C. Baccigalupi, A. J. Banday, R. B. Barreiro, J. G. Bartlett, E. Battaner, K. Benabed, A. Benoît, A. Benoit-Lévy, J. P. Bernard, M. Bersanelli, P. Bielewicz, J. Bobin, J. J. Bock, A. Bonaldi, J. R. Bond, J. Borrill, F. R. Bouchet, F. Boulanger, M. Bridges, M. Bucher, C. Burigana, R. C. Butler, J. F. Cardoso, A. Catalano, A. Chamballu, R. R. Chary, X. Chen, H. C. Chiang, L. Y. Chiang, P. R. Christensen, S. Church, D. L. Clements, S. Colombi, L. P. L. Colombo, C. Combet, F. Couchot, A. Coulais, B. P. Crill, A. Curto, F. Cuttaia, L. Danese, R. D. Davies, P. de Bernardis, A. de Rosa, G. de Zotti, J. Delabrouille, J. M. Delouis, J. T. Dempsey, F. X. Désert, C. Dickinson, J. M. Diego, H. Dole, S. Donzelli, O. Doré, M. Douspis, X. Dupac, G. Efstathiou, T. A. Enßlin, H. K. Eriksen, E. Falgarone, F. Finelli, O. Forni, M. Frailis, E. Franceschi, Y. Fukui, S. Galeotta, K. Ganga, M. Giard, Y. Giraud-Héraud, J. González-Nuevo, K. M. Górski, S. Gratton, A. Gregorio, A. Gruppuso, T. Handa, F. K. Hansen, D. Hanson, D. Harrison, S. Henrot-Versillé, C. Hernández-Monteagudo,

D. Herranz, S. R. Hildebrandt, P. Hily-Blant, E. Hivon, M. Hobson, W. A. Holmes, A. Hornstrup, W. Hovest, K. M. Huffenberger, G. Hurier, A. H. Jaffe, T. R. Jaffe, J. Jewell, W. C. Jones, M. Juvela, E. Keihänen, R. Keskitalo, T. S. Kisner, J. Knoche, L. Knox, M. Kunz, H. Kurki-Suonio, G. Lagache, A. Lähteenmäki, J. M. Lamarre, A. Lasenby, R. J. Laureijs, C. R. Lawrence, R. Leonardi, J. León-Tavares, J. Lesgourgues, M. Liguori, P. B. Lilje, M. Linden-Vørnle, M. López-Caniego, P. M. Lubin, J. F. Macías-Pérez, B. Maffei, N. Mandolesi, M. Maris, D. J. Marshall, P. G. Martin, E. Martínez-González, S. Masi, M. Massardi, S. Matarrese, F. Matthai, P. Mazzotta, P. McGehee, A. Melchiorri, L. Mendes, A. Mennella, M. Migliaccio, S. Mitra, M. A. Miville-Deschênes, A. Moneti, L. Montier, T. J. T. Moore, G. Morgante, J. Morino, D. Mortlock, D. Munshi, J. A. Murphy, T. Nakajima, P. Naselsky, F. Nati, P. Natoli, C. B. Netterfield, H. U. Nørgaard-Nielsen, F. Noviello, D. Novikov, I. Novikov, T. Okuda, S. Osborne, C. A. Oxborrow, F. Paci, L. Pagano, F. Pajot, R. Paladini, D. Paoletti, F. Pasian, G. Patanchon, O. Perdereau, L. Perotto, F. Perrotta, F. Piacentini, M. Piat, E. Pierpaoli, D. Pietrobon, S. Plaszczynski, E. Pointecouteau, G. Polenta, N. Ponthieu, L. Popa, T. Poutanen, G. W. Pratt, G. Prézeau, S. Prunet, J. L. Puget, J. P. Rachen, W. T. Reach, R. Rebolo, M. Reinecke, M. Remazeilles, C. Renault, S. Ricciardi, T. Riller, I. Ristorcelli, G. Rocha, C. Rosset, G. Roudier, M. Rowan-Robinson, J. A. Rubiño-Martín, B. Rusholme, M. Sandri, D. Santos, G. Savini, D. Scott, M. D. Seiffert, E. P. S. Shellard, L. D. Spencer, J. L. Starck, V. Stolyarov, R. Stompor, R. Sudiwala, R. Sunyaev, F. Sureau, D. Sutton, A. S. Suur-Uski, J. F. Sygnet, J. A. Tauber, D. Tavagnacco, L. Terenzi, H. S. Thomas, L. Toffolatti, M. Tomasi, K. Torii, M. Tristram, M. Tucci, J. Tuovinen, G. Umana, L. Valenziano, J. Valiviita, B. Van Tent, P. Vielva, F. Villa, N. Vittorio, L. A. Wade, B. D. Wandelt, I. K. Wehus, H. Yamamoto, T. Yoda, D. Yvon, A. Zacchei, and A. Zonca. Planck 2013 results. XIII. Galactic CO emission. A&A, 571:A13, Nov. 2014. doi: 10.1051/0004-6361/201321553.

Planck Collaboration, P. A. R. Ade, N. Aghanim, M. Arnaud, M. Ashdown, J. Aumont, C. Baccigalupi, A. J. Banday, R. B. Barreiro, J. G. Bartlett, N. Bartolo, E. Battaner, R. Battye, K. Benabed, A. Benoît, A. Benoit-Lévy, J. P. Bernard, M. Bersanelli, P. Bielewicz, J. J. Bock, A. Bonaldi, L. Bonavera, J. R. Bond, J. Borrill, F. R. Bouchet, F. Boulanger, M. Bucher, C. Burigana, R. C. Butler, E. Calabrese, J. F. Cardoso, A. Catalano, A. Challinor, A. Chamballu, R. R. Chary, H. C. Chiang, J. Chluba, P. R. Christensen, S. Church, D. L. Clements, S. Colombi, L. P. L. Colombo, C. Combet, A. Coulais, B. P. Crill, A. Curto, F. Cuttaia, L. Danese, R. D. Davies, R. J. Davis, P. de Bernardis, A. de Rosa, G. de Zotti, J. Delabrouille, F. X. Désert, E. Di Valentino, C. Dickinson, J. M. Diego, K. Dolag, H. Dole, S. Donzelli, O. Doré, M. Douspis, A. Ducout, J. Dunkley, X. Dupac, G. Efstathiou, F. Elsner, T. A. Enßlin, H. K. Eriksen, M. Farhang, J. Fergusson, F. Finelli, O. Forni, M. Frailis, A. A. Fraisse, E. Franceschi, A. Frejsel, S. Galeotta, S. Galli, K. Ganga, C. Gauthier, M. Gerbino, T. Ghosh, M. Giard, Y. Giraud-Héraud, E. Giusarma, E. Gjerløw, J. González-Nuevo, K. M. Górski, S. Gratton, A. Gregorio, A. Gruppuso, J. E. Gudmundsson, J. Hamann, F. K. Hansen, D. Hanson, D. L. Harrison, G. Helou, S. Henrot-Versillé, C. Hernández-Monteagudo, D. Herranz, S. R. Hildebrand t, E. Hivon, M. Hobson, W. A. Holmes, A. Hornstrup, W. Hovest, Z. Huang, K. M. Huffenberger, G. Hurier, A. H. Jaffe, T. R. Jaffe, W. C. Jones, M. Juvela, E. Keihänen, R. Keskitalo, T. S. Kisner, R. Kneissl, J. Knoche, L. Knox, M. Kunz, H. Kurki-Suonio, G. Lagache, A. Lähteenmäki, J. M. Lamarre, A. Lasenby, M. Lattanzi, C. R. Lawrence, J. P. Leahy, R. Leonardi, J. Lesgourgues, F. Levrier, A. Lewis, M. Liguori, P. B. Lilje, M. Linden-Vørnle, M. López-Caniego, P. M. Lubin, J. F. Macías-Pérez, G. Maggio, D. Maino, N. Mandolesi, A. Mangilli, A. Marchini, M. Maris, P. G. Martin, M. Martinelli, E. Martínez-González, S. Masi, S. Matarrese, P. McGehee, P. R. Meinhold, A. Melchiorri, J. B. Melin, L. Mendes, A. Mennella, M. Migliaccio, M. Millea, S. Mitra, M. A. Miville-Deschênes, A. Moneti, L. Montier, G. Morgante, D. Mortlock, A. Moss, D. Munshi, J. A. Murphy, P. Naselsky, F. Nati, P. Natoli, C. B. Netterfield, H. U. Nørgaard-Nielsen, F. Noviello, D. Novikov, I. Novikov, C. A. Oxborrow, F. Paci, L. Pagano, F. Pajot, R. Paladini, D. Paoletti, B. Partridge, F. Pasian, G. Patanchon, T. J. Pearson, O. Perdereau, L. Perotto, F. Perrotta, V. Pettorino, F. Piacentini, M. Piat, E. Pierpaoli, D. Pietrobon, S. Plaszczynski, E. Pointecouteau, G. Polenta, L. Popa, G. W. Pratt, G. Prézeau, S. Prunet, J. L. Puget, J. P. Rachen, W. T. Reach, R. Rebolo, M. Reinecke, M. Remazeilles, C. Renault, A. Renzi, I. Ristorcelli, G. Rocha, C. Rosset, M. Rossetti, G. Roudier, B. Rouillé d'Orfeuil, M. Rowan-Robinson, J. A. Rubiño-Martín, B. Rusholme, N. Said, V. Salvatelli, L. Salvati, M. Sandri, D. Santos, M. Savelainen, G. Savini, D. Scott, M. D. Seiffert, P. Serra, E. P. S. Shellard, L. D. Spencer, M. Spinelli, V. Stolyarov, R. Stompor, R. Sudiwala, R. Sunyaev, D. Sutton, A. S. Suur-Uski, J. F.

Sygnet, J. A. Tauber, L. Terenzi, L. Toffolatti, M. Tomasi, M. Tristram, T. Trombetti, M. Tucci, J. Tuovinen, M. Türler, G. Umana, L. Valenziano, J. Valiviita, F. Van Tent, P. Vielva, F. Villa, L. A. Wade, B. D. Wandelt, I. K. Wehus, M. White, S. D. M. White, A. Wilkinson, D. Yvon, A. Zacchei, and A. Zonca. Planck 2015 results. XIII. Cosmological parameters. A&A, 594:A13, Sept. 2016. doi: 10.1051/0004-6361/201525830.

E. Platts, A. Weltman, A. Walters, S. P. Tendulkar, J. E. B. Gordin, and S. Kandhai. A Living Theory Catalogue for Fast Radio Bursts. *arXiv e-prints*, Oct. 2018.

Z. Pleunis. *Fast radio burst detection and morphology with the CHIME telescope*. PhD thesis, McGill University, 2021.

Z. Pleunis, D. C. Good, V. M. Kaspi, R. Mckinven, S. M. Ransom, P. Scholz, K. Bandura, M. Bhardwaj, P. J. Boyle, C. Brar, T. Cassanelli, P. Chawla, F. (Adam) Dong, E. Fonseca, B. M. Gaensler, A. Josephy, J. F. Kaczmarek, C. Leung, H.-H. Lin, K. W. Masui, J. Mena-Parra, D. Michilli, C. Ng, C. Patel, M. Rafiei-Ravandi, M. Rahman, P. Sanghavi, K. Shin, K. M. Smith, I. H. Stairs, and S. P. Tendulkar. Fast Radio Burst Morphology in the First CHIME/FRB Catalog. ApJ, 923(1):1, Dec. 2021. doi: 10.3847/1538-4357/ac33ac.

A. H. Prestwich, J. A. Irwin, R. E. Kilgard, M. I. Krauss, A. Zezas, F. Primini, P. Kaaret, and B. Boroson. Classifying X-Ray Sources in External Galaxies from X-Ray Colors. ApJ, 595(2):719–726, Oct. 2003. doi: 10.1086/377366.

D. C. Price, C. Flynn, and A. Deller. A comparison of Galactic electron density models using PyGEDM. PASA, 38:e038, Aug. 2021. doi: 10.1017/pasa.2021.33.

J. X. Prochaska and Y. Zheng. Probing Galactic haloes with fast radio bursts. MNRAS, 485(1):648–665, May 2019. doi: 10.1093/mnras/stz261.

J. X. Prochaska, J.-P. Macquart, M. McQuinn, S. Simha, R. M. Shannon, C. K. Day, L. Marnoch, S. Ryder, A. Deller, K. W. Bannister, et al. The low density and magnetization of a massive galaxy halo exposed by a fast radio burst. *Science*, 366(6462): 231–234, 2019.

S. Raby. Axion star collisions with neutron stars and fast radio bursts. Phys. Rev. D, 94 (10):103004, Nov. 2016. doi: 10.1103/PhysRevD.94.103004.

M. Rafiei-Ravandi and K. M. Smith. Mitigating radio frequency interference in CHIME/FRB real-time intensity data. *arXiv e-prints*, art. arXiv:2206.07292, June 2022.

M. Rafiei-Ravandi, K. M. Smith, D. Li, K. W. Masui, A. Josephy, M. Dobbs, D. Lang, M. Bhardwaj, C. Patel, K. Bandura, S. Berger, P. J. Boyle, C. Brar, D. Breitman, T. Cassanelli, P. Chawla, F. Adam Dong, E. Fonseca, B. M. Gaensler, U. Giri, D. C. Good, M. Halpern, J. Kaczmarek, V. M. Kaspi, C. Leung, H.-H. Lin, J. Mena-Parra, B. W. Meyers, D. Michilli, M. Münchmeyer, C. Ng, E. Petroff, Z. Pleunis, M. Rahman, P. Sanghavi, P. Scholz, K. Shin, I. H. Stairs, S. P. Tendulkar, K. Vanderlinde, and A. Zwaniga. CHIME/FRB Catalog 1 Results: Statistical Cross-correlations with Large-scale Structure. ApJ, 922(1):42, Nov. 2021. doi: 10.3847/1538-4357/ac1dab.

K. M. Rajwade, M. B. Mickaliger, B. W. Stappers, V. Morello, D. Agarwal, C. G. Bassa, R. P. Breton, M. Caleb, A. Karastergiou, E. F. Keane, and D. R. Lorimer. Possible periodic activity in the repeating FRB 121102. MNRAS, 495(4):3551–3558, July 2020. doi: 10.1093/mnras/staa1237.

V. Ravi. The prevalence of repeating fast radio bursts. *Nature Astronomy*, 3:928–931, July 2019. doi: 10.1038/s41550-019-0831-y.

V. Ravi, C. J. Law, D. Li, K. Aggarwal, S. Burke-Spolaor, L. Connor, T. J. W. Lazio, D. Simard, J. Somalwar, and S. P. Tendulkar. The host galaxy and persistent radio counterpart of FRB 20201124A. *arXiv e-prints*, art. arXiv:2106.09710, June 2021.

A. E. Reines, J. J. Condon, J. Darling, and J. E. Greene. A New Sample of (Wandering) Massive Black Holes in Dwarf Galaxies from High-resolution Radio Observations. ApJ, 888(1):36, Jan. 2020. doi: 10.3847/1538-4357/ab4999.

R. Rengelink, Y. Tang, A. De Bruyn, G. Miley, M. Bremer, H. Roettgering, and M. Bremer. The westerbork northern sky survey (wenss)-i. a 570 square degree mini-survey around the north ecliptic pole. *Astronomy and Astrophysics Supplement Series*, 124(2):259–280, 1997.

L. Resmi, J. Vink, and C. H. Ishwara-Chandra. Implications of the lowest frequency detection of the persistent counterpart of FRB121102. *arXiv e-prints*, art. arXiv:2010.14334, Oct. 2020.

R. Reynolds. Warm ionized gas in the local interstellar medium. *Advances in Space Research*, 34(1):27–34, 2004.

R. J. Reynolds, S. L. Tufte, D. T. Kung, P. R. McCullough, and C. Heiles. A Comparison of Diffuse Ionized and Neutral Hydrogen Away from the Galactic Plane: H alpha -emitting H i Clouds. ApJ, 448:715, Aug. 1995. doi: 10.1086/175999.

S. P. Reynolds, G. G. Pavlov, O. Kargaltsev, N. Klingler, M. Renaud, and S. Mereghetti. Pulsar-Wind Nebulae and Magnetar Outflows: Observations at Radio, X-Ray, and Gamma-Ray Wavelengths. Space Sci. Rev., 207(1-4):175–234, July 2017. doi: 10.1007/s11214-017-0356-6.

A. Ridnaia, D. Svinkin, D. Frederiks, A. Bykov, S. Popov, R. Aptekar, S. Golenetskii, A. Lysenko, A. Tsvetkova, M. Ulanov, et al. A peculiar hard x-ray counterpart of a galactic fast radio burst. *arXiv preprint arXiv:2005.11178*, 2020.

R. W. Romani and S. Johnston. Giant Pulses from the Millisecond Pulsar B1821-24. ApJ, 557(2):L93–L96, Aug. 2001. doi: 10.1086/323415.

J. N. Rouder. Optional stopping: No problem for bayesians. *Psychonomic bulletin & review*, 21(2):301–308, 2014.

A. J. Ruiter, L. Ferrario, K. Belczynski, I. R. Seitenzahl, R. M. Crocker, and A. I. Karakas. On the formation of neutron stars via accretion-induced collapse in binaries. 484(1): 698–711. doi: 10.1093/mnras/stz001.

R. E. Rutledge, R. J. Brunner, T. A. Prince, and C. Lonsdale. XID: Cross-Association of ROSAT/Bright Source Catalog X-Ray Sources with USNO A-2 Optical Point Sources. ApJS, 131(1):335–353, Nov. 2000. doi: 10.1086/317363.

G. B. Rybicki and A. P. Lightman. *Radiative Processes in Astrophysics*. Wiley-Vch, 1986.

S. D. Ryder, K. W. Bannister, S. Bhandari, A. T. Deller, R. D. Ekers, M. Glowacki, A. C. Gordon, K. Gourdji, C. W. James, C. D. Kilpatrick, W. Lu, L. Marnoch, V. A. Moss, J. X. Prochaska, H. Qiu, E. M. Sadler, S. Simha, M. W. Sammons, D. R. Scott, N. Tejos, and R. M. Shannon. Probing the distant universe with a very luminous fast radio burst at redshift 1. *arXiv e-prints*, art. arXiv:2210.04680, Oct. 2022.

T. Sakamoto, E. Troja, A. Lien, B. Zhang, S. B. Cenko, V. Cunningham, and E. Berger. FRB131104 Swift/BAT Data Revisited: No Evidence of a Gamma-Ray Counterpart. ApJ, 908(2):137, Feb. 2021. doi: 10.3847/1538-4357/abcda0.

H. Salo, E. Laurikainen, J. Laine, S. Comerón, D. A. Gadotti, R. Buta, K. Sheth, D. Zaritsky, L. Ho, J. Knapen, E. Athanassoula, A. Bosma, S. Laine, M. Cisternas, T. Kim, J. C. Muñoz-Mateos, M. Regan, J. L. Hinz, A. Gil de Paz, K. Menendez-Delmestre, T. Mizusawa, S. Erroz-Ferrer, S. E. Meidt, and M. Querejeta. The Spitzer Survey of Stellar Structure in Galaxies (S^4G): Multi-component Decomposition Strategies and Data Release. ApJS, 219(1):4, July 2015. doi: 10.1088/0067-0049/219/1/4.

S. Savaglio, K. Glazebrook, and D. Le Borgne. The Galaxy Population Hosting Gamma-Ray Bursts. ApJ, 691(1):182–211, Jan. 2009. doi: 10.1088/0004-637X/691/1/182.

K. Schawinski, D. Thomas, M. Sarzi, C. Maraston, S. Kaviraj, S.-J. Joo, S. K. Yi, and J. Silk. Observational evidence for AGN feedback in early-type galaxies. MNRAS, 382 (4):1415–1431, Dec. 2007. doi: 10.1111/j.1365-2966.2007.12487.x.

E. F. Schlafly and D. P. Finkbeiner. Measuring Reddening with Sloan Digital Sky Survey Stellar Spectra and Recalibrating SFD. ApJ, 737(2):103, Aug. 2011. doi: 10.1088/0004-637X/737/2/103.

D. J. Schlegel, D. P. Finkbeiner, and M. Davis. Maps of Dust Infrared Emission for Use in Estimation of Reddening and Cosmic Microwave Background Radiation Foregrounds. ApJ, 500(2):525–553, June 1998. doi: 10.1086/305772.

S. E. Schneider, T. X. Thuan, J. G. Mangum, and J. Miller. Northern Dwarf and Low Surface Brightness Galaxies. II. The Green Bank Neutral Hydrogen Survey. ApJS, 81: 5, July 1992. doi: 10.1086/191684.

P. Scholz, L. G. Spitler, J. W. T. Hessels, S. Chatterjee, J. M. Cordes, V. M. Kaspi, R. S. Wharton, C. G. Bassa, S. Bogdanov, F. Camilo, F. Crawford, J. Deneva, J. van Leeuwen, R. Lynch, E. C. Madsen, M. A. McLaughlin, M. Mickaliger, E. Parent, C. Patel, S. M. Ransom, A. Seymour, I. H. Stairs, B. W. Stappers, and S. P. Tendulkar. The Repeating Fast Radio Burst FRB 121102: Multi-wavelength Observations and Additional Bursts. ApJ, 833(2):177, Dec. 2016. doi: 10.3847/1538-4357/833/2/177.

P. Scholz, S. Bogdanov, J. W. T. Hessels, R. S. Lynch, L. G. Spitler, C. G. Bassa, G. C. Bower, S. Burke-Spolaor, B. J. Butler, S. Chatterjee, J. M. Cordes, K. Gourdji, V. M. Kaspi, C. J. Law, B. Marcote, M. A. McLaughlin, D. Michilli, Z. Paragi, S. M. Ransom, A. Seymour, S. P. Tendulkar, and R. S. Wharton. Simultaneous X-Ray, Gamma-Ray, and Radio Observations of the Repeating Fast Radio Burst FRB 121102. ApJ, 846(1): 80, Sept. 2017. doi: 10.3847/1538-4357/aa8456.

P. Scholz, A. Cook, M. Cruces, J. Hessels, V. Kaspi, W. Majid, A. Naidu, A. Pearlman, L. Spitler, K. Bandura, et al. Simultaneous x-ray and radio observations of the repeating fast radio burst frb 180916. j0158+ 65. *arXiv preprint arXiv:2004.06082*, 2020.

P. Scholz, A. Cook, M. Cruces, J. W. T. Hessels, V. M. Kaspi, W. A. Majid, A. Naidu, A. B. Pearlman, L. G. Spitler, K. M. Bandura, M. Bhardwaj, T. Cassanelli, P. Chawla, B. M. Gaensler, D. C. Good, A. Josephy, R. Karuppusamy, A. Keimpema, A. Y. Kirichenko, F. Kirsten, J. Kocz, C. Leung, B. Marcote, K. Masui, J. Mena-Parra, M. Merryfield, D. Michilli, C. J. Naudet, K. Nimmo, Z. Pleunis, T. A. Prince, M. Rafiei-Ravandi, M. Rahman, K. Shin, K. M. Smith, I. H. Stairs, S. P. Tendulkar, and K. Vanderlinde. Simultaneous X-Ray and Radio Observations of the Repeating Fast Radio Burst FRB $\sim$ 180916.J0158+65. ApJ, 901(2):165, Oct. 2020. doi: 10.3847/1538-4357/abb1a8.

E. Schulz. Scaling Relations of Mass, Velocity, and Radius for Disk Galaxies. ApJ, 836 (2):151, Feb. 2017. doi: 10.3847/1538-4357/aa5b88.

J. G. Scott and J. O. Berger. An exploration of aspects of bayesian multiple testing. *Journal of statistical planning and inference*, 136(7):2144–2162, 2006.

P. H. Sell, D. Pooley, A. Zezas, S. Heinz, J. Homan, and W. H. G. Lewin. Luminosity

Functions and Point-source Properties from Multiple Chandra Observations of M81. ApJ, 735(1):26, July 2011. doi: 10.1088/0004-637X/735/1/26.

A. M. Serenelli, S. Basu, J. W. Ferguson, and M. Asplund. New Solar Composition: The Problem with Solar Models Revisited. ApJ, 705(2):L123–L127, Nov. 2009. doi: 10.1088/0004-637X/705/2/L123.

A. Seymour, D. Michilli, and Z. Pleunis. DM_phase: Algorithm for correcting dispersion of radio signals, Oct. 2019.

C. E. Shannon. Communication in the Presence of Noise. *IEEE Proceedings*, 37:10–21, Jan. 1949. doi: 10.1109/JPROC.1998.659497.

R. M. Shannon, J. P. Macquart, K. W. Bannister, R. D. Ekers, C. W. James, S. Osłowski, H. Qiu, M. Sammons, A. W. Hotan, M. A. Voronkov, R. J. Beresford, M. Brothers, A. J. Brown, J. D. Bunton, A. P. Chippendale, C. Haskins, M. Leach, M. Marquarding, D. McConnell, M. A. Pilawa, E. M. Sadler, E. R. Troup, J. Tuthill, M. T. Whiting, J. R. Allison, C. S. Anderson, M. E. Bell, J. D. Collier, G. Gürkan, G. Heald, and C. J. Riseley. The dispersion-brightness relation for fast radio bursts from a wide-field survey. Nature, 562(7727):386–390, Oct. 2018. doi: 10.1038/s41586-018-0588-y.

J. R. Shaw, K. Sigurdson, M. Sitwell, A. Stebbins, and U.-L. Pen. Coaxing cosmic 21 cm fluctuations from the polarized sky using m-mode analysis. *Physical Review D*, 91(8): 083514, 2015.

K. Sheth, M. Regan, J. L. Hinz, A. Gil de Paz, K. Menéndez-Delmestre, J.-C. Muñoz-Mateos, M. Seibert, T. Kim, E. Laurikainen, H. Salo, D. A. Gadotti, J. Laine, T. Mizusawa, L. Armus, E. Athanassoula, A. Bosma, R. J. Buta, P. Capak, T. H. Jarrett, D. M. Elmegreen, B. G. Elmegreen, J. H. Knapen, J. Koda, G. Helou, L. C. Ho, B. F. Madore, K. L. Masters, B. Mobasher, P. Ogle, C. Y. Peng, E. Schinnerer, J. A. Surace, D. Zaritsky, S. Comerón, B. de Swardt, S. E. Meidt, M. Kasliwal, and M. Aravena. The Spitzer Survey of Stellar Structure in Galaxies (S4G). PASP, 122(898):1397, Dec. 2010. doi: 10.1086/657638.

T. W. Shimwell, M. J. Hardcastle, C. Tasse, P. N. Best, H. J. A. Röttgering, W. L. Williams, A. Botteon, A. Drabent, A. Mechev, A. Shulevski, R. J. van Weeren, L. Bester,

M. Brüggen, G. Brunetti, J. R. Callingham, K. T. Chyży, J. E. Conway, T. J. Dijkema, K. Duncan, F. de Gasperin, C. L. Hale, M. Haverkorn, B. Hugo, N. Jackson, M. Mevius, G. K. Miley, L. K. Morabito, R. Morganti, A. Offringa, J. B. R. Oonk, D. Rafferty, J. Sabater, D. J. B. Smith, D. J. Schwarz, O. Smirnov, S. P. O'Sullivan, H. Vedantham, G. J. White, J. G. Albert, L. Alegre, B. Asabere, D. J. Bacon, A. Bonafede, E. Bonnassieux, M. Brienza, M. Bilicki, M. Bonato, G. Calistro Rivera, R. Cassano, R. Cochrane, J. H. Croston, V. Cuciti, D. Dallacasa, A. Danezi, R. J. Dettmar, G. Di Gennaro, H. W. Edler, T. A. Enßlin, K. L. Emig, T. M. O. Franzen, C. García-Vergara, Y. G. Grange, G. Gürkan, M. Hajduk, G. Heald, V. Heesen, D. N. Hoang, M. Hoeft, C. Horellou, M. Iacobelli, M. Jamrozy, V. Jelić, R. Kondapally, P. Kukreti, M. Kunert-Bajraszewska, M. Magliocchetti, V. Mahatma, K. Małek, S. Mandal, F. Massaro, Z. Meyer-Zhao, B. Mingo, R. I. J. Mostert, D. G. Nair, S. J. Nakoneczny, B. Nikiel-Wroczyński, E. Orrú, U. Pajdosz-Śmierciak, T. Pasini, I. Prandoni, H. E. van Piggelen, K. Rajpurohit, E. Retana-Montenegro, C. J. Riseley, A. Rowlinson, A. Saxena, C. Schrijvers, F. Sweijen, T. M. Siewert, R. Timmerman, M. Vaccari, J. Vink, J. L. West, A. Wołowska, X. Zhang, and J. Zheng. The LOFAR Two-metre Sky Survey. V. Second data release. A&A, 659:A1, Mar. 2022. doi: 10.1051/0004-6361/202142484.

K. Shin, K. W. Masui, M. Bhardwaj, T. Cassanelli, P. Chawla, M. Dobbs, F. A. Dong, E. Fonseca, B. M. Gaensler, A. Herrera-Martín, J. Kaczmarek, V. Kaspi, C. Leung, M. Merryfield, M. Münchmeyer, A. B. Pearlman, M. Rafiei-Ravandi, K. Smith, and S. P. Tendulkar. Inferring the Energy and Distance Distributions of Fast Radio Bursts using the First CHIME/FRB Catalog. *arXiv e-prints*, art. arXiv:2207.14316, July 2022.

V. Simha, D. H. Weinberg, C. Conroy, R. Dave, M. Fardal, N. Katz, and B. D. Oppenheimer. Parametrising Star Formation Histories. *arXiv e-prints*, art. arXiv:1404.0402, Apr. 2014.

J. D. Simon. The Faintest Dwarf Galaxies. ARA&A, 57:375–415, Aug. 2019. doi: 10.1146/annurev-astro-091918-104453.

M. F. Skrutskie, R. M. Cutri, R. Stiening, M. D. Weinberg, S. Schneider, J. M. Carpenter, C. Beichman, R. Capps, T. Chester, J. Elias, J. Huchra, J. Liebert, C. Lonsdale, D. G. Monet, S. Price, P. Seitzer, T. Jarrett, J. D. Kirkpatrick, J. E. Gizis, E. Howard, T. Evans,

J. Fowler, L. Fullmer, R. Hurt, R. Light, E. L. Kopan, K. A. Marsh, H. L. McCallon, R. Tam, S. Van Dyk, and S. Wheelock. The Two Micron All Sky Survey (2MASS). AJ, 131(2):1163–1183, Feb. 2006. doi: 10.1086/498708.

P. Slane. *Pulsar Wind Nebulae*, page 2159. 2017. doi: 10.1007/978-3-319-21846-5_95.

A. Smercina, E. F. Bell, C. T. Slater, P. A. Price, J. Bailin, and A. Monachesi. D1005+ 68: A new faint dwarf galaxy in the m81 group. *The Astrophysical Journal Letters*, 843(1): L6, 2017.

A. Smercina, E. F. Bell, P. A. Price, C. T. Slater, R. D'Souza, J. Bailin, R. S. de Jong, I. S. Jang, A. Monachesi, and D. Nidever. The Saga of M81: Global View of a Massive Stellar Halo in Formation. *arXiv e-prints*, art. arXiv:1910.14672, Oct. 2019.

C. Sotomayor-Beltran, C. Sobey, J. W. T. Hessels, G. de Bruyn, A. Noutsos, A. Alexov, J. Anderson, A. Asgekar, I. M. Avruch, R. Beck, M. E. Bell, M. R. Bell, M. J. Bentum, G. Bernardi, P. Best, L. Birzan, A. Bonafede, F. Breitling, J. Broderick, W. N. Brouw, M. Brueggen, B. Ciardi, F. de Gasperin, R. J. Dettmar, A. van Duin, S. Duscha, J. Eisloeffel, H. Falcke, R. A. Fallows, R. Fender, C. Ferrari, W. Frieswijk, M. A. Garrett, J. Griessmeier, T. Grit, A. W. Gunst, T. E. Hassall, G. Heald, M. Hoeft, A. Horneffer, M. Iacobelli, E. Juette, A. Karastergiou, E. Keane, J. Kohler, M. Kramer, V. I. Kondratiev, L. V. E. Koopmans, M. Kuniyoshi, G. Kuper, J. van Leeuwen, P. Maat, G. Macario, S. Markoff, J. P. McKean, D. D. Mulcahy, H. Munk, E. Orru, H. Paas, M. Pandey-Pommier, M. Pilia, R. Pizzo, A. G. Polatidis, W. Reich, H. Roettgering, M. Serylak, J. Sluman, B. W. Stappers, M. Tagger, Y. Tang, C. Tasse, S. ter Veen, R. Vermeulen, R. J. van Weeren, R. A. M. J. Wijers, S. J. Wijnholds, M. W. Wise, O. Wucknitz, S. Yatawatta, and P. Zarka. ionFR: Ionospheric Faraday rotation, Mar. 2013.

L. G. Spitler, P. Scholz, J. W. T. Hessels, S. Bogdanov, A. Brazier, F. Camilo, S. Chatterjee, J. M. Cordes, F. Crawford, J. Deneva, R. D. Ferdman, P. C. C. Freire, V. M. Kaspi, P. Lazarus, R. Lynch, E. C. Madsen, M. A. McLaughlin, C. Patel, S. M. Ransom, A. Seymour, I. H. Stairs, B. W. Stappers, J. van Leeuwen, and W. W. Zhu. A repeating fast radio burst. Nature, 531(7593):202–205, Mar. 2016. doi: 10.1038/nature17168.

N. Sridhar, B. D. Metzger, P. Beniamini, B. Margalit, M. Renzo, L. Sironi, and K. Kovlakas. Periodic Fast Radio Bursts from Luminous X-ray Binaries. ApJ, 917(1):13, Aug. 2021. doi: 10.3847/1538-4357/ac0140.

D. L. Streiner and G. R. Norman. Correction for multiple testing: is there a resolution? *Chest*, 140(1):16–18, 2011.

W.-H. Sun, X. Zhou, W.-P. Chen, D. Burstein, R. Windhorst, J. Ma, Y.-I. Byun, Z.-J. Jiang, and J.-S. Chen. Intergalactic stellar distributions in the interacting m81/m82 galaxy group. *The Astrophysical Journal Letters*, 630(2):L133, 2005.

D. Tanoglidis, A. Drlica-Wagner, K. Wei, T. S. Li, J. Sánchez, Y. Zhang, A. H. G. Peter, A. Feldmeier-Krause, J. Prat, K. Casey, A. Palmese, C. Sánchez, J. DeRose, C. Conselice, L. Gagnon, T. M. C. Abbott, M. Aguena, S. Allam, S. Avila, K. Bechtol, E. Bertin, S. Bhargava, D. Brooks, D. L. Burke, A. C. Rosell, M. C. Kind, J. Carretero, C. Chang, M. Costanzi, L. N. da Costa, J. De Vicente, S. Desai, H. T. Diehl, P. Doel, T. F. Eifler, S. Everett, A. E. Evrard, B. Flaugher, J. Frieman, J. García-Bellido, D. W. Gerdes, R. A. Gruendl, J. Gschwend, G. Gutierrez, W. G. Hartley, D. L. Hollowood, D. Huterer, D. J. James, E. Krause, K. Kuehn, N. Kuropatkin, M. A. G. Maia, M. March, J. L. Marshall, F. Menanteau, R. Miquel, R. L. C. Ogando, F. Paz-Chinchón, A. K. Romer, A. Roodman, E. Sanchez, V. Scarpine, S. Serrano, I. Sevilla-Noarbe, M. Smith, E. Suchyta, G. Tarle, D. Thomas, D. L. Tucker, A. R. Walker, and DES Collaboration. Shadows in the Dark: Low-surface-brightness Galaxies Discovered in the Dark Energy Survey. ApJS, 252(2): 18, Feb. 2021. doi: 10.3847/1538-4365/abca89.

T. M. Tauris, D. Sanyal, S. C. Yoon, and N. Langer. Evolution towards and beyond accretion-induced collapse of massive white dwarfs and formation of millisecond pulsars. A&A, 558:A39, Oct. 2013. doi: 10.1051/0004-6361/201321662.

J. H. Taylor. A Sensitive Method for Detecting Dispersed Radio Emission. A&AS, 15: 367, June 1974.

M. Taylor, D. Cinabro, B. Dilday, L. Galbany, R. R. Gupta, R. Kessler, J. Marriner, R. C. Nichol, M. Richmond, D. P. Schneider, and J. Sollerman. The Core Collapse Supernova

Rate from the SDSS-II Supernova Survey. ApJ, 792(2):135, Sept. 2014. doi: 10.1088/0004-637X/792/2/135.

E. Tempel, R. Kipper, A. Tamm, M. Gramann, M. Einasto, T. Sepp, and T. Tuvikene. Friends-of-friends galaxy group finder with membership refinement. Application to the local Universe. A&A, 588:A14, Apr. 2016. doi: 10.1051/0004-6361/201527755.

S. P. Tendulkar, V. M. Kaspi, and C. Patel. Radio Nondetection of the SGR 1806-20 Giant Flare and Implications for Fast Radio Bursts. ApJ, 827(1):59, Aug. 2016. doi: 10.3847/0004-637X/827/1/59.

S. P. Tendulkar, C. Bassa, J. M. Cordes, G. C. Bower, C. J. Law, S. Chatterjee, E. A. Adams, S. Bogdanov, S. Burke-Spolaor, B. J. Butler, et al. The host galaxy and redshift of the repeating fast radio burst frb 121102. *The Astrophysical Journal Letters*, 834(2):L7, 2017.

S. P. Tendulkar, A. Gil de Paz, A. Y. Kirichenko, J. W. T. Hessels, M. Bhardwaj, F. Ávila, C. Bassa, P. Chawla, E. Fonseca, V. M. Kaspi, A. Keimpema, F. Kirsten, T. J. W. Lazio, B. Marcote, K. Masui, K. Nimmo, Z. Paragi, M. Rahman, D. Reverte Payá, P. Scholz, and I. Stairs. The 60-pc Environment of FRB 20180916B. *arXiv e-prints*, art. arXiv:2011.03257, Nov. 2020.

The CHIME/FRB Collaboration, :, M. Amiri, B. C. Andersen, K. Bandura, S. Berger, M. Bhardwaj, M. M. Boyce, P. J. Boyle, C. Brar, D. Breitman, T. Cassanelli, P. Chawla, T. Chen, J. F. Cliche, A. Cook, D. Cubranic, A. P. Curtin, M. Deng, M. Dobbs, Fengqiu, Dong, G. Eadie, M. Fandino, E. Fonseca, B. M. Gaensler, U. Giri, D. C. Good, M. Halpern, A. S. Hill, G. Hinshaw, A. Josephy, J. F. Kaczmarek, Z. Kader, J. W. Kania, V. M. Kaspi, T. L. Landecker, D. Lang, C. Leung, D. Li, H.-H. Lin, K. W. Masui, R. Mckinven, J. Mena-Parra, M. Merryfield, B. W. Meyers, D. Michilli, N. Milutinovic, A. Mirhosseini, M. Münchmeyer, A. Naidu, L. Newburgh, C. Ng, C. Patel, U.-L. Pen, E. Petroff, T. Pinsonneault-Marotte, Z. Pleunis, M. Rafiei-Ravandi, M. Rahman, S. M. Ransom, A. Renard, P. Sanghavi, P. Scholz, J. R. Shaw, K. Shin, S. R. Siegel, A. E. Sikora, S. Singh, K. M. Smith, I. Stairs, C. M. Tan, S. P. Tendulkar, K. Vanderlinde, H. Wang, D. Wulf, and A. V. Zwaniga. The First CHIME/FRB Fast Radio Burst Catalog. *arXiv e-prints*, art. arXiv:2106.04352, June 2021.

The LIGO Scientific Collaboration, the Virgo Collaboration, the KAGRA Collaboration, the CHIME/FRB Collaboration, :, R. Abbott, T. D. Abbott, F. Acernese, K. Ackley, C. Adams, N. Adhikari, R. X. Adhikari, V. B. Adya, C. Affeldt, D. Agarwal, M. Agathos, K. Agatsuma, N. Aggarwal, O. D. Aguiar, L. Aiello, A. Ain, P. Ajith, T. Akutsu, S. Albanesi, A. Allocca, P. A. Altin, A. Amato, C. Anand, S. Anand, A. Ananyeva, S. B. Anderson, W. G. Anderson, M. Ando, T. Andrade, N. Andres, T. Andrić, S. V. Angelova, S. Ansoldi, J. M. Antelis, S. Antier, S. Appert, K. Arai, K. Arai, Y. Arai, S. Araki, A. Araya, M. C. Araya, J. S. Areeda, M. Arène, N. Aritomi, N. Arnaud, S. M. Aronson, K. G. Arun, H. Asada, Y. Asali, G. Ashton, Y. Aso, M. Assiduo, S. M. Aston, P. Astone, F. Aubin, C. Austin, S. Babak, F. Badaracco, M. K. M. Bader, C. Badger, S. Bae, Y. Bae, A. M. Baer, S. Bagnasco, Y. Bai, L. Baiotti, J. Baird, R. Bajpai, M. Ball, G. Ballardin, S. W. Ballmer, A. Balsamo, G. Baltus, S. Banagiri, D. Bankar, J. C. Barayoga, C. Barbieri, B. C. Barish, D. Barker, P. Barneo, F. Barone, B. Barr, L. Barsotti, M. Barsuglia, D. Barta, J. Bartlett, M. A. Barton, I. Bartos, R. Bassiri, A. Basti, M. Bawaj, J. C. Bayley, A. C. Baylor, M. Bazzan, B. Bécsy, V. M. Bedakihale, M. Bejger, I. Belahcene, V. Benedetto, D. Beniwal, T. F. Bennett, J. D. Bentley, M. BenYaala, F. Bergamin, B. K. Berger, S. Bernuzzi, C. P. L. Berry, D. Bersanetti, A. Bertolini, J. Betzwieser, D. Beveridge, R. Bhandare, U. Bhardwaj, D. Bhattacharjee, S. Bhaumik, I. A. Bilenko, G. Billingsley, S. Bini, R. Birney, O. Birnholtz, S. Biscans, M. Bischi, S. Biscoveanu, A. Bisht, B. Biswas, M. Bitossi, M. A. Bizouard, J. K. Blackburn, C. D. Blair, D. G. Blair, R. M. Blair, F. Bobba, N. Bode, M. Boer, G. Bogaert, M. Boldrini, L. D. Bonavena, F. Bondu, E. Bonilla, R. Bonnand, P. Booker, B. A. Boom, R. Bork, V. Boschi, N. Bose, S. Bose, V. Bossilkov, V. Boudart, Y. Bouffanais, A. Bozzi, C. Bradaschia, P. R. Brady, A. Bramley, A. Branch, M. Branchesi, J. E. Brau, M. Breschi, T. Briant, J. H. Briggs, A. Brillet, M. Brinkmann, P. Brockill, A. F. Brooks, J. Brooks, D. D. Brown, S. Brunett, G. Bruno, R. Bruntz, J. Bryant, J. Buchanan, T. Bulik, H. J. Bulten, A. Buonanno, R. Buscicchio, D. Buskulic, C. Buy, R. L. Byer, L. Cadonati, G. Cagnoli, C. Cahillane, J. Calderón Bustillo, J. D. Callaghan, T. A. Callister, E. Calloni, J. Cameron, J. B. Camp, M. Canepa, S. Canevarolo, M. Cannavacciuolo, K. C. Cannon, H. Cao, Z. Cao, E. Capocasa, E. Capote, G. Carapella, F. Carbognani, J. B. Carlin, M. F. Carney, M. Carpinelli, G. Carrillo, G. Carullo, T. L. Carver, J. Casanueva Diaz, C. Casentini, G. Castaldi, S. Caudill, M. Cavaglià, F. Cavalier, R. Cavalieri, M. Ceasar,

G. Cella, P. Cerdá-Durán, E. Cesarini, W. Chaibi, K. Chakravarti, S. Chalathadka Subrahmanya, E. Champion, C. H. Chan, C. Chan, C. L. Chan, K. Chan, M. Chan, K. Chandra, P. Chanial, S. Chao, P. Charlton, E. A. Chase, E. Chassande-Mottin, C. Chatterjee, D. Chatterjee, D. Chatterjee, M. Chaturvedi, S. Chaty, C. Chen, H. Y. Chen, J. Chen, K. Chen, X. Chen, Y. B. Chen, Y. R. Chen, Z. Chen, H. Cheng, C. K. Cheong, H. Y. Cheung, H. Y. Chia, F. Chiadini, C.-Y. Chiang, G. Chiarini, R. Chierici, A. Chincarini, M. L. Chiofalo, A. Chiummo, G. Cho, H. S. Cho, R. K. Choudhary, S. Choudhary, N. Christensen, H. Chu, Q. Chu, Y.-K. Chu, S. Chua, K. W. Chung, G. Ciani, P. Ciecielag, M. Cieślar, M. Cifaldi, A. A. Ciobanu, R. Ciolfi, F. Cipriano, A. Cirone, F. Clara, E. N. Clark, J. A. Clark, L. Clarke, P. Clearwater, S. Clesse, F. Cleva, E. Coccia, E. Codazzo, P. F. Cohadon, D. E. Cohen, L. Cohen, M. Colleoni, C. G. Collette, A. Colombo, M. Colpi, C. M. Compton, J. Constancio, M., L. Conti, S. J. Cooper, P. Corban, T. R. Corbitt, I. Cordero-Carrión, S. Corezzi, K. R. Corley, N. Cornish, D. Corre, A. Corsi, S. Cortese, C. A. Costa, R. Cotesta, M. W. Coughlin, J. P. Coulon, S. T. Countryman, B. Cousins, P. Couvares, D. M. Coward, M. J. Cowart, D. C. Coyne, R. Coyne, J. D. E. Creighton, T. D. Creighton, A. W. Criswell, M. Croquette, S. G. Crowder, J. R. Cudell, T. J. Cullen, A. Cumming, R. Cummings, L. Cunningham, E. Cuoco, M. Curyło, P. Dabadie, T. Dal Canton, S. Dall'Osso, G. Dálya, A. Dana, L. M. DaneshgaranBajastani, B. D'Angelo, S. Danilishin, S. D'Antonio, K. Danzmann, C. Darsow-Fromm, A. Dasgupta, L. E. H. Datrier, S. Datta, V. Dattilo, I. Dave, M. Davier, G. S. Davies, D. Davis, M. C. Davis, E. J. Daw, R. Dean, D. DeBra, M. Deenadayalan, J. Degallaix, M. De Laurentis, S. Deléglise, V. Del Favero, F. De Lillo, N. De Lillo, W. Del Pozzo, L. M. DeMarchi, F. De Matteis, V. D'Emilio, N. Demos, T. Dent, A. Depasse, R. De Pietri, R. De Rosa, C. De Rossi, R. DeSalvo, R. De Simone, S. Dhurandhar, M. C. Díaz, J. Diaz-Ortiz, M., N. A. Didio, T. Dietrich, L. Di Fiore, C. Di Fronzo, C. Di Giorgio, F. Di Giovanni, M. Di Giovanni, T. Di Girolamo, A. Di Lieto, B. Ding, S. Di Pace, I. Di Palma, F. Di Renzo, A. K. Divakarla, A. Dmitriev, Z. Doctor, L. D'Onofrio, F. Donovan, K. L. Dooley, S. Doravari, I. Dorrington, M. Drago, J. C. Driggers, Y. Drori, J. G. Ducoin, P. Dupej, O. Durante, D. D'Urso, P. A. Duverne, S. E. Dwyer, C. Eassa, P. J. Easter, M. Ebersold, T. Eckhardt, G. Eddolls, B. Edelman, T. B. Edo, O. Edy, A. Effler, S. Eguchi, J. Eichholz, S. S. Eikenberry, M. Eisenmann, R. A. Eisenstein, A. Ejlli, E. Engelby, Y. Enomoto, L. Errico, R. C. Essick, H. Estellés, D. Estevez, Z. Etienne,

T. Etzel, M. Evans, T. M. Evans, B. E. Ewing, V. Fafone, H. Fair, S. Fairhurst, A. M. Farah, S. Farinon, B. Farr, W. M. Farr, N. W. Farrow, E. J. Fauchon-Jones, G. Favaro, M. Favata, M. Fays, M. Fazio, J. Feicht, M. M. Fejer, E. Fenyvesi, D. L. Ferguson, A. Fernandez-Galiana, I. Ferrante, T. A. Ferreira, F. Fidecaro, P. Figura, I. Fiori, M. Fishbach, R. P. Fisher, R. Fittipaldi, V. Fiumara, R. Flaminio, E. Floden, H. Fong, J. A. Font, B. Fornal, P. W. F. Forsyth, A. Franke, S. Frasca, F. Frasconi, C. Frederick, J. P. Freed, Z. Frei, A. Freise, R. Frey, P. Fritschel, V. V. Frolov, G. G. Fronzé, Y. Fujii, Y. Fujikawa, M. Fukunaga, M. Fukushima, P. Fulda, M. Fyffe, H. A. Gabbard, B. U. Gadre, J. R. Gair, J. Gais, S. Galaudage, R. Gamba, D. Ganapathy, A. Ganguly, D. Gao, S. G. Gaonkar, B. Garaventa, C. García-Núñez, C. García-Quirós, F. Garufi, B. Gateley, S. Gaudio, V. Gayathri, G. G. Ge, G. Gemme, A. Gennai, J. George, O. Gerberding, L. Gergely, P. Gewecke, S. Ghonge, A. Ghosh, A. Ghosh, S. Ghosh, S. Ghosh, B. Giacomazzo, L. Giacoppo, J. A. Giaime, K. D. Giardina, D. R. Gibson, C. Gier, M. Giesler, P. Giri, F. Gissi, J. Glanzer, A. E. Gleckl, P. Godwin, E. Goetz, R. Goetz, N. Gohlke, B. Goncharov, G. González, A. Gopakumar, M. Gosselin, R. Gouaty, D. W. Gould, B. Grace, A. Grado, M. Granata, V. Granata, A. Grant, S. Gras, P. Grassia, C. Gray, R. Gray, G. Greco, A. C. Green, R. Green, A. M. Gretarsson, E. M. Gretarsson, D. Griffith, W. Griffiths, H. L. Griggs, G. Grignani, A. Grimaldi, S. J. Grimm, H. Grote, S. Grunewald, P. Gruning, D. Guerra, G. M. Guidi, A. R. Guimaraes, G. Guixé, H. K. Gulati, H. K. Guo, Y. Guo, A. Gupta, A. Gupta, P. Gupta, E. K. Gustafson, R. Gustafson, F. Guzman, S. Ha, L. Haegel, A. Hagiwara, S. Haino, O. Halim, E. D. Hall, E. Z. Hamilton, G. Hammond, W. B. Han, M. Haney, J. Hanks, C. Hanna, M. D. Hannam, O. Hannuksela, H. Hansen, T. J. Hansen, J. Hanson, T. Harder, T. Hardwick, K. Haris, J. Harms, G. M. Harry, I. W. Harry, D. Hartwig, K. Hasegawa, B. Haskell, R. K. Hasskew, C. J. Haster, K. Hattori, K. Haughian, H. Hayakawa, K. Hayama, F. J. Hayes, J. Healy, A. Heidmann, A. Heidt, M. C. Heintze, J. Heinze, J. Heinzel, H. Heitmann, F. Hellman, P. Hello, A. F. Helmling-Cornell, G. Hemming, M. Hendry, I. S. Heng, E. Hennes, J. Hennig, M. H. Hennig, A. G. Hernandez, F. Hernandez Vivanco, M. Heurs, S. Hild, P. Hill, Y. Himemoto, A. S. Hines, Y. Hiranuma, N. Hirata, E. Hirose, S. Hochheim, D. Hofman, J. N. Hohmann, D. G. Holcomb, N. A. Holland, I. J. Hollows, Z. J. Holmes, K. Holt, D. E. Holz, Z. Hong, P. Hopkins, J. Hough, S. Hourihane, E. J. Howell, C. G. Hoy, D. Hoyland, A. Hreibi, B.-H. Hsieh, Y. Hsu, G.-Z. Huang, H.-Y. Huang, P. Huang, Y.-C. Huang, Y. J. Huang,

Y. Huang, M. T. Hübner, A. D. Huddart, B. Hughey, D. C. Y. Hui, V. Hui, S. Husa, S. H. Huttner, R. Huxford, T. Huynh-Dinh, S. Ide, B. Idzkowski, A. Iess, B. Ikenoue, S. Imam, K. Inayoshi, C. Ingram, Y. Inoue, K. Ioka, M. Isi, K. Isleif, K. Ito, Y. Itoh, B. R. Iyer, K. Izumi, V. JaberianHamedan, T. Jacqmin, S. J. Jadhav, S. P. Jadhav, A. L. James, A. Z. Jan, K. Jani, J. Janquart, K. Janssens, N. N. Janthalur, P. Jaranowski, D. Jariwala, R. Jaume, A. C. Jenkins, K. Jenner, C. Jeon, M. Jeunon, W. Jia, H. B. Jin, G. R. Johns, A. W. Jones, D. I. Jones, J. D. Jones, P. Jones, R. Jones, R. J. G. Jonker, L. Ju, P. Jung, K. Jung, J. Junker, V. Juste, K. Kaihotsu, T. Kajita, M. Kakizaki, C. V. Kalaghatgi, V. Kalogera, B. Kamai, M. Kamiizumi, N. Kanda, S. Kandhasamy, G. Kang, J. B. Kanner, Y. Kao, S. J. Kapadia, D. P. Kapasi, S. Karat, C. Karathanasis, S. Karki, R. Kashyap, M. Kasprzack, W. Kastaun, S. Katsanevas, E. Katsavounidis, W. Katzman, T. Kaur, K. Kawabe, K. Kawaguchi, N. Kawai, T. Kawasaki, F. Kéfélian, D. Keitel, J. S. Key, S. Khadka, F. Y. Khalili, S. Khan, E. A. Khazanov, N. Khetan, M. Khursheed, N. Kijbunchoo, C. Kim, J. C. Kim, J. Kim, K. Kim, W. S. Kim, Y. M. Kim, C. Kimball, N. Kimura, M. Kinley-Hanlon, R. Kirchhoff, J. S. Kissel, N. Kita, H. Kitazawa, L. Kleybolte, S. Klimenko, A. M. Knee, T. D. Knowles, E. Knyazev, P. Koch, G. Koekoek, Y. Kojima, K. Kokeyama, S. Koley, P. Kolitsidou, M. Kolstein, K. Komori, V. Kondrashov, A. K. H. Kong, A. Kontos, N. Koper, M. Korobko, K. Kotake, M. Kovalam, D. B. Kozak, C. Kozakai, R. Kozu, V. Kringel, N. V. Krishnendu, A. Królak, G. Kuehn, F. Kuei, P. Kuijer, A. Kumar, P. Kumar, R. Kumar, R. Kumar, J. Kume, K. Kuns, C. Kuo, H.-S. Kuo, Y. Kuromiya, S. Kuroyanagi, K. Kusayanagi, S. Kuwahara, K. Kwak, P. Lagabbe, D. Laghi, E. Lalande, T. L. Lam, A. Lamberts, M. Landry, B. B. Lane, R. N. Lang, J. Lange, B. Lantz, I. La Rosa, A. Lartaux-Vollard, P. D. Lasky, M. Laxen, A. Lazzarini, C. Lazzaro, P. Leaci, S. Leavey, Y. K. Lecoeuche, H. K. Lee, H. M. Lee, H. W. Lee, J. Lee, K. Lee, R. Lee, J. Lehmann, A. Lemaître, M. Leonardi, N. Leroy, N. Letendre, C. Levesque, Y. Levin, J. N. Leviton, K. Leyde, A. K. Y. Li, B. Li, J. Li, K. L. Li, T. G. F. Li, X. Li, C.-Y. Lin, F.-K. Lin, F.-L. Lin, H. L. Lin, L. C. C. Lin, F. Linde, S. D. Linker, J. N. Linley, T. B. Littenberg, G. C. Liu, J. Liu, K. Liu, X. Liu, F. Llamas, M. Llorens-Monteagudo, R. K. L. Lo, A. Lockwood, L. T. London, A. Longo, D. Lopez, M. Lopez Portilla, M. Lorenzini, V. Loriette, M. Lormand, G. Losurdo, T. P. Lott, J. D. Lough, C. O. Lousto, G. Lovelace, J. F. Lucaccioni, H. Lück, D. Lumaca, A. P. Lundgren, L. W. Luo, J. E. Lynam, R. Macas,

M. MacInnis, D. M. Macleod, I. A. O. MacMillan, A. Macquet, I. Magaña Hernandez, C. Magazzù, R. M. Magee, R. Maggiore, M. Magnozzi, S. Mahesh, E. Majorana, C. Makarem, I. Maksimovic, S. Maliakal, A. Malik, N. Man, V. Mandic, V. Mangano, J. L. Mango, G. L. Mansell, M. Manske, M. Mantovani, M. Mapelli, F. Marchesoni, M. Marchio, F. Marion, Z. Mark, S. Márka, Z. Márka, C. Markakis, A. S. Markosyan, A. Markowitz, E. Maros, A. Marquina, S. Marsat, F. Martelli, I. W. Martin, R. M. Martin, M. Martinez, V. A. Martinez, V. Martinez, K. Martinovic, D. V. Martynov, E. J. Marx, H. Masalehdan, K. Mason, E. Massera, A. Masserot, T. J. Massinger, M. Masso-Reid, S. Mastrogiovanni, A. Matas, M. Mateu-Lucena, F. Matichard, M. Matiushechkina, N. Mavalvala, J. J. McCann, R. McCarthy, D. E. McClelland, P. K. McClincy, S. McCormick, L. McCuller, G. I. McGhee, S. C. McGuire, C. McIsaac, J. McIver, T. McRae, S. T. McWilliams, D. Meacher, M. Mehmet, A. K. Mehta, Q. Meijer, A. Melatos, D. A. Melchor, G. Mendell, A. Menendez-Vazquez, C. S. Menoni, R. A. Mercer, L. Mereni, K. Merfeld, E. L. Merilh, J. D. Merritt, M. Merzougui, S. Meshkov, C. Messenger, C. Messick, P. M. Meyers, F. Meylahn, A. Mhaske, A. Miani, H. Miao, I. Michaloliakos, C. Michel, Y. Michimura, H. Middleton, L. Milano, A. L. Miller, A. Miller, B. Miller, M. Millhouse, J. C. Mills, E. Milotti, O. Minazzoli, Y. Minenkov, N. Mio, L. M. Mir, M. Miravet-Tenés, C. Mishra, T. Mishra, T. Mistry, S. Mitra, V. P. Mitrofanov, G. Mitselmakher, R. Mittleman, O. Miyakawa, A. Miyamoto, Y. Miyazaki, K. Miyo, S. Miyoki, G. Mo, E. Moguel, K. Mogushi, S. R. P. Mohapatra, S. R. Mohite, I. Molina, M. Molina-Ruiz, M. Mondin, M. Montani, C. J. Moore, D. Moraru, F. Morawski, A. More, C. Moreno, G. Moreno, Y. Mori, S. Morisaki, Y. Moriwaki, B. Mours, C. M. Mow-Lowry, S. Mozzon, F. Muciaccia, A. Mukherjee, D. Mukherjee, S. Mukherjee, S. Mukherjee, S. Mukherjee, N. Mukund, A. Mullavey, J. Munch, E. A. Muñiz, P. G. Murray, R. Musenich, S. Muusse, S. L. Nadji, K. Nagano, S. Nagano, A. Nagar, K. Nakamura, H. Nakano, M. Nakano, R. Nakashima, Y. Nakayama, V. Napolano, I. Nardecchia, T. Narikawa, L. Naticchioni, B. Nayak, R. K. Nayak, R. Negishi, B. F. Neil, J. Neilson, G. Nelemans, T. J. N. Nelson, M. Nery, P. Neubauer, A. Neunzert, K. Y. Ng, S. W. S. Ng, C. Nguyen, P. Nguyen, T. Nguyen, L. Nguyen Quynh, W. T. Ni, S. A. Nichols, A. Nishizawa, S. Nissanke, E. Nitoglia, F. Nocera, M. Norman, C. North, S. Nozaki, L. K. Nuttall, J. Oberling, B. D. O'Brien, Y. Obuchi, J. O'Dell, E. Oelker, W. Ogaki, G. Oganesyan, J. J. Oh, K. Oh, S. H. Oh, M. Ohashi, N. Ohishi,

M. Ohkawa, F. Ohme, H. Ohta, M. A. Okada, Y. Okutani, K. Okutomi, C. Olivetto, K. Oohara, C. Ooi, R. Oram, B. O'Reilly, R. G. Ormiston, N. D. Ormsby, L. F. Ortega, R. O'Shaughnessy, E. O'Shea, S. Oshino, S. Ossokine, C. Osthelder, S. Otabe, D. J. Ottaway, H. Overmier, A. E. Pace, G. Pagano, M. A. Page, G. Pagliaroli, A. Pai, S. A. Pai, J. R. Palamos, O. Palashov, C. Palomba, H. Pan, K. Pan, P. K. Panda, H. Pang, P. T. H. Pang, C. Pankow, F. Pannarale, B. C. Pant, F. H. Panther, F. Paoletti, A. Paoli, A. Paolone, A. Parisi, H. Park, J. Park, W. Parker, D. Pascucci, A. Pasqualetti, R. Passaquieti, D. Passuello, M. Patel, M. Pathak, B. Patricelli, A. S. Patron, S. Patrone, S. Paul, E. Payne, M. Pedraza, M. Pegoraro, A. Pele, F. E. Peña Arellano, S. Penn, A. Perego, A. Pereira, T. Pereira, C. J. Perez, C. Périgois, C. C. Perkins, A. Perreca, S. Perriès, J. Petermann, D. Petterson, H. P. Pfeiffer, K. A. Pham, K. S. Phukon, O. J. Piccinni, M. Pichot, M. Piendibene, F. Piergiovanni, L. Pierini, V. Pierro, G. Pillant, M. Pillas, F. Pilo, L. Pinard, I. M. Pinto, M. Pinto, K. Piotrzkowski, M. Pirello, M. D. Pitkin, E. Placidi, L. Planas, W. Plastino, C. Pluchar, R. Poggiani, E. Polini, D. Y. T. Pong, S. Ponrathnam, P. Popolizio, E. K. Porter, R. Poulton, J. Powell, M. Pracchia, T. Pradier, A. K. Prajapati, K. Prasai, R. Prasanna, G. Pratten, M. Principe, G. A. Prodi, L. Prokhorov, P. Prosposito, L. Prudenzi, A. Puecher, M. Punturo, F. Puosi, P. Puppo, M. Pürrer, H. Qi, V. Quetschke, R. Quitzow-James, F. J. Raab, G. Raaijmakers, H. Radkins, N. Radulesco, P. Raffai, S. X. Rail, S. Raja, C. Rajan, K. E. Ramirez, T. D. Ramirez, A. Ramos-Buades, J. Rana, P. Rapagnani, U. D. Rapol, A. Ray, V. Raymond, N. Raza, M. Razzano, J. Read, L. A. Rees, T. Regimbau, L. Rei, S. Reid, S. W. Reid, D. H. Reitze, P. Relton, A. Renzini, P. Rettegno, M. Rezac, F. Ricci, D. Richards, J. W. Richardson, L. Richardson, G. Riemenschneider, K. Riles, S. Rinaldi, K. Rink, M. Rizzo, N. A. Robertson, R. Robie, F. Robinet, A. Rocchi, S. Rodriguez, L. Rolland, J. G. Rollins, M. Romanelli, R. Romano, C. L. Romel, A. Romero-Rodríguez, I. M. Romero-Shaw, J. H. Romie, S. Ronchini, L. Rosa, C. A. Rose, D. Rosińska, M. P. Ross, S. Rowan, S. J. Rowlinson, S. Roy, S. Roy, S. Roy, D. Rozza, P. Ruggi, K. Ryan, S. Sachdev, T. Sadecki, J. Sadiq, N. Sago, S. Saito, Y. Saito, K. Sakai, Y. Sakai, M. Sakellariadou, Y. Sakuno, O. S. Salafia, L. Salconi, M. Saleem, F. Salemi, A. Samajdar, E. J. Sanchez, J. H. Sanchez, L. E. Sanchez, N. Sanchis-Gual, J. R. Sanders, A. Sanuy, T. R. Saravanan, N. Sarin, B. Sassolas, H. Satari, S. Sato, T. Sato, O. Sauter, R. L. Savage, T. Sawada, D. Sawant, H. L. Sawant, S. Sayah, D. Schaetzl, M. Scheel, J. Scheuer, M. Schiworski, P. Schmidt,

S. Schmidt, R. Schnabel, M. Schneewind, R. M. S. Schofield, A. Schönbeck, B. W. Schulte, B. F. Schutz, E. Schwartz, J. Scott, S. M. Scott, M. Seglar-Arroyo, T. Sekiguchi, Y. Sekiguchi, D. Sellers, A. S. Sengupta, D. Sentenac, E. G. Seo, V. Sequino, A. Sergeev, Y. Setyawati, T. Shaffer, M. S. Shahriar, B. Shams, L. Shao, A. Sharma, P. Sharma, P. Shawhan, N. S. Shcheblanov, S. Shibagaki, M. Shikauchi, R. Shimizu, T. Shimoda, K. Shimode, H. Shinkai, T. Shishido, A. Shoda, D. H. Shoemaker, D. M. Shoemaker, S. ShyamSundar, M. Sieniawska, D. Sigg, L. P. Singer, D. Singh, N. Singh, A. Singha, A. M. Sintes, V. Sipala, V. Skliris, B. J. J. Slagmolen, T. J. Slaven-Blair, J. Smetana, J. R. Smith, R. J. E. Smith, J. Soldateschi, S. N. Somala, K. Somiya, E. J. Son, K. Soni, S. Soni, V. Sordini, F. Sorrentino, N. Sorrentino, H. Sotani, R. Soulard, T. Souradeep, E. Sowell, V. Spagnuolo, A. P. Spencer, M. Spera, R. Srinivasan, A. K. Srivastava, V. Srivastava, K. Staats, C. Stachie, D. A. Steer, J. Steinlechner, S. Steinlechner, D. J. Stops, M. Stover, K. A. Strain, L. C. Strang, G. Stratta, A. Strunk, R. Sturani, A. L. Stuver, S. Sudhagar, V. Sudhir, R. Sugimoto, H. G. Suh, T. Z. Summerscales, H. Sun, L. Sun, S. Sunil, A. Sur, J. Suresh, P. J. Sutton, T. Suzuki, T. Suzuki, B. L. Swinkels, M. J. Szczepańczyk, P. Szewczyk, M. Tacca, H. Tagoshi, S. C. Tait, H. Takahashi, R. Takahashi, A. Takamori, S. Takano, H. Takeda, M. Takeda, C. J. Talbot, C. Talbot, H. Tanaka, K. Tanaka, K. Tanaka, T. Tanaka, T. Tanaka, A. J. Tanasijczuk, S. Tanioka, D. B. Tanner, D. Tao, L. Tao, E. N. Tapia San Martín, C. Taranto, J. D. Tasson, S. Telada, R. Tenorio, J. E. Terhune, L. Terkowski, M. P. Thirugnanasambandam, M. Thomas, P. Thomas, J. E. Thompson, S. R. Thondapu, K. A. Thorne, E. Thrane, S. Tiwari, S. Tiwari, V. Tiwari, A. M. Toivonen, K. Toland, A. E. Tolley, T. Tomaru, Y. Tomigami, T. Tomura, M. Tonelli, A. Torres-Forné, C. I. Torrie, I. Tosta e Melo, D. Töyrä, A. Trapananti, F. Travasso, G. Traylor, M. Trevor, M. C. Tringali, A. Tripathee, L. Troiano, A. Trovato, L. Trozzo, R. J. Trudeau, D. S. Tsai, D. Tsai, K. W. Tsang, T. Tsang, J.-S. Tsao, M. Tse, R. Tso, K. Tsubono, S. Tsuchida, L. Tsukada, D. Tsuna, T. Tsutsui, T. Tsuzuki, K. Turbang, M. Turconi, D. Tuyenbayev, A. S. Ubhi, N. Uchikata, T. Uchiyama, R. P. Udall, A. Ueda, T. Uehara, K. Ueno, G. Ueshima, C. S. Unnikrishnan, F. Uraguchi, A. L. Urban, T. Ushiba, A. Utina, H. Vahlbruch, G. Vajente, A. Vajpeyi, G. Valdes, M. Valentini, V. Valsan, N. van Bakel, M. van Beuzekom, J. F. J. van den Brand, C. Van Den Broeck, D. C. Vander-Hyde, L. van der Schaaf, J. V. van Heijningen, J. Vanosky, M. H. P. M. van Putten, N. van Remortel, M. Vardaro, A. F. Vargas, V. Varma, M. Vasúth, A. Vecchio,

G. Vedovato, J. Veitch, P. J. Veitch, J. Venneberg, G. Venugopalan, D. Verkindt, P. Verma, Y. Verma, D. Veske, F. Vetrano, A. Viceré, S. Vidyant, A. D. Viets, A. Vijaykumar, V. Villa-Ortega, J. Y. Vinet, A. Virtuoso, S. Vitale, T. Vo, H. Vocca, E. R. G. von Reis, J. S. A. von Wrangel, C. Vorvick, S. P. Vyatchanin, L. E. Wade, M. Wade, K. J. Wagner, R. C. Walet, M. Walker, G. S. Wallace, L. Wallace, S. Walsh, J. Wang, J. Z. Wang, W. H. Wang, R. L. Ward, J. Warner, M. Was, T. Washimi, N. Y. Washington, K. Watada, J. Watchi, B. Weaver, S. A. Webster, M. Weinert, A. J. Weinstein, R. Weiss, C. M. Weller, F. Wellmann, L. Wen, P. Weßels, K. Wette, J. T. Whelan, D. D. White, B. F. Whiting, C. Whittle, D. Wilken, D. Williams, M. J. Williams, A. R. Williamson, J. L. Willis, B. Willke, D. J. Wilson, W. Winkler, C. C. Wipf, T. Wlodarczyk, G. Woan, J. Woehler, J. K. Wofford, I. C. F. Wong, C. Wu, D. S. Wu, H. Wu, S. Wu, D. M. Wysocki, L. Xiao, W.-R. Xu, T. Yamada, H. Yamamoto, K. Yamamoto, K. Yamamoto, T. Yamamoto, K. Yamashita, R. Yamazaki, F. W. Yang, L. Yang, Y. Yang, Y. Yang, Z. Yang, M. J. Yap, D. W. Yeeles, A. B. Yelikar, M. Ying, K. Yokogawa, J. Yokoyama, T. Yokozawa, J. Yoo, T. Yoshioka, H. Yu, H. Yu, H. Yuzurihara, A. Zadrożny, M. Zanolin, S. Zeidler, T. Zelenova, J. P. Zendri, M. Zevin, M. Zhan, H. Zhang, J. Zhang, L. Zhang, T. Zhang, Y. Zhang, C. Zhao, G. Zhao, Y. Zhao, Y. Zhao, R. Zhou, Z. Zhou, X. J. Zhu, Z. H. Zhu, A. B. Zimmerman, M. E. Zucker, J. Zweizig, M. Bhardwaj, P. J. Boyle, T. Cassanelli, F. Dong, E. Fonseca, V. Kaspi, C. Leung, K. W. Masui, B. W. Meyers, D. Michilli, C. Ng, A. B. Pearlman, E. Petroff, Z. Pleunis, M. Rafiei-Ravandi, M. Rahman, S. Ransom, P. Scholz, K. Shin, K. Smith, I. Stairs, S. P. Tendulkar, and A. V. Zwaniga. Search for Gravitational Waves Associated with Fast Radio Bursts Detected by CHIME/FRB During the LIGO–Virgo Observing Run O3a. *arXiv e-prints*, art. arXiv:2203.12038, Mar. 2022.

C. A. Theissen, A. A. West, and S. Dhital. Motion Verified Red Stars (MoVeRS): A Catalog of Proper Motion Selected Low-mass Stars from WISE, SDSS, and 2MASS. AJ, 151 (2):41, Feb. 2016. doi: 10.3847/0004-6256/151/2/41.

D. Thornton, B. Stappers, M. Bailes, B. Barsdell, S. Bates, N. D. R. Bhat, M. Burgay, S. Burke-Spolaor, D. J. Champion, P. Coster, N. D'Amico, A. Jameson, S. Johnston, M. Keith, M. Kramer, L. Levin, S. Milia, C. Ng, A. Possenti, and W. van Straten. A Population of Fast Radio Bursts at Cosmological Distances. *Science*, 341:53–56, July 2013.

N. A. Tikhonov, O. A. Galazutdinova, and I. O. Drozdovsky. Thick disks and halos of spiral galaxies M 81, NGC 55 and NGC 300. A&A, 431:127–142, Feb. 2005. doi: 10.1051/0004-6361:20047042.

D. Tody. The iraf data reduction and analysis system. In *Instrumentation in astronomy VI*, volume 627, pages 733–748. International Society for Optics and Photonics, 1986.

D. Tody. IRAF in the Nineties. In R. J. Hanisch, R. J. V. Brissenden, and J. Barnes, editors, *Astronomical Data Analysis Software and Systems II*, volume 52 of *Astronomical Society of the Pacific Conference Series*, page 173, Jan. 1993.

J. L. Tonry, C. W. Stubbs, K. R. Lykke, P. Doherty, I. S. Shivvers, W. S. Burgett, K. C. Chambers, K. W. Hodapp, N. Kaiser, R. P. Kudritzki, E. A. Magnier, J. S. Morgan, P. A. Price, and R. J. Wainscoat. The Pan-STARRS1 Photometric System. 750(2):99. doi: 10.1088/0004-637X/750/2/99.

T. Totani. Cosmological Fast Radio Bursts from Binary Neutron Star Mergers. PASJ, 65: L12, Oct. 2013. doi: 10.1093/pasj/65.5.L12.

Ø. D. Trier and A. K. Jain. Goal-directed evaluation of binarization methods. *IEEE Transactions on Pattern Analysis & Machine Intelligence*, (12):1191–1201, 1995.

J. Truemper. The ROSAT mission. *Advances in Space Research*, 2(4):241–249, Jan. 1982. doi: 10.1016/0273-1177(82)90070-9.

J. W. Tukey. *Exploratory Data Analysis: Limited Preliminary Ed.* Addison-Wesley Publishing Company, 1970.

R. B. Tully. Galaxy Groups: A 2MASS Catalog. AJ, 149(5):171, May 2015. doi: 10.1088/0004-6256/149/5/171.

R. B. Tully, H. M. Courtois, and J. G. Sorce. Cosmicflows-3. AJ, 152(2):50, Aug. 2016. doi: 10.3847/0004-6256/152/2/50.

J. Tumlinson, M. S. Peeples, and J. K. Werk. The circumgalactic medium. *Annual Review of Astronomy and Astrophysics*, 55:389–432, 2017.

Y. Ueda, Y. Ishisaki, T. Takahashi, K. Makishima, and T. Ohashi. The ASCA Medium Sensitivity Survey (the GIS Catalog Project): Source Catalog. ApJS, 133(1):1–52, Mar. 2001. doi: 10.1086/319189.

H. J. Vala and A. Baxi. A review on otsu image segmentation algorithm. *International Journal of Advanced Research in Computer Engineering & Technology (IJARCET)*, 2 (2):387–389, 2013.

S. Van den Bergh. Luminosity classifications of dwarf galaxies. *The Astronomical Journal*, 71:922–926, 1966.

S. van den Bergh, W. Li, and A. V. Filippenko. Classifications of the Host Galaxies of Supernovae, Set III. PASP, 117(834):773–782, Aug. 2005. doi: 10.1086/431435.

J. van Leeuwen, E. Kooistra, L. Oostrum, L. Connor, J. E. Hargreaves, Y. Maan, I. Pastor-Marazuela, E. Petroff, D. van der Schuur, A. Sclocco, S. M. Straal, D. Vohl, S. J. Wijnholds, E. A. K. Adams, B. Adebahr, J. Attema, C. G. Bassa, J. E. Bast, A. Bilous, W. J. G. de Blok, O. M. Boersma, A. H. W. M. Coolen, H. Dénes, S. Damstra, J. P. R. de Reijer, D. W. Gardenier, Y. G. Grange, A. W. Gunst, K. M. Hess, H. A. Holties, B. Hut, A. Kutkin, G. Marcel Loose, D. M. Lucero, Á. Mika, K. Mikhailov, R. Morganti, V. A. Moss, H. Mulder, M. J. Norden, T. A. Oosterloo, E. Orrú, Z. Paragi, A. P. Schoenmakers, K. J. C. Stuurwold, S. ter Veen, W. A. van Cappellen, J. M. van der Hulst, G. N. J. van Diepen, Y. Y. Wang, A. W. Zanting, and J. Ziemke. The Apertif Radio Transient System (ARTS): Design, Commissioning, Data Release, and Detection of the first 5 Fast Radio Bursts. *arXiv e-prints*, art. arXiv:2205.12362, May 2022.

E. Vasiliev. Proper motions and dynamics of the Milky Way globular cluster system from Gaia DR2. MNRAS, 484(2):2832–2850, Apr. 2019. doi: 10.1093/mnras/stz171.

T. Velusamy, W. D. Langer, J. L. Pineda, and P. F. Goldsmith. [C ii] 158 μm line detection of the warm ionized medium in the Scutum-Crux spiral arm tangency. A&A, 541:L10, May 2012. doi: 10.1051/0004-6361/201219303.

S. D. Vergani, R. Salvaterra, J. Japelj, E. Le Floc'h, P. D'Avanzo, A. Fernandez-Soto, T. Krühler, A. Melandri, S. Boissier, S. Covino, M. Puech, J. Greiner, L. K. Hunt, D. Perley, P. Petitjean, T. Vinci, F. Hammer, A. Levan, F. Mannucci, S. Campana, H. Flores,

A. Gomboc, and G. Tagliaferri. Are long gamma-ray bursts biased tracers of star formation? Clues from the host galaxies of the Swift/BAT6 complete sample of LGRBs . I. Stellar mass at z < 1. A&A, 581:A102, Sept. 2015. doi: 10.1051/0004-6361/201425013.

S. D. Vergani, J. Palmerio, R. Salvaterra, J. Japelj, F. Mannucci, D. A. Perley, P. D'Avanzo, T. Krühler, M. Puech, S. Boissier, S. Campana, S. Covino, L. K. Hunt, P. Petitjean, and G. Tagliaferri. The chemical enrichment of long gamma-ray bursts nurseries up to z = 2. A&A, 599:A120, Mar. 2017. doi: 10.1051/0004-6361/201629759.

F. Verrecchia, C. Casentini, M. Tavani, A. Ursi, S. Mereghetti, M. Pilia, M. Cardillo, A. Addis, G. Barbiellini, L. Baroncelli, A. Bulgarelli, P. W. Cattaneo, A. Chen, E. Costa, E. Del Monte, A. Di Piano, A. Ferrari, V. Fioretti, F. Longo, F. Lucarelli, N. Parmiggiani, G. Piano, C. Pittori, A. Rappoldi, and S. Vercellone. AGILE Observations of Fast Radio Bursts. ApJ, 915(2):102, July 2021. doi: 10.3847/1538-4357/abfda7.

D. Volpi, L. Del Zanna, E. Amato, and N. Bucciantini. Non-thermal emission from relativistic mhd simulations of pulsar wind nebulae: from synchrotron to inverse compton. *Astronomy & Astrophysics*, 485(2):337–349, 2008.

A. von Kienlin, C. A. Meegan, W. S. Paciesas, P. N. Bhat, E. Bissaldi, M. S. Briggs, E. Burns, W. H. Cleveland, M. H. Gibby, M. M. Giles, A. Goldstein, R. Hamburg, C. M. Hui, D. Kocevski, B. Mailyan, C. Malacaria, S. Poolakkil, R. D. Preece, O. J. Roberts, P. Veres, and C. A. Wilson-Hodge. The Fourth Fermi-GBM Gamma-Ray Burst Catalog: A Decade of Data. ApJ, 893(1):46, Apr. 2020. doi: 10.3847/1538-4357/ab7a18.

C. R. H. Walker, Y.-Z. Ma, and R. P. Breton. Constraining the redshifts of unlocalised fast radio bursts. A&A, 638:A37, June 2020. doi: 10.1051/0004-6361/201833157.

J.-S. Wang and D. Lai. Fast Radio Burst Counterparts and Their Implications for the Central Engine. ApJ, 892(2):135, Apr. 2020. doi: 10.3847/1538-4357/ab7dbf.

W. Wang, R. Luo, H. Yue, X. Chen, K. Lee, and R. Xu. FRB 121102: A Starquake-induced Repeater? ApJ, 852(2):140, Jan. 2018. doi: 10.3847/1538-4357/aaa025.

W. Wang, B. Zhang, X. Chen, and R. Xu. Coherent Radio Emission from a Twisted Magnetosphere after a Magnetar-quake. ApJ, 875(2):84, Apr. 2019. doi: 10.3847/1538-4357/ab0e71.

W.-Y. Wang, R. Xu, and X. Chen. On the Magnetospheric Origin of Repeating Fast Radio Bursts. ApJ, 899(2):109, Aug. 2020a. doi: 10.3847/1538-4357/aba268.

W.-Y. Wang, B. Zhang, X. Chen, and R. Xu. On the magnetoionic environments of fast radio bursts. MNRAS, 499(1):355–361, Nov. 2020b. doi: 10.1093/mnras/staa2693.

D. J. Westpfahl, P. H. Coleman, J. Alexander, and T. Tongue. The geometry of the hi of several members of the m81 group: The hi is fractal. *The Astronomical Journal*, 117(2): 868, 1999.

R. Wielebinski and R. Beck. *Cosmic magnetic fields*, volume 664. Springer Science & Business Media.

V. Wild, O. Almaini, M. Cirasuolo, J. Dunlop, R. McLure, R. Bowler, J. Ferreira, E. Bradshaw, R. Chuter, and W. Hartley. A new method for classifying galaxy SEDs from multiwavelength photometry. MNRAS, 440(2):1880–1898, May 2014. doi: 10.1093/mnras/stu212.

B. F. Williams, J. J. Dalcanton, A. C. Seth, D. Weisz, A. Dolphin, E. Skillman, J. Harris, J. Holtzman, L. Girardi, R. S. de Jong, K. Olsen, A. Cole, C. Gallart, S. M. Gogarten, S. L. Hidalgo, M. Mateo, K. Rosema, P. B. Stetson, and T. Quinn. The ACS Nearby Galaxy Survey Treasury. I. The Star Formation History of the M81 Outer Disk. AJ, 137 (1):419–430, Jan. 2009. doi: 10.1088/0004-6256/137/1/419.

P. K. G. Williams and E. Berger. No Precise Localization for FRB 150418: Claimed Radio Transient Is AGN Variability. ApJ, 821(2):L22, Apr. 2016. doi: 10.3847/2041-8205/821/2/L22.

G. Worthey. Comprehensive Stellar Population Models and the Disentanglement of Age and Metallicity Effects. ApJS, 95:107, Nov. 1994. doi: 10.1086/192096.

E. L. Wright, P. R. M. Eisenhardt, A. K. Mainzer, M. E. Ressler, R. M. Cutri, T. Jarrett, J. D. Kirkpatrick, D. Padgett, R. S. McMillan, M. Skrutskie, S. A. Stanford, M. Cohen, R. G. Walker, J. C. Mather, D. Leisawitz, I. Gautier, Thomas N., I. McLean, D. Benford, C. J. Lonsdale, A. Blain, B. Mendez, W. R. Irace, V. Duval, F. Liu, D. Royer, I. Heinrichsen, J. Howard, M. Shannon, M. Kendall, A. L. Walsh, M. Larsen, J. G. Cardon, S. Schick, M. Schwalm, M. Abid, B. Fabinsky, L. Naes, and C.-W. Tsai. The Wide-field Infrared Survey Explorer (WISE): Mission Description and Initial On-orbit Performance. AJ, 140(6):1868–1881, Dec. 2010. doi: 10.1088/0004-6256/140/6/1868.

H. Xu, J. R. Niu, P. Chen, K. J. Lee, W. W. Zhu, S. Dong, B. Zhang, J. C. Jiang, B. J. Wang, J. W. Xu, C. F. Zhang, H. Fu, A. V. Filippenko, E. W. Peng, D. J. Zhou, Y. K. Zhang, P. Wang, Y. Feng, Y. Li, T. G. Brink, D. Z. Li, W. Lu, Y. P. Yang, R. N. Caballero, C. Cai, M. Z. Chen, Z. G. Dai, S. G. Djorgovski, A. Esamdin, H. Q. Gan, P. Guhathakurta, J. L. Han, L. F. Hao, Y. X. Huang, P. Jiang, C. K. Li, D. Li, H. Li, X. Q. Li, Z. X. Li, Z. Y. Liu, R. Luo, Y. P. Men, C. H. Niu, W. X. Peng, L. Qian, L. M. Song, D. Stern, A. Stockton, J. H. Sun, F. Y. Wang, M. Wang, N. Wang, W. Y. Wang, X. F. Wu, S. Xiao, S. L. Xiong, Y. H. Xu, R. X. Xu, J. Yang, X. Yang, R. Yao, Q. B. Yi, Y. L. Yue, D. J. Yu, W. F. Yu, J. P. Yuan, B. B. Zhang, S. B. Zhang, S. N. Zhang, Y. Zhao, W. K. Zheng, Y. Zhu, and J. H. Zou. A fast radio burst source at a complex magnetised site in a barred galaxy. *arXiv e-prints*, art. arXiv:2111.11764, Nov. 2021.

J. Xu and J. L. Han. Extragalactic dispersion measures of fast radio bursts. *Research in Astronomy and Astrophysics*, 15(10):1629, Oct. 2015. doi: 10.1088/1674-4527/15/10/002.

S. Yamasaki and T. Totani. The galactic halo contribution to the dispersion measure of extragalactic fast radio bursts. *The Astrophysical Journal*, 888(2):105, 2020.

H. Yang and Y.-C. Zou. Orbit-induced Spin Precession as a Possible Origin for Periodicity in Periodically Repeating Fast Radio Bursts. ApJ, 893(2):L31, Apr. 2020. doi: 10.3847/2041-8213/ab800f.

Y.-P. Yang and B. Zhang. Fast Radio Bursts as Strong Waves Interacting with the Ambient Medium. ApJ, 892(1):L10, Mar. 2020. doi: 10.3847/2041-8213/ab7ccf.

Y.-P. Yang, J.-P. Zhu, B. Zhang, and X.-F. Wu. Pair Separation in Parallel Electric Field in Magnetar Magnetosphere and Narrow Spectra of Fast Radio Bursts. ApJ, 901(1):L13, Sept. 2020. doi: 10.3847/2041-8213/abb535.

J. Yao, R. Manchester, and N. Wang. A new electron-density model for estimation of pulsar and frb distances. *The Astrophysical Journal*, 835(1):29, 2017.

O. Yaron, E. Ofek, A. Gal-Yam, and A. Sass. Fast Radio Bursts (FRBs) now reported to and distributed via the TNS. *Transient Name Server AstroNote*, 70:1, Mar. 2020.

J. Ye, K. Wang, and Y.-F. Cai. Superconducting cosmic strings as sources of cosmological fast radio bursts. *European Physical Journal C*, 77(11):720, Nov. 2017. doi: 10.1140/epjc/s10052-017-5319-2.

S.-X. Yi, H. Gao, and B. Zhang. Multi-wavelength afterglows of fast radio bursts. *The Astrophysical Journal Letters*, 792(1):L21, 2014.

B. Zackay and E. O. Ofek. An Accurate and Efficient Algorithm for Detection of Radio Bursts with an Unknown Dispersion Measure, for Single-dish Telescopes and Interferometers. ApJ, 835(1):11, Jan. 2017. doi: 10.3847/1538-4357/835/1/11.

L. V. Zadorozhna. Fast radio bursts as electromagnetic radiation from cusps on superconducting cosmic strings. *Advances in Astronomy and Space Physics*, 5(1):43–50, Sept. 2015. doi: 10.17721/2227-1481.5.43-50.

J. J. Zanazzi and D. Lai. Periodic Fast Radio Bursts with Neutron Star Free Precession. ApJ, 892(1):L15, Mar. 2020. doi: 10.3847/2041-8213/ab7cdd.

B. Zhang. A Possible Connection between Fast Radio Bursts and Gamma-Ray Bursts. ApJ, 780(2):L21, Jan. 2014. doi: 10.1088/2041-8205/780/2/L21.

B. Zhang. A "Cosmic Comb" Model of Fast Radio Bursts. ApJ, 836(2):L32, Feb. 2017. doi: 10.3847/2041-8213/aa5ded.

B. Zhang. FRB 121102: A Repeatedly Combed Neutron Star by a Nearby Low-luminosity Accreting Supermassive Black Hole. ApJ, 854(2):L21, Feb. 2018. doi: 10.3847/2041-8213/aaadba.

B. Zhang. The physical mechanisms of fast radio bursts. Nature, 587(7832):45–53, Nov. 2020. doi: 10.1038/s41586-020-2828-1.

G. Q. Zhang, H. Yu, J. H. He, and F. Y. Wang. Dispersion Measures of Fast Radio Burst Host Galaxies Derived from IllustrisTNG Simulation. 900(2):170. doi: 10.3847/1538-4357/abaa4a.

Y. Zhang, J.-J. Geng, and Y.-F. Huang. Fast Radio Bursts from the Collapse of Strange Star Crusts. ApJ, 858(2):88, May 2018. doi: 10.3847/1538-4357/aabaee.

P. Zhou, X. Zhou, Y. Chen, J.-S. Wang, J. Vink, and Y. Wang. Revisiting the Distance, Environment, and Supernova Properties of SNR G57.2+0.8 that Hosts SGR 1935+2154. ApJ, 905(2):99, Dec. 2020. doi: 10.3847/1538-4357/abc34a.

H. Zou, J. Gao, X. Zhou, and X. Kong. Photometric Redshifts and Stellar Masses for Galaxies from the DESI Legacy Imaging Surveys. ApJS, 242(1):8, May 2019. doi: 10.3847/1538-4365/ab1847.